INTERNATIONAL DOCTORAL
SCHOOL OF THE USC

Ramón Ángel
Ruiz Fernández

PhD Thesis

Inside the precision era: exploring new physics through quark flavor transitions at LHCb

Santiago de Compostela, 2024

Doctoral Programme in Nuclear and Particles Physics

INTERNATIONAL DOCTORAL SCHOOL OF THE USC

UNIVERSIDADE DE SANTIAGO DE COMPOSTELA

DOCTORAL THESIS

INSIDE THE PRECISION ERA: EXPLORING NEW PHYSICS THROUGH QUARK FLAVOR TRANSITIONS AT LHCB

Author

Ramón Ángel Ruiz Fernández

Supervisors: Veronika Georgieva Chobanova

Jonathan Richard Ellis

Promotor: Diego Martínez Santos

DOCTORAL PROGRAMME IN NUCLEAR AND PARTICLE PHYSICS

SANTIAGO DE COMPOSTELA, 2024

Abstract

The Standard Model (SM) of Particle Physics is a quantum field theory that describes elementary particles and their interactions. While experiments have repeatedly confirmed its predictions, the SM cannot explain several phenomena such as dark matter or the matter-antimatter misbalance present in the observed Universe. Therefore, new physics (NP) models are needed. This thesis explores these issues in three different approaches. First, to test the SM, the most accurate measurement of the CP violating phase $\phi_s^{c\bar{c}s}$ is achieved by the analysis of $B_s^0 \to J/\psi K^+ K^-$ decays collected by the LHCb detector during the data-taking years 2015-2018. The complex phase $\phi_s^{c\bar{c}s}$ is directly related to the complex phase present in the parametrization of the CKM matrix and therefore responsible for the CP violation within the SM in the quark sector. The CP violation present in the CKM matrix is not enough to explain the matter-antimatter imbalance and hence, is a perfect place for looking for NP footprints. This analysis is categorized as a golden channel as it also constitutes the world's best measurement of the decay width of the B_s^0 meson, the difference between decay widths of the mass eigenstates of the B_s^0 meson and the CP violating parameter $|\lambda|$, which is related with the CP violation present in the decay. Second, to improve future measurements of CP violation in the interference between the decay and the decay through mixing, advancements in the flavor tagging algorithm technique using the inclusive approach are analyzed. This experimental technique is used to infer through the information present in the tracks of the event the flavor of the B meson at the production point. For this, a DeepSet classifier is implemented and relative improvements to the classical techniques of 22% and 37% in $B_s^0 \to D_s^- \pi^+$ and $B^0 \to J/\psi K^*$, respectively are observed. Finally, the implications of the measurement of $\phi_s^{c\bar{c}s}$ as well as other flavor precision observables in the context of supersymmetric models, which address some of the limitations of the SM, such as providing a valid DM candidate are reported in this thesis.

Limiar

O Modelo Estándar (SM) da Física de Partículas é unha teoría cuántica de campos que describe as partículas elementais e as súas interaccións. Aínda que os experimentos confirmaron repetidamente as súas predicións, o SM non pode explicar varios fenómenos como a materia escura ou o desequilibrio materia-antimateria presente no Universo observado. Polo tanto, necesítanse modelos de nova física (NP). Esta tese explora estas cuestións en tres enfoques diferentes. En primeiro lugar, para probar o SM, a medición máis precisa da fase que viola a simetría CP, $\phi_s^{c\bar{c}s}$, conséguese mediante a análise de decaementos do tipo $B_s^0 \to J/\psi K^+K^-$ recollidos polo detector LHCb durante os anos de toma de datos 2015-2018. A fase complexa $\phi_s^{c\bar{c}s}$ está directamente relacionada coa fase complexa presente na parametrización da matriz CKM, responsable da violación CP dentro do SM no sector dos quarks. A violación CP presente na matriz CKM non é suficiente para explicar o desequilibrio materia-antimateria sendo esta medida un lugar perfecto para buscar contribucións de NP. Esta análise clasifícase como unha canle dourada xa que tamén constitúe a mellor medida do mundo do ancho de desintegración do mesón B_s^0, a diferenza entre os anchos de desintegración dos estados propios de masa do mesón B_s^0 e o parámetro de violación CP, $|\lambda|$, que está relacionado coa violación CP presente na decaemento. En segundo lugar, para mellorar futuras medidas de violación CP na interferencia entre o decaemento e o decaemento a través da mestura, analízanse os avances na técnica do algoritmo de etiquetado de sabor mediante o enfoque inclusivo. Esta técnica experimental úsase para inferir, a través da información presente nas trazas do evento, o sabor do mesón B no punto de produción. Para iso, implementouse un clasificador cunha arquitectura DeepSet e obsérvanse melloras relativas ás técnicas clásicas do 22% e 37% en $B_s^0 \to D_s^- \pi^+$ e $B^0 \to J/\psi K^*$, respectivamente. Finalmente, analízanse nesta tese as implicacións da medición de $\phi_s^{c\bar{c}s}$ así como doutros observables de precisión do sabor no contexto dos modelos supersimétricos, que abordan algunhas das limitacións do SM, como proporcionar un candidato de materia escura válido.

Preface

This thesis describes my work during the period 2020 to 2024. The first chapter serves as a necessary introduction to the Standard Model (SM). I made all the SM predictions of observables and figures presented in this chapter, with important input from Diego Martinez Santos. The second chapter serves as an introduction to the experimental conditions under which this thesis was developed. I created every figure presented in this chapter myself. Chapter three describes the objectives and methods developed during this thesis. Chapter four summarizes the world's best measurement of the $\phi_s^{c\bar{c}s}$ phase within the LHCb collaboration. My main contributions included the study and validation of the decay time and angular efficiencies, the flavor tagging calibration, including the analysis of the calibration modes, the implementation of different corrections to the final decay time and angular fit, and the evaluation of several systematics and cross-checks. I also contributed to the implementation of the selection, the mass fit and the decay-time resolution procedures in the analysis framework developed in Santiago. I created all the figures presented in this chapter except Figure 4.2, Figure 4.20, and Figure 4.21 which were provided by the HFLAV collaboration [1]. Important contributions to the analysis came from the rest of the proponents of the ϕ_s analysis, especially Marcos Romero Lamas, Peilian Li, Sevda Esen, Valeriia Lukashenko, Diego Martinez Santos, and Veronika Chobanova. Chapter 5 is dedicated to the study of Inclusive Flavor Tagging. My contributions involve all parts of the chapter, from the production of the tuples, contributions to the training, the calibration of the output of the NN, performance studies, and the sensitivity study of ϕ_s. Important contributions to this study came from John Wendel and Veronika Chobanova. The Inclusive Flavor Tagging technique was not implemented in the baseline of the ϕ_s measurement because, at the time of completing the ϕ_s measurement, the Inclusive Flavor Tagging yielded a slightly lower performance than the combination of classical taggers. Chapter 6 focuses on phenomenological studies within SUSY theories. The first part was performed by the MasterCode collaboration, where the scan was performed by Ian Pang, Emanuele Bagnaschi, and Miriam Lucio Martinez. My main contributions to this part were the evaluation of the flavor constraints, maintaining the framework in the Santiago cluster, and producing the plots shown in this thesis. Important contributions to this section came from the rest of the members of the MasterCode collaboration. Finally, my contributions to the study of the FV SUSY models involved developing the scan framework, implementing all the observables, calculating the constraints, running the sampling, and performing all the figures shown in this chapter as well as discussing the results. All calculations were performed by Teppei Kitahara. Important contributions to this project came from Miriam Lucio Martinez and Diego Martinez Santos.

Contents

Abstract **iii**

Limiar (abstract in Galician) **iv**

1 Introduction **1**
1.1 The Standard Model of Particle Physics . . . 1
1.1.1 Flavor phenomenology . . . 3
1.1.2 Effective Field Theories . . . 5
1.1.3 Where to look? Flavor Changing Transition . . . 6
1.2 The Need for New Physics . . . 10
1.2.1 Dark Matter . . . 11
1.2.2 Matter Antimatter imbalance . . . 11
1.2.3 Neutrino Masses . . . 11
1.2.4 Inclusion of Gravity . . . 12
1.2.5 Some "anomalies" to follow up... . . . 12
1.2.6 Theoretical Motivations . . . 13

2 Experimental conditions **14**
2.1 The Large Hadron Collider . . . 14
2.2 The LHCb detector . . . 15
2.2.1 Magnet . . . 16
2.2.2 Tracking and vertexing . . . 17
2.2.3 Particle identification system . . . 19
2.3 Trigger . . . 21
2.3.1 L0 Trigger . . . 21
2.3.2 High Level Trigger . . . 22
2.4 The LHCb Software . . . 22
2.5 Data taking periods and conditions . . . 23

3 Objectives and methodology **24**
3.1 Objectives . . . 24
3.2 Methodology . . . 25

4 The world's best measurement of $\phi_s^{c\bar{c}s}$ **26**
4.1 Introduction . . . 26
4.1.1 Types of CP Violation in B decays . . . 27
4.1.2 Difference between ϕ_s^{12} and $\phi_s^{c\bar{c}s}$ . . . 27

4.1.3 Theoretical and Experimental status before this measurement 28
4.2 Phenomenology of the decay $B_s^0 \to J/\psi KK$ 29
4.3 Selection 32
4.3.1 Variables used in selection 32
4.3.2 Trigger Strategy and Stripping selection 33
4.3.3 Background categories in simulation 33
4.3.4 MC corrections to match the data 34
4.3.5 Boosted Decision Tree-based selection 36
4.3.6 Peaking backgrounds contributions 39
4.3.7 Mass fits and computation of sWeights 39
4.4 Analysis 41
4.4.1 Mass Dependence 41
4.4.2 Decay time Resolution 42
4.4.3 Decay time bias 44
4.4.4 Decay time Acceptance 46
4.4.5 Angular Acceptance 51
4.4.6 Flavor Tagging 57
4.5 Results 62
4.5.1 Model with experimental corrections 62
4.5.2 Polarization independent results 64
4.5.3 Polarization dependent results 64
4.6 Cross-checks and systematics 67
4.6.1 Consistency checks and validations 67
4.6.2 Systematic uncertainties 70
4.7 Conclusions 73

5 The novel Inclusive Flavor Tagging **76**
5.1 Introduction 77
5.2 Training 77
5.2.1 BDT-based track classification 80
5.2.2 DeepSet training 81
5.3 Calibration 85
5.3.1 $B_s^0 \to D_s^- \pi^+$ calibration 88
5.3.2 $B^0 \to J/\psi K^{*0}$ calibration 96
5.4 Performance studies 101
5.4.1 Alternative calibration method 102
5.4.2 Removing background tracks 103
5.4.3 Dependence of the tagging power on kinematic and event properties . 103
5.5 $\phi_s^{c\bar{c}s}$ sensitivity study 105
5.6 Summary of Results and Conclusions 108

6 Quark-flavor transitions in Supersymmetry **110**
6.1 Introduction and Motivation 110
6.1.1 Minimal Supersymmetric Standard Model 111
6.1.2 SUSY Breaking 113

6.1.3 SUSY Dark Matter . . . 114
6.2 Flavor Simplified models: cMSSM . . . 116
6.3 Full model in Mass Insertion approximation . . . 125
6.3.1 Formalism . . . 125
6.3.2 Parameter scan . . . 127
6.3.3 Observables . . . 129
6.3.4 Results . . . 135
6.4 Conclusions . . . 144

7 Results and conclusions **146**

8 Resumo (Extended summary in Galician) **148**

Appendices **155**

A Inputs used for SM predictions **156**

B Simulation samples used in $\phi_s^{c\bar{c}s}$ measurement **157**

C MSSM contributions **159**

D Plot projections NMFV **167**

E Figure authorisation **173**

Bibliography **174**

Chapter 1

Introduction

Particle physics involves the dynamic exploration of nature's most fundamental building blocks, the elementary particles and their interactions. At the forefront of our understanding, stands the Standard Model of Particle Physics. This theory has demonstrated remarkable predictive accuracy in numerous measurements and has addressed significant theoretical challenges. It provides a Lorentz invariant quantum description of both strong and electroweak interactions, categorizing the elementary particles into fermions with half-spin and gauge bosons, the interactions mediators, characterized by having an integer spin. Fermions are further divided into leptons, solely affected by electroweak force, and quarks, affected by both strong and electroweak interactions. The unique nature of the strong interaction confines quarks into mesons or baryons. Leptons, not influenced by strong interactions, can exist freely in nature. This quantum description of our universe represents the culmination of more than 60 years of hard work by particle physicists and stands as one of the greatest milestones in science. However, despite its successes the Standard Model is not without its limitations, leading us to speculate about the need for a more fundamental theory. A brief overview of the Standard Model will be described in this initial chapter as well as the intriguing open questions that persist beyond this framework.

1.1 The Standard Model of Particle Physics

The Standard Model (SM) is a quantum field theory of the strong, electromagnetic, and weak interactions. The group representation of internal symmetries is given by [2, 3]:

$$G_{SM} = SU(3)_C \times SU(2)_T \times U(1)_Y. \tag{1.1}$$

The symmetry group $SU(3)_C$ (where C refers to color) is associated with Quantum Chromodynamics (QCD), which describes the strong interaction. In contrast, the direct product $SU(2)_T \times U(1)_Y$ (where T refers to the weak isospin and Y to the hypercharge) characterizes the electroweak interaction [3]. Matter comprises gauge bosons, which mediate interactions, and fermionic states, on which these interactions act. Eight gluons mediate QCD while the electroweak (EW) bosons are constituted by the massless photon, γ, and the massive $W^{\pm}$ and Z^0 bosons. This is the result of the electroweak symmetry breaking produced after the

Higgs field acquires a nonzero vacuum expectation value (VEV), breaking the group symmetry of the SM to $G_{SM} \rightarrow SU(3) \times U(1)_{EM}$ [3]. Due to this symmetry breaking the SM predicts a particle with zero spin, first observed at LHC by ATLAS and CMS collaborations in 2012 [4, 5]. The SM is described by the following density Lagrangian [2]:

$$\begin{aligned}\mathcal{L}_{SM} = & -\frac{1}{4}G^a_{\mu\nu}G^{\mu\nu,a} - \frac{1}{4}W^a_{\mu\nu}W^{\mu\nu,a} - \frac{1}{4}B_{\mu\nu}B^{\mu\nu} \\ & + \sum_{i=1}^{3} \bar{L}_i i\not{D} L_i + \bar{E}_{R,i} i\not{D} E_{R,i} + \bar{Q}_i i\not{D} Q_i + \bar{U}_{R,i} i\not{D} U_{R,i} + \bar{D}_{R,i} i\not{D} D_{R,i} \\ & + |D_\mu \phi|^2 - V(\phi) \\ & - \bar{Q}\phi y^D d_R - \bar{Q}\phi^c y^U U_R - \bar{O}\phi^c y^E E_R + h.c.,\end{aligned} \tag{1.2}$$

where the first line corresponds to the kinetic terms of the gauge bosons, while the second line shows the kinetics of the fermions and the interactions between the fermions and the gauge bosons [2]. These first two lines constitute the gauge component of the SM and are commonly known as the "elegant part" because everything is fixed by local gauge symmetry. The only degrees of freedom are the coupling constants of the electroweak and strong interaction (α and α_s), the mass of the W boson (m_W), and the Weinberg angle, θ_W.

The second and third lines of Eq. 1.2 are referred to as the "Higgs part". The second line describes the Higgs potential, the kinematics of the Higgs field, and the interactions of the Higgs field with the gauge bosons while the last line corresponds to the interaction between the fermions and the Higgs field, known as Yukawa terms [2]. The "Higgs part" incorporates a total of 15 degrees of freedom, of which 13 come from the Yukawa terms. This is the origin of the flavor phenomenology that will be exploited in this thesis.

The SM fermions which acquire elemental mass through their interaction with the Higgs field, are represented in the SM internal group symmetry by [3]:

$$\begin{aligned}&\text{Quarks: } Q_{L,i} = (3, 2, +\frac{1}{6}) \;\; U_{R,i} = (3, 1, -\frac{1}{3}) \;\; D_{R,i} = (3, 1, -1/3), \\ &\text{Leptons: } \quad L_{L,i} = (1, 2, -\frac{1}{2}) \quad E_{R,i} = (1, 1, -\frac{1}{2}).\end{aligned} \tag{1.3}$$

The numbers in parentheses indicate the representation under strong and electroweak interactions, as well as the hypercharge respectively. The leptons do not interact with gluons, so they are singlets under $SU(3)$. Weak interaction only affects left parts, so only $\mathcal{Q}_L$ and $\mathcal{L}_L$ are charged under $SU(2) \times U(1)$, which makes the SM a parity-violating theory. The subscript, i, indicates the fermion generation, differentiated only by their masses. These masses are particularly different between generations and are degrees of freedom within the theory. A schematic representation of the particle content of the SM can be found in Fig. 1.1.

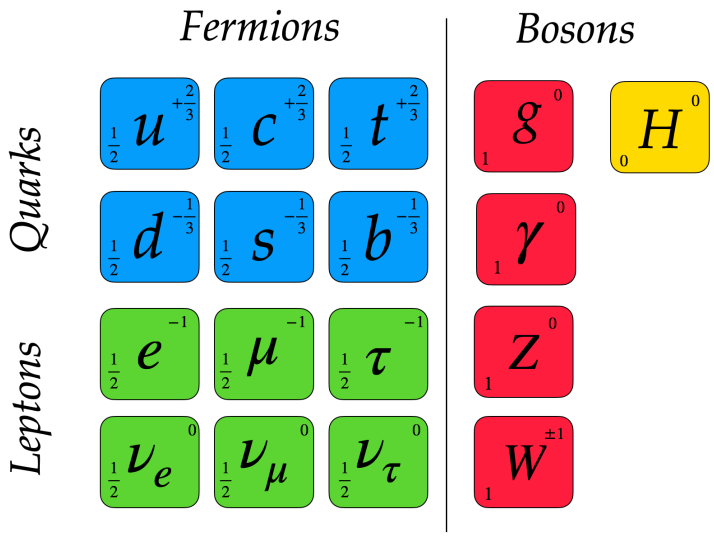

FIGURE 1.1: Elemental particles present in the SM. Electric charge and spin are shown for each field.

1.1.1 Flavor phenomenology

Ordinary matter consists mainly of the first family of quarks and leptons namely the up and down quarks, the electron, and the electron neutrino as can illustrated in Fig. 1.1. The second and third generations are essentially just heavier copies of this first family. These heavier copies are produced in high-energy collisions and decay weekly into the first generation of fermions.

The SM description of fermion masses is considered unsatisfactory and implies the addition of arbitrariness due to the introduction of free parameters into the theory. Specifically, there are six quark masses, three charged lepton masses, three mixing angles, and one complex phase[1]. It is important to note that in this argument neutrinos are not considered as they are assumed to be massless within the SM, although experimental evidence since 1998 shows that they must have tiny but non-zero mass [6]. This would imply an addition of more free parameters that will depend on the exact nature of the neutrinos.

The second line of Eq. 1.2 is invariant under $[U(3)]^5$ symmetry, where 3 stands for the number of generations and 5 for the independent representations as given in Eq. 1.3. However, the Yukawa terms, which correspond to the last line of Eq. 1.2, break this global symmetry down to $[U(1)]^4$ [2]. This translates into four accidental symmetries within the SM, baryon number, and three individual lepton flavor number conservations[2] [2].

[1] By adding the Higgs physical mass and the vacuum expectation value, a total of 15 degrees of freedom are added by the Higgs part of Eq. 1.2

[2] These symmetries are not exact at $T >> 0$, as non-perturbative solutions of the SM EW fields produce baryon and lepton number violating processes known as sphaleron [7].

The Yukawa matrices $y^{D,U,E}$ of Eq. 1.2 are 3×3 arbitrary matrices that cannot be simultaneously diagonalized using only the flavor rotations of $[U(3)]^5$. This is easy to understand as Yukawa matrices need bi-unitary transformations to be diagonalized. Taking as an example the quark sector, 4 matrices will be needed to diagonalize $y^{U,D}$ but only 3 are available [2]:

$$\mathcal{Q} \to V_L^u \mathcal{Q}_L \quad \mathcal{U}_R \to V_R^u \mathcal{U}_R \quad \mathcal{D}_R \to V_R^d \mathcal{D}_R, \tag{1.4}$$

where V_L^u, V_R^u and V_R^d are 3×3 unitary matrices. Expanding the last line of Eq. 1.2 for quarks and applying this rotation, the following expression is obtained [2]:

$$\mathcal{L}_{Y,quarks} = -\bar{\mathcal{Q}}\phi(V_L^u)^\dagger V_L^d \hat{y}^D d_R - -\bar{\mathcal{Q}}\phi\hat{y}^U u_R + h.c., \tag{1.5}$$

where h.c. stands for the hermitian conjugate. Note that the first term of Eq. 1.5 is non-diagonal which implies that further diagonalization is needed to obtain the mass (physical) eigenstates :

$$d_L \to d'_L = (V_L^u)^\dagger V_L^d d_L = V_{CKM} d_L = \begin{pmatrix} V_{ud} & V_{us} & V_{ub} \\ V_{cd} & V_{cs} & V_{cb} \\ V_{td} & V_{ts} & V_{tb} \end{pmatrix} d_L, \tag{1.6}$$

here d'_L represents the original flavor eigenstates, d_L denotes the mass eigenstates, and V_{CKM} stands for the CKM matrix, named after Cabibbo, Kobayashi and Maskawa [8, 9]. It is essential to note, that this mismatch between flavor eigenstates and mass eigenstates is responsible for quark flavor transitions in SM. This is not the case for leptons, as in SM right-handed neutrinos do not exist. Incorporating them would introduce the Pontecorvo-Maki-Nakagawa-Sakata (PMNS) matrix [10, 11], analogous to the CKM matrix but in the lepton sector. Nevertheless, this straightforward extension assumes that neutrinos are Dirac particles, which may not be the case, as the tiny mass of neutrinos compared with electrons can point to them being Majorana particles. Experiments are underway to understand the particular nature of neutrinos.

The CKM matrix defined in Eq. 1.6, is a unitary 3×3 matrix that can be parametrized by three angles and one complex phase[3]. This complex phase constitutes the only complex coupling of the SM and is responsible for the presence of matter-antimatter asymmetry within the model. More specifically, this phase implies a violation of the CP symmetry (CPV), where C stands for charge-conjugation that transforms particles into anti-particles and P stands for Parity equivalent to a point reflection. The CPV is one of the Sakharov conditions needed to observe a Universe dominated by matter [12][4]. This is a unique feature of the SM and predicts a strong correlation among all the CPV processes, providing a way of over-constraining and testing the SM. Chapter 4 of this thesis consists of the precise measurement of one observable related to this complex phase, the measurement of $\phi_s^{c\bar{c}s}$.

[3]With only two generations, no phases are needed, leading to total matter-antimatter annihilation.

[4]There is another complex phase in $\mathcal{L}_{QCD}$, the θ term but it is experimentally constrained to be $\leq 10^{-10}$ due to non-observation of neutron and Hg permanent EDMs [13].

Experiments have shown that the CKM matrix is almost the identity matrix:

$$V_{CKM} = \begin{pmatrix} 0.97461 & 0.22386 & 0.00167-0.00384i \\ -0.22373-0.00017i & 0.97374 & 0.042160 \\ 0.00780-0.00374i & -0.04147-0.00086i & 0.99910 \end{pmatrix}, \tag{1.7}$$

where the numbers correspond to a private fit using the Bjorken-Dunietz parametrization [14] when excluding potential heavy New Physics contributions, particularly Minimal Supersymmetric Standard Model (MSSM) contributions (the inputs used for this fit are listed in the first block of App. A). For the absolute values of the V_{CKM} elements, the most likely transitions are those between the same generation, showing a hierarchical structure for the rest. Additionally, it can be seen that the complex phases of the CKM matrix are small, implying that CP violation is highly suppressed in the SM.

Before continuing with the description of some important flavor observables for testing New Physics (NP), an important theoretical tool needs to be described first, the low-energy effective Lagrangians.

1.1.2 Effective Field Theories

An important feature of weak decays of hadrons is that they involve different energy scales. Taking for example B meson decays, they involve at least the EW scale ($\mu = M_W$) for the flavor changing transitions and the b quark mass as the energy released in the decay ($\mu = M_B \simeq m_b$). The idea behind effective field theories is that we can successfully describe a physics process by only using the degrees of freedom important for the processes and "integrating out" the others [15]. A typical example is the Fermi theory of neutron decay where the W boson was integrated out because it was not discovered by that time, a schematic representation can be seen in Fig. 1.2. This Effective Hamiltonians takes the following form using the Operator Product Expansion (OPE) [16]:

$$H_{eff} = \frac{G_F}{\sqrt{2}} \sum_i V^i_{CKM} C_i(\mu) \mathcal{Q}_i(\mu), \tag{1.8}$$

where G_F is the Fermi constant, V^i_{CKM} represents the CKM elements involved, Q_i are the local operators that include only the initial and final field states, and finally the Wilson Coefficients $C_i(\mu)$ describe the strength of the operators Q_i and summarize the physics contributions at higher energy scale (shorter distance) than μ [16]. Having defined H_{eff}, the decay amplitude of a B meson (B) into a final state F is evaluated as [16]:

$$A(B \to F) = \frac{G_F}{\sqrt{2}} \sum_i V^i_{CKM} C_i(\mu) \langle F| Q_i(\mu) |B\rangle, \tag{1.9}$$

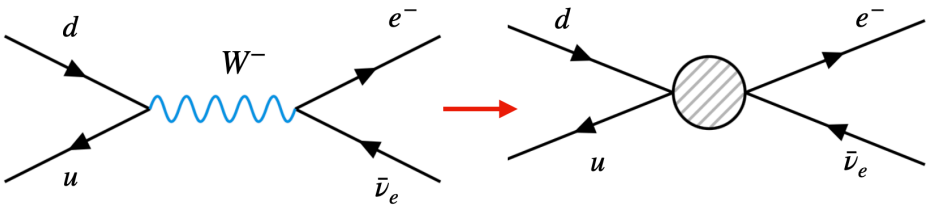

FIGURE 1.2: Schematic example of integrating out the W^- boson in a neutron decay. On the left tree-level contribution to the decay while the effective four-fermion interaction is illustrated on the right plot.

where the hadronic matrix elements of Q_i between B (initial state) and F (final state) are represented by $\langle F|\, Q_i(\mu)\, |B\rangle$ [16]. These matrix elements summarize the contributions from scales lower than μ. Therefore, the advantage of OPE is that it allows us to differentiate between short-distance (perturbative) calculations of $C_i(\mu)$ and long-distance (nonperturbative) matrix elements $\langle Q_i(\mu)\rangle$ [16]. In extensions of the SM involving heavy NP, deviations from the values of the Wilson coefficients within the SM are expected due to the inclusion of new diagrams. Usually, this is parametrized as follows, taking as reference the SM calculation

$$\Delta C_i(\mu) = C_i^{NP}(\mu) - C_i^{SM}(\mu), \tag{1.10}$$

1.1.3 Where to look? Flavor Changing Transition

The mismatch between flavor and mass eigenstates implies flavor-changing transitions through tree-level interactions of the $W^\pm$ bosons or rarer loop-suppressed Flavor Changing Neutral Currents (FCNC) processes. Testing the SM and searching for NP footprints, involves two main approaches: direct and indirect detection. Direct detection entails producing new particles in high-energy colliders, which inherently depends on the unknown masses of these particles. The second approach, indirect detection infers the existence of new particles through quantum fluctuations, resulting in (typically small) deviations in certain observables [2]. To detect NP by this second approach, the quantum contribution of new particles needs to be comparable with the SM prediction of this observable, highlighting the importance of FCNC processing.

In this thesis, the focus lies on indirect detection and the implications of very precise measurements in the flavor sector for the SM and Beyond SM (BSM) theories. A very important type of process here is FCNC as in SM they are loop-suppressed, and therefore the NP contribution can compete with the SM one. One particular but important example of FCNCs is the one known as box-diagrams ($\Delta F = 2$ transition) responsible for meson - antimeson mixing (see Fig. 1.3).

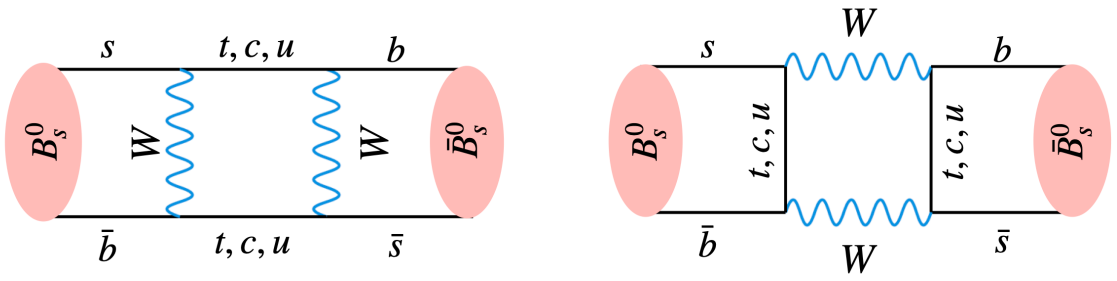

FIGURE 1.3: Box diagram for B_s^0-$\bar{B}_s^0$ mixing. This diagram consists of two parts, the off-shell part, M_{12} which receives contributions from all the particles listed, and the on-shell part, Γ_{12}, which receives contributions only from u and c quarks.

Of particular interest is the case of B^0 and B_s^0 mixing, given that $m_b >> \Lambda_{QCD}$, which is a key ingredient to do precise SM predictions[5]. The time evolution of the $\left|B_q^0\right\rangle = |(\bar{b}q)\rangle$ and their antiparticle $\left|\bar{B}_q^0\right\rangle = |(b\bar{q})\rangle$ can be described by the following differential equation [17]:

$$
\begin{aligned}
i\frac{\partial}{\partial t}\begin{pmatrix}\left|B_q^0(t)\right\rangle \\ \left|\bar{B}_q^0(t)\right\rangle\end{pmatrix} &= \left[\hat{M}^q - \frac{i}{2}\hat{\Gamma}^q\right]\begin{pmatrix}\left|B_q^0(t)\right\rangle \\ \left|\bar{B}_q^0(t)\right\rangle\end{pmatrix} \\
&= \begin{pmatrix}M_{11} - \frac{i}{2}\Gamma_{11} & M_{12} - \frac{i}{2}\Gamma_{12} \\ M_{21} - \frac{i}{2}\Gamma_{21} & M_{22} - \frac{i}{2}\Gamma_{22}\end{pmatrix}\begin{pmatrix}\left|B_q^0(t)\right\rangle \\ \left|\bar{B}_q^0(t)\right\rangle\end{pmatrix},
\end{aligned}
\tag{1.11}
$$

where $\hat{M}^q$ and $\hat{\Gamma}^q$ are 2×2 matrices related to the masses and lifetimes of the B_q^0 and $\bar{B}_q^0$ mesons. In the flavor space, these matrices are not diagonal and are governed by the box diagram of Fig. 1.3. Particularly, these box diagrams can include contributions from on-shell particles (Γ_{12}) or virtual ones (M_{12}). The latter contribution is of particular interest to this thesis as it is also sensitive to heavy NP particles.

Imposing CPT invariance the matrix elements must satisfy $M_{11} = M_{22}$, $\Gamma_{11} = \Gamma_{22}$, $M_{21} = M_{12}^*$ and $\Gamma_{21} = \Gamma_{12}^*$. Now, for getting the physical eigenstates one must diagonalize the Hamiltonian, which gives rise to $\left|B_{q,H}^0\right\rangle$ and $\left|B_{q,L}^0\right\rangle$ where H, L stands for heavy and light respectively. Expanding these eigenvalues and dropping terms of $\mathcal{O}(|\Gamma_{12}/M_{12}|^2)$ one can obtain the following relations [17]:

[5] K^0 and D^0 mixing are also very interesting as they are even more suppressed in the SM, however, they are theoretical and experimental challenges

$$\begin{aligned} \Delta M_q &\equiv M_H^s - M_L^s \simeq 2|M_{12}^q|, \\ \Gamma_q &\equiv \Gamma_L^q - \Gamma_H^q \simeq 2|\Gamma_{12}^q| cos\phi_s^{12}, \\ a_{sl}^q &\simeq \frac{|\Gamma_{12}^q|}{|M_{12}^q|} \sin\phi_q^{12}, \end{aligned} \tag{1.12}$$

with the mixing phase defined as:

$$\phi_q^{12} \equiv \arg\left(-\frac{M_{12}^q}{\Gamma_{12}^q}\right). \tag{1.13}$$

Focusing on the off-shell part because of its sensitivity to heavy NP, M_{12} is calculated to be [17]:

$$M_{12}^q = -|V_{tq}^* V_{tb}|^2 \frac{G_F^2 m_W^2 \eta_B m_{Bq} B_{Bq} f_{Bq}^2 S_0(m_t^2/m_W^2)}{12\pi^2}, \tag{1.14}$$

Taking this parametrization, and using the CKM elements of Eq. 1.7 along with the inputs of App. A, the following SM predictions for the B_s^0 and the B^0 meson are obtained:

$$\begin{aligned} \Delta M_s^{SM} &= (18.13 \pm 0.69)\text{ps}^{-1}, \\ \Delta M_d^{SM} &= (0.524 \pm 0.045)\text{ps}^{-1}. \end{aligned} \tag{1.15}$$

These SM predictions are compatible with the latest literature, see for example Ref. [18].

The second FCNC to be described involves $\Delta F = 1$ transitions. Specifically, this discussion begins with the inclusive rare decay $B \to X_s\gamma$. This decay is sensitive to the following operators [2]:

$$Q_7 = \frac{e}{16\pi^2} m_b (\bar{s}_L \sigma^{\mu\nu} b_R) F_{\mu\nu}, \qquad Q_8 = \frac{g_s}{16\pi^2} m_b (\bar{s}_L \sigma^{\mu\nu} T^a b_R) G_{\mu\nu}^a, \tag{1.16}$$

Which are the magnetic and chromo-magnetic operators. This inclusive decay has played an important role in constraining NP, particularly the branching ratio. Both theoretical prediction and experimental measurement are very precise, leaving small room for NP. Concretely latest global fits to experimental data constraints C7 as $\Delta C_7 = 0.0 \pm 0.2$ [19]. To conclude with the status of $b \to s\gamma$ transitions, it is noteworthy to mention the difference of CP asymmetries in $B^- \to X_s^- \gamma$, and $\bar{B}^{\to} X_s^0 \gamma$, which was measured by Babar to be $(+5.0 \pm 3.9 \pm 1.5)\%$ [20]. In the SM, this observable is predicted to be exactly zero, making it highly sensitive to NP, particularly to imaginary parts of C_7 and C_8.

Another set of EW penguins that received a lot of attention in recent years is the $b \to s l^+ l^-$ and $b \to d l^+ l^-$ transitions. These transitions are sensitive to two new operators (apart from the ones in $B \to X_s \gamma$) [15]:

$$Q_9^l = \frac{e}{16\pi^2} m_b (\bar{s}_L \gamma^\mu b_L) \sum_l (\bar{l} \gamma^\mu l), \quad Q_{10}^l = \frac{e}{16\pi^2} m_b (\bar{s}_L \gamma^\mu b_L) \sum_l (\bar{l} \gamma^\mu \gamma^5 l), \tag{1.17}$$

which are respectively the vector and axial operators. Note that within the SM, the Wilson coefficients of the operators Q_9 and Q_{10} are lepton universal, although this may not be the case for some NP scenarios. Even after the LHCb update of R_K and R_{K^*} [21], global model independent fits suggest that NP is favored over SM for explaining neutral current anomalies. However, lepton flavor violation solutions are no longer preferred as large universal C_9^U contributions can also explain experimental data [19]. It is important to note, that before attributing these deviations to NP, further theoretical and experimental work is required, as these contributions could also be mimicked by hadronic effects, particularly $c\bar{c}$ loops [22].

Continuing with $\Delta F = 1$ processes, the status of the rare decay $B_q \to l^+ l^-$ will now be described. In the SM, these processes are not only loop suppressed (see Fig. 1.4) but also helicity suppressed [15]. The helicity suppression factor is proportional to m_l^2/m_B^2 [15] and is the reason why the di-muon mode is easier to investigate than the di-electron mode. The di-tau mode is very promising as the SM prediction is enhanced (~ 280 times) but it is very challenging from the experimental point of view [15]. The best experimental measurement comes from LHCb [23] and is several orders of magnitude above the SM prediction [2].

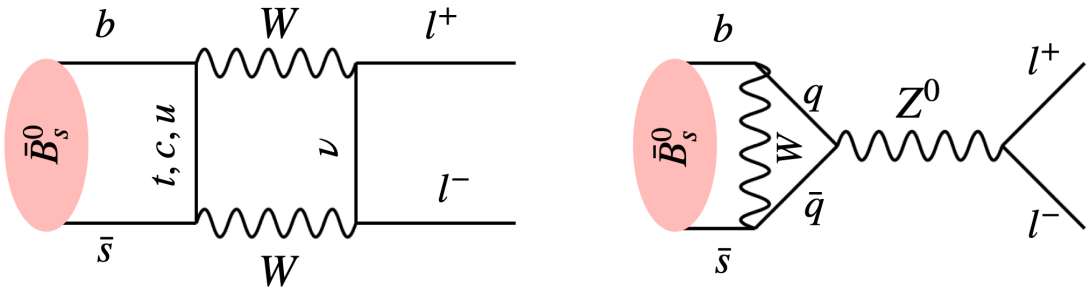

FIGURE 1.4: Loop Feynman diagrams contributions to $B_s^0 \to l^+ l^-$ within the SM.

Focusing now on the di-muon case, we can use the parametrization from [24, 25] and recalculate it with the CKM elements of Eq. 1.7 along with the parameters provided in App. A, obtaining:

$$\begin{aligned} \mathcal{B}(B_s^0 \to \mu^+ \mu^-) &= (3.69 \pm 0.11) \times 10^{-9}, \\ \mathcal{B}(B^0 \to \mu^+ \mu^-) &= (1.015 \pm 0.068) \times 10^{-10}. \end{aligned} \tag{1.18}$$

Apart from the B-sector, which is already measurable, there are also efforts in $D^0 \to \mu^+\mu^+$ and $K_S^0 \to \mu^+\mu^-$ decays. The SM prediction for $D^0 \to \mu^+\mu^-$ can be calculated using $D^0 \to \gamma\gamma$ from Belle [26], yielding $BR^{SM}(D^0 \to \mu^+\mu^-) < 2 \times 10^{-11}$, while the experimental combination of LHCb using Run 1 and Run 2 data samples is found to be at 95% CL, $BR^{EXP}(D^0 \to \mu^+\mu^-) < 3.5 \times 10^{-9}$ [27]. The case of $K_S^0 \to \mu^+\mu^-$ is particularly interesting as the SM prediction is more precise with $BR^{SM}(K_S^0 \to \mu^+\mu^-) = (5.18 \pm 1.5_{LD} \pm 0.02_{SD}) \times 10^{-12}$ [28], while the experimental upper limit at 95% CL is $BR^{EXP}(K_s^0 \to \mu^+\mu^-) < 2.4 \times 10^{-10}$ using Run 1 and Run 2 data [29]. The LHCb Upgrade 2 could bring down the precision of $K_s^0 \to \mu\mu$ to the SM level, making this particular decay very promising for the future.

To finalize this section we are going to talk about the tree-level decay $B^+ \to \tau^+\nu$. The reason is that in the MSSM this Branching Ratio (BR) receives an enhancement factor $\propto (\tan\beta)^4$. In the SM this process is mediated by an $W^\pm$ exchange and the BR can be parametrized as [2]:

$$\mathcal{B}^{SM}(B^+ \to \tau^+\nu) = \frac{G_F^2 m_{B^+} m_\tau^2}{8\pi}\left(1 - \frac{m_\tau^2}{m_{B^+}^2}\right)^2 f_{B^+}^2 |V_{ub}|^2 \tau_{B^+} = (1.112 \pm 0.092) \times 10^{-4}, \quad (1.19)$$

where the CKM elements of Equation 1.7 and the inputs listed in App. A were used. To summarize this section a summary of some of the SM predictions of the flavor observables that will be studied during the thesis as well as the latest experimental measurement combinations are shown in Table 1.1.

Observables	SM Prediction	Experimental Value
ΔM_s	$(18.13 \pm 0.69)\text{ps}^{-1}$	$(17.765 \pm 0.057)\text{ps}^{-1}$ [1]
ΔM_d	$(0.524 \pm 0.044)\text{ps}^{-1}$	$(0.5065 \pm 0.0019)\text{ps}^{-1}$ [1]
$\mathcal{B}(B_s^0 \to \mu\mu)$	$(3.69 \pm 0.11) \times 10^{-9}$	$(3.52 \pm 0.33) \times 10^{-9}$ [30, 31, 32]
$\mathcal{B}(B^0 \to \mu\mu)$	$(1.015 \pm 0.068) \times 10^{-10}$	$(4.1 \times 4.6) \times 10^{-10}$ [30, 31, 32]
$\mathcal{B}(B^+ \to \tau\nu)$	$(11.12 \pm 0.92) \times 10^{-4}$	$(10.9 \pm 2.4) \times 10^{-4}$ [33]

TABLE 1.1: Comparison between Standard Model predictions and experimental values for some of the observables used in this thesis.

1.2 The Need for New Physics

In §1.1.3 some interesting observables aimed at discovering New Physics were described. This pursuit stems from our firm belief that the SM cannot be the ultimate theory, given its unresolved questions. These questions, which will be described in the remainder of this chapter, lead us to think that SM is just an effective theory valid up to a determined energy scale.

1.2.1 Dark Matter

One of the most important puzzles within the Standard Model (SM) is the absence of a viable candidate for Dark Matter (DM). This hypothetical form of matter interacts neither with light nor with baryonic matter, save for gravitational effects. Within the framework of the cosmological model ΛCDM, DM is five times more prevalent in the Universe than ordinary matter. In the SM, the only candidates are neutrinos, which are relativistic and hence not "cold", and MACHOs (Massive Astrophysical Compact Halo Objects), which are baryonic and can only account for a small fraction of DM. There is ample evidence supporting the existence of DM, including the anomalous rotational speeds of galaxies, the anisotropies in the cosmic microwave background, and gravitational lensing. Generally, at the time of writing this thesis, the existence of DM is accepted and the SM cannot explain it. Additionally, another enigmatic component in the Universe, Dark Energy, accounts for 68% of the total energy content (assuming again ΛCDM) and is responsible for the accelerating expansion of the Universe. However, its nature remains completely unknown. In conclusion, despite the incredible precision provided by the SM for most of the observables tested in colliders, astronomical evidence indicates that the SM can only explain about 5 % of the total content of the Universe.

1.2.2 Matter Antimatter imbalance

After the Big Bang, an equal amount of particles and antiparticles were presumably produced. However, despite this theoretical balance, we have not observed any galaxies composed of antimatter; everything we see appears to be composed of matter. When anti-matter is produced in colliders, for example, it quickly annihilates with matter to produce energy. Intriguingly, a remanent of matter has prevailed giving rise to the Universe that we observe it. Within the SM there are only two terms that can produce this imbalance, the θ term in the QCD Lagrangian and the complex phase of the CKM matrix. The first one is experimentally constrained to be $< 10^{-10}$ because of the non-measurement of the electric dipole moment of the neutron. The phase of the CKM matrix is also far from being able to explain this apparent discrepancy. As highlighted previously SM can only account for approximately the 5 % of the Universe, yet the reason why it seems to be exclusively made by matter remains unknown.

1.2.3 Neutrino Masses

Experimental evidence, from neutrino oscillations [6], indicates that neutrinos have a tiny but non-zero mass. This is not explained within the SM. While it is feasible to employ a similar procedure as in the quark sector to add mass to neutrinos, assuming that they are Dirac particles, it also presents a problem: explaining why neutrino mass is so small compared with electron mass. Alternatively, neutrinos could be Majorana particles that acquire mass due to the Seesaw mechanism (which could explain their smallness). Several experiments

are currently underway to understand the true nature of neutrinos, but regardless of the outcome, it is clear that explanations will have to go beyond SM physics.

1.2.4 Inclusion of Gravity

The Standard Model cannot incorporate quantum gravity. Quantum gravity effects become significant at extremely high energies (about 10^{19} GeV), which means the Standard Model cannot describe physics accurately at these energy levels.

1.2.5 Some "anomalies" to follow up...

- a_μ: The anomalous magnetic moment of the muon is considered a long-standing anomaly. This quantity was measured with an extraordinary precision by BNL-E821 and FNAL-E989 experiments, yielding $a_\mu^{EXP,WA} = 116592059(22) \times 10^{-11}$ [34, 35]. The tension appears on the theory side. Taking the data-driven method based on e^+e^- annihilation data up to 2020 [36] shows a discrepancy of 5σ. In recent years, lattice computations have become more competitive and have shown a significant deviation from the previous prediction, reducing the discrepancy with the measurement [37]. Furthermore, a new preliminary measurement of the $e^+e^- \to \pi^+\pi^-$ cross-section from the CMD-3 experiment disagrees with previous e^+e^- data [38], going in lattice direction.
- Cabibbo Anomaly Angle (CAA): As explained in this chapter the CKM matrix must be unitary to conserve probability, taking the first row and first column of the CKM matrix from Ref. [33], one gets $|V_{ud}|^2 + |V_{us}|^2 + |V_{ub}|^2 = 0.99848 \pm 0.00070$ which shows a 2.2σ tension with the unity.
- Tension at the 2σ level between exclusive and inclusive determination of V_{cb} and V_{ub}.
- Charged current B decays: These are tree-level transitions ($b \to cl\nu$) that consist of an interchange of a $W^\pm$ boson. The anomaly is present in the ratio of Branching Ratios $R(D^*) = Br(B \to D^{(*)}\tau\nu)/Br(B \to D^{(*)}\{e,\mu\}\nu)$. This observable shows a $> 3\sigma$ tension. The idea that this observable competes at tree level with the SM led some theorists to speculate to an NP that couples heavily to 3rd generation [39].
- $b \to sl^+l^-$ transitions: In the post R_K era there are still some discrepancies with the experiment in the observable $P5'$, and some branching ratios like BR($B_s \to \phi\mu^+\mu^-$) and BR($B^+ \to K\mu^+\mu^-$) (see Ref. [39] for a complete list).
- Nonleptonic B decays: The prediction for the ratio between longitudinal branching ratios of $\bar{B}_s \to K^{*0}\bar{K}^{*0}$ and $\bar{B} \to K^{*0}\bar{K}^{*0}$, $L_{K^{*0}\bar{K}^{*0}}$, show a $\sim 2.5\sigma$ tension with the experiment [40]. The measured branching ratios of $\bar{B}^0_{(s)} \to D^{(*)+}_{(s)}\{\pi^-, K^-\}$ show a 4σ discrepancy with the SM prediction based on QCD factorization [41]. This section also includes the long-standing $B \to K\pi$ puzzle (see Ref. [42] for a recent review).
- Forward-backward asymmetries of the bottom (A^b_{FB}) quark observed at LEP presents a $\sim 2.5\sigma$ tension with the SM prediction [43].

1.2.6 Theoretical Motivations

1.2.6.1 Unification of interactions

Looking at the energy dependence of the coupling strengths, it can be seen that they tend to converge at an energy scale around $\sim 10^{16}$ GeV, although the exact unification is not possible within the SM. This problem is directly related to the arbitrary number of free parameters that conform to the SM, as in principle a Grand Unified Theory (GUT) can predict some correlation between these degrees of freedom [2].

1.2.6.2 The hierarchy problem

No symmetry protects the Higgs mass within the SM. This instability manifests in the quantum corrections to the Higgs mass calculations, which exhibit a quadratic dependence on the energy scale at which the SM is examined [44]:

$$m_h^2 = (m_h^2)^0 + \lambda\Lambda^2, \tag{1.20}$$

where Λ is the UV momentum cut-off, (m_h^0) is the tree-level Higgs boson mass and λ is of the order of the EM coupling constant. The fine-tuning required between the bare mass and the radiative corrections to maintain the Higgs mass in the EW scale is considered unnatural. This is usually called in the literature hierarchy problems and is one of the main reasons to think that NP should be around the TeV scale.

In conclusion, the SM presents several intriguing challenges that suggest the possible emergence of NP at an energy scale not far from the TeV scale. This thesis will focus on two main challenges: the matter-antimatter imbalance and the study of potential candidates for DM, as well as some experimental anomalies presented before such as the anomalous magnetic moment of the muon and the anomalies present in $b \to sll$ data. To address these challenges, the measurement of the $\phi_s^{c\bar{c}s}$ phase - a crucial component of CPV within the SM - is presented in Chapter 4. This quantity is expected to be very small in the SM, making it highly sensitive to NP. Improvements in the strategies for future measurements of CPV quantities in the interference, specifically in the flavor tagging techniques, are discussed in Chapter 5. Finally, DM and its connection with flavor phenomenology within Supersymmetric theories is studied in Chapter 6. The data analyzed in both, Chapter 4 and Chapter 5, were recollected by the LHCb detector during the 2015-2018 data-taking period. An overview of the detector is provided in Chapter 2.

Chapter 2

Experimental conditions

This chapter provides an overview of the experimental framework in which this thesis is performed, the LHCb detector, one of the key detectors at the Large Hadron Collider (LHC). The LHCb detector specializes in precise measurements of flavor observables primarily through the analysis of decays of heavy hadrons. As discussed in Chapter 1, indirect detection is a powerful tool for inferring New Physics, and the motivation behind constructing the LHCb detector stemmed from our limited understanding of the flavor sector within the SM.

2.1 The Large Hadron Collider

The Large Hadron Collider (LHC) is the largest particle collider, located at The European Organization for Nuclear Research (CERN by its French abbreviation). The LHC is a circular ring of almost 27 km situated 100 meters underground to be protected from cosmic rays. It is mainly designed to study proton-proton collisions, but the physics program is extended to also study heavy ion collisions. Two beams of these protons go in opposite directions respectively, inside their tubes maintained with ultra-vacuum conditions. These beams are forced to collide at four interaction points at a rate of 40 MHz. At these interaction points stand the largest detectors designed to collect the data. The main experiments installed at LHC are as follows:

- ATLAS (A toroidal LHC Apparatus): It is the largest experiment at the LHC and is mainly dedicated to direct detection. It was designed for the study of the Higgs Boson and general high transverse momentum (p_T) searches, particularly supersymmetric particles, leptoquarks (LQ), and other massive particles predicted by BSM theories.
- CMS (Compact Muon Solenoid): The main objective of CMS is similar to that of ATLAS, focusing mainly on direct detection and the general search for heavy New Physics (NP). The indirect detection program of CMS differs significantly from ATLAS, as they focus on enhancing the purity of the data sample by using efficient trigger strategies. This enables them to conduct very competitive CP violation measurements.
- ALICE (A large Ion collider): It is dedicated to the study of quark-gluon plasma (QGP), a state of matter produced at very high densities and energies. The conditions are very

similar to those believed to have existed in the Universe just after the Big Bang, leading to the hypothesis that the Universe was populated by QGP during this period.

- LHCb (Large Hadron Collider beauty): It is a forward spectrometer mainly designed for the study of the CP violation in decays of heavy hadrons. The data analyzed in this thesis corresponds to the data collected by this experiment, which will be described in more detail in the next section.

2.2 The LHCb detector

The LHCb is a single-arm forward spectrometer dedicated to the study of heavy flavor physics. Its main objective is to indirectly uncover the presence of NP particles in CP violation and heavy hadron decay measurements. Beyond this, the LHCb collaboration has a broad physics program that includes the study of the production of electroweak bosons in the forward region, the study of exotic hadrons such as tetraquarks and pentaquarks, measurements of quarkonia production in proton-lead collision, search for lepton flavor and lepton number violation, long-lived particles among others, which convert LHCb in a general-purpose experiment [45].

A notable difference between the LHCb detector experiment concerning the other main LHC experiments is that it is a forward spectrometer. The design choice is motivated by the $b\bar{b}$ quark pair production mechanism in p-p collisions at high energies, which is predominantly produced in the same forward or backward cone concerning the direction of the beam. This is because these heavy quark pairs originate from highly asymmetric proton collisions in gluon-gluon fusions [46]. Specifically, the LHCb angular acceptance covers the angle defined with respect to the beam of 15 and 300 mrad in the bending plane (XZ) and 15 to 250 mrad in the non-bending plane (YZ, see Fig. 2.1). This angular acceptance is typically specified in terms of pseudorapidity (η) as $1.6 \leq \eta \leq 4.9$, where η is defined as [45]:

$$\eta = -\frac{1}{2} \ln \frac{p + p_Z}{p - p_Z} = -\ln \tan \frac{\theta}{2}, \tag{2.1}$$

where p is the total momentum of the particle, p_Z, is the momentum of the particle along the beam axis, and θ is the angle between the particle trajectory and the beam. A schematic layout of the detector in the non-bending (YZ) plane can be found in Fig. 2.1.

While the unique shape of the detector optimizes the amount of $b\bar{b}$ pairs collected, the LHCb detector also encounters inherent challenges as a precision measurement detector within a hadron collider. The main obstacle is distinguishing the decays of interest from background tracks, which are typically between 10 and 200 times more likely [45]. To accomplish this, the focus must be on identifying the main signatures of b and c hadron decays. These particles often have significant lifetimes, leading to substantial flight distances (around 1 cm for B decays for example). Additionally, they are heavy (m > 1 GeV), resulting in decay products with high transverse momentum as the mass difference between the parent particles and the

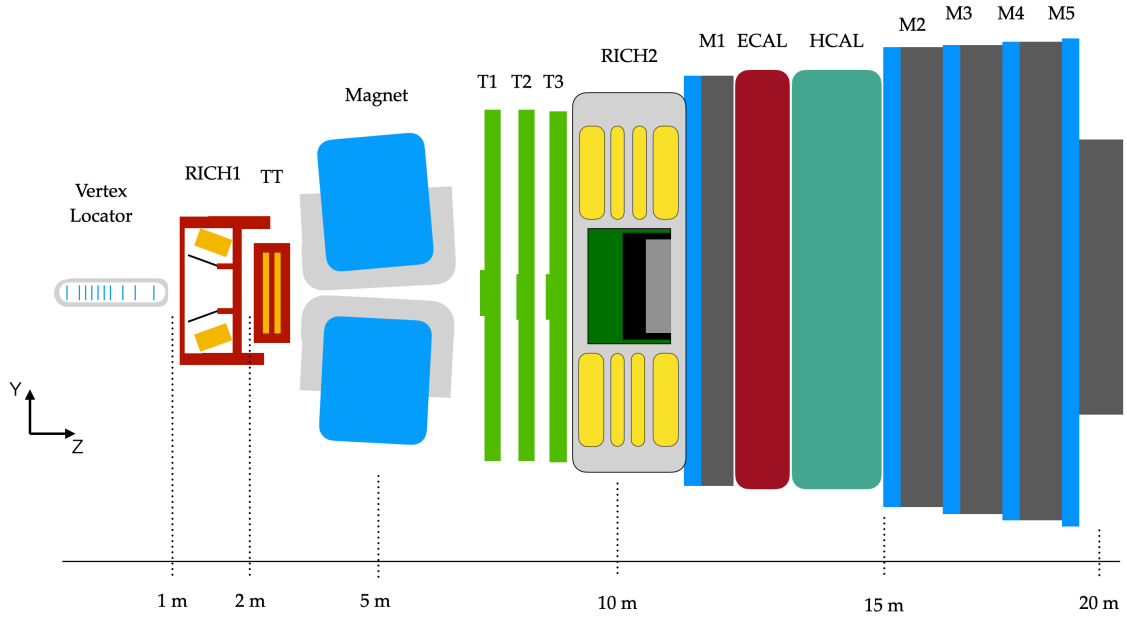

FIGURE 2.1: Side view of the LHCb detector in the non-bending plane, the B-field is aligned with the y-axis.

final state is large. Therefore the LHCb detector must have excellent vertex and momentum resolution as fundamental ingredients. Bearing this in mind, the LHCb subdetectors can be categorized as follows:

- Magnet: Bend charged particles allowing for momentum measurement.
- Tracking system: Measures trajectories of charged particles. Consists of the VELO (Vertex Locator), near the interaction point, to distinguish between the primary vertex (B meson production) and the secondary vertex (where B meson decays), the TT (Trigger Tracker) upstream of the magnet, and the three Tracking stations downstream of the magnet.
- Particle identification system: Subdetectors that identify the particle that produced the trajectory. It consists of the RICHs (Ring Imaging Cherenkkov detectors), which identify particles by their Cherenkov effect, ECAL (Electromagnetic Calorimeter) to detect electrons and photons, HCAL (Hadron Calorimeter) to detect hadrons and the muon chambers to detect the muons.

2.2.1 Magnet

A dipole magnet [47] is used by the LHCb detector to measure the momentum of charged particles. The magnetic field integral is 4 T.m. and is measured with a relative precision at the order of a few times 10^{-4}. The peak of the B-field is also measured with a precision of a

few millimeters [45]. This precision is necessary to achieve the excellent momentum resolution required. To control systematic effects, the direction of the magnetic field is periodically changed.

2.2.2 Tracking and vertexing

Heavy hadrons, such as B mesons, produced in high-energy p-p collisions, have a significant boost, decaying within a few centimeters inside the Vertex Locator. Additional information is obtained from the kinematic properties of the decay products, where the tracking system plays a crucial role. It provides measurements of the trajectories of the charged decay products, which, combined with information from the magnet, allow us to infer the charge and momentum of the charged final states. Subsequently, each component within this system will be explained in detail. For a better understanding, consider also consulting Fig. 2.2 while reading this section.

2.2.2.1 Vertex Locator (VELO)

The VErtex LOcator (VELO) [48] is the tracking detector that measures a particle's production and decay vertices, referred to as primary (PV) and secondary vertex (SV), respectively. This is generally the most important and sensitive part of the reconstruction process.

The VELO detector is composed of 21 stations of silicon detectors, with each station consisting of two halves positioned on opposite sides of the beam [49]. Each module half contains two detectors: the R sensor that measures the radial coordinate of the trajectory, and a Φ detector, with strips in the almost radial direction, subdivided into inner and outer region that determines the azimuthal coordinate ϕ. The 3D coordinate system is completed by adding the sensor coordinate (z) within the experiment. This cylindrical geometry is selected to facilitate the rapid reconstruction of tracks and vertices [45].

The VELO sensors are operated in a vacuum, which is isolated from the LHC vacuum by a thick 300 μm aluminum structure known as RF-Foil [45]. This additional material decreases the quality of tracking observables, such as the impact parameter (IP) as particles produced in p-p collisions may interact with it. From the analysis point of view, the RF foil is also important due to its particular shape, which implies that this is typically simplified in simulations (depending on the kinematics of the decay), leading to potential differences between simulation and data.

Under stable beam conditions, the VELO is positioned at a radial distance of 7 mm from the beam, ensuring excellent vertex resolution at the μm level. The resolution for determining the IP is approximately 20 μm, while the measurement of the decay length ranges from 220 μm to 370 μ m [45]. This translates into a decay time resolution of around 45 fs, enabling the measurement of the B_s^0 meson oscillations. To mitigate radiation damage during unstable beam conditions, the two halves of the VELO can be separated by up to 6 cm.

2.2.2.2 Tracking System

In addition to the VELO, the Tracking system is composed of the Tracker Turicensis or Trigger Tracker (TT) positioned upstream of the magnet and three Tracking stations (T1, T2, and T3) situated downstream of the magnet (see Fig. 2.1). Each of the four stations consists of four detection layers with vertical strips, where the second (third) layer is rotated by +5º (-5º) to make 3D reconstruction possible.

The TT is utilized to reconstruct particles with low momenta that are bent by the Magnet out of the LHCb acceptance. It also provides information for the Level-1 trigger to assign transverse momentum to tracks with large IP [50].

As the occupancy is higher closer to the beam the TT and the inner parts of the T-stations (Inner Tracker) use silicon microstrip sensors. The TT is entirely silicon-based (unlike the T-stations which are hybrid) due to its use for Level-1 Trigger. Since they employ the same technology, they are commonly grouped under the name of Silicon Tracker (ST). The spatial resolution is 5μm implying that momentum resolution is dominated by multiple scattering [50].

The remaining part of the T-stations is a drift-tube gas detector called an Outer Tracker (OT). It is constituted by 64 gas straw tube modules with a drift time read out below 50 ns and 200 μm of spacial resolution [51].

Regarding the subdetectors involved, in LHCb the tracks are classified as follows: (see Fig. 2.2 for a schematic representation).

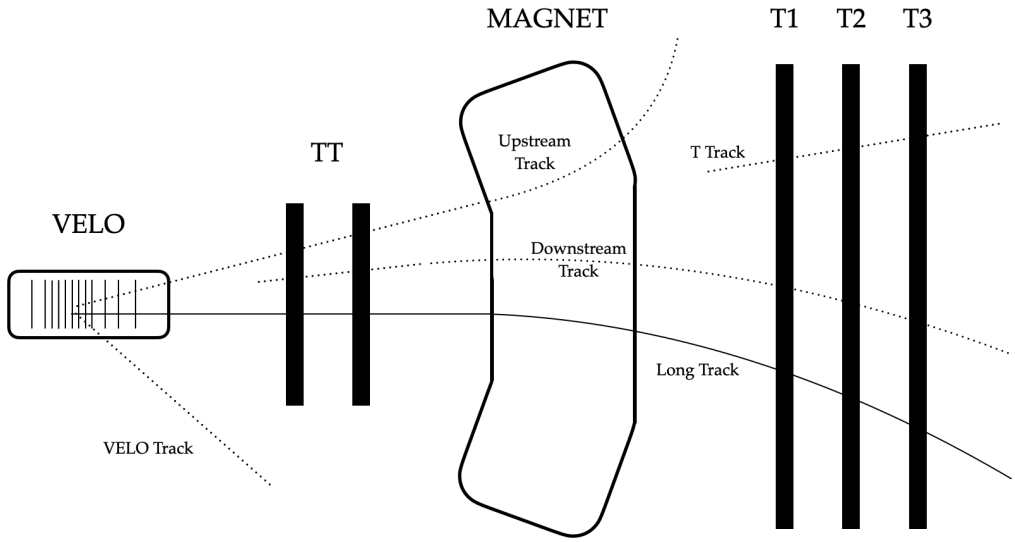

FIGURE 2.2: Classification of tracks at LHCb frameworks attending to the subdetectors involved.

- Long Tracks: These trajectories involve hits in all the tracking subdetectors, from the VELO to the T-stations. They provide the most precise momentum measurement.
- Upstream Tracks: They have hits from the VELO and the TT. Typically, it corresponds to particles with low momentum that are bent out by the magnet. This type of track is used for the training of the flavor tagging (FT) algorithms (see Chapter 5).
- Downstream Tracks: Hits in the TT and the T-stations are typically associated with strange physics where the lifetimes are bigger (and therefore decay after the VELO) like K_S^0, Λ^0...
- VELO tracks: only hits in VELO that are used for PV reconstruction and pile-up (number of PVs) measurements used for the trigger.
- T-Tracks: Tracks with hits only in the T-stations.
- Ghost Tracks: Tracks that do not correspond to real particles, typically combinations of hits of different particles or detector noise. It is reduced by using a Kalman Filter [52] which takes into account multiple scattering.

2.2.3 Particle identification system

The tracking system provides information about the trajectories of the charged particles, but it is also needed to identify which particle produces each track. In LHCb, there are three types of detectors designated for this function: the Ringing Imaging Cherenkov (RICH) detectors, The calorimeters, and the muon chambers.

2.2.3.1 RICH

The RICH detectors enable the identification of charged particles by measuring the angle of emission of Cherenkov radiation [49]. These photons are emitted when a charged particle passes through a medium with a refractive index (n) greater than one, a value precisely known by the gas within the detector. By combining the measurement of this angle with the particle momentum and trajectory, it becomes possible to infer the mass, and therefore to identify the particle.

There are two RICH detectors at LHCb, one upstream of the magnet just before the TT, and the other downstream of the T-stations (see Fig. 2.1). The upstream detector, RICH1, covers the momentum range from 2 to 60 GeV/c (low momentum), while the RICH2 covers the high momentum range from 15 to 100 GeV/c [49]. The angular acceptance of the RICH1 covers the full angular acceptance of the LHCb, while the RICH2 only covers from $\pm$15 to $\pm$120 (100) mrad in the bending (non-bending) plane [49]. The RICH detectors are mainly used to differentiate between kaons, protons, and pions. In general, the misidentification is higher for high-momentum particles, where the most complicated is the differentiation between kaons and pions. The RICH has an excellent angular resolution and the efficiency of identification is independent of the track charge [49].

2.2.3.2 Calorimeter sytem

The calorimeter system of LHCb has several functions. It identifies photons, electrons, and hadrons, measures their energy and position, and selects candidates with high transverse energy, which is used as an input for the first trigger level that makes decisions after 4μs of the interaction [45]. It is constituted by a Scintillating Pad Detector (SPD), a Preshower (PS), an electromagnetic calorimeter (ECAL), and a hadronic calorimeter (HCAL) [49, 53].

- The SPD and PS system is composed of two rectangular scintillators separated by a thick (15 mm) lead converter. The SPD allows to differentiation of neutrals from charged particles (to reject $\pi^0 \to \gamma\gamma$ background) as only charged particles produced showers in the scintillator. The lead converter allows differentiation between electrons and photons from neutral and charged hadrons, as the latter tend to have a larger interaction length and leave a smaller shower in the PS detector (to reject charged pions) [49].
- The ECAL is a structure of 66 layers formed by sampling scintillators and lead panels which are placed at 12.5 m of the interaction point [49]. Its primary function is to detect electrons and photons.
- The HCAL, used mainly for identifying hadrons, primarily kaons, and pions, has a structure similar to the ECAL with alternating layers of scintillators and iron panels [49].

The relative energy resolution decreases with the energy with a factor $\sim 1/\sqrt{E}$, with ECAL being substantially more precise than the HCAL [45].

2.2.3.3 Muon Chambers

Muon detection is fundamental for the LHCb physics program. The reason is that muons are long-lived particles that interact minimally with material. This allows for measurements at the very end of the detector, resulting in very clean signatures due to low occupancy. This implies that one can exploit these particles to carry out precision tests of the SM, as will be described in Chapter 4.

There are five muon stations: M1, situated just after the RICH2, and M2, M3, M4, and M5 located at the very end of the detector (see Fig. 2.1). To improve the p_T measurement of the track that will be used for the trigger selection, station M1 is positioned before the calorimeter system. Stations M2-M5 are interleaved with iron layers to select penetrating muons [45]. Stations M1 to M3 have better spatial resolution (in the bending plane) and are used for obtaining the track direction and measuring the p_T of the candidate with 20% of resolution. Stations M4-M5 have lower resolution and are used for identifying the most penetrating particles.

The total output of each PID detector is a difference of logarithmic likelihoods (DLL) variable that differentiates between two particle hypotheses, usually between a pion and another particle. The reason for using the pions as a reference is because it is the most abundant

track. Another variable used for particle identification is the `ProbNN` variables which are derived from Neural Networks (NN). The data used for this NN combines information from all the particle identification subdetectors. A notable use of the PID system outputs is the selection of signal candidates in the data samples.

2.3 Trigger

The LHCb detector was designed to operate at a lower instantaneous luminosity (2×10^{32} cm^{-2} s^{-1}) than CMS and ATLAS. This is achieved by using a less focusing beam. The reason for this is to primarily have single interactions per bunch crossing, which reduces the occupancy, as the detector was designed for doing precision measurements. Despite this, the amount of data produced in the collider is far from being storable, due to computational and storage limitations. Therefore, the objective of the trigger is to reduce this rate while keeping most of the important signal events needed for physics analysis. The LHCb trigger consists of two main parts: the L0 trigger, implemented in hardware, which reduces the event rate from 40 MHz to $\sim$ 1 MHz, and the High-Level Trigger (HLT), implemented in software, which further reduces the rate to 2-5 kHz [45].

2.3.1 L0 Trigger

At 40 MHz, the entire detector cannot be read out, and only the information from the muon and calorimeter system is used. Therefore, the main goal of the L0 trigger is to select events with a muon with high p_T or large energy deposits in the calorimeters, as these are typical signals from B events. A decision must be made before $4\mu s$. Depending on the particle that triggers the L0, the system can distinguish between the muon L0, the electron-photon L0, or the hadron L0.

The muon trigger selects the event if there is one muon with $p_T > 1.76$ GeV/c or a pair of muons fulfilling $p_{T1}p_{T2} > 1.6$ GeV/c in the event [54]. The hadron (electron and photon) trigger selects the event if the transverse energy deposited in the calorimeter is bigger than $E_T > 3.6$ GeV ($E_T > 3.0$ GeV) [54]. The output rate of 1 MHz is composed of 400 kHz triggered by the muon trigger, 450 kHz triggered by the hadron trigger, and 150 kHz triggered by the electron-photon trigger. In general, the efficiency of the muon trigger ($\approx$ 90%) is much better than the hadronic trigger. For the hadronic trigger, the efficiency is around 60% in the case of $B^0 \to h^+h^-$, while for charm decays, due to the lower mass of the signal candidate, the efficiency is even smaller ($\sim$ 30%) [54].

These requirements translate into some dependence between the trigger efficiency and the transverse momentum of the mother particle. For the hadronic decays it varies between 0 % to 100% in the range of the momentum of the parent particle 0-20 GeV/c, while in the case of muons, it varies between 80% to 100% [54].

2.3.2 High Level Trigger

Events with a positive decision in the L0 trigger are processed by the High-Level Trigger (HLT), which is completely software-based. The HLT consists of two stages, HLT1 and HLT2.

The HLT1 performs a partial event reconstruction, due to limitations in the computing power, and the strategy is as follows. VELO segment tracks are reconstructed and selected if they have a large IP or associated hits in the muon chambers (for the case of a positive L0 Muon decision). Then a search in the T-stations is performed to look for tracks consistent with high p_T. Finally, if the event has a track with a high p_T the event is accepted and goes to the HLT2.

Events with a positive decision go to the HLT2, where all the tracks with a $p_T > 300\text{MeV}/c$ are reconstructed. HLT2 lines are much more exclusive than HLT1 and depend heavily on the channel studied. The function of HLT2 is not only to be the final filter of the event selection but also to be used for calibration of the detector used in the next run. Usually, the trigger configuration changes during each run and is identified by the TCK (Trigger Configuration Key). This constitutes another possible difference between simulation and data as MC is usually simulated with the most representative TCK of each period. The selected event can be TOS (Triggered on Signal) if the signal satisfies the trigger criteria or TIS (Triggered Independent of Signal) if some other signature of the event fired the trigger.

2.4 The LHCb Software

In this section, we briefly describe the LHCb data flow focusing on the software components, for both real data and Monte Carlo (MC) simulations. MC simulations are crucial for understanding the effect of selection requirements, and detector effects that are present in data, as well as to test analysis strategies or even to evaluate systematic uncertainties. For these reasons, MC simulations should be processed by the same tools as data. In LHCb, data and MC are processed using custom applications based on the Gaudi framework [55]. A schematic view of these applications can be seen in Fig. 2.3.

The entire simulation process is handled by `GAUSS` [56]. For doing so it makes use of `PYTHIA` [57], which simulates the p-p collisions with a specific LHCb configuration, then `EVTGEN` manages the decay of unstable particles as the B mesons and finally it uses the `GEANT4` toolkit [58] which propagates the particles through the detector. Then the output of `Gauss` is taken by `BOOLE` which simulates the digitalization process and adds the L0 decision to closely match the output of the real detector.

The rest of the process is shared between real data and MC. The HLT is supervised by the `MOORE` application. Then `BRUNEL` performs the offline reconstruction process which consists of transforming the triggered raw events, so the detector hits, into reconstructed tracks with the information from the particle identification (RICH, calorimeters, muon chambers)

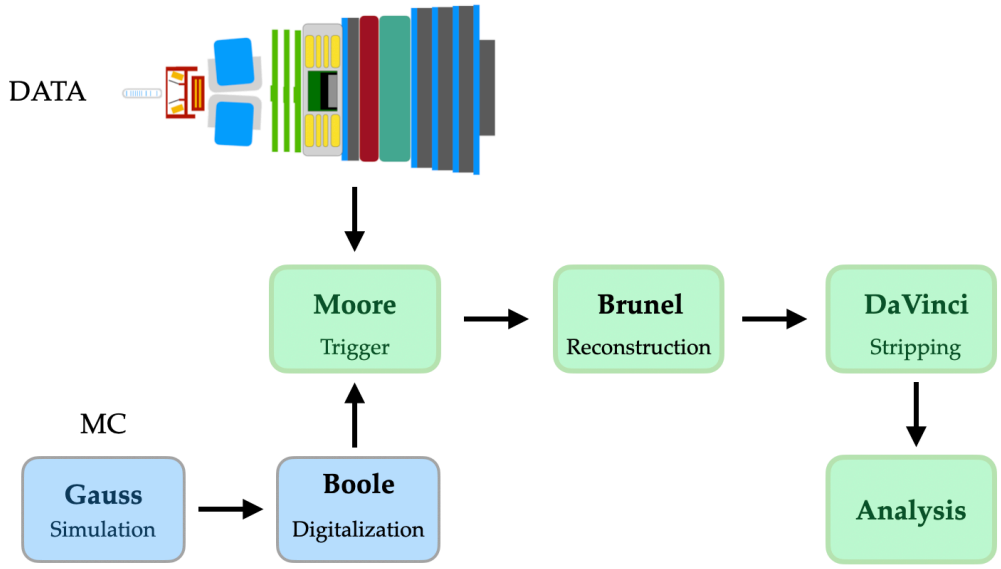

FIGURE 2.3: Schematic representation of the LHCb data flow.

linked. Finally, `DaVinci` performs the offline (Stripping) selection and produces the ROOT file that then is used as a starting point for analysts.

2.5 Data taking periods and conditions

The data analyzed in this thesis, both in the Chapter 4 and in the Chapter 5, correspond to the Run 2 data collected by the LHCb experiment from 2015 to 2018. During Run 2 the LHC operated at center-of-mass energy $\sqrt{s} = 13$ TeV and it recorded almost 6 fb^{-1} of integrated luminosity. At this energy, the $b\bar{b}$ cross section is around 5.6×10^{-4} b, which implies that approximately $\sim 10^{12}$ of B mesons were recorded by LHCb detector during this period. Particularly for the B-species analyzed in this thesis, it recorded around 3.5×10^{11} of B^0, 3.5×10^{11} of $B^{\pm}$ and 8.4×10^{10} of B_s^0 mesons. Note that this count exceeds the yields of both Belle and the projected output of Belle II by 2035 due to its smaller $\sigma_{b\bar{b}}$, which is on the order of nb.

Chapter 3

Objectives and methodology

This thesis has three clear objectives that aim to learn more about the matter-antimatter imbalance and DM problem present within the SM.

3.1 Objectives

The first objective is the world's best measurement of the $\phi_s^{c\bar{c}s}$ phase using the Run 2 data collected by the LHCb experiment during the 2015-2018 data-taking period. In principle, NP should contain new sources of CP violation that can alter crucial SM predictions like the one for the $\phi_s^{c\bar{c}s}$ phase. Additionally, this analysis also yields the world's best measurement of the decay width differences of mass eigenstates of the B_s^0 meson, the decay width of the B_s^0 meson, and the CP violating parameter, $|\lambda|$, so that it implies an important step forward in the understanding of the B_s^0 system.

The second objective is the improvement of the analysis strategies used in future CP Violation measurements, specifically in the flavor tagging of the B mesons. Flavor tagging is an experimental technique used to infer the flavor of the B mesons at the production stage, which is a very complicated task in a proton-proton collider. Our objective is to study the inclusive approach which involves utilizing all the tracks produced in the event in a Neural Network (NN) to infer the flavor of the produced B meson.

The third objective consists of the phenomenological study of SUSY theories. SUSY is still a very attractive BSM theory as it can explain DM as well as alleviate/fix the imbalance of matter-antimatter by adding complex parameters to the Lagrangian. However, SUSY was not discovered either in direct or indirect detection, which has put strong constraints on the available input space of the model. Our objective is to study the implications of the latest measurements provided by the scientific community both in simplified and non-minimal flavor violation SUSY theories.

3.2 Methodology

The methodology of the first objective involves two main parts, the selection of the data candidates and the analysis strategy performed in $B_s^0 \to J/\psi KK$ decays. For the selection of the data samples, simulation samples are used, so the first thing that is needed is to correct the simulation samples to closely match the data. Then, a Boosted Decision Tree is employed to suppress the combinatorial background further. To finalize the selection, the sPlot technique is used to statistically subtract the remaining background. Subsequently, it is necessary to account for different experimental effects like the decay time resolution, mass dependence of the KK system, flavor tagging and non-uniform decay time, and angular efficiencies. The physics parameters are estimated by maximizing the log-likelihood (LL) of all background-subtracted candidates to perform the final measurement. Finally, a study of the systematic effects that affect the final result as well as diverse cross-checks of the measurement are provided.

For the second objective, the improvement in the flavor tagging technique, the methodology is split into two main parts, first the training of the inclusive NN and second the comparison of the results with the classical tools. The training is subdivided into two, first a BDT is employed to classify each of the tracks present in each event. Then the NN implemented with a DeepSet architecture takes this output as well as other features like kinematic, isolation, and particle identification information of each track to produce the NN output. Then the output of the NN needs to be calibrated to ensure its physical meaning which is the probability that the NN decision is wrong. The results are compared with those obtained from the classical combination of techniques and diverse cross-checks and studies are provided to ensure the reliability of the results obtained.

The last objective involves the phenomenological study of SUSY theories which can address some of the problems present in the SM. This is done in two steps. First, the study of a flavor simplified benchmark model called the constrained Minimal Supersymmetric Standard Model, is performed within the MasterCode framework. Then, a study of the phenomenology of quark flavor transitions in a full model with flavor violation in b decays is carried out using a GPU framework developed during this thesis. The GPUs are interesting for this purpose as they allow us to study NP theories with a large number of degrees of freedom in a reasonable amount of computational time. The most relevant flavor constraints are encoded in this framework and the implications of these observables in the input space available in this general theory with flavor violation are studied.

Chapter 4

The world's best measurement of $\phi_S^{c\bar{c}s}$

In this chapter, the measurement of the interference phase $\phi_s^{c\bar{c}s}$ in $B_s^0 \to J/\psi KK$ decays is described, using the full data recorded by the LHCb detector during the Run 2 data taking, which corresponds to the period 2015-2018. This analysis yields the world-best measurement of most of the physics parameters of the B_s^0 system, particularly the phase $\phi_s^{c\bar{c}s}$, the decay width difference between mass eigenstates, $\Delta\Gamma_s \equiv \Gamma_L - \Gamma_H$, the decay width Γ_s, and the CP violation parameter $|\lambda|$ that will be described later.

As discussed in Chapter 1, the main motivation of this measurement is the lack of understanding of the CP violation, or in other words the known matter anti-matter imbalance problem. In the SM, CP violation originates in the quark sector due to the presence of a CP-violating phase in the parametrization of the CKM matrix[1]. Nevertheless, the amount of CP violation in the quark sector is insufficient to satisfy the Sakharov conditions [12], and therefore is insufficient to explain the current visible Universe. This fact motivates this measurement, as New Physics (NP), which potentially should introduce new sources of CP violation, can modify this observable. In Chapter 6 the specific example of Supersymmetry with Non-Minimal Flavor Violation will be studied.

This chapter is organized as follows. First, in §4.1 and §4.2, some concepts necessary for understanding the measurement of $\phi_s^{c\bar{c}s}$ are introduced. Then, the selection of the data collected by the LHCb detector as well as all the components required for the decay time and angular analysis of $B_s^0 \to J/\psi K^+K^-$ decays are explained in §4.3 and §4.4, respectively. Finally, the chapter concludes with a discussion of the results, along with an explanation of the main sources of systematic effects which are given in §4.5.

4.1 Introduction

This section serves as a necessary introduction for the measurement of $\phi_s^{c\bar{c}s}$. In §4.1.1, a brief description of the types of CP violation that can be measured in B meson decays is provided. §4.1.2 describes the difference between the observable measured in this chapter and the one

[1] In the SM the CP-violating θ_{QCD} term is also present but is heavily constrained by EDM measurements as seen in the Chapter 1.

referenced in Eq. 1.13. Finally, an overview of the theoretical and experimental status before this measurement is given in §4.1.3.

4.1.1 Types of CP Violation in B decays

CP violation can manifest (and therefore be measured) in three different ways in the neutral meson system:

- Direct CP violation. The amplitude of the decay $B_s^0 \to f$, (A_f), is different from the one in the conjugate process $\bar{B}_s^0 \to \bar{f}$, $(\bar{A}_{\bar{f}})$. In the case of $B_s^0 \to J/\psi K^+K^-$, this will necessary imply that $|A_f| \neq |\bar{A}_f|$. This is the only manifestation of CP violation in charged mesons.
- CP violation in the mixing. The rate of $B_s^0 \to \bar{B}_s^0$ differs from the conjugate process, $\bar{B}_s^0 \to B_s^0$. Denoting the probability amplitude of the process $\langle B_s^0 | B_L \rangle$, by p, and the probability amplitude $\langle B_s^0 | B_H \rangle$ by q, CP violation in the mixing will necessarily imply that $|q/p| \neq 1$. This effect is small for B^0 and B_s^0 mesons.
- CP violation in the interference between the mixing and the decay. This CP violation arises due to a quantum interference between the decay $B_s^0 \to f$ and the decay through mixing $B_s^0 \to \bar{B}_s^0 \to f$. This implies that f must be accessed by B_s^0 and $\bar{B}_s^0$ decays. This phenomenon occurs if $\phi_{(s)}^f = -\arg(\lambda_f) \neq 0$, where λ_f is defined as:

$$\lambda_f = \eta_f \frac{q}{p} \frac{\bar{A}_f}{A_f} \tag{4.1}$$

  where η_f is the eigenvalue under a CP transformation and can take the values +1 for CP-even or -1 for CP-odd final states. In the analysis of the $B_s^0 \to J/\psi K^+K^-$ decays, the magnitude ($|\lambda|$) and the phase ($\phi_s^{c\bar{c}s}$) of the CP violating parameter $\lambda_{c\bar{c}s}$ will be measured.

4.1.2 Difference between ϕ_s^{12} and $\phi_s^{c\bar{c}s}$

Sometimes in the bibliography, the quantity ϕ_s^{12} (see Chapter 1) is confused with $\phi_s^{c\bar{c}s}$. As introduced in Eq. 1.13, ϕ_s^{12} represents the interference between the off-shell (M_{12}) and the on-shell (Γ_{12}) parts of the box diagrams of Fig. 1.3. Therefore, this phase is sensitive to the CKM elements $(V_{tb}V_{ts}^*)^2$ (mixing), $(V_{cb}V_{cs}^*)^2$, $V_{cb}V_{cs}^*V_{ub}V_{us}^*$ and $(V_{ub}V_{us}^*)^2$ due to all the possible combinations of internal on-shell quarks in the Γ_{12} diagram [59].

In the case of $\phi_s^{c\bar{c}s}$ (this measurement), we are again sensitive to $(V_{tb}V_{ts}^*)^2$ due to the possible mixing, but only to $(V_{cb}V_{cs}^*)^2$ coming from the ratio of possible decays. In the SM, neglecting loop contributions, this phase is predicted to be $-2\beta_s \equiv \arg[(V_{tb}V_{ts}^*)^2/(V_{cb}V_{cs}^*)^2]$ [59].

4.1.3 Theoretical and Experimental status before this measurement

As said, $\phi_s^{c\bar{c}s}$ is predicted within the SM, and ignoring subleading contributions, to be $-2\beta_s$. This can be seen from Fig. 1.3 and the tree level decay of Fig. 4.1. The mixing of Fig. 1.3 is sensitive to $(V_{tb}V_{ts}^*)^2$ while the ratio of $b \to c\bar{c}s$ and $\bar{b} \to \bar{c}c\bar{s}$ tree level transitions is sensitive to $(V_{cb}V_{cs}^*)^2$. This quantity can be indirectly obtained by global fits to experimental data, given by [60]:

$$-2\beta_s = -0.0368^{+0.0009}_{-0.0006}\text{rad}, \tag{4.2}$$

which is tiny and extremely precise, becoming a perfect observable to look for NP. However, the issue arises when considering subleading contributions (penguin pollution) within the SM. Historically, these contributions were considered insignificant. However, with the current level of experimental precision and the lack of significant new physics effects, they can no longer be ignored.

These contributions originate from non-perturbative QCD effects, which depend on the particular final state ($\Delta\phi_s^f$). A common approach to this complicated task involves relying on SU(3) flavor symmetry of the QCD interaction, to relate $B_s^0 \to J/\psi\phi$ (doubly Cabbibo suppressed penguins) with $B^0 \to J/\psi\rho^0$ and $B_s^0 \to J/\psi K^{*0}$ (Cabbibo favored). A recent study gives the following estimation of this pollution $\Delta\phi_s = 3^{+10}_{-12}$ mrad [61]. Nevertheless, this method has the obvious disadvantage that $SU(3)$ symmetry-breaking effects (due to the different mass of the quarks) are difficult to quantify. Furthermore, there are already known examples where SU(3) breaking effects are significant, such as in the fragmentation of the b quark into a B^0 or a B_s^0 meson [62]. In conclusion, more work is needed, both from the theoretical and experimental side, as controlling these contributions becomes imperative shortly. A schematic but comprehensive list of processes contributing to $B_s^0 \to J/\psi\phi$ can be found in Fig. 4.1.

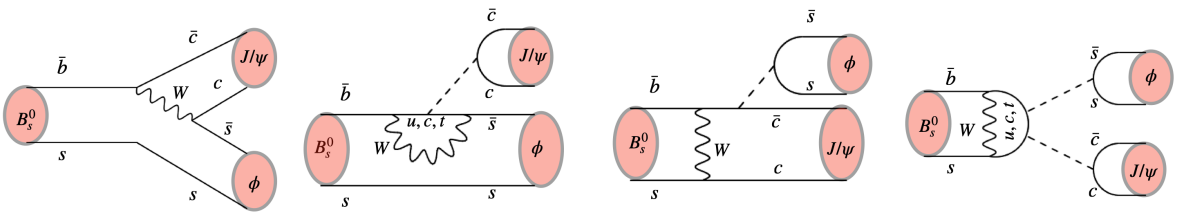

FIGURE 4.1: From left to right: Tree, penguin, exchange, and annihilation contributions to the $B_s^0 \to J/\psi\phi$ decay.

The experimental status before the update of this measurement can be found in Fig. 4.2. The plots on Fig. 4.2 show the individual 68% confidence interval contours of the experiments ATLAS [63, 64], CMS [65, 66], LHCb [67, 68, 69, 70, 71, 72, 73, 74], CDF [75], and D0 [76] in

the planes $\phi_s^{c\bar{c}s}$ vs $\Delta\Gamma_s$ (left) and Γ_s vs $\Delta\Gamma_s$ (right). Also, the HFLAV combination is shown as well as the SM prediction [1]. Note that the SM prediction in the ϕ_s plane comes directly from $-2\beta_s$, so it ignores subleading contributions discussed previously.

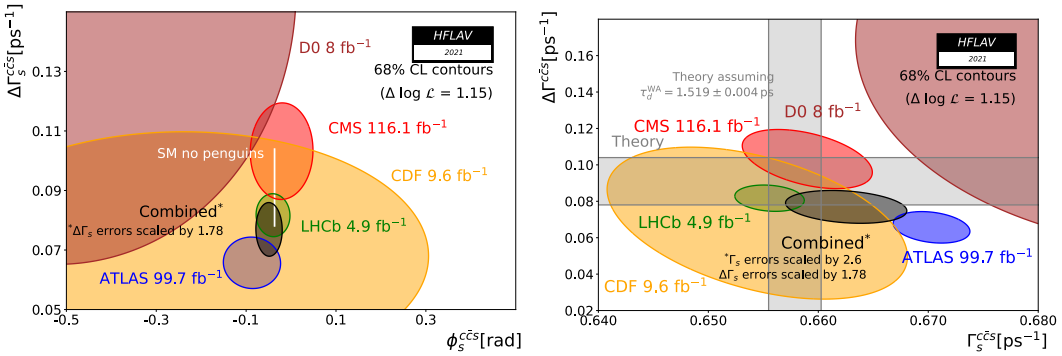

FIGURE 4.2: HFLAV status of the B_s^0 system before this measurement [1]. The $\phi_s^{c\bar{c}s} vs \Delta\Gamma_s$ plane is shown in the left panel while $\Gamma_s vs \Delta\Gamma_s$ can be found on the right.

The world averages previous to this measurement yield [1]:

$$\begin{aligned} \phi_s^{c\bar{c}s} &= -49 \pm 19 \text{ mrad}, \\ \Delta\Gamma_s &= 0.084 \pm 0.005 \text{ ps}^{-1}, \\ \Gamma_s &= 0.663 \pm 0.0024 \text{ ps}^{-1}. \end{aligned} \tag{4.3}$$

The SM prediction for $\Delta\Gamma_s$ is taken from Ref. [18]. The "SM prediction" for Γ_s uses the wold average $\tau_d = 1.519 \pm 0.004$ ps and the SM prediction of $\tau(B_s^0)/\tau(B^0)$ from Ref. [77]. They read

$$\begin{aligned} \Delta\Gamma_s &= 0.091 \pm 0.013 \text{ ps}^{-1}, \\ \Gamma_s &= 0.6578 \pm 0.0024 \text{ ps}^{-1}. \end{aligned} \tag{4.4}$$

4.2 Phenomenology of the decay $B_s^0 \to J/\psi KK$

The analysis of the $B_s^0 \to J/\psi(\to \mu^+\mu^-)K^+K^-$ decay is performed within a region of the K^+K^- mass distribution primarily influenced by the $\phi(1020)$ (hereafter ϕ) resonance. The B_s^0 is a pseudo-scalar (spin 0), while both the J/ψ and ϕ are spin-1 (vectors) particles. According to angular momentum conservation, the orbital angular momentum between the pair of kaons and the pair of muons can be 0, 2 (CP-even), or 1 (CP-odd). Additionally, there is also a CP-odd S-wave contribution in the K^+K^- distribution analyzed, assumed to be due to an $f_0(980)$ contribution. Therefore, an angular analysis is needed to disentangle the CP-even and CP-odd components, as they have different contributions to the decay rate.

Four polarization amplitudes contribute to the decay, $A_p = |A_p|e^{i\delta_p}$ where $p \in \{0, \|, \perp, S\}$ refers to the longitudinal, parallel, perpendicular and S-wave respectively. As $\phi_s^{c\bar{c}s}$ originates

from the interference between the mixing and the decay through mixing, also an analysis of the decay time of the B_s^0 meson will be required to resolve the B_s^0 oscillation.

Therefore, the evolution of the B_s^0 and its decay can be described by the decay time of the B_s^0 meson, three helicity angles that parametrize the kinematics of the final state, and two masses $m(\mu^+\mu^-)$ and $m(K^+K^-)$. The pair of muons is selected to originate from a J/ψ, which is a narrow resonance, and thus its mass is fixed to a constant. The dependence on the $m(K^+K^-)$ is addressed by dividing the analysis into six $m(K^+K^-)$ bins and by using corrective (effective coupling) factors for the interference S-P wave terms. This method is known as the C_{SP} factors and will be described later in §4.4.1.

The three helicity angles are $\Omega = \left(\cos\theta_K, \cos\theta_\mu, \psi\right)$. In the $\mu^+\mu^-$ (K^+K^-) frame, θ_μ (θ_K) denotes the angle between the direction of the μ^+ (K^+) particle and the direction opposite to the momentum of the B_s^0 meson. The angle ψ is defined as the angle between the decay planes of the K^+K^- and $\mu^+\mu^-$ systems [67]. A schematic representation of the definition of the angles can be found in Fig. 3 of Ref. [67].

The theoretical decay rate of a B_s^0 meson produced at the interaction point (t=0), can be expressed by a sum of ten terms:

$$\frac{d^4\Gamma}{dt d\cos\theta_K d\cos\theta_\mu \psi} = \sum_{i=0}^{10} N_k h_k(t) f_k(\theta_k, \theta_\mu, \psi), \tag{4.5}$$

where the decay time dependence is as follows,

$$h_k(t) = \frac{3}{4\pi} e^{-\Gamma_s t} \left\{ a_K \cosh\frac{\Delta\Gamma_s t}{2} + b_K \sinh\frac{\Delta\Gamma_s t}{2} + c_k \cos\Delta m_s t + d_k \sin\Delta m_s t \right\}. \tag{4.6}$$

The decay rate for an initial $\bar{B}_s^0$ meson, is derived from Eq. 4.6 by changing the signs of the c_k and d_k coefficients. The index k in Eq. 4.5 denotes each of the possible combinations for the square of the polarization amplitudes: three from the P-wave, one for the S-wave, and six interference terms. N_k, $f_k(\theta_K, \theta_\mu, \phi)$, a_k, b_k, c_k and d_k are given in Table 4.1. The a_k, b_k, c_k, and d_k coefficients also depend on the strong phases (one per polarization state δ_0, $\delta_\parallel$, $\delta_\perp$ and δ_S). Note that, because of having six m_{KK} bins, six different S-wave phases, ($\delta_{s,i}$), and six different S-wave amplitudes, $A_{S,i}$, will be measured.

Two measurements will be presented. One assumes that λ_f is independent of the polarization state ($\lambda_f = \lambda$), which will constitute the baseline, and another relaxes this condition. The latter result is motivated even within the SM, as if the penguin's contributions are not negligible different shifts per polarization state are expected.

TABLE 4.1: Angular and time dependent coefficients defined in Eq. 4.5 and Eq. 4.6 for the polarization dependent case [68]. The independent one can be obtained by doing $\lambda_{0,\parallel,\perp,S} = \lambda$.

a_k	b_k	c_k	d_k	f_k	N_k
$\frac{1}{2}(1+\lvert\lambda_0\rvert^2)$	$-\lvert\lambda_0\rvert\cos(\phi_0)$	$\frac{1}{2}(1-\lvert\lambda_0\rvert^2)$	$\lvert\lambda_0\rvert\sin(\phi_0)$	$c_K^2 s_l^2$	$\lvert A_0\rvert^2$
$\frac{1}{2}(1+\lvert\lambda_\parallel\rvert^2)$	$-\lvert\lambda_\parallel\rvert\cos\left(\phi_\parallel\right)$	$\frac{1}{2}(1-\lvert\lambda_\parallel\rvert^2)$	$\lvert\lambda_\parallel\rvert\sin\left(\phi_\parallel\right)$	$\frac{1}{2}s_K^2(1-c_\phi^2 s_l^2)$	$\lvert A_\parallel\rvert^2$
$\frac{1}{2}(1+\lvert\lambda_\perp\rvert^2)$	$\lvert\lambda_\perp\rvert\cos(\phi_\perp)$	$\frac{1}{2}(1-\lvert\lambda_\perp\rvert^2)$	$-\lvert\lambda_\perp\rvert\sin(\phi_\perp)$	$\frac{1}{2}s_K^2(1-s_\phi^2 s_l^2)$	$\lvert A_\perp\rvert^2$
$\frac{1}{2}\Big[\sin\left(\delta_\perp-\delta_\parallel\right)-\lvert\lambda_\perp\lambda_\parallel\rvert$ $\sin\left(\delta_\perp-\delta_\parallel-\phi_\perp+\phi_\parallel\right)\Big]$	$\frac{1}{2}\Big[\lvert\lambda_\perp\rvert\sin\left(\delta_\perp-\delta_\parallel-\phi_\perp\right)$ $+\lvert\lambda_\parallel\rvert\sin\left(\delta_\parallel-\delta_\perp-\phi_\parallel\right)\Big]$	$\frac{1}{2}\Big[\sin\left(\delta_\perp-\delta_\parallel\right)+\lvert\lambda_\perp\lambda_\parallel\rvert$ $\sin\left(\delta_\perp-\delta_\parallel-\phi_\perp+\phi_\parallel\right)\Big]$	$-\frac{1}{2}\Big[\lvert\lambda_\perp\rvert\cos\left(\delta_\perp-\delta_\parallel-\phi_\perp\right)$ $+\lvert\lambda_\parallel\rvert\cos\left(\delta_\parallel-\delta_\perp-\phi_\parallel\right)\Big]$	$s_K^2 s_l^2 s_\phi c_\phi$	$\lvert A_\perp A_\parallel\rvert$
$\frac{1}{2}\Big[\cos\left(\delta_0-\delta_\parallel\right)+\lvert\lambda_0\lambda_\parallel\rvert$ $\cos\left(\delta_0-\delta_\parallel-\phi_0+\phi_\parallel\right)\Big]$	$-\frac{1}{2}\Big[\lvert\lambda_0\rvert\cos\left(\delta_0-\delta_\parallel-\phi_0\right)$ $+\lvert\lambda_\parallel\rvert\cos\left(\delta_\parallel-\delta_0-\phi_\parallel\right)\Big]$	$\frac{1}{2}\Big[\cos\left(\delta_0-\delta_\parallel\right)-\lvert\lambda_0\lambda_\parallel\rvert$ $\cos\left(\delta_0-\delta_\parallel-\phi_0+\phi_\parallel\right)\Big]$	$-\frac{1}{2}\Big[\lvert\lambda_0\rvert\sin\left(\delta_0-\delta_\parallel-\phi_0\right)$ $+\lvert\lambda_\parallel\rvert\sin\left(\delta_\parallel-\delta_0-\phi_\parallel\right)\Big]$	$\sqrt{2}s_K c_K s_l c_l c_\phi$	$\lvert A_0 A_\parallel\rvert$
$-\frac{1}{2}\Big[\sin(\delta_0-\delta_\perp)-\lvert\lambda_0\lambda_\perp\rvert$ $\sin(\delta_0-\delta_\perp-\phi_0+\phi_\perp)\Big]$	$\frac{1}{2}\Big[\lvert\lambda_0\rvert\sin(\delta_0-\delta_\perp-\phi_0)$ $+\lvert\lambda_\perp\rvert\sin(\delta_\perp-\delta_0-\phi_\perp)\Big]$	$-\frac{1}{2}\Big[\sin(\delta_0-\delta_\perp)+\lvert\lambda_0\lambda_\perp\rvert$ $\sin(\delta_0-\delta_\perp-\phi_0+\phi_\perp)\Big]$	$-\frac{1}{2}\Big[\lvert\lambda_0\rvert\cos(\delta_0-\delta_\perp-\phi_0)$ $+\lvert\lambda_\perp\rvert\cos(\delta_\perp-\delta_0-\phi_\perp)\Big]$	$-\sqrt{2}s_K c_K s_l c_l s_\phi$	$\lvert A_0 A_\perp\rvert$
$\frac{1}{2}(1+\lvert\lambda_S\rvert^2)$	$\lvert\lambda_S\rvert\cos(\phi_S)$	$\frac{1}{2}(1-\lvert\lambda_S\rvert^2)$	$-\lvert\lambda_S\rvert\sin(\phi_S)$	$\frac{1}{3}s_l^2$	$\lvert A_S\rvert^2$
$\frac{1}{2}\Big[\cos\left(\delta_S-\delta_\parallel\right)-\lvert\lambda_S\lambda_\parallel\rvert$ $\cos\left(\delta_S-\delta_\parallel-\phi_S+\phi_\parallel\right)\Big]$	$\frac{1}{2}\Big[\lvert\lambda_S\rvert\cos\left(\delta_S-\delta_\parallel-\phi_S\right)$ $-\lvert\lambda_\parallel\rvert\cos\left(\delta_\parallel-\delta_S-\phi_\parallel\right)\Big]$	$\frac{1}{2}\Big[\cos\left(\delta_S-\delta_\parallel\right)+\lvert\lambda_S\lambda_\parallel\rvert$ $\cos\left(\delta_S-\delta_\parallel-\phi_S+\phi_\parallel\right)\Big]$	$\frac{1}{2}\Big[\lvert\lambda_S\rvert\sin\left(\delta_S-\delta_\parallel-\phi_S\right)$ $-\lvert\lambda_\parallel\rvert\sin\left(\delta_\parallel-\delta_S-\phi_\parallel\right)\Big]$	$\frac{2}{\sqrt{6}}s_K s_l c_l c_\phi$	$\lvert A_S A_\parallel\rvert$
$-\frac{1}{2}\Big[\sin(\delta_S-\delta_\perp)+\lvert\lambda_S\lambda_\perp\rvert$ $\sin(\delta_S-\delta_\perp-\phi_S+\phi_\perp)\Big]$	$-\frac{1}{2}\Big[\lvert\lambda_S\rvert\sin(\delta_S-\delta_\perp-\phi_S)$ $-\lvert\lambda_\perp\rvert\sin(\delta_\perp-\delta_S-\phi_\perp)\Big]$	$-\frac{1}{2}\Big[\sin(\delta_S-\delta_\perp)-\lvert\lambda_S\lambda_\perp\rvert$ $\sin(\delta_S-\delta_\perp-\phi_S+\phi_\perp)\Big]$	$-\frac{1}{2}\Big[-\lvert\lambda_S\rvert\cos(\delta_S-\delta_\perp-\phi_S)$ $+\lvert\lambda_\perp\rvert\cos(\delta_\perp-\delta_S-\phi_\perp)\Big]$	$-\frac{2}{\sqrt{6}}s_K s_l c_l s_\phi$	$\lvert A_S A_\perp\rvert$
$\frac{1}{2}\Big[\cos(\delta_S-\delta_0)-\lvert\lambda_S\lambda_0\rvert$ $\cos(\delta_S-\delta_0-\phi_S+\phi_0)\Big]$	$\frac{1}{2}\Big[\lvert\lambda_S\rvert\cos(\delta_S-\delta_0-\phi_S)$ $-\lvert\lambda_0\rvert\cos(\delta_0-\delta_S-\phi_0)\Big]$	$\frac{1}{2}\Big[\cos(\delta_S-\delta_0)+\lvert\lambda_S\lambda_0\rvert$ $\cos(\delta_S-\delta_0-\phi_S+\phi_0)\Big]$	$\frac{1}{2}\Big[\lvert\lambda_S\rvert\sin(\delta_S-\delta_0-\phi_S)$ $-\lvert\lambda_0\rvert\sin(\delta_0-\delta_S-\phi_0)\Big]$	$\frac{2}{\sqrt{3}}c_K s_l^2$	$\lvert A_S A_0\rvert$

4.3 Selection

This section will describe the selection of $B_s^0 \to J/\psi K^+K^-$ candidates. First, some of the most relevant variables used for selecting the data are explained in §4.3.1. The trigger strategy and the stripping selection chosen are explained in §4.3.2. Simulation samples play a crucial role in this process, as necessary information is extracted from them to select the data. Therefore, it is essential to correct simulation samples to closely match the data, as discussed in §4.3.4. Subsequently, a Boosted Decision Tree is employed to further suppress combinatorial background as detailed in §4.3.5. Finally, the sPlot technique is utilized through a fit to the invariant mass distribution ($m(J/\psi K^+K^-)$) to statistically subtract the background as explained in §4.3.7.

4.3.1 Variables used in selection

The variables used in the trigger and stripping strategy to select $B_s^0 \to J/\psi KK$ decays are explained below.

- $\Delta\mathcal{L}_{ij}$: Difference in likelihoods between a track corresponding to a particle hypothesis "i" and a track corresponding to a particle hypothesis "j" (see §2.2.3).
- ProbNNi: Ooutput of an NN that uses the information from all the particle identification subdetectors. It represents the probability of a track being a particle "i" (see §2.2.3).
- χ^2_{IP}: The impact parameter (IP) is the shortest perpendicular distance between the trajectory of a track and a vertex (usually the PV). The χ^2_{IP} indicates the significance of a track originating from a vertex. This variable is usually utilized for selecting displaced tracks.
- χ^2_{DOCA}: Indicates the significance of the distance of closest approach (DOCA). The DOCA is the closest distance between two tracks, thus this variable indicates the significance of both tracks originating from the same vertex.
- χ^2_{track}: Indicates the quality of the track, or in other words, the confidence that the hits in the tracking systems correspond to a single track.
- χ^2_{vtx}: χ^2 probability from the vertex fit, reflects the accuracy of the vertex position determination during the fit.
- $\chi^2_i/nDoF$: χ^2 probability normalized by the number of degrees of freedom used in the fit "i".
- σ_t: Error estimation in the decay time obtained from the vertex fit.
- χ^2_{DTF}: χ^2 probability of the vertex fit when constraining the B_s^0 to originate from the PV and the J/ψ mass to the world average [33]. This variable is obtained from the Decay Tree fitter algorithm [52].

4.3.2 Trigger Strategy and Stripping selection

Events are required to pass a hardware trigger that selects events containing a muon or a kaon with high transverse momentum. Subsequently, the HLT1, which is the first stage of the software trigger (see §2.3), relies on the following trigger lines:

- `Jpsi_Hlt1DiMuonHighMassDecision_TOS`: Two well-identified opposite charged muons with an invariant mass larger than 2.7 GeV/c^2 are required in the event.
- `B_Hlt1TrackMuonDecision_TOS`: Select events with at least one muon with high p_T (> 1 GeV/c) and a large $\chi^2_{IP} > 35$.
- `B_Hlt1TwoTrackMVADecision _TOS`: Events with two opposite charged tracks with a high sum of p_T and a $\chi^2_{IP} > 4$ are selected.

The second and third lines, produce a non-uniform decay time efficiency (below 5 ps) due to IP requirements[2]. This separates our events into two categories, the unbiased category which triggered the `Jpsi_Hlt1DiMuonHighMassDecision_TOS` line, and the biased category, triggered by the line `B_Hlt1TrackMuonDecision_TOS` or by `B_Hlt1TwoTrackMVADecision_TOS`.

After the HLT1 selection, the HLT2 line, `Jpsi_Hlt2DiMuonDetachedJPsiDecision_TOS`, requires a pair of muons with an invariant mass within 120 MeV/c^2 of the J/ψ mass. Additionally, it requires the J/ψ to have a flight distance significance (FDS) greater than three, which removes J/ψ produced at PV and also implies a non-uniform decay time efficiency. This issue is extensively studied in §4.4.4.

Furthermore, a positive `StrippingBetaSBs2JpsiPhiDetachedLine` decision is required to select the event. Stripping cuts are summarized in Table 4.2.

Finally, to define the analysis region, avoid boundary effects, and suppress more combinatorial background the following selection criteria is applied:

- 0.3 < t < 15 ps
- $\sigma_t < 0.15$ ps
- 5200 MeV/c^2 < m($J/\psi K^+K^-$) < 5550 MeV/c^2
- 990 MeV/c^2 < m(K^+K^-) < 1050 MeV/c^2

4.3.3 Background categories in simulation

The simulation events can be categorized into different background categories (`B_BKGCAT`) based on the relationship between the reconstructed objects (MC Particles) and the generated ones (MC True Particles).

- Category 0, Signal ($\sim$ 89% of the total sample): Each final state particle has an associated generated particle with the same PID (correct reconstructed mass). All these MC

[2]These requirements are lifetime biasing as they usually require a significant decay length of the B meson.

TABLE 4.2: Stripping selection criteria used for further selecting $B_s^0 \to J/\psi K^+K^-$ candidates.

	Variable	Cut
B_s^0	$m(J/\psi K^+K^-)$	$\in [5150, 5550]\text{MeV/c}^2$
	$\chi^2_{\text{vtx}}/\text{nDoF}$	< 20
	t	> 0.2 ps
$\mu^+\mu^-$	$\Delta\ln\mathcal{L}_{\mu\pi}\ (\mu^\pm)$	> 0
	$p_T\ (\mu^\pm)$	> 500 MeV/c
	χ^2_{DOCA}	< 20
	$\chi^2_{\text{vtx}}/\text{nDoF}$	< 16
	$m(\mu^+\mu^-)$	$\in [3016.9, 3176.9]\,\text{MeV}/c^2$
K^+K^-	χ^2_{DOCA}	< 30
	$p_T\ (\phi)$	> 500 MeV/c
	$m(K^+K^-)$	$\in [980, 1060]\,\text{MeV}/c^2$
	$\chi^2_{\text{vtx}}/\text{nDoF}$	< 25
	$\Delta\ln\mathcal{L}_{K\pi}\ (K^\pm)$	> 0
	$\chi^2_{\text{track}}/\text{nDoF}\ (K^\pm)$	< 5

particles share a common MCParticle mother, which has the same identification as the reconstructed decay mother. This implies that the decay chain can only differ from the decay descriptor by intermediate resonances.

- Category 10, Quasi-signal: Same as 0, but at least one reconstructed intermediate state does not match the generated intermediate state. Only present in the S-wave MC which is used for calculating the C_{SP} factors.
- Category 50, Low mass background ($\sim 3\%$): One reconstructed MC final state particle is not matched to particles used to form the candidate. Typically due to energy loss through photon emission.
- Category 60, Ghosts ($\sim 8\%$): At least one final state is a ghost track (see §2.2.2.2).

Categories 0, 10, and 50 are used typically to study signal shape. Category 60 is retained in simulation as these events are also present in data, and could potentially have a different acceptance. Therefore, as the simulation will be used to extract information on the efficiencies, it is important to keep these events in the analysis. Additionally, category 60 has a background component which is subtracted using the sPlot technique as will be described for data in §4.3.7.

4.3.4 MC corrections to match the data

The next step in the analysis will be to further suppress the combinatorial background through a Boosted Decision Tree (BDT) based selection. This algorithm is trained on simulation and uses kinetic information and particle identification variables as features, as will

be described in §4.3.5. Before doing that, it is important to ensure that simulation variables correctly describe the data. To achieve this, a correction in the PID identification and some kinematic variables is needed as it is known that these variables in simulation poorly describe real data.

4.3.4.1 Particle Identification Variables Correction

The PID variables in the simulation are known to differ from those in the data. Specifically, the variables that need correction are `Prob_NNk` for kaons and `Prob_NNmu` for muons, as they are the final states of the analysis. Additionally, corrections are also needed in `Prob_NNp` and `Prob_NN`π, as misidentification backgrounds such as $B^0 \to J/\psi K\pi$ and $\Lambda_b^0 \to J/\psi pK$ are present in the signal region and the PID variables are used to suppress them.

The set of scripts of the `PIDCalib` package is used for this purpose, following the strategy described in Ref. [78]. This approach considers the PID dependency among the PID variables based on the p, p_T of the track, and event multiplicity (`nTracks`). Specifically, for correcting the muon variables the PID resampling technique is utilized, which independently (and therefore without taking into account correlation with the rest of the variables) generates the PID response based on calibration particle density functions. To achieve this, $J/\psi \to \mu^+\mu^-$ decays are used as a calibration sample. Meanwhile, for hadrons, the PID transformation method is used, in which the PID is transformed to fit the data while preserving the correlation of the corrected variables. The hadron PID variables are corrected using the $D^* \to D^0(\to K\pi)\pi$ decay channel as calibration mode.

Fig. 4.3 shows the distribution of the PID simulation variables compared to sWeighted data, after applying the selection cuts described in §4.3.2 for 2018 as an example. A good agreement is obtained after applying these corrections.

4.3.4.2 Gradient Boosting Reweighter

To correct kinematics, event, and selection variables that will be used in §4.3.5, the Gradient Boosting (GB) reweighting technique [79] is employed. Specifically, the features that are corrected include:

- The track χ^2 variables ($\chi^2_{track}/nDoF$) of the final state particles.
- Kinematics of the B_s^0 meson, specifically the p_T and the pseudorapidity (η).
- Number of long tracks, preferred over just the number of tracks for being this distribution in simulation closer to data.

Due to different L0 thresholds, the corrections are performed per year except for the 2015 simulation sample which is trained against 2016 real data due to the low amount of data collected in 2015. The distributions of the simulation variables with and without the correction are compared with background subtracted data in Fig. 4.4. For illustration, 2018 data and simulation, are shown.

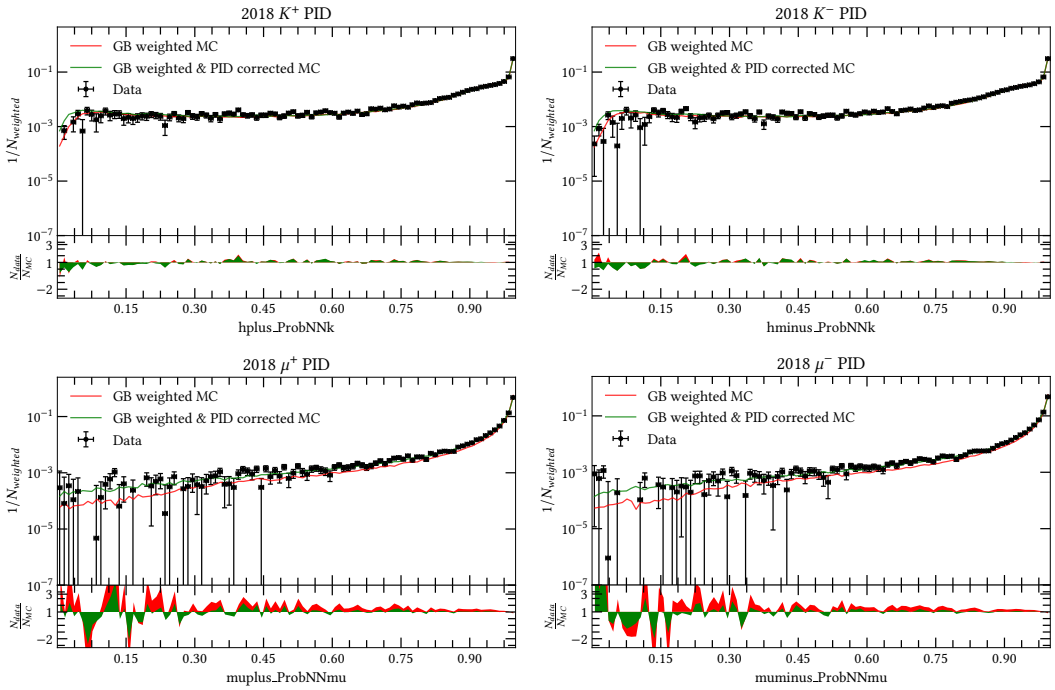

FIGURE 4.3: Comparison of PID variables in data and simulation. Signal events are shown with black points, MC without PID correction is shown in red, and MC with PID correction in green. As an example only 2018 is shown. The corrections described in §4.3.4.2 are also included for consistency.

4.3.5 Boosted Decision Tree-based selection

A BDT-based selection is employed to reject combinatorial background still present in real data while preserving as much signal as possible. The BDT training is performed in 2016, 2017, and 2018. Again, due to limited data in the 2015 sample, BDT training of 2016 is directly applied to 2015. For the training, the simulation sample of $B_s^0 \to J/\psi\phi$ with `B_BKGCAT 0||50` is used as signal incorporating the corrections explained in §4.3.4. As background, data candidates within the $J/\psi K^+K^-$ invariant mass range $5450 < m(J/\psi K^+K^-) < 5550$ MeV/c^2 (right sideband, predominantly populated by combinatorial background) are utilized. The training variables are listed in order of importance as follows:

- The minimum of the logarithm of the kaon PIDs (ProbNNk).
- The logarithm of the B_s^0 decay tree fit χ^2 (χ^2_{DTF}).
- The logarithm of the B_s^0 impact parameter χ^2 (χ^2_{IP}).
- The B_s^0 decay vertex χ^2 ($\chi^2_{vtx}/nDoF$).
- The maximum of the kaon track probability ($\chi^2_{track}/nDoF$).
- The transverse momentum of the ϕ (p_T^{ϕ}).

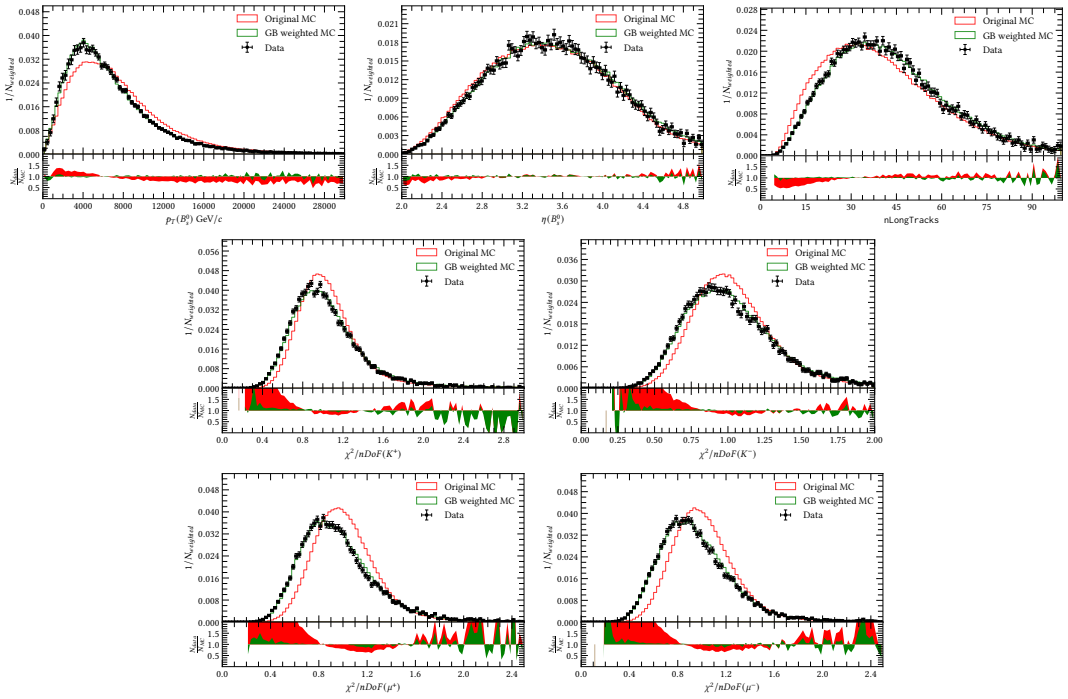

FIGURE 4.4: Projections of the variables corrected using the GB-reweighting technique for 2018 data samples. Background subtracted data is shown with black points, the red histogram shows the simulation without corrections while the green histogram includes the GBweight correction. A good agreement is observed between corrected simulation and background-subtracted data.

- The maximum of the muon track probability ($\chi^2_{track}/nDoF$).
- The logarithm of the J/ψ decay vertex χ^2 ($\chi^2_{vtx}/nDoF$).
- The B^0_s transverse momentum (p^B_T).
- The minimum of the logarithm of the muon PIDs (ProbNNmu).

For the determination of the χ^2_{DTF} variables, both the J/ψ mass, fixed to the current world average [33], and the position of the PV are constrained.

To optimize the BDT, the following figure of merit (FOM) is used:

$$FOM = \frac{(\sum_i sw_i)^2}{\sum_i sw_i^2}, \tag{4.7}$$

where the sum goes through all the candidates. The per-event weight sw_i is determined from a preliminary invariant mass fit using a similar strategy (albeit less sophisticated) to the one described in §4.3.7. The formula in 4.7, represents the statistical power or the effective signal and is inversely proportional to the smallness of the uncertainties in the determination of the parameters of interest.

The BDT improves the signal-to-background ratio by a factor of 50. After the BDT selection, there are approximately 157759 (3191), 101050 (69010), 108171 (59293), and 127411 (65090) signal (background) candidates in the mass window region of $5320 < m(J/\psi K^+K^-) < 5420\,\mathrm{MeV}/c^2$ for 2015, 2016, 2017 and 2018, respectively. The FOM distributions, as well as the $m(J/\psi K^+K^-)$ distributions after the BDT selection, can be found in Fig. 4.5.

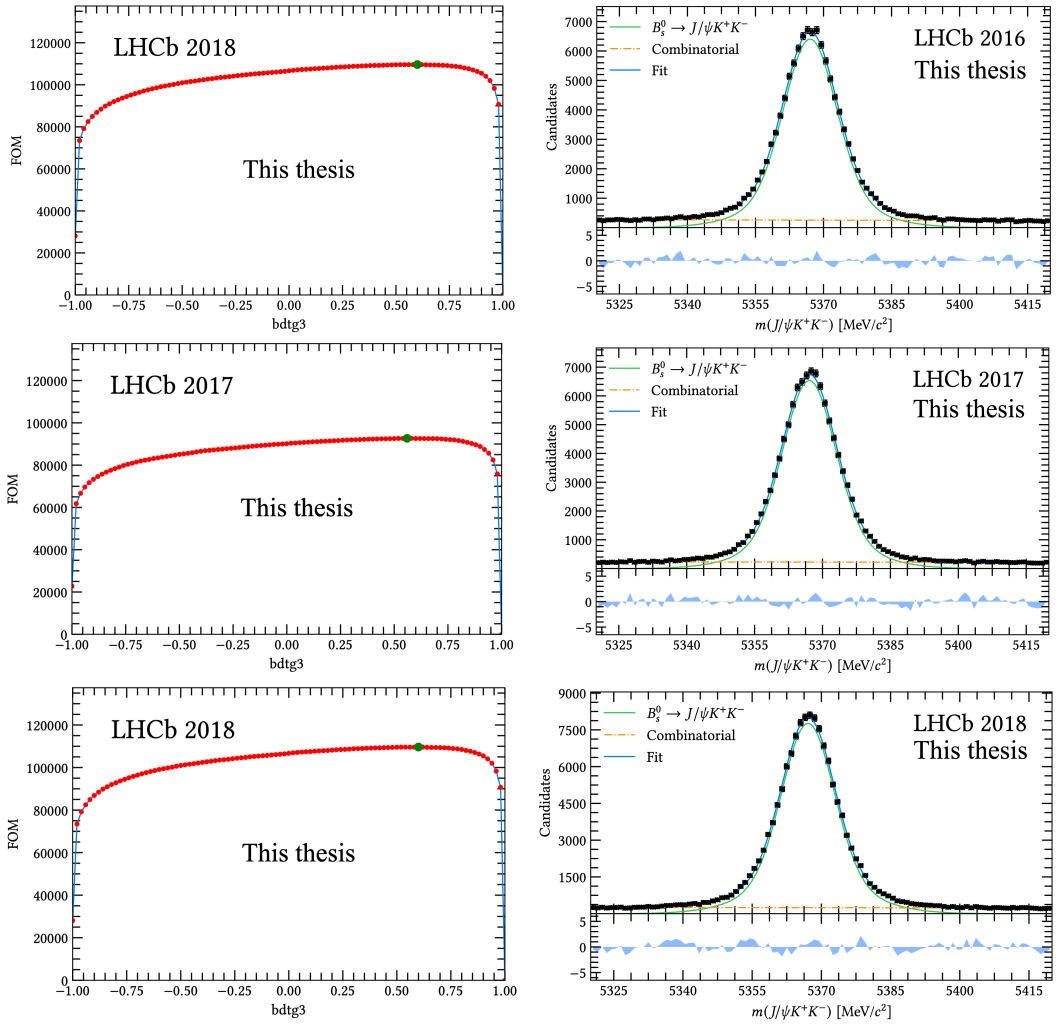

FIGURE 4.5: On the left, the FOM distribution used to optimize the BDT selection is shown (red). The optimal point found is highlighted in green resulting in values of 0.58, 0.56, and 0.60 for 2016, 2017, and 2018 respectively. On the right, the invariant mass distribution after the optimal (green) cut can be seen. The blue solid line shows the total fit while the green line and red lines show the signal and remaining background components respectively.

4.3.6 Peaking backgrounds contributions

In addition to the signal candidate and the combinatorial background, other potential contributions were also studied in the mass window of the analysis.

- $B^0 \to J/\psi K^{*0}(\to K\pi)$, where the pion is misidentified as a kaon. This background is removed by applying a veto if the $m(J/\psi K\pi)$ invariant mass is within $15\,\mathrm{MeV}/c^2$ of the B^0 nominal mass [33] or if the "kaon" has a `Prob_NN`$\pi > 0.7$ (high probability of being a pion) or `Prob_NNk`< 0.35 (low probability of being a kaon). As the expected remaining B^0 events that pass the veto are small compared with the number of signal candidates, no further actions are required.
- $\Lambda_b^0 \to J/\psi pK$, where the proton is misidentified as a kaon. Again, a mass veto is applied if the $m(J/\psi Kp)$ is within $15\,\mathrm{MeV}/c^2$ of the known Λ_b^0 mass [33], and a PID veto if the kaon has a `Prob_NNp` >0.7 (high probability of being a proton). Around 4700 Λ_b^0 candidates are expected to pass the vetoes. The remaining background candidates are statistically subtracted by the injection of simulated events with a negative sum of weights equal to the expected number of remaining Λ_b^0 baryons, which effectively removes this contribution.
- $B^0 \to J/\psi K^+K^-$, this background component is modeled in the final invariant mass fit as described in §4.3.7.

4.3.7 Mass fits and computation of sWeights

After the BDT selection, the amount of background is drastically reduced but some remnants are still present as can be seen in Fig. 4.5. To extract the parameters of interest, the candidates are weighted to statistically subtract the background using the sPlot method [80].

The data sample is split into forty-eight subsamples with their signal fractions and signal shapes. The subsamples account for four years of data-taking (2015, 2016, 2017, and 2018), two triggers categories ("biased" and "unbiased" as seen in 4.3.2), and six $m(K^+K^-)$ bins ([990, 1008, 1016, 1020, 1024, 1032, 1050] MeV/c^2) to take into account the different S-wave contribution as discussed in 4.4.1.

The mass fit model includes a contribution from the signal, combinatorial background, and reflection backgrounds, $\Lambda_b^0 \to J/\psi pK$ and $B^0 \to J/\psi K^+K^-$. As mentioned, the Λ_b is suppressed by vetoes, and the remaining component is statistically subtracted with weights from the simulation. The signal component is modeled with a double-sided Crystal Ball (DSCB) function [81]. The DSCB uses as a conditional variable the per-event mass error to take into account the correlation between the $cos\theta_\mu$ and the mass resolution[3]. The $B^0 \to J/\psi K^+K^-$ background is modeled with a DSCB sharing all shape parameters with the signal component but the mean which is shifted by the known mass difference of $m(B_s^0)$

[3]This is needed because the sPlot method requires the discriminating variable (invariant mass) to be independent of the variables of interest (angles and decay time) but the mass resolution depends on the transverse momentum of muons ($\cos\theta_\mu$).

and $m(B^0)$ [33]. The combinatorial background is modeled by an exponential function. The full PDF is as follows:

$$\begin{aligned} pdf =& N_{sig} DSCB(x;\mu,\alpha_1,\alpha_2,n_1,n_2,s_1,s_2|\sigma_m) \\ &+ N_{B^0} DSCB(x;\mu_{B^0},\alpha_1,\alpha_2,n_1,n_2,s_1,s_2|\sigma_m) \\ &+ N_{comb} e^{-bm}, \end{aligned} \tag{4.8}$$

where N_{sig}, N_{B^0} and N_{comb} are the number of signal, B^0 and combinatorial background candidates respectively. The mean of the distribution is denoted by μ, α_1, α_2, n_1 and n_2 are the tail parameters of the signal shape. s_1 and s_2 are scale factors to model the correlation between σ_m and $\cos\theta_\mu$ and b is the coefficient that model the exponential of the background component.

The signal shape is obtained from simulation with `B_BKGCAT=0,50` for each of the $m(K^+K^-)$ bins, trigger categories and years. Then, maintaining the signal shape fixed, the signal yield, the slope of the exponential, the mean of the distribution, and the parameters s_1 and s_2 which model the mass width are fitted. The same procedure is used with full signal MC (`B_BKGCAT=0,50,60`) to subtract the background component of category 60.

The invariant mass distributions ($m(J/\psi K^+K^-)$) and the fit projections are shown in Fig. 4.6. The total number of signal candidates are 16181 ± 135, 103319 ± 342, 105465 ± 343, and 123870 ± 476 for 2015, 2016, 2017, and 2018 respectively.

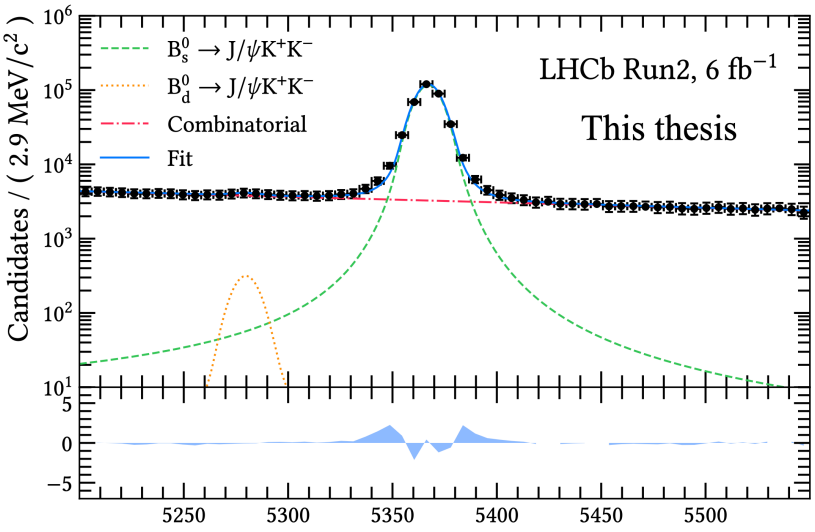

FIGURE 4.6: Distribution of $m(J/\psi K^+K^-)$ variable and likelihood fit projections for all the years, $m(K^+K^-)$ bins and trigger categories combined.

4.4 Analysis

In this section, the analysis strategy will be described. The analysis strategy involves several steps that must be addressed before the measurement of the CP violating phase $\phi_s^{c\bar{c}s}$. These steps include the dependence of the S-wave contribution on the invariant mass of the kaons, described in §4.4.1; the decay time resolution caused by the detector, discussed in §4.4.2; the impact of the VELO misalignment, detailed in §4.4.3; decay time and angular acceptance effects resulting from both detector and the candidate selection, described in §4.4.4 and §4.4.5; and finally, the calibration of the NN output used to identify the flavor of the B meson at the production stage, outlined in §4.4.6.

4.4.1 Mass Dependence

The decay rate shown in Eq. 4.5 deliberately avoids the $m(K^+K^-)$ dependence. In principle, this equation is only valid for a specific value of $m(K^+K^-)$ as the S-wave lineshape has a different dependence on $m(K^+K^-)$ than the P-wave. This implies, that one should treat the $m(K^+K^-)$ as a fit variable, however, the limited knowledge of the S-wave contribution[4] motivates the analysis strategy known as the C_{SP} factors. This strategy takes into account the S-P wave amplitude interference by an effective coupling, C_{SP} in the signal PDF (i.e. $N_K \to C_{SP}N_K$ for the S-P wave interference terms). This interference term can be defined as:

$$C_{SP}e^{i\theta_{SP}} = \frac{\int_{m_L}^{m_H} p(m) * s^*(m) * \epsilon(m_{KK})dm}{\sqrt{\int_{m_L}^{m_H} |p(m)dm|^2 \int_{m_L}^{m_H} |s(m)dm|^2}}, \tag{4.9}$$

where p(m) and s(m) are the P-wave and S-wave lineshapes respectively, m_L and m_H are the lowest and highest values of m_{KK} in each of the bins. The C_{SP} factor is, therefore, defined as a real number. The complex phase θ_{SP}, is absorbed in the measurement of $\delta_{S,i} - \delta_\perp$. The function, $\epsilon_i(m_{KK})$, accounts for the non-uniform efficiency correction.

The P-wave and S-wave are assumed in the baseline to be a $\phi(1020)$ (Breit Wigner distribution) and a $f_0(980)$ resonances (modeled with a Flatté distribution). The $\epsilon_i(m_{KK})$ is obtained in each bin of the true dikaon mass by the ratio of the histogram of an LHCb MC (with f_0 and ϕ) divided by a histogram of a standalone (and therefore without efficiency effects) `evtGen` MC, generated with same parameter inputs as the LHCb MC. The B_s^0 candidates of the full MC are truth-matched (`B_BKGCAT` $\in (0||10||50)$) and the reconstructed mass is required to be within each bin. The C_{SP} factors, which are listed in Table 4.3, are common for all the data-taking years.

[4] It is not clear if it is a non-resonance, a $f_0(980)$ or an admixture of both.

TABLE 4.3: Baseline values of the C_{SP} factors used in the fit to the data calculated from simulated samples from all years of data taking.

m_{KK} [MeV/c^2]	Baseline
$[990 - 1008]$	0.8458
$[1008 - 1016]$	0.8673
$[1016 - 1020]$	0.8127
$[1020 - 1024]$	0.8558
$[1024 - 1032]$	0.9359
$[1032 - 1050]$	0.9735

4.4.2 Decay time Resolution

The experimental finite decay time resolution produces two primary effects in Eq. 4.5. Firstly, it reduces the mixing amplitude by a dilution factor (D<1), thereby biasing ϕ_s towards smaller values. Secondly, it induces a net migration of events to bigger decay times, resulting in a bias towards larger lifetime values[5]. The per-event decay time error, denoted as σ_t, and extracted from the track fit, can be expressed as:

$$\sigma_t^2 = \left(\frac{m}{p}\right)^2 \sigma_L^2 + \left(\frac{t}{p}\right)^2 \sigma_p^2 + \text{correlation}, \tag{4.10}$$

which incorporates two contributions: the vertex position error (prompt term), denoted as σ_L, and the momentum measurement error, represented by σ_p. However, this decay time error does not precisely correspond to the true detector resolution due to our limited knowledge of the subdetector resolution. Consequently, it requires to be calibrated.

The prompt term is typically estimated by analyzing the decay time distribution of prompt decays, in our case random $\mu^+\mu^-K^+K^-$ combinations produced at the collision point. The decay time distribution of this sample is illustrated in Fig. 4.7. The tail on the positive side contains contributions from real decay and resolution effects, while the tail on the negative side is primarily dominated by the finite decay time resolution. Therefore, the negative side of the decay time distribution (highlighted in blue in Fig. 4.7) is utilized to calibrate the decay time error.

To account for the decay time resolution the physical PDF ($\mathcal{P}_{phys}$) is convolved with a resolution function:

$$\mathcal{P}_{obs}(t) = R(t) \otimes \mathcal{P}_{phys}(t) = \int_{-\infty}^{+\infty} dt R(t;t')\mathcal{P}_{phys}(t'), \tag{4.11}$$

where $R(t;t')$ is the resolution function. Performing the integral for each of the decay time

[5]This is because the convolution of a Gaussian with an exponential typically decreases more slowly than the exponential alone.

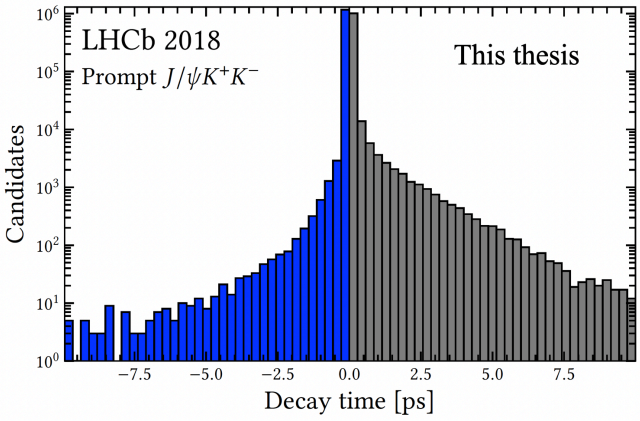

FIGURE 4.7: Time distribution in the real data prompt J/ψ sample combined with two random K^+K^- tracks obtained from the 2018 data sample. The left tail (blue) is dominated by resolution effects, while in the right tail also real decays contribute.

terms of Eq. 4.6, one can observe that each of the decay time functions shapes of $\mathcal{P}_{phys}$ remains unchanged [82]. The resolution is fully encoded in the observed amplitudes, which are modified by the following dilution factor:

$$D = \int_{-\infty}^{+\infty} dt' R(t') \cos\left(\Delta m t'\right). \tag{4.12}$$

To arrive at this solution, it is only necessary to assume that the resolution function is time-invariant and symmetric around a mean value ($R(t - t' - \mu)$), without needing to parametrize this function.

If we consider the negative tail of Fig. 4.7 as a representation of the resolution effect, the integral of Eq. 4.12 is simply calculated by the following sum over events with a negative decay time ($t < 0$):

$$D = \frac{1}{N} \sum \cos\left(\Delta m t_i\right). \tag{4.13}$$

Three corrections need to be considered. First, due to a known VELO misalignment the decay time of the prompt candidates is biased, and thus not centered around zero, so only events with $t < \mu$ will enter in Eq. 4.13.

Second, there is a small contribution of real decays (such as B decays) in $t < \mu$, so a small correction is needed by estimating this contribution in a fit:

$$D_{corr} = \frac{1}{1 - f_{ll}} D - \frac{f_{ll}}{1 - f_{ll}} D_{ll}, \tag{4.14}$$

where D_{corr} is the corrected dilution, D_{ll} is the dilution from non-prompt events and f_{ll} is the fraction yield of non prompt decays in $t < \mu$. These parameters are obtained from a fit

to the decay time distribution of prompt candidates using the following pdf:

$$\mathcal{P}(t) = \mathcal{G}(t) \otimes [f_{prompt}\delta(t) + f_{ll}(f_{sl}e^{-t/\tau_1} + (1 - f_{sl}e^{-t/\tau_2}) + f_{wpv}W(t))]. \tag{4.15}$$

The resolution, $\mathcal{G}(t)$, is modeled by the sum of two Gaussians with a shared mean and different widths. The $W(t)$ function represents the wrong PV (WPV) vertices function, which is empirically derived using the `PVmixer` tool. This tool adds a randomly selected PV from a different event to the current event. The resulting distribution is fitted to the following pdf:

$$W(t) = f_1 e^{-|t|/\tau_1} + (1 - f_1)e^{-|t|/\tau_2}. \tag{4.16}$$

The third and final correction is to account for the different kinematics of the prompt candidates and real B meson decays (signal). For this purpose, the following ratio of simulation samples is used:

$$D_{data,signal} = \frac{D_{MC,signal}}{D_{MC,prompt}} D_{prompt}. \tag{4.17}$$

The effective width from the obtained dilution factor is recovered, as follows:

$$\sigma_{eff} = \sqrt{-2lnD/\Delta m_s^2}. \tag{4.18}$$

This procedure is repeated in ten bins of σ_t (eight in the case of 2015 data due to limited statistics). A linear binned likelihood fit is performed to obtain a calibration that translates the decay time error from the track fit to the obtained true decay time error:

$$\sigma_{eff} = p_0 + p_1(\sigma_t - \sigma_{avg}). \tag{4.19}$$

To mitigate the correlation between the calibration parameters p_0 and p_1, an offset σ_{avg} is used, representing the average of the σ_t distribution. The calibration parameters, alongside the effective decay time resolutions, computed as the weighted average of the σ_{eff} obtained in each bin, are shown in Table 4.4. The per-year calibration fits are illustrated in Fig. 4.8. These calibration parameters are utilized to calibrate the decay time error of the signal candidates. The resolution is accounted for in the decay time angular fit by a per-event single-Gaussian that convolves the pdf, with a width equal to the calibrated decay time error.

4.4.3 Decay time bias

A bias in the decay time distribution of prompt J/ψ candidates is observed during Run 1 and Run 2 data taking years, with the latter showing a more significant effect. This issue was investigated in the measurement of Δm_s in $B_s^0 \to D_s^- \pi^+$ decays [83] and found to be caused

TABLE 4.4: decay time error calibration parameters and σ_{eff} obtained for each year for the signal sample.

Year	σ_{eff} [fs]	p_0[fs]	p_1
2015	42.66 ± 0.02	44.5 ± 0.2	0.949 ± 0.020
2016	42.32 ± 0.01	44.3 ± 0.1	0.919 ± 0.010
2017	41.93 ± 0.01	42.5 ± 0.1	0.968 ± 0.012
2018	40.96 ± 0.01	41.9 ± 0.1	0.987 ± 0.013

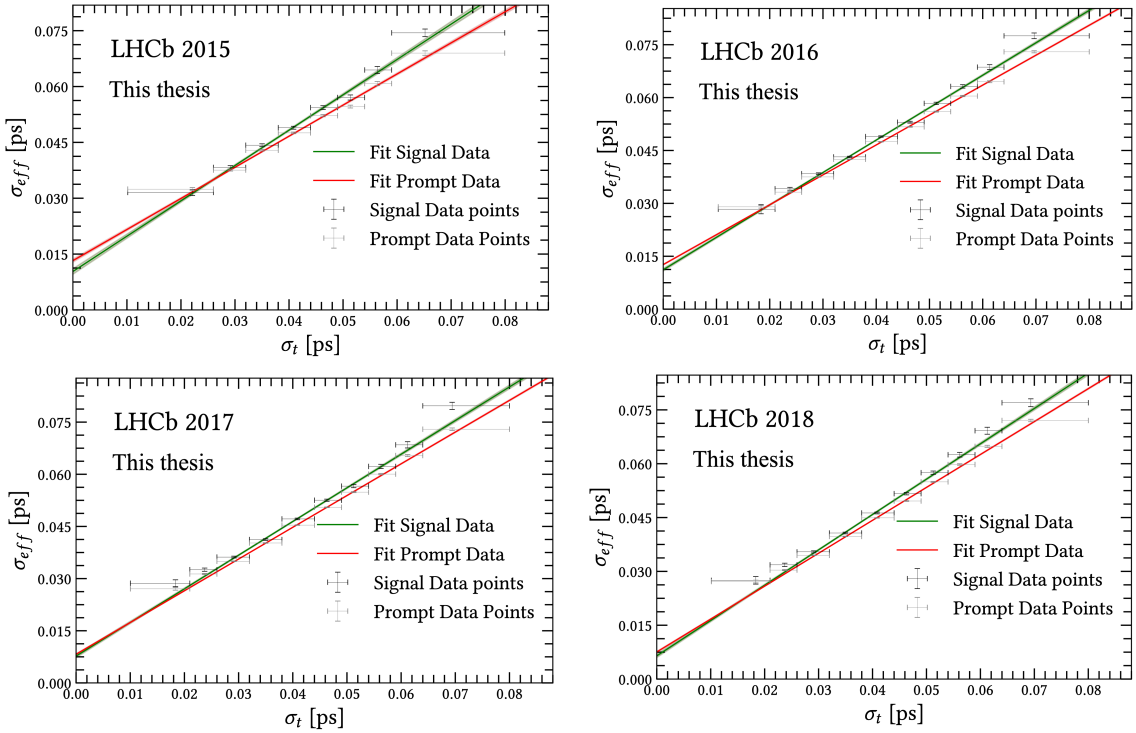

FIGURE 4.8: Per year calibrations obtained for the signal $B_s^0 \to J/\psi K^+K^-$ data sample (baseline) are shown in green. For comparison, results obtained directly from prompt candidates are shown in red. Light red and light green bands correspond to one statistical uncertainty for signal and prompt data fits respectively.

by a VELO misalignment. This misalignment translates into a bias in the reconstructed decay lengths and, consequently, in the reconstructed decay time.

The bias correction follows the same strategy as described in Ref. [83]. This bias is obtained in prompt data, and as it is expected to depend on the kinematic of the particular decay, properly translated to the signal mode via a calibration curve based on signal and prompt simulations. To obtain the calibration, prompt and signal MC are processed with different misalignments in T_x (x-coordinate of VELO halves modules) between -20 and 20 μm. Subsequently, a fit to the $t - t_{true}$ distribution is performed, taking the deviation of the mean (μ) obtained from 0 as the bias. This way, an x-value (from the MC prompt) and a y-value (from signal MC) are obtained for each misalignment. The resulting figure can be seen in Fig. 4.9. A linear binned likelihood fit is performed to the distribution yielding:

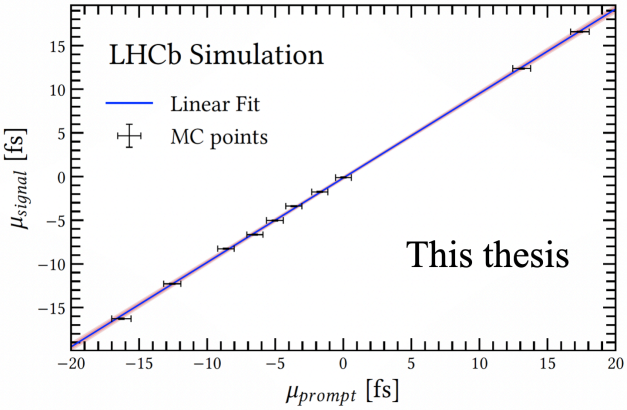

FIGURE 4.9: Decay time bias obtained for each MC, prompt (x-values), and signal (y-values), after being artificially misaligned.

$$\langle \mu \rangle_{B_s^0 \to J/\psi K^+K^-} = (0.967 \pm 0.010) \times \langle \mu \rangle_{prompt J/\psi + K^+K^-} (-0.158 \pm 0.070). \tag{4.20}$$

The calibration of Eq. 4.20 is utilized to translate the biases observed in prompt data to signal data. This correction is incorporated in the final decay time angular fit by convolving the final pdf with a single-Gaussian with a per-event σ_{eff} (see §4.4.2) and mean (μ), fixed to the bias obtained for signal in each year. These final decay time biases, those obtained from prompt data, and the corresponding translated biases to the signal mode are shown in Table 4.5.

4.4.4 Decay time Acceptance

As previously introduced in §4.3.2, the reconstruction efficiency is not uniform as a function of decay time as can be seen already in simulation (see Fig. 4.10). Not correcting properly for this effect will introduce a bias in all the parameters of interest, particularly impacting the measurement of Γ_s. In Fig. 4.10, three main effects can be distinguished:

TABLE 4.5: decay time bias obtained from prompt data (left column) and signal data (right column) for each year of data-taking

Year	Prompt Bias [fs]	Signal Bias [fs]
2015	5.18 ± 0.13	4.85 ± 0.13
2016	6.494 ± 0.047	6.122 ± 0.045
2017	7.538 ± 0.044	7.131 ± 0.043
2018	6.234 ± 0.047	5.87 ± 0.045

- A lower decay time acceptance is present in the biased trigger category. This was already explained in §4.3.2 and arises from selection criteria based on requiring an SV (where the B_s^0 decays) separated from the PV. This criterion exploits the characteristic flight distance of the $B^0_{(s)}$ mesons, which typically traverses a length of approximately 1cm before decaying, effectively serving as a means to discriminate signal from combinatorial background. However, this approach is lifetime biasing.
- Drop in the efficiency around 1-2 ps. This feature is associated with the PV reconstruction in the VELO. If the B_s^0 decays promptly (close to the PV), including B_s^0 daughter tracks in the reconstruction of the PV will (almost) not matter. In cases where the SV is displaced, the PV reconstruction algorithm will not include daughter tracks in the reconstruction of the PV. In the intermediate region (1-2 ps), some B_s^0 daughter tracks may influence the PV search, leading to a bias towards shorter lifetimes and the corresponding drop in efficiency.
- An upper decay time acceptance is observed in both categories. This is mainly caused by the VELO algorithm used for track fitting, which assumes that the tracks originate from the beam collision point. As a consequence events where the B meson experienced significant displacement are less efficiently reconstructed.

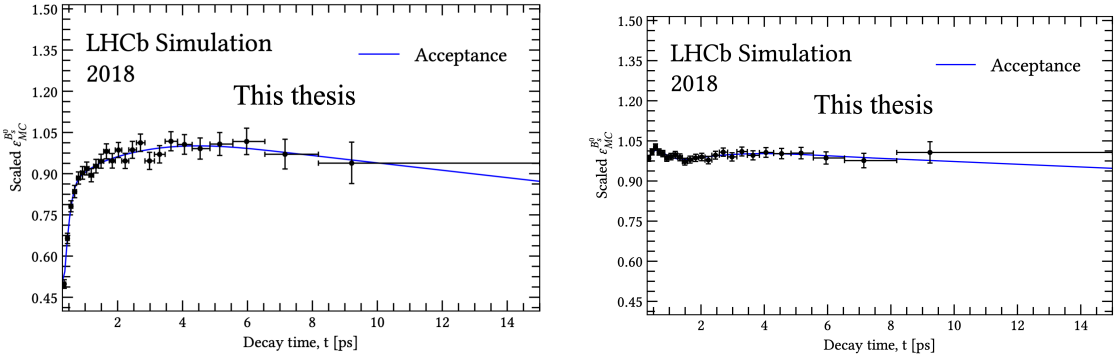

FIGURE 4.10: Acceptance shape obtained for 2018 signal MC simulated with $\Delta\Gamma = 0$ for both trigger categories, biased on the left and unbiased on the right.

The baseline approach to correct the non-uniform decay time efficiency is a data-driven method utilizing $B^0 \to J/\psi K^{*0}(892)(\to K^+\pi^-)$ as a control channel. It assumes that the

decay time and angular acceptances factorize, thereby allowing for independent correction of both effects. The decay time acceptance of the signal, $\epsilon_{B_s^0}^{Data}$ is parametrized as:

$$\epsilon_{B_s^0}^{Data} = \epsilon_{B^0}^{Data} \times \frac{\epsilon_{B_s^0}^{MC}}{\epsilon_{B^0}^{MC}}, \tag{4.21}$$

where $\epsilon_{B^0}^{Data}$, $\epsilon_{B^0}^{MC}$ and $\epsilon_{B_s^0}^{MC}$ represent the decay time efficiency of the real $B^0 \to J/\psi K\pi$ data and the decay time efficiency of $B^0 \to J/\psi K^{*0}$, $B_s^0 \to J/\psi\phi$ simulations samples, respectively.

4.4.4.1 Sample Corrections

A weighting procedure is applied to the three samples used in the determination of the time acceptance. This is because the determination of these efficiencies relies on the physics and kinematic distributions of the samples, so it is crucial to minimize these differences.

The control sample is fully triggered, selected, and sWeighted (background subtracted) in a similar way to the signal mode. This is done to ensure that the selection of the control sample closely matches the signal sample, thereby avoiding the introduction of systematic effects. Additionally, the control sample is GB-reweighted to match the p, p_T, and $m(K\pi)$ distributions seen in signal data. Simulation samples receive polarity, physics, and kinematic corrections. The polarity weight ensures that the fraction of events of the two magnet polarities matches the corresponding data. The physics weight (pdf weight) is a per-event weight calculated as the ratio of the differential decay rates (Eq. 4.5) calculated with the simulated generated physics parameters and the ones observed in data (Run1 measurement). Furthermore, B_s^0 MC and B^0 MC are further reweighted in p_T and p to match the signal and reweighted control data respectively.

4.4.4.2 Model and Strategy

Cubic B-splines are employed to describe the non-uniform decay time efficiency shape. Specifically, a model with three knots is chosen, defining a cubic polynomial at each of these knots. The function is imposed to be continuously differentiable at every knot, which implies that the function can be described by just five coefficients. The knot's positions are chosen to be roughly equally populated (exponentially distanced):

$$k = \{0.3, 0.91, 1.96, 9.0\} ps. \tag{4.22}$$

The region between the last knot and the maximum of the decay time distribution is modeled using linear extrapolation. Additionally, the first coefficient is fixed to the unity to fix the arbitrary scale. The pdf (for each sample) is as follows:

$$\mathcal{P}(t) = \{a_i + b_i t + c_i t^2 + d_i t^3\} \left(e^{-\Gamma t} \otimes \frac{1}{\sigma\sqrt{(2\pi)}} e^{-(x-\mu)^2/2\sigma^2} \right). \tag{4.23}$$

The resolution model is described by a per-event single-Gaussian function as discussed in Sections §4.4.2 and §4.4.3. Parameters describing the resolution function are shown in Table 4.6. Subscripts i, of the coefficients of the efficiency function indicate that they are knot dependent. A simultaneous unbinned likelihood fit is performed on the three samples, with the following combination of splines (denoted by s) to ultimately extract the spline of the signal:

- B_s^0 MC : $s^{B_s^0}_{MC}$.
- B^0 MC : $\frac{s^{B^0}_{MC}}{s^{B_s^0}_{MC}} \times s^{B_s^0}_{MC}$.
- B^0 data: $\frac{s^{B^0}_{MC}}{s^{B_s^0}_{MC}} \times s^{B_s^0}_{Data}$.

The three splines are fitted simultaneously: one spline corresponds to B_s^0 MC, another to the efficiency of the ratio of B^0 and B_s^0 MCs and the third represents (based on Eq. 4.21) the decay time efficiency of B_s^0 signal data. Fig. 4.11 shows the efficiency obtained for $B^0 \to J/\psi K^{*0}$ 2018 data taking in this last step. The coefficients obtained for each year and trigger category for B_s^0 data are shown in Table 4.7.

TABLE 4.6: Resolutions and decay withs for each sample. Resolutions are obtained using the procedure described in §4.4.2. Decay widths are fixed to the generated values and world average [33] for simulated and real data respectively.

	B^0 data	B^0 MC	B_s^0 MC
σ [fs]	42.44	38.64	41.7
Γ [ps^{-1}]	0.65789	0.65833	0.6613701

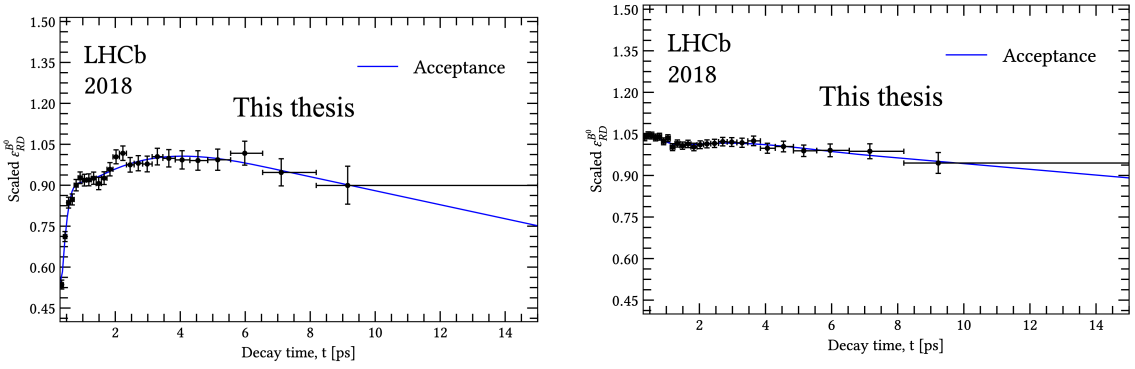

FIGURE 4.11: Acceptance shape obtained in 2018 $B^0 \to J/\psi K^{*0}$ data for both trigger categories, biased, showed on the left, and unbiased category on the right.

TABLE 4.7: Decay time acceptance coefficients for all years and both trigger categories.

		Year			
		2015	2016	2017	2018
Unbiased	c_1	1.0 ± 0	1.0 ± 0	1.0 ± 0	1.0 ± 0
	c_2	0.986 ± 0.053	1.009 ± 0.038	1.056 ± 0.029	1.037 ± 0.028
	c_3	0.963 ± 0.034	0.989 ± 0.025	0.976 ± 0.018	0.977 ± 0.018
	c_4	1.046 ± 0.071	1.012 ± 0.051	1.073 ± 0.036	1.028 ± 0.035
	c_5	1.018 ± 0.029	0.982 ± 0.060	0.944 ± 0.044	0.929 ± 0.040
	c_6	0.915 ± 0.064	0.943 ± 0.048	0.986 ± 0.035	0.946 ± 0.033
Biased	c_1	1.0 ± 0	1.0 ± 0	1.0 ± 0	1.0 ± 0
	c_2	1.39 ± 0.15	2.00 ± 0.15	1.78 ± 0.13	2.07 ± 0.15
	c_3	1.57 ± 0.12	2.12 ± 0.11	1.99 ± 0.10	2.08 ± 0.11
	c_4	1.63 ± 0.21	2.61 ± 0.25	2.17 ± 0.17	2.51 ± 0.20
	c_5	1.73 ± 0.23	2.30 ± 0.23	1.95 ± 0.17	2.15 ± 0.20
	c_6	1.28 ± 0.16	2.25 ± 0.20	1.70 ± 0.13	2.13 ± 0.18

4.4.4.3 Cross-checks

To validate the decay time acceptance procedure, lifetime measurements of $\tau(B^0)$ and $\tau(B^+)$ are performed using $B^0 \to J/\psi K^{*0}$ and $B^+ \to J/\psi K^+$ data samples respectively.

B^0 lifetime measurement

The B^0 data and simulation samples are split into two independent sets. One will act as a control sample, and the other as pseudo signal data in Eq. 4.21. Different selection criteria are introduced between the pseudo signal data and the control channel to mimic the differences between $B_s^0 \to J/\psi K^+K^-$ and $B^0 \to J/\psi K^{*0}$. The lifetime of the B^0 ($\tau(B^0)$) is then measured in the pseudo signal data and compared with the PDG value [33]. Two independent checks are performed. One where the control sample candidates satisfy $m(K\pi) < 980\,\text{MeV}/c^2$, while the pseudo-data candidates verify $m(K\pi) > 980$. This is to mimic what happens in our baseline procedure as $m(\phi) > m(K^{*0})$. The second one, where the control and pseudo-data belong to complementary regions depending on the opening angle α (between the K and π), $\alpha < 0.025$ and $\alpha > 0.025$ for pseudo-signal and control sample respectively. This is again to mimic what happens in data as $\phi \to K^+K^-$, has a smaller average opening angle than $K^{*0} \to K\pi$ (bigger mass difference between final states and mother). The results are shown in Table 4.8, where an overall good agreement can be seen for both checks. Note that only statistical errors are considered.

B^+ lifetime measurement

TABLE 4.8: Lifetime measurements (ps) of B^0 pseudo signal for complementary regions of $m(K^{*0})$ and $K-\pi$ opening angle. The number in brackets shows the deviation obtained from the measurement to the WA $\tau(B^0) = 1.520 \pm 0.004$ ps [33].

Year	m($K\pi$)	α
2015	1.533 ± 0.025 (0.54σ)	1.527 ± 0.0274 (0.24σ)
2016	1.532 ± 0.012 (0.91σ)	1.515 ± 0.012 (-0.38σ)
2017	1.5161 ± 0.0083 (-0.42σ)	1.5051 ± 0.0097 (-1.42σ)
2018	1.5151 ± 0.0086 (-0.51σ)	1.517 ± 0.010 (-0.27σ)

The B^+ lifetime measurement is performed following the same procedure as explained in this section but replacing the B_s^0 with B^+ tuples in Eq. 4.21. The B^+ selection is different from the B_s^0 signal to account for the missing fourth track. Results of the $\tau(B^+)/\tau(B^0)$ ratio are shown in Table 4.9 and compared with the world average (WA = 1.076 ± 0.004) [33]. A good agreement has been observed for all the years.

TABLE 4.9: Values of $\tau(B^+)/\tau(B^0)$ (WA=1.076 ± 0.004) obtained for the validation of the time acceptance. A good p-value is seen for all years of data-taking

Year	$\tau(B^+)/\tau(B^0)$
2015	1.0856 ± 0.0079 (1.09σ)
2016	1.0829 ± 0.0043 (1.17σ)
2017	1.0833 ± 0.0035 (1.37σ)
2018	1.0823 ± 0.0038 (1.15σ)

4.4.5 Angular Acceptance

The remaining three fit observables are the three helicity angles defined in §4.2. As performed with the decay time acceptance, the non-uniform reconstruction efficiency on these angles must also be taken into account. This non-uniform efficiency is mostly caused by momenta and transverse momenta selection requirements defined in Section §4.3 as well as the own angular acceptance of the LHCb detector (see Chapter 2). The angular acceptance is modeled using the well-established method of the angular weights [84], obtained from fully simulated samples iteratively corrected to match the real data.

4.4.5.1 Normalization weights

For adding detector effects in the angular observables to Eq. 4.5, the differential cross-rate is multiplied by an angular acceptance function $a(\Omega)$. The parameters of interest will be obtained by maximizing the log-likelihood function [85]:

$$\ln L(\Theta) = \sum_{i=0}^{N} \ln \frac{\sum_k N_k h_k(t_i) f_k(\Omega_i) a_k(\Omega_i)}{\int \sum_k N_k h_k(t) f_k(\Omega) a_k(\Omega) dt d\Omega} = \sum_{i=0}^{N} \ln \frac{\sum_k N_k h_k(t_i) f_k(\Omega_i)}{\sum_k w_k \int h_k dt}, \quad (4.24)$$

where in the last step the normalization weights w_k were defined. The arbitrary scale present in the acceptance correction (only ratios of w_k with different k matter) is solved by fixing $\omega_0 = 1$. As described in Ref. [85], the normalization weights can be obtained from simulated accepted events, as follows:

$$\omega_k \approx \sum_{i=0}^{accepted} f_K(\Omega_{reco}) \frac{\frac{d\Gamma(t_{true})}{dt}}{\frac{d\Gamma^4(\Omega_{true}, t_{true})}{dt d\Omega}}. \quad (4.25)$$

Note that in this derivation, the assumption that the efficiency correction can be performed independently for helicity angles is made (avoiding the correlations with the decay time correction). This assumption is cross-checked by calculating the angular weights in bins of decay time, as will be demonstrated at the end of this section.

4.4.5.2 Simulation Corrections

The angular weights are obtained from simulation events. As seen in Eq. 4.25, the calculation of the angular weights depends on the physics parameters of the sample. This implies that the generated physics parameters used for simulating the MC should be corrected to match the ones observed in the data. Additionally, the angular efficiency also depends on the kinematic information of the final states (particularly in the momenta and transverse momenta of the final states). To take into account both effects, a data-driven iterative method is used to match the simulation to data. A schematic representation can be seen in Fig. 4.12.

Initially, a correction is applied to the simulation to match the same fraction of polarities as observed in real data. Following this, a kinematic correction is performed on the kinematics of the B_s^0 as well as on $m(KK)$ to incorporate the S-wave component into the simulation. Subsequently, the iterative procedure starts. An angular and decay time fit is performed on data to determine the physics parameters (step 1 in Fig. 4.12). Then, per-event weights are calculated by the ratio of the differential decay rates evaluated with the physics parameters obtained from the fit to data and the ones used to generate the MC (step 2 in Fig. 4.12). Further, the MC is corrected by applying a GB-reweighting to the kinematic variables of kaons (step 3 in Fig. 4.12). Afterward, the angular weights are recomputed with all these corrections, making an iteration of the iterative procedure (step 4 in Fig. 4.12). These updated angular weights are used again to perform another angular and decay time fit of

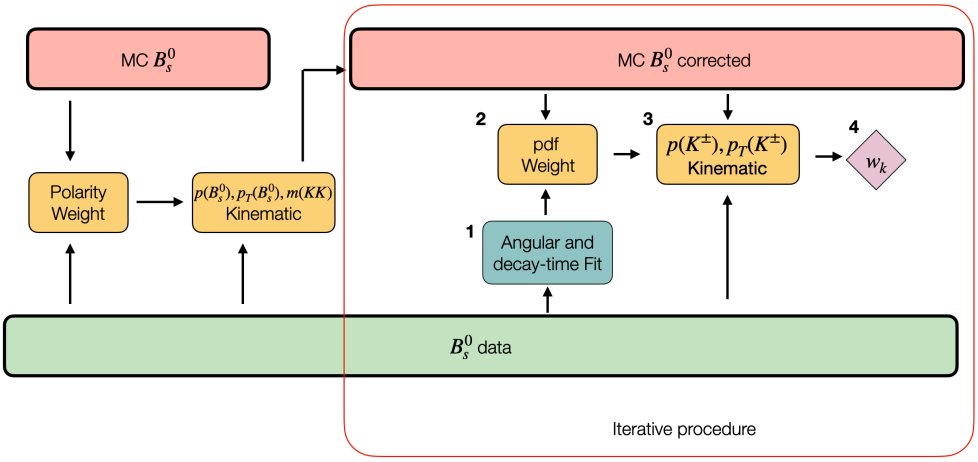

FIGURE 4.12: Schematic representation of the MC corrections performed during the angular acceptance procedure. The algorithm in the red box is repeated until each convergence of each w_k.

the data. The iterative process finishes when the angular weights no longer change with additional iterations.

4.4.5.3 Results

A uniform angular efficiency would imply the following w_k values:

$$w_k = \{1, 1, 1, 0, 0, 0, 1, 0, 0, 0\}. \tag{4.26}$$

That is one for the terms $A_i A_j^*$ when $i = j$ and zero for the rest. The baseline values for the normalization weights are shown in Table 4.10. It can be observed that they are compatible with a uniform angular efficiency within a few percent. The angular efficiencies for both trigger categories and each decay angle are illustrated in Fig. 4.13 for 2018 as an example.

4.4.5.4 Cross-checks

To validate the angular acceptance procedure, various studies are conducted using real data from control samples and simulated data. Additionally, the angular and decay-time factorization assumption is tested by calculating the angular weights in bins of the decay time.

TABLE 4.10: Normalization weights obtained for each year and trigger category. w_0 is skipped from this table and fixed to unity, see text for more details.

		2015	2016	2017	2018
BIASED	w_1	1.0352 ± 0.0065	1.0196 ± 0.0065	1.0211 ± 0.0049	1.0240 ± 0.0049
	w_2	1.0276 ± 0.0062	1.0177 ± 0.0060	1.0197 ± 0.0048	1.0151 ± 0.0048
	w_3	0.0023 ± 0.0053	0.0009 ± 0.0042	0.0005 ± 0.0040	0.0002 ± 0.0036
	w_4	0.0003 ± 0.0028	0.0009 ± 0.0027	0.0004 ± 0.0024	0.0018 ± 0.0023
	w_5	0.0004 ± 0.0029	0.00008 ± 0.0029	0.0033 ± 0.0023	-0.0020 ± 0.0023
	w_6	1.0224 ± 0.0046	1.0112 ± 0.0041	1.0139 ± 0.0034	1.0098 ± 0.0032
	w_7	-0.0085 ± 0.0037	-0.0046 ± 0.0035	-0.0018 ± 0.0031	0.0002 ± 0.0029
	w_8	0.0004 ± 0.0040	0.0021 ± 0.0035	0.0038 ± 0.0031	-0.0029 ± 0.0030
	w_9	-0.0405 ± 0.0089	0.0076 ± 0.0080	-0.0028 ± 0.0065	-0.0008 ± 0.0063
UNBIASED	w_1	1.0276 ± 0.0032	1.0333 ± 0.0031	1.0340 ± 0.0023	1.0270 ± 0.0024
	w_2	1.0300 ± 0.0032	1.0326 ± 0.0030	1.0326 ± 0.0023	1.0279 ± 0.0023
	w_3	0.0025 ± 0.0024	0.0049 ± 0.0022	0.0015 ± 0.0019	-0.0014 ± 0.0019
	w_4	-0.0037 ± 0.0015	-0.0003 ± 0.0014	0.0019 ± 0.0011	0.0005 ± 0.0011
	w_5	-0.0004 ± 0.0015	0.0003 ± 0.0014	-0.00002 ± 0.0011	0.0024 ± 0.0011
	w_6	1.0083 ± 0.0021	1.0140 ± 0.0021	1.0097 ± 0.0016	1.0085 ± 0.0016
	w_7	-0.0020 ± 0.0020	0.0032 ± 0.0018	-0.0002 ± 0.0014	0.0022 ± 0.0014
	w_8	-0.0011 ± 0.0019	0.0030 ± 0.0018	0.0004 ± 0.0015	0.0008 ± 0.0014
	w_9	0.0034 ± 0.0042	0.0010 ± 0.0039	-0.0033 ± 0.0030	-0.0033 ± 0.0031

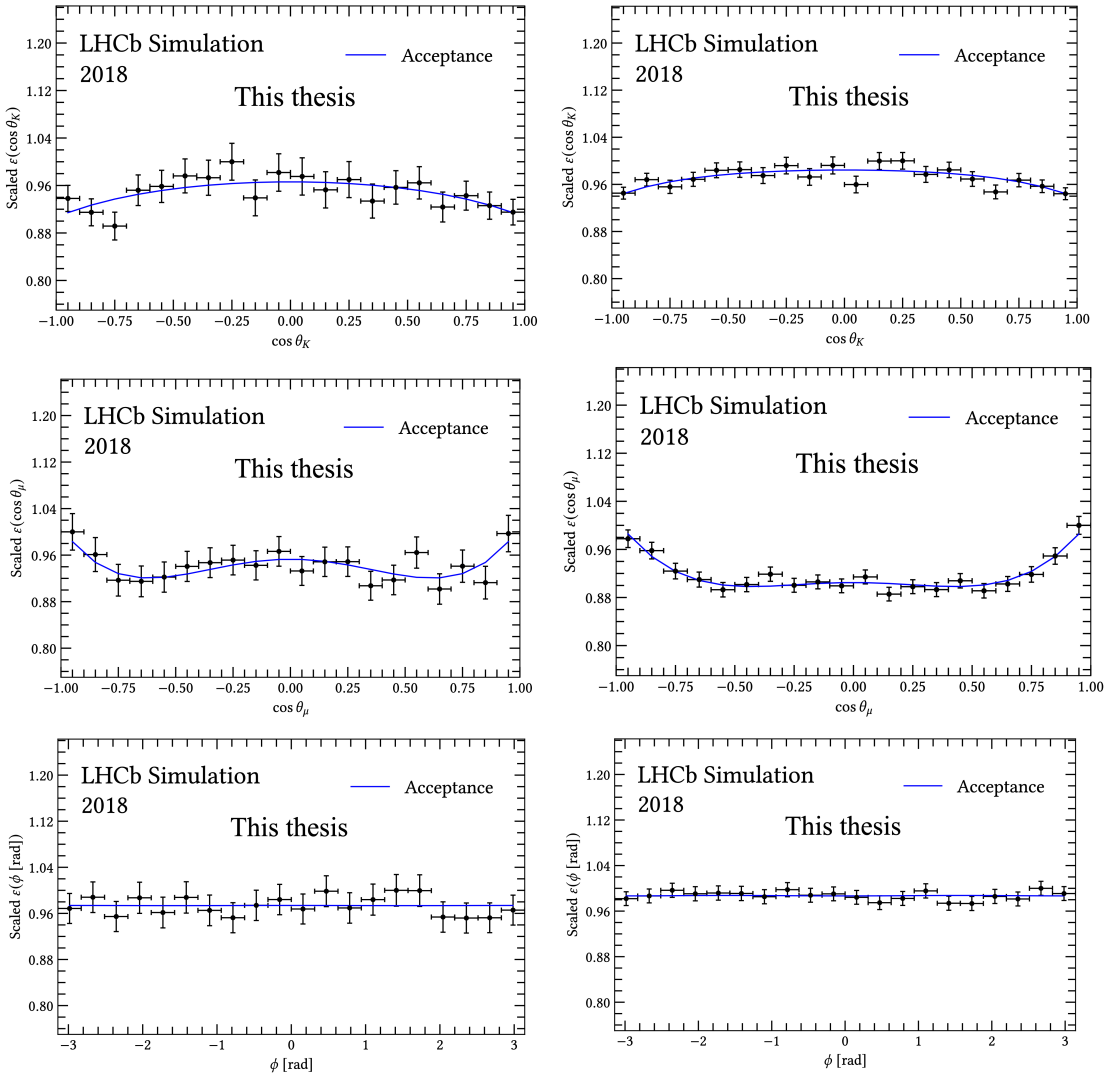

FIGURE 4.13: Angular Acceptance projection for 2018 signal MC for both trigger categories, biased (left) and unbiased (right).

4.4.5.5 Angular and decay time factorization

One of our assumptions is that the decay time and angular efficiencies can be evaluated independently, implying that these corrections factorize. This assumption is verified by calculating the normalization weights in three equally populated decay time bins. A good agreement is observed for both trigger categories [86].

4.4.5.6 Validation with $B^0 \to J/\psi K^{*0}$ real data

To test the method, the control channel $B^0 \to J/\psi K^{*0}$ is analyzed. Using the method described in this section, the results are compared with those from Run 1 analysis [87]. Similarly to the baseline procedure, the $m(K\pi)$ spectrum is split into four equally populated bins [826, 861, 896, 931, 966] MeV/c^2 to account for the different S-wave contributions. The same correction strategy is applied to this channel by replacing a K with a π. For this cross-check, no study of systematics is performed, meaning that only statistical errors are taken into account. An overall 0.03 p-value with the measurement reported in Ref. [87] is obtained.

4.4.5.7 Validation with B_s^0 MC

Another set of cross-checks is performed by utilizing only simulated B_s^0 events. Specifically, events are selected based on truth-matched `B_BKGCAT` $= 0, 50$ for simplicity. The candidates are split into two non-overlapping sets based on whether their event number is even or odd. One set serves as pseudo-data while the other is the corresponding MC used to determine the normalization weights.

To differentiate the data from the MC, two scenarios are considered. In the first scenario, an event with a kaon having low transverse momentum is penalized. This is achieved by applying a per-event weight defined as $w = p_T^3/(a + p_T)^3$ where a is a constant fixed to 200 MeV/c. In the second scenario, a GB-reweighting is applied to the pseudo-data to match the $p(K^\pm), p_T(K^\pm)$ distributions observed in the data. For the case of the $\Delta\Gamma = 0$ MC, utilizing all the Run 2 simulation years, an overall p-value of 0.45 and 0.29 for the first and second scenarios respectively using the baseline procedure is obtained. This p-value is calculated by comparing the parameters used to generate the MC with those derived from the decay time and angular fit. Conversely, when no corrections are applied an overall p-value of below 0.001 and 0.001 is obtained, respectively, highlighting the significance of the entire simulation correction during the angular acceptance procedure.

4.4.5.8 More variables in the iterative procedure

Various corrections and approaches were tested compared to the final baseline one observed in Fig. 4.12. The inclusion of corrections in $p(B_s^0)$, $p_T(B_s^0)$ and $m(K^+K^-)$ inside each iteration is also examined, as well as introducing corrections in the kinematics of the muons ($p(\mu^\pm)$, $p_T(\mu^\pm)$). However, these corrections yielded the same result as the baseline approach, while requiring higher computational resources. Therefore, the baseline configuration was chosen.

4.4.6 Flavor Tagging

As elucidated at the beginning of this chapter, $\phi_s^{c\bar{c}s}$ arises from the interference between the decay and the decay through mixing in $b \to c\bar{c}s$ transitions. Hence, it is crucial, for achieving enough precision in measuring $\phi_s^{c\bar{c}s}$, to accurately identify the flavor of the B meson at the production point. This task is extremely complicated in a p-p collider environment.

At LHCb, two types of flavor tagging algorithms are distinguished, classical taggers, which exploit specific event and/or track signatures, and the new Inclusive Flavor Tagger (IFT), which uses information from the entire event. The development of the latter will be described in Chapter 5, as for the baseline of this analysis, only the classical flavor taggers were used[6]. The classical taggers can be further categorized into:

- Same Side (SS) taggers. The b quarks are primarily produced in $b\bar{b}$ pairs, as explained in §2.2, one produces the signal B hadron (used for a particular physics analysis) and the other the OS B hadron. Along with the signal B hadron, a lighter charged hadron is produced, which is charged correlated with the flavor of the signal B hadron. For the case of the B_s^0 meson, this hadron is typically a kaon, while for the case of B^0 mesons, it could be a proton or a pion. The SS algorithm exploits the information of the charge of this track to identify the flavor of the produced B meson.
- Opposite Side (OS) taggers. These algorithms utilize information from the opposite B hadron. For this, information from the decay products of the opposite B is used to infer its flavor and, consequently, infer the flavor of the signal B meson. These OS taggers include different classification algorithms that use information on the charge of leptons (OSe, OSμ) produced in semileptonic B decays, charge of kaons produced via $b \to c \to s$ transitions (OSK), the charge of the reconstructed D meson from $b \to c$ transitions (OSc) and the charge of the SV (OSVtx).

[6] At the time of completing this project, the IFT yielded a slightly lower performance than the combination of classical taggers and therefore was not used in this analysis.

These algorithms provide two sources of information. First, the tagging decision, with values +1 for tagged B_s^0, -1 for tagged $\bar{B}_s^0$ or 0 for untagged events. Secondly, tagged events, provide an estimation of the mistag probability (η), which denotes the probability of this decision being incorrect. This mistag probability must be calibrated to ensure that it accurately reflects the true mistag probability (ω).

4.4.6.1 Flavor tagging dilution

In a similar way to the dilution explained in §4.4.2, the mixing amplitude is also reduced by a dilution factor due to imperfect flavor tagging. To comprehend this, it is necessary to define some quantities. The tagging efficiency is defined as the fraction of tagged events in the entire sample:

$$\epsilon_{tag} = \frac{N_{tag}}{N_{tot}} = \frac{N_W + N_R}{N_W + N_R + N_U}, \tag{4.27}$$

where N_W, N_R, and N_U represent the number of wrong-tagged events, the number of correctly tagged events, and the number of untagged events respectively. Additionally, the true mistag probability is defined as:

$$\omega = \frac{N_W}{N_R + N_W}, \tag{4.28}$$

Now, all the ingredients are available to see that the observed time-dependent CP asymmetry ($\mathcal{A}_{CP}^{obs}$) is reduced by a dilution factor depending on the mistag as follows:

$$\begin{aligned}
\mathcal{A}_{CP}^{obs}(t) &= \frac{N_{\bar{B}}^{obs}(t) - N_B^{obs}(t)}{N_{\bar{B}}^{obs}(t) + N_B^{obs}(t)} \\
&= \frac{(1-\omega)N_{\bar{B}}^{true}(t) + \omega N_B^{true}(t) - (1-\omega)N_B^{true}(t) - \omega N_{\bar{B}}^{true}(t)}{N_{\bar{B}}^{true}(t) + N_B^{true}(t)} \\
&= (1-2\omega)A_{CP}^{true}(t).
\end{aligned} \tag{4.29}$$

The statistical error of $\mathcal{A}_{CP}^{true}$ is therefore, proportional to:

$$\sigma(\mathcal{A}^{true}) \propto \frac{1}{\sqrt{\epsilon_{tag}N}(1-2\omega)} = \frac{1}{\sqrt{\epsilon_{eff}N}}. \tag{4.30}$$

Here the quantity $\epsilon_{eff} = \epsilon_{tag}(1-2\omega)^2$ is introduced, which is often referred to as a performance metric of the flavor tagging algorithm. As $\sigma(A^{true}) \propto \sigma(\phi_s^{c\bar{c}s})$, one can observe that the sensitivity to $\phi_s^{c\bar{c}s}$ is highly dependent on the performance of the flavor tagging algorithms.

4.4.6.2 Mistag calibration

The output of the Neural Network (η), needs to be calibrated to ensure that it corresponds to the true mistag probability (ω). For this, a linear dependency is assumed:

$$\omega(q,\eta) = (p_0 + q\frac{\Delta p_0}{2}) + (p_1 + q\frac{\Delta p_1}{2})(\eta - \bar{\eta}), \tag{4.31}$$

where q is +1 (-1) for an initial B_s^0 ($\bar{B}_s^0$) event. For calibration purposes, only flavor-specific decays are used. This is because, in these decays, the flavor of the B meson at the SV is inferred by the final states, reducing the complexity of the problem and allowing us to simplify the calibration. For the case of the OS taggers, no information on the fragmentation quark is needed, so usually, because of statistical and simplicity reasons, $B^+ \to J/\psi K^+$ is used. For the case of SSK, a flavor-specific decay of a B_s^0 meson is needed, choosing for this analysis $B_s^0 \to D_s^- \pi^+$.

4.4.6.3 Calibration of the OS tagger

The background subtracted $B^+ \to J/\psi K^+$ sample is GB-weighted in `nTracks`, nPVs, pseudo-rapidity and $p_T(B)$ to background subtracted $B_s^0 \to J/\psi K^+ K^-$, following the strategy described in §4.3.4.2. This is necessary to reduce the portability error (the error caused by the differences between the calibration sample and the signal sample) as the tagging performance is known to depend on these variables.

Since the B^+ is a charged meson, and therefore cannot oscillate, the charge of the final state kaon determines the flavor of the B meson at the production point. Hence, the pdf can be simply defined as:

$$\mathcal{P} = (1-a)\omega(q,\eta) + a(1-\omega(q,\eta)), \tag{4.32}$$

where ω is defined in Eq. 4.31, and $a = 1$ ($a = 0$) if the event has been correctly (incorrectly) tagged. An unbinned likelihood fit is performed to B^+ data to extract the calibration parameters of Eq. 4.31 ($p_0, p_1, \Delta p_0, \Delta p_1$). The calibration results can be found in Table 4.11, while the distributions of ω versus η for each year are displayed in Fig. 4.14.

TABLE 4.11: Results of the OS tagger calibration in $B^+ \to J/\psi K^+$ for all the years of the data-taking. First uncertainty is statistical and second is systematic.

	2015 + 2016	2017	2018
p_0	$0.3831 \pm 0.0007 \pm 0.0009$	$0.3821 \pm 0.0007 \pm 0.0006$	$0.3832 \pm 0.0006 \pm 0.0009$
p_1	$0.8518 \pm 0.0060 \pm 0.0163$	$0.8297 \pm 0.0065 \pm 0.0122$	$0.8406 \pm 0.0059 \pm 0.0079$
Δp_0	0.0092 ± 0.0013	0.0123 ± 0.0014	0.0114 ± 0.0013
Δp_1	0.0141 ± 0.0119	0.0510 ± 0.0135	0.0133 ± 0.0118

4.4.6.4 Calibration of the SS tagger

The case of the $B_s^0 \to D_s^- \pi^+$ is more complex. The B_s^0 meson oscillates, which implies that it is necessary to disentangle the oscillation by fitting the decay time distribution of the tagged events to get the flavor of the B_s^0 meson at the production point. To fit the decay time, accounting for the decay time resolution, and decay time acceptance is necessary. The pdf is given by:

$$\begin{aligned} P(t|\sigma_t) &= \epsilon(t) \left[\Gamma(t') * G(t - t'|\sigma_t)\right] \\ \Gamma(t) &= e^{-\Gamma_s t} \left[\cosh\left(\frac{1}{2}\Delta\Gamma_s t\right) + q_{mix}(1 - 2\omega(\eta)) \cos(\Delta m_s t)\right], \end{aligned} \tag{4.33}$$

where q_{mix} is equal to -1 (+1) if the meson has (not) oscillated, according to the charge of the final state pion and the tagging decision; $\epsilon(t)$ denotes the decay time efficiency which is modeled through a cubic-spline with knots at $t \in [0.4, 0.5, 1.0, 1.5, 2.0, 3.0, 12.0, 15.0]$. The decay time resolution G is modeled by a single Gaussian function where the decay time error, σ_t, is used as a conditional variable. The calibration of σ_t is determined by studying prompt D_s^- decays combined with an oppositely charged track. Before the calibration, the background subtracted $B_s^0 \to D_s^- \pi^+$ sample is GB-weighted in `nTracks`, nPVs, pseudo-rapidity and $p_T(B)$ to background subtracted $B_s^0 \to J/\psi K^+ K^-$, following the strategy described in Section §4.3.4.2.

The flavor tagging calibration results can be found in Table 4.12, while the distributions of ω versus η for each year are displayed in Fig. 4.15

4.4.6.5 Tagging power in $B_s^0 \to J/\psi K^+ K^-$

Once the calibration for each tagging algorithm and data-taking year is obtained, the mistag probability of the signal sample $B_s^0 \to J/\psi K^+ K^-$ is corrected. The tagging power is then calculated as follows:

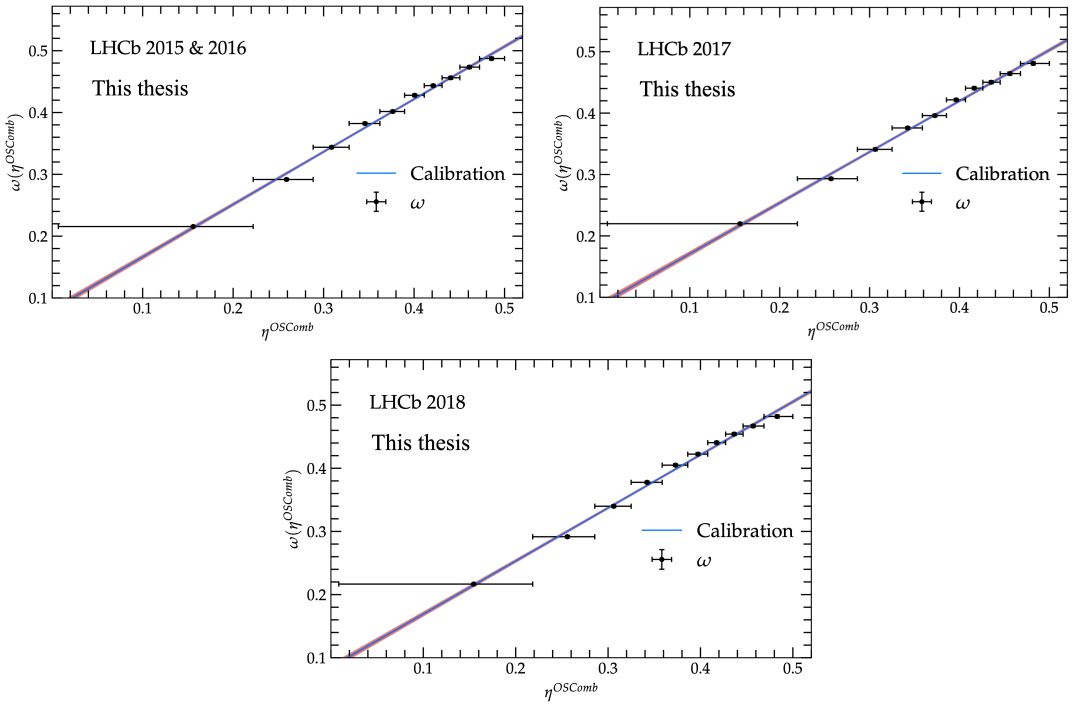

FIGURE 4.14: True vs estimated mistag probabilities for the OS tagger in $B^+ \to J/\psi K^+$ for all the years of the data-taking. The solid blue line shows the calibration, with dark and light red bands corresponding to 1 and 2 statistical uncertainties.

$$\begin{aligned} \epsilon_{eff} =& \frac{\sum_i sw_i (A_i - B_i)^2/(A_i + B_i)^2}{\sum_i sw_i}, \\ A_i =& (1 + q_i^{OS}(1 - 2\omega_i^{OS}))(1 + q_i^{SS}(1 - 2\omega_i^{SS})), \\ B_i =& (1 - q_i^{OS}(1 - 2\omega_i^{OS}))(1 - q_i^{SS}(1 - 2\omega_i^{SS})), \end{aligned} \tag{4.34}$$

where sw_i is the per-event weight defined in §4.3.7. Table 4.13 shows the tagging performances obtained for the signal sample for each of the data taking years.

TABLE 4.12: Results of the SSK tagger calibration in $B_s^0 \to D_s^- \pi^+$ for all the years of the data-taking. First uncertainty is statistical and second is systematic.

	$2015 + 2016$	2017	2018
p_0	$0.4459 \pm 0.0051 \pm 0.0026$	$0.4387 \pm 0.0048 \pm 0.0016$	$0.4431 \pm 0.0050 \pm 0.0021$
p_1	$0.7357 \pm 0.0608 \pm 0.0235$	$0.6382 \pm 0.0574 \pm 0.0414$	$0.7321 \pm 0.0594 \pm 0.0361$
Δp_0	-0.0164 ± 0.0009	-0.0158 ± 0.0008	-0.0158 ± 0.0007
Δp_1	0.0277 ± 0.0089	0.0143 ± 0.0083	0.0229 ± 0.0077

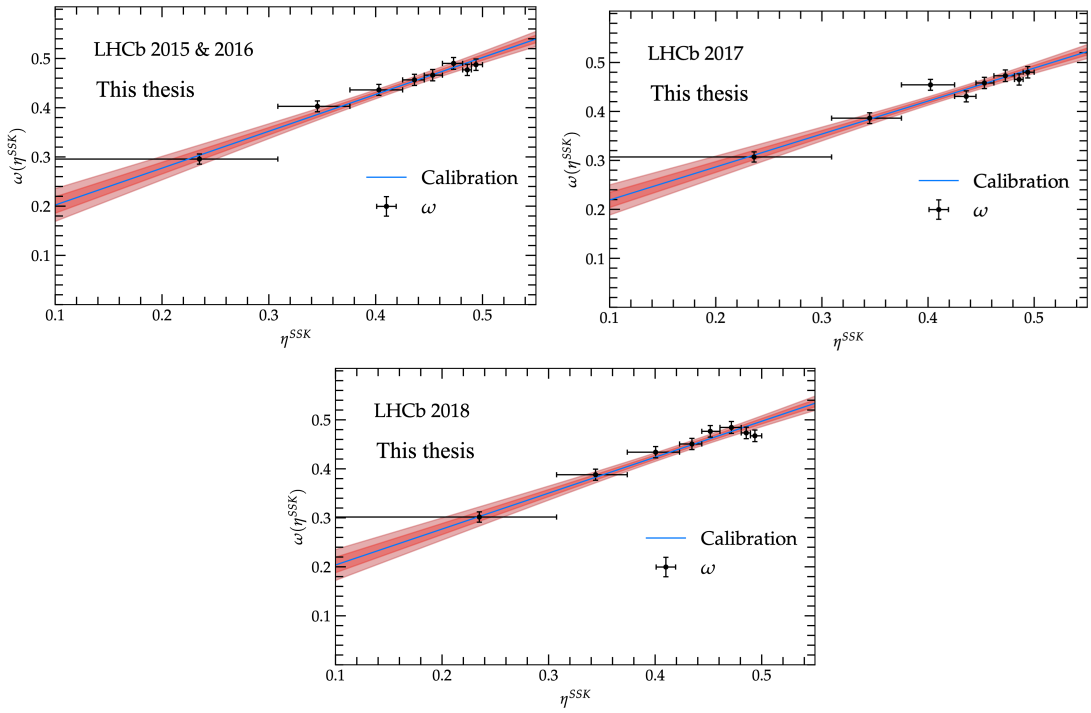

FIGURE 4.15: True vs estimated mistag probabilities for the SSK tagger in $B_s^0 \to D_s^- \pi^+$ for all the years of the data-taking. The solid blue line shows the calibration, with dark and light red bands corresponding to 1 and 2 statistical uncertainties.

4.5 Results

In this section, the measured physics parameters estimated by maximizing the log-likelihood ($\log L$) are presented. First, in §4.5.1, the experimental effects discussed in §4.4 are integrated into the theoretical decay rate described in Eq. 4.5. Subsequently, two measurements are conducted: one assuming that the CP-violating parameters are independent of the final state, as detailed in §4.5.2, and another approach, outlined in §4.5.3, where this assumption of polarization independence is relaxed.

4.5.1 Model with experimental corrections

The main parameters of interest are $\phi_s^{c\bar{c}s}$, $\Delta\Gamma_s$, Γ_s, $|\lambda|$ and Δm_s. Additionally, due to the angular analysis, two P-wave polarization amplitudes, ($|A_0|^2$ and $|A_\perp|^2$)[7]. six S-wave amplitudes ($A_{S,i}$, one per m_{KK} bin), and the corresponding strong phases per polarization state ($\delta_\parallel - \delta_0$, $\delta_\perp - \delta_0$, $\delta_{S,i} - \delta_\perp$) are also measured[8]. Instead of

[7] Note that only two P-wave amplitudes are free parameters as they must satisfy $|A_0|^2 + |A_\perp|^2 + |A_\parallel|^2 = 1$.

[8] This is because the pdf is only sensitive to differences of strong phases and we set the δ_0 arbitrarily to 0.

TABLE 4.13: Tagging performance observed in $B_s^0 \to J/\psi K^+K^-$.

	Tagger	$\epsilon_{tag}(\%)$	$(1-2\omega)^2$	$\epsilon_{eff}(\%)$
2015+2016	$OS-only$	11.34	0.0776	0.88 ± 0.01
	$SS-only$	42.58	0.0278	0.97 ± 0.14
	$OS+SS$	23.93	0.0974	2.33 ± 0.06
	$Total$	77.85	0.0495	4.18 ± 0.15
2017	$OS-only$	11.11	0.0792	0.88 ± 0.01
	$SS-only$	43.16	0.0218	0.94 ± 0.14
	$OS+SS$	24.45	0.0982	2.40 ± 0.07
	$Total$	78.67	0.0536	4.22 ± 0.16
2018	$OS-only$	11.17	0.0814	0.91 ± 0.01
	$SS-only$	42.96	0.0235	1.01 ± 0.14
	$OS+SS$	24.80	0.0987	2.45 ± 0.07
	$Total$	78.93	0.0552	4.36 ± 0.16

measuring $\delta_{S,i} - \delta_0$ differences of $\delta_{S,i} - \delta_\perp$ are fitted due to high correlations ($> 90\%$) between these parameters.

Additionally, instead of Γ_s, the difference of decay widths between the B_s^0 and B^0 mesons, defined as $\Delta\Gamma_d^s = \Gamma_s - \Gamma_d$, is measured. This is because it can be measured independently of the Γ_d used in the decay time acceptance (see §4.4.4), and therefore can be measured with higher precision [68]. Defining $\Gamma_d = \Gamma_d^0 + \delta\Gamma_d$, where Γ_d^0 is the chosen value in §4.4.4, the $\epsilon_{B_s^0}^{Data}$ is expressed as (see Eq. 4.21) [68]:

$$\epsilon_{B_s^0}^{Data}(t,\Gamma_d) \propto \frac{1}{e^{-\Gamma_d t} \otimes G(t,\sigma,\mu)} = \frac{e^{\delta\Gamma_d}}{e^{-\Gamma_d^0 t} \otimes G(t,\sigma,\mu)} = \epsilon_{B_s^0}^{Data}(t,\Gamma_d^0) \times e^{\delta\Gamma_d}. \quad (4.35)$$

Expressing Γ_s as $\Delta\Gamma_d^s + \Gamma_d^0 + \delta\Gamma_d$, the time-dependent part of the pdf is [68]:

$$\begin{aligned} \mathcal{P}(t) &\sim \epsilon_{B_s^0}^{Data}(t,\Gamma_d^0) \times e^{\delta\Gamma_d} \times [e^{-\Gamma_s t} \otimes G(t|\mu,\sigma] \\ &= \epsilon_{B_s^0}^{Data}(t,\Gamma_d^0) \times [e^{-(\Delta\Gamma_d^s t + \Gamma_d^0)} \otimes G(t|\mu,\sigma)], \end{aligned} \quad (4.36)$$

which is independent of $\delta\Gamma_d$. So the value of $\Delta\Gamma_d^s$ can be measured independently of the chosen Γ_d^0 in §4.4.4. The full pdf for all years (y), trigger categories (c) in each m_{KK} bins ($i \in [1,6]$) can be expressed as:

$$\mathcal{P}^i_{y,c}(t,\Omega|\sigma,\mu,\tilde{q}_{\bar{B}^0_s},\tilde{q}_{B^0_s}) = \\ \sum_{k=1}^{10}\frac{1}{N_{y,c}}\tilde{N}^i_k f_k(\Omega)\epsilon_{y,t}(t)\times\left\{G(t|\mu,\sigma_t)\otimes\left(\tilde{q}_{B^0_s}h_k(t|B^0_s)+\tilde{q}_{\bar{B}^0_s}h_k(t|\bar{B}^0_s)\right)\right\}, \tag{4.37}$$

where $\tilde{N}^i_k = N^i_k$ for k<8 while for the S-P wave interference terms (k=8,9,10), it takes the form $\tilde{N}^i_k = C_{SP}N^i_k$. The functions $f_K(\Omega)$ and $h_k(t)$, were defined in Eq. 4.5. The decay time efficiency is described by $\epsilon_{y,t}(t)$ as discussed in §4.4.4. The resolution model is encoded in $G(t|\mu,\sigma_t)$ as discussed in §4.4.2 and §4.4.3. The $\tilde{q}_{B^0_s}$ and $\tilde{q}_{\bar{B}^0_s}$ functions encode SS and OS flavor taggers information, taking the form:

$$\begin{aligned}\tilde{q}_{B^0_s} =&(1+q_{OS})(1-2\omega_{OS})(1+q_{SS})(1-2\omega_{SS}),\\ \tilde{q}_{\bar{B}^0_s} =&(1-q_{OS})(1-2\omega_{OS})(1-q_{SS})(1-2\omega_{SS}).\end{aligned} \tag{4.38}$$

Finally the normalization of the pdf, $N_{y,c}$ is defined as:

$$N_{y,c} = \int_{t=0.3\text{ps}}^{t=15\text{ps}}\int_\Omega\sum_i\sum_k w_k P_{i,k}(t,\Omega|\mu,\sigma_t,\tilde{q}_{\bar{B}^0_s},\tilde{q}_{B^0_s})dtd\Omega, \tag{4.39}$$

where w_k is the normalization weight calculated in §4.4.5.

4.5.2 Polarization independent results

The polarization-independent results can be seen in Table 4.14 and the fit projections in each of the variables are displayed in Fig. 4.16. The tagging calibration parameters and the spline coefficients of the time acceptance are added as Gaussian constraints to the fit taking into account the corresponding covariance matrix. The asymmetric errors are obtained with `MINOS` through a likelihood scan. The $B^0_s - \bar{B}^0_s$ asymmetry as a function of the decay time is displayed in Fig. 4.17 where the candidates were weighted taking into account the dilution from flavor tagging and the dilution from decay time resolution. The one-dimension likelihood profiles for the main parameters of interest are displayed in Fig. 4.18.

4.5.3 Polarization dependent results

The results considering the potential dependence on the polarization of the CP parameters ϕ_s and $|\lambda|$ are shown in Table 4.15. As in the baseline, the asymmetric errors are obtained with Minos, and the tagging calibration parameters and the spline

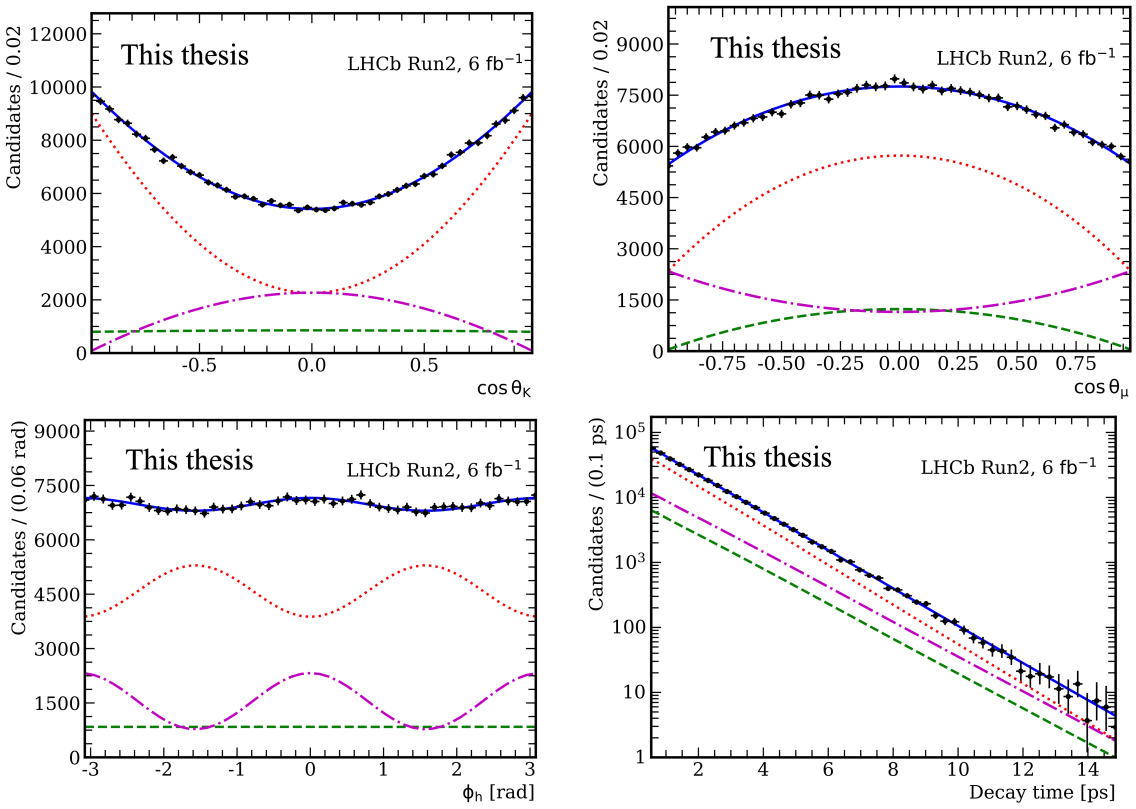

FIGURE 4.16: Helicity angles and decay time fit projections from background subtracted $B_s^0 \to J/\psi K^+K^-$ candidates. The solid blue line shows the total contribution. CP-even, CP-odd, and S-wave contributions are shown in red, purple, and green respectively.

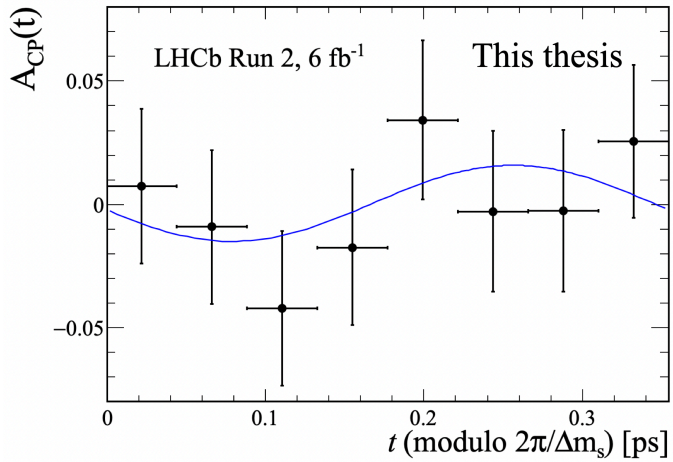

FIGURE 4.17: Weighted $B_s^0 - \bar{B}_s^0$ asymmetry as a function of decay time. Data points are shown in black, while the fit projection is shown in blue. To improve the visibility, data points are weighted, and the entire decay-time distribution is projected onto a single oscillation period.

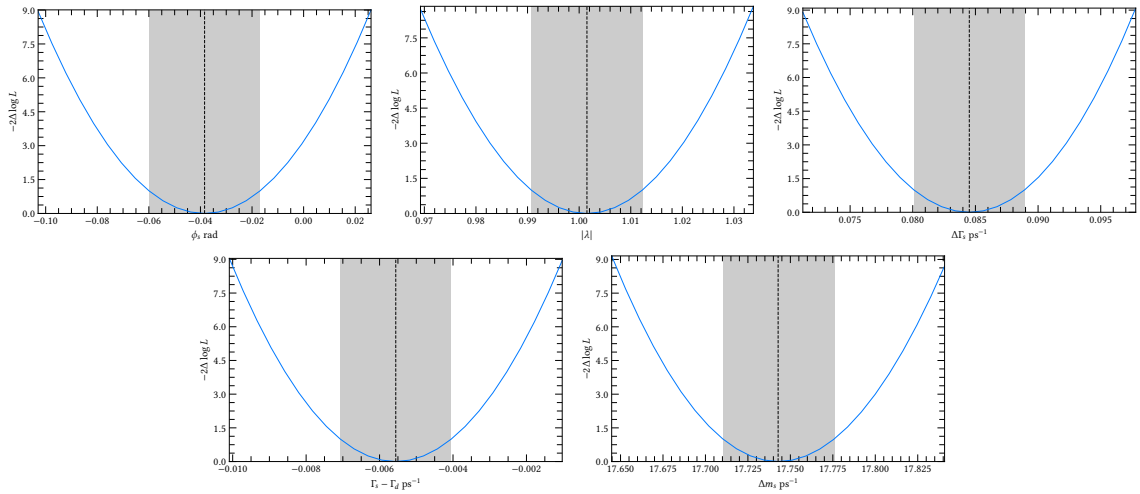

FIGURE 4.18: Likelihood profiles in blue for the main parameters of interest in the polarization-independent approach. The gray band corresponds to $-2\text{Log}L = 1$.

TABLE 4.14: Parameter obtained for the polarization-independent fit in comparison with the previous results of Run 1 [67] and Run 2 [68].

Parameter	baseline	Run 2, 2fb^{-1}	Run 1
ϕ_s[rad]	-0.0386 $\pm$ 0.0215	$-0.083^{+0.041}_{-0.041}$	-0.058 ± 0.049
$\lvert\lambda$	1.001 $\pm$ 0.011	$1.012^{+0.016}_{-0.015}$	0.964 ± 0.019
$\Delta\Gamma_d^s$[ps^{-1}]	-0.0056 $^{+0.0013}_{-0.0015}$	$-0.0041^{+0.0024}_{-0.0023}$	0.0024 ± 0.0027
$\Delta\Gamma_s$[ps^{-1}]	0.0845$\pm$0.0044	$0.0773^{+0.0076}_{-0.0077}$	0.0805 ± 0.0091
Δm_s[ps^{-1}]	17.743 $\pm$ 0.033	$17.703^{+0.057}_{-0.059}$	$17.711^{+0.055}_{-0.057}$
$\lvert A_\perp\rvert^2$	0.2463 $\pm$ 0.0023	$0.2456^{+0.0040}_{-0.0040}$	0.2504 ± 0.0049
$\lvert A_0\rvert^2$	0.5179 $\pm$ 0.0017	$0.5186^{+0.0029}_{-0.0029}$	0.5241 ± 0.0034
$\lvert A_S^1\rvert^2$	0.472 $\pm$ 0.024	$0.492^{+0.043}_{-0.043}$	0.426 ± 0.054
$\lvert A_S^2\rvert^2$	$0.0421^{+0.0048}_{-0.0046}$	$0.0406^{+0.0082}_{-0.0075}$	0.059 ± 0.017
$\lvert A_S^3\rvert^2$	$0.0029^{+0.0013}_{-0.0009}$	$0.0044^{+0.0030}_{-0.0017}$	0.0101 ± 0.0067
$\lvert A_S^4\rvert^2$	$0.0037^{+0.0025}_{-0.0019}$	$0.0069^{+0.0062}_{-0.0045}$	0.0103 ± 0.0061
$\lvert A_S^5\rvert^2$	$0.0508^{+0.0070}_{-0.0068}$	$0.073^{+0.013}_{-0.013}$	0.049 ± 0.015
$\lvert A_S^6\rvert^2$	0.151 $\pm$ 0.011	$0.152^{+0.019}_{-0.018}$	0.193 ± 0.025
$\delta_\parallel - \delta_0$[rad]	3.146 $\pm$ 0.061	$3.062^{+0.082}_{-0.074}$	$3.258^{+0.099}_{-0.181}$
$\delta_\perp - \delta_0$[rad]	$2.903^{+0.075}_{-0.074}$	$2.64^{+0.13}_{-0.13}$	$3.08^{+0.14}_{-0.15}$
$\delta_{S1} - \delta_\perp$[rad]	$2.05^{+0.12}_{-0.14}$	$2.21^{+0.17}_{-0.20}$	0.84 ± 0.20
$\delta_{S2} - \delta_\perp$[rad]	$1.62^{+0.18}_{-0.19}$	$1.56^{+0.29}_{-0.29}$	2.15 ± 0.28
$\delta_{S3} - \delta_\perp$[rad]	$1.16^{+0.37}_{-0.29}$	$1.09^{+0.47}_{-0.36}$	0.47 ± 0.21
$\delta_{S4} - \delta_\perp$[rad]	$-0.15^{+0.12}_{-0.15}$	$-0.28^{+0.16}_{-0.26}$	-0.34 ± 0.17
$\delta_{S5} - \delta_\perp$[rad]	$-0.637^{+0.068}_{-0.076}$	$-0.536^{+0.090}_{-0.102}$	-0.59 ± 0.15
$\delta_{S6} - \delta_\perp$[rad]	$-1.013^{+0.074}_{-0.083}$	$-1.10^{+0.13}_{-0.16}$	-0.90 ± 0.14

coefficients of the time acceptance are added as Gaussian constraints to the fit.

TABLE 4.15: Results of the polarization dependent approach for the main parameters of interest.

Parameters	Values
ϕ_s^0 [rad]	-0.0343 ± 0.0231
$\phi_s^{\parallel} - \phi_s^0$ [rad]	$-0.0019^{+0.0212}_{-0.0214}$
$\phi_s^{\perp} - \phi_s^0$ [rad]	$-0.0008^{+0.0198}_{-0.0206}$
$\phi_s^S - \phi_s^0$ [rad]	$0.0224^{+0.0273}_{-0.0262}$
$\lvert\lambda^0\rvert$	$0.9687^{+0.0248}_{-0.0243}$
$\lvert\lambda^{\parallel}/\lambda^0\rvert$	$0.9821^{+0.0554}_{-0.0523}$
$\lvert\lambda^{\perp}/\lambda^0\rvert$	$1.1073^{+0.0816}_{-0.0755}$
$\lvert\lambda^S/\lambda^0\rvert$	$1.1210^{+0.0844}_{-0.0778}$
$\Gamma_s - \Gamma_d$ [ps^{-1}]	$-0.0056^{+0.0013}_{-0.0015}$
$\Delta\Gamma_s$ [ps^{-1}]	0.0846 ± 0.0044
Δm_s [ps^{-1}]	17.750 ± 0.033

4.6 Cross-checks and systematics

The results presented in Section §4.5 are validated through various cross-checks and systematic studies. Consistency checks and validations are summarized in Section §4.6.1, and the primary sources of systematic uncertainties are detailed in Section §4.6.2.

4.6.1 Consistency checks and validations

The studies described in this section include various agreement analyses between non-overlapping regions of the datasets as detailed in Section §4.6.1.1. The impact of generating the simulation samples with the most representative TCK of each period is explained in Section §4.6.1.2. Finally, the validation of the statistical error using the bootstrapping technique is described in Section §4.6.1.3.

4.6.1.1 Cross-checks in subsets of the data

To test the stability of our results, the analysis is repeated on subsets of the data. The agreement between the results is assessed using the p-value, calculated based on the number of degrees of freedom ($nDoF$):

$$p = 1 - CDF(\chi^2, nDoF) \tag{4.40}$$

Assuming that all the detector effects are correctly accounted for, the results in all subsets must be consistent. The first block of Table 4.16 displays the agreement for each of the main parameters of interest, where the p-value obtained only takes into account statistical errors, which implies that the agreement is greater. No significant deviations or inconsistencies are found.

TABLE 4.16: P-values obtained for each of the consistency checks performed on subsets of data for the main parameters of interest. A p-value of one signifies perfect agreement, while a p-value of zero indicates null agreement. Note that only statistical errors are considered.

Subsets	$\phi_s[\text{rad}]$	$\Delta\Gamma_s[\text{ps}^{-1}]$	$\Gamma_d^s[\text{ps}^{-1}]$	$\lvert\lambda\rvert$	$\Delta m_s[\text{ps}^{-1}]$
Magnet Polarity	0.827	0.943	0.264	0.439	0.637
Trigger Category	0.466	0.640	0.490	0.484	0.194
Data taking year	0.076	0.710	0.406	0.151	0.381
$p_T(B_s^0)$	0.288	0.763	0.043	0.634	0.358
$\eta(B_s^0)$	0.822	0.350	0.567	0.678	0.040
Tagging Algorithm	0.241	0.040	0.756	0.108	0.395
number of PVs	0.829	0.022	0.158	0.588	0.034
$\Delta\text{Log}L_{K\pi}$	0.481	0.066	0.169	0.214	0.212
L0TCKs	0.997	0.405	0.596	0.687	0.931
HLT1TCKs	0.026	0.071	0.211	0.060	0.026

4.6.1.2 Effect of the different TCKs

During a data-taking period, the thresholds of the L0 lines vary, while the MC is usually simulated with the most representative one of each period. To validate this assumption, B_s^0 and B^0 data samples are split into two categories based on whether they match the Trigger Configuration (key) present in the simulation. A good agreement is seen between the two data samples (see Table 4.16 L0TCKs row).

Not all the candidates from the 2016 real data have passed the same HLT1 selection criteria. However, the simulation was only produced with the most representative HLT1 configuration observed in the data. To assess this effect, a new 2016 MC with mixed HLT1 TCK is generated to mimic the data, and the results are compared with the baseline. A good consistency is observed between both data samples (see Table 4.16 HLT1TCKs row).

4.6.1.3 Bootstrapping

The reliability of the uncertainties on the physics parameters is evaluated by applying the bootstrapping technique to the data. One thousand pseudo-samples are created by randomly selecting events from the data sample until matching data statistics. After creating the samples, the decay time angular fit is repeated. The root Mean Square (RMS) is obtained from the central values distribution. A comparison between the RMS obtained and the errors provided by HESSE is shown in Table 4.17 for the main parameters of interest. The central values distributions can be found in Fig. 4.19. Some small differences are observed between bootstrapping and fit errors, especially in the Δm_s observable. Because some physics parameters are known to have less pronounced minima or asymmetric errors, the baseline statistical errors are obtained using MINOS (likelihood profiles).

TABLE 4.17: Variation in the statistical uncertainties for the main parameters of interest using the errors provided by the fit (HESSE) and the ones obtained with bootstrapping for the full Run 2 data.

Parameter	HESSE	Bootstrapping
ϕ_s [rad]	0.0215	0.02211 ± 0.00049
$\lvert\lambda\rvert$	0.0108	0.01188 ± 0.00027
$\Delta\Gamma_d^s$ [ps^{-1}]	0.00141	$0.00135 \pm$ 3e-05
$\Delta\Gamma_s$ [ps^{-1}]	0.00443	0.00433 ± 0.0001
Δm_s [ps^{-1}]	0.0327	0.04135 ± 0.00092

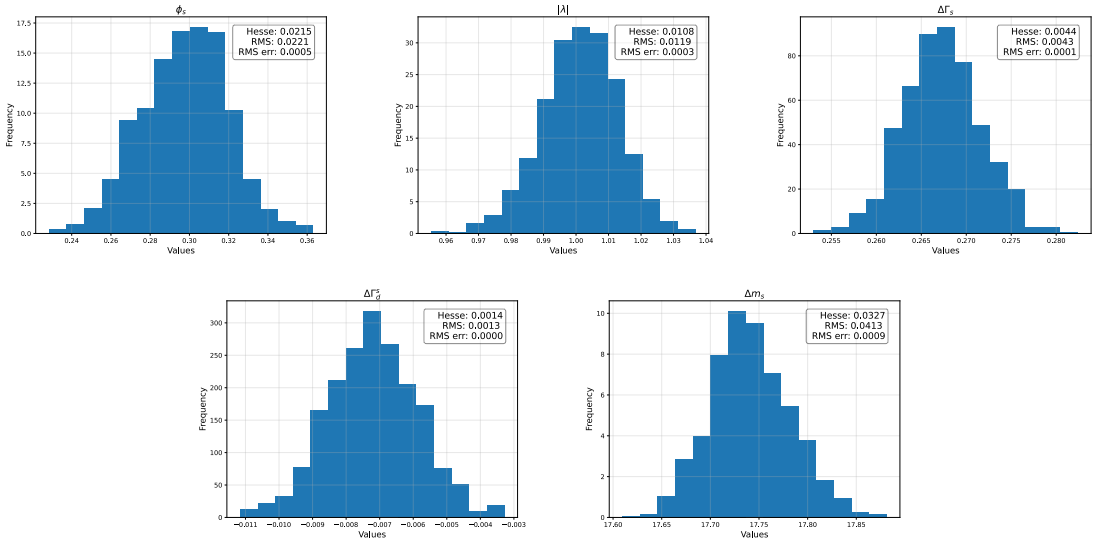

FIGURE 4.19: Central value distribution obtained from 1000 bootstrapped samples. The error from each fit (HESSE) and the RMS of the histogram are displayed for comparison.

4.6.2 Systematic uncertainties

Systematic uncertainties for the main parameters of interest are summarized in Table 4.18. Note that flavor tagging, statistical effect from spline coefficients, and B_c^+ contribution are already accounted for in the statistical error. The sources of potential systematic effects and the methods used to evaluate them are described below.

TABLE 4.18: Systematic uncertainties for the main parameters of interest.

Source	ϕ_s [rad]	$\Delta\Gamma_s$ [ps^{-1}]	$\Delta\Gamma_d^s$ [ps^{-1}]	$\lvert\lambda\rvert$	Δm_s [ps^{-1}]
Multiple cand.	0.0027	0.0001	0.00014	0.0022	0.0024
PID	0.0027	0.0015	0.0005	0.0027	0.0046
Time res. calibration	0.0003	−	−	0.0002	0.0005
Time res. translation	0.0008	−	−	0.0003	0.0009
Lifetime bias	-	+0.0003	-	-	-
Time bias correction	−0.0006	0.0005	0.0003	−0.0005	−0.0044
Time acc. simulation	0.00002	-0.0004	0.00025	0.00001	-0.00003
Ang. acc. statistical	0.0025	0.0002	0.0001	0.0032	0.0013
Mass factorization	0.0042	0.0016	0.0012	0.0019	0.0018
MF statistical	0.0005	0.0001	0.0002	0.0009	0.0011
MF width parametrization	0.0003	0.0004	0.0002	0.0002	0.0003
C_{SP} factors	0.0001	0.0001	−	0.0003	0.0004
Momentum scale	0.0004	−	0.0001	−	0.0013
Length scale	0.0004	−	0.0002	−	0.0031
D-wave	0.00019	0.00027	0.00013	−	0.00024
GB-weight configuration	0.0001	0.0003	0.0002	0.0001	0.0031
Category 60	0.00017	−	0.0002	0.0010	0.00010
Angular resolution	0.0002	0.0001	-	0.0001	0.0002
Analysis validation	-	-	-	-	-
Tot. syst.	0.0064	0.0024	0.0014	0.0053	0.0086
Stat.	0.022	0.0044	0.0014	0.011	0.033

Multiple Candidates. The number of events containing more than one candidate is approximately 0.3% in the signal region. This primarily arises from events with a shared J/ψ combined with different kaon tracks. The difference between the baseline result and removing the clones by randomly selecting one candidate is chosen as the systematic uncertainty.

PID correction. The systematic error associated with PID correction includes two main sources. Firstly, it considers the finite statistics of the template used for PID correction, and secondly, it accounts for the parametrization of the Kernel Density Estimation (KDE) used for obtaining the final PDF. For the first source, four different templates from bootstrapped samples are used, while for the second one, a template obtained with a modified kernel width is employed. The maximum difference for each parameter is taken as a systematic uncertainty.

Mass fit (MF) statistical. The per-event sWeights depends on the parameters obtained from the invariant mass fit. To assess the effect of the statistical error, the parameters are varied within the statistical error and the sWeights are recalculated accordingly. The maximum difference is taken as a systematic uncertainty.

Mass fit (MF) width parametrization. Alternative parameterizations are chosen to model the correlation between the mass width and the per-event mass error (parabolic and cubic polynomials). The maximum difference is taken as a systematic uncertainty.

Mass factorization. The baseline procedure assumes that the invariant mass is independent of the variables (decay time and helicity angles). To check this assumption the sWeights are recalculated in bins of the decay time and the three helicity angles, and then the full analysis is repeated. The difference with the baseline is taken as a systematic uncertainty.

Category 60. This simulation category contains a background component that is also present in the data. In the baseline the sWeights are calculated for the entire simulation sample. To cross-check the background rejection of the baseline treatment, the sWeights are recalculated for simulation only using category 60. Subsequently, the obtained sWeights are merged with the rest of `B_BKGCATs`. The acceptances and final fit are repeated. The difference between this approach and the baseline one is taken as a systematic uncertainty.

Decay time resolution statistical effect. To assess the effect of the statistical uncertainty of the calibration parameters coming from the decay time resolution correction, 100 values are generated from Gaussian distributions with a mean and a width fixed from the calibration fit. This effect is found to be negligible.

Decay time resolution translation. The effect of translating from prompt samples to signal sample (see Eq. 4.17) is checked by using directly the calibration obtained from inclusive prompt samples (red curves in Fig. 4.8). The differences are found to be negligible.

Induced lifetime bias due to decay time resolution. A single Gaussian model cannot account for nongaussian tails in the exact decay time error distribution. This effect is expected to be partially corrected by the decay time acceptance, however, a conservative approach for assessing the systematic uncertainty is chosen. The decay time distribution is symmetrized around the fitted μ (from the negative tail) and the

averaged decay time is computed in the integration range. The differences obtained between this check and the expected correction due to finite integration interval are assigned as systematic. This effect is negligible in $\Delta\Gamma_d^s$ (similar bias in B_s^0 and B^0) while for $\Delta\Gamma_s$ it is at the level of $0.0003\,\mathrm{ps}^{-1}$.

Decay time bias correction. The mean shift in the resolution model may not be enough to correct the effect of the VELO misalignment. An associated systematic uncertainty is computed by the difference between the values used to generate the simulation of a misaligned MC with the ones obtained from the baseline correction of this effect.

Decay time acceptance from different simulation samples. The signal MC with $\Delta\Gamma_s \neq 0$ is used to evaluate this systematic uncertainty. First, the simulation is weighted to have a distribution compatible with $\Delta\Gamma_s = 0$, the decay time efficiency is recalculated with this MC, and the systematic is obtained by the difference between the physics parameters obtained and the ones of the baseline.

Statistical of spline coefficients. The spline coefficients are Gaussian constrained with the respective covariance matrix in the final decay time and angular fit and therefore this effect is already taken into account in the statistical error.

GB-weight configuration. A set of 100 different GB-weight configurations are chosen in the decay time and angular acceptance procedures. The systematic is obtained by the difference between the averaged results and the baseline.

Angular acceptance statistical. The nominal fit is repeated with 100 pseudo-angular weights obtained from the respective multi-gaussian distribution. The systematic is obtained by the difference between the averaged mean from these results and those from the baseline.

Angular resolution. In our analysis strategy, the potential effect of the angular resolution is not considered. The S-wave MC is used as pseudo-data to compute this systematic, by recalculating the angular acceptance and angular and decay time fit using the generator-level helicity angles or the reconstructed ones. Decay time resolution and flavor tagging calibration are also used (taken from the simulation) to make the test more realistic. The differences are negligible for the parameters of interest.

C_{SP} systematic uncertainty. Three different models are chosen to model the S-wave lineshape. The angular and decay time fit is repeated with the recalculated C_{SP} factors. The differences are found to be negligible.

Flavor tagging systematics. Various sources are considered, including alternative mass models chosen in the invariant fit (negligible), alternative calibration model (second-order polynomial instead of linear fit), and the MC portability error that includes the differences between signal and calibration modes. Since these parameters

are Gaussian constraints in the angular and decay time fit, these effects are absorbed in the statistical error.

Momentum and length scale error. Length and momentum scale uncertainties are introduced to the S-wave MC. The entire analysis strategy is repeated using the S-wave MC as pseudo-data. The differences concerning the default S-wave are taken as systematic uncertainties.

B_c^+ contribution. The decay $B_c^+ \to B_s^0\pi^+$, which pollutes the signal sample, may potentially bias our $\Delta\Gamma_d^s$ and $\Delta\Gamma_s$ measurements. This is because the PV of the B_c^+ can be potentially confused with the PV of the B_s^0 and therefore the estimated decay length is biased to larger values. The observed biases in MC for the lifetime are added to the decay time and angular fit, considering them fully correlated by adding a new parameter, s: $\Delta\Gamma_d^s \to \Delta\Gamma_d^s + s_0 + \sigma(s_0)s$ and $\Delta\Gamma_s \to \Delta\Gamma_s + s_0 + \sigma(s_1)s$, where s_0 ($\sigma(s_0)$) and s_1 ($\sigma(s_1)$) are the biases (uncertainties) seen in simulation for $\Delta\Gamma_d^s$ and $\Delta\Gamma_s$ respectively. To account for the correlation between s_0 and s_1, s is applied as a constraint by the reparametrization $-2\log\mathcal{L} \to -2\log\mathcal{L} + s^2$

Neglecting D-wave. The analysis strategy ignores the contribution from the D-wave present in the high $m(KK)$ region. To validate this assumption a new MC is generated with a large (33%) f2 (D-wave) contribution. Subsequently, the fit is repeated in the KK region of the analysis. The systematic uncertainty is calculated by the observed bias concerning the default S-wave MC.

Analysis validation. As discussed throughout this chapter, the analysis strategy includes certain assumptions, such as the factorization of all efficiencies (thus allowing for independent correction). To validate this, S-wave MC (including all `B_BKGCAT`) merged with the combinatorial background generated using ML is used. The results are compared with the generated values used for producing the MC. Any effect not covered by the previously assessed systematics that enters this test (like mass factorization) is assigned as systematic uncertainties. Negligible differences are observed for the main parameters of interest.

4.7 Conclusions

The flavor-tagged decay time and angular analysis of the $B_s^0 \to J/\psi K^+K^-$ decay is presented using the full Run 2 dataset recorded by the LHCb experiment during the period 2015-2018. This analysis constitutes the world's best measurement of the CP-violation and decay width parameters of the B_s^0 system. The results are found to be:

$$\begin{aligned}
\phi_s^{c\bar{c}s} &= -39 \pm 22 \pm 6 \text{ mrad} \\
\Delta\Gamma_s &= 0.0845 \pm 0.0044 \pm 0.0024 \text{ ps}^{-1} \\
\Delta\Gamma_d^s &= -0.0056^{+0.0013}_{-0.0015} \pm 0.0014 \text{ ps}^{-1} \\
|\lambda| &= 1.001 \pm 0.011 \pm 0.005
\end{aligned} \tag{4.41}$$

The results are consistent with the previous measurement using 2015 and 2016 data [68]. The results show no evidence of CP violation in the decay ($|\lambda|$ compatible with one) and no evidence of CP violation in the interference between the decay and the decay through previous mixing ($\phi_s^{c\bar{c}s}$ compatible with 0). No correlation is observed between the CP violation parameters and the polarization of the final state. The results are consistent with SM predictions and with previous LHCb measurements. The combination with the other experiments leads to the following world average for the CP violating phase $\phi_s^{c\bar{c}s}$ [1]:

$$\phi_s^{c\bar{c}s} = -40 \pm 16 \text{ mrad} \tag{4.42}$$

The HFLAV contour plots of $\phi_s^{c\bar{c}s}$ versus $\Delta\Gamma_s$ before (left panel) and after (right panel) this measurement are displayed in Fig. 4.20 [1].

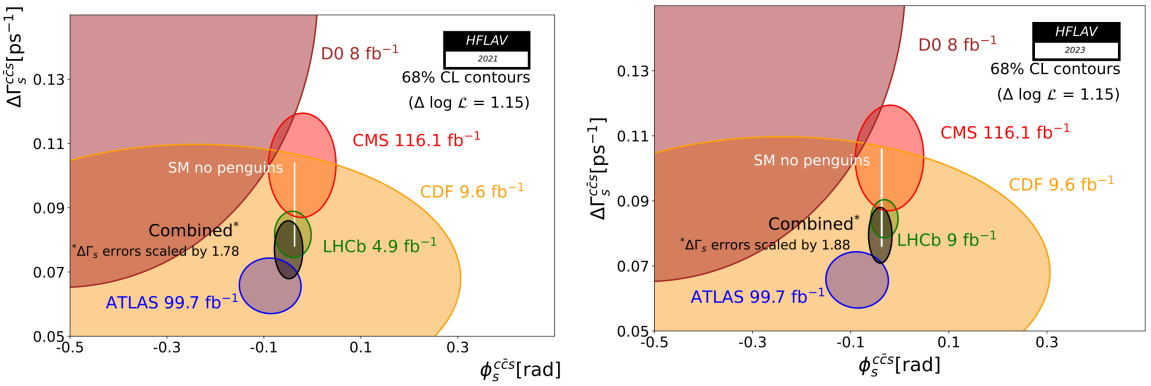

FIGURE 4.20: HFLAV status of the $\phi_s^{c\bar{c}s}$ vs $\Delta\Gamma_s$ plane, before (left) and after (right) this measurement [1]. See Section §4.1.3 for details

In 2024, the CMS collaboration reported an updated measurement of $\phi_s^{c\bar{c}s}$ in $B_s^0 \to J/\psi K^+K^-$ decays, incorporating enhanced flavor tagging and trigger strategies [88]. The preliminary combination provided by the HFLAV collaboration yields the following 2024 world average for $\phi_s^{c\bar{c}s}$ [1]:

$$\phi_s^{c\bar{c}s} = -53 \pm 15 \text{ mrad} \tag{4.43}$$

The latest state-of-the-art contour plots in the planes $\phi_s^{c\bar{c}s}$ versus $\Delta\Gamma_s$ and Γ_s versus $\Delta\Gamma_s$ incorporating the recent measurement from the CMS collaboration [88], are shown in Fig. 4.21 [1]:

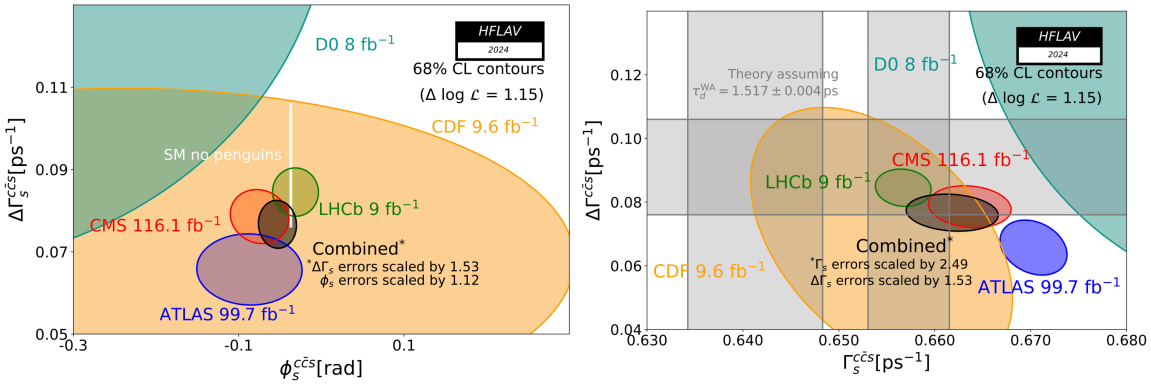

FIGURE 4.21: HFLAV status of the $\phi_s^{c\bar{c}s}$ vs $\Delta\Gamma_s$ plane (left) and $\Delta\Gamma_s$ vs Γ_s plane (right) after the CMS measurement [88, 1]. See Section §4.1.3 for details.

Chapter 5

The novel Inclusive Flavor Tagging

The measurement of flavor oscillations of neutral B mesons and time-dependent CP asymmetries requires knowledge of the flavor of the B meson at the time of its production. This is a complicated task in a p-p collider environment mainly due to the high multiplicity present in each event. The experimental technique used to infer the flavor of the B meson at the production stage is referred to as flavor tagging (FT).

The reason why this task is fundamental was detailed in Section §4.4.6.1, and is based on that the observed time-dependent CP asymmetry is reduced by a dilution factor depending on the performance of the FT algorithms. Concretely, the statistical error of $\mathcal{A}_{CP}^{\text{true}}$ is proportional to:

$$\sigma(A^{\text{true}}) \propto \frac{1}{\sqrt{N}} \frac{1}{\sqrt{\epsilon_{\text{eff}}}} \tag{5.1}$$

Where ϵ_{eff} constitutes the tagging power (see §4.4.6.1) and reflects the percentage of effective statistics exploited due to the performance of the flavor tagging algorithms. Thus, improving the performance of the FT algorithms directly involves improving the sensitivity to CPV observables.

In this section, a new technique based on deep learning algorithms used to infer the flavor of the B meson at the production stage (near the collision point), known as the inclusive FT, is explored. This technique is called inclusive because it uses all available tracks in the event, except the signal tracks, that are useful to flavor tag the signal B mesons (this includes long and upstream tracks see §2.2.2.2 for details).

This chapter is organized as follows: First, §5.1 introduces the definitions necessary to understand this experimental technique. Next, §5.2 explains the training of the NN responsible for inferring the flavor of the B mesons at the production stage. Following that, §5.3 details the calibration of the NN output to ensure it accurately represents the true mistag probability, thus ensuring a reliable physical interpretation. Some performance studies and cross-checks are presented in §5.4. Then, §5.5 examines the potential impact of these advancements on the measurement of the

CP violation interference phase, $\phi_s^{c\bar{c}s}$. Finally §5.6 presents a summary of the results obtained and the conclusions drawn.

5.1 Introduction

After the production of a $b\bar{b}$ pair in a pp collision, the pair hadronizes independently into two b-hadrons, one containing a b quark and the other a $\bar{b}$ quark. One of the b-hadrons can potentially be used for physics analysis, constituting the signal candidate. Additionally, tracks related to the signal B meson, the opposite b-hadron as well as tracks unrelated to the $b\bar{b}$ pair are produced. These tracks can be categorized as:

- Same-side fragmentation track (SSF), a lighter charged hadron (pion, kaon, or a proton) produced along with the signal B meson.
- Opposite Side decay tracks (OSD), associated with the decay of the opposite b-hadron.
- Opposite Side fragmentation tracks (OSF), lighter charged tracks produced along with the opposite b-hadron.
- Background tracks, tracks not associated with the $b\bar{b}$ pair.
- Signal tracks, contain the signal B meson track as well as the daughter tracks produced in the B meson decay. This type of track is not directly used for the training of the NN.

The SSF tracks depend on the type of the signal B meson used. Pions and protons are produced alongside a B^0 meson, while kaons are produced with the B_s^0 meson. Therefore, at least two different classifiers are needed: one for performing the flavor tagging of the B^0 mesons and another one for the B_s^0 mesons. In the next section, the focus will be on training these two Neural Networks (NNs). An additional complication arises due to the specific data structure: the number of tracks per event (and therefore per NN decision) varies with each event. This complex data structure motivates the study of a deep neural network architecture called DeepSet [89], selected for its flexibility with input data, as described in §5.2.2.

5.2 Training

To perform the training, simulated samples are needed to accurately determine the flavor of the B meson at the production stage using true identification information variables. As mentioned earlier, at least two NNs are needed: one to tag the B^0 mesons and another to tag the B_s^0 mesons, due to different fragmentation processes.

As introduced in §4.4.6.1, to assure the physical meaning of the output of the NN, a calibration is needed. This calibration is typically performed on real decays to avoid systematic errors associated with differences between MC and real data. Calibration modes are flavor-specific decays as described in §4.4.6.3 and §4.4.6.4. The reason for using these special decays is very simple, with flavor specific decays the flavor of the neutral B meson at decay time can be inferred from the charge of the daughter particles. This simplifies the task, as it only requires disentangling the flavor mixing oscillation in the decay time likelihood fit to determine the flavor at the production point. The common modes used for this purpose, are the signal modes $B^0 \to J/\psi(\to \mu^+\mu^-)K^{*0}(\to K^+\pi^-)$ and $B_s^0 \to D_s^-(\to K^+K^-\pi^-)\pi^+$. Therefore, the training of the NN is performed on simulation samples of these modes.

The performance of the NN depends on the size of the simulation sample, so both NNs are trained on the combined 2016 to 2018 dataset. The total number of events and tracks for each simulation sample per decay channel and year of the data taking are shown in Table 5.1.

TABLE 5.1: Number of events and number of tracks for each of the simulation samples used for training the NN.

MC sample	Number of events	Number of tracks
2016 $B_s^0 \to D_s\pi$	$\sim 1.2 \times 10^6$	$\sim 5.2 \times 10^7$
2017 $B_s^0 \to D_s\pi$	$\sim 4.7 \times 10^5$	$\sim 2.0 \times 10^7$
2018 $B_s^0 \to D_s\pi$	$\sim 4.1 \times 10^5$	$\sim 1.8 \times 10^7$
2016 $B^0 \to J/\psi K^{*0}$	$\sim 1.2 \times 10^6$	$\sim 5.5 \times 10^7$
2017 $B^0 \to J/\psi K^{*0}$	$\sim 4.1 \times 10^5$	$\sim 1.7 \times 10^7$
2018 $B^0 \to J/\psi K^{*0}$	$\sim 4.1 \times 10^5$	$\sim 1.7 \times 10^7$

The $B^0 \to J/\psi(\mu^+\mu^-)K^{*0}(\to K^+\pi^-)$ candidates are selected using the strategy of the stripping line `BetaSBd2JpsiKstarDetachedLine`. The cuts performed by the stripping line are very similar to the one used in §4.3.2, except for the mass window of the B^0 candidates and the selection of the K^{*0} candidates. On top of the stripping selection, some loose cuts are applied to further suppress the combinatorial background, maintaining as much signal as possible. The different selection criteria applied to this mode compared to the ones already explained in §4.3.2 are shown in Table 5.2.

The selection of $B_s^0 \to D_s^-\pi^+$ candidates follows the strategy implemented in the `StrippingB0DPID2HHHBeauty2CharmLine` line. Rectangular cuts are applied in addition to the stripping line to further select signal candidates and reduce potential backgrounds. This step is even more important for the $B_s^0 \to D_s^-\pi^+$ than for the $B^0 \to J/\psi K^{*0}$ decay channel, as various sources of partially reconstructed backgrounds could contaminate the signal distribution. A summary of the selection requirements is shown in Table 5.3.

TABLE 5.2: Selection criteria used to select signal candidates in $B^0 \to J/\psi K^{*0}$, only differences with respect to §4.3.2 are shown.

	Variable	Selection requirement
B^0	$m(J/\psi K^+K^-)$	$\in$ [5150, 5450]MeV/c^2
	$\chi^2_{\rm vtx}$/nDoF	< 25
$\mu^+\mu^-$	$m(\mu^+\mu^-)$	$\in [3036, 3156]\,{\rm MeV}/c^2$
$K^+\pi^-$	χ^2_{IP}	> 2
	$m(K^+K^-)$	$\in [826, 966]\,{\rm MeV}/c^2$

TABLE 5.3: Selection criteria used to select signal candidates in $B^0_s \to D^-_s\pi^+$ decays.

Particle	Description	Requirement
B^0_s	χ^2_{IP}	< 16
	t	> 0.2 ps
	$m(D^-_s\pi^+)$	$\in$ [5000,6000] MeV/c^2
	B_{DIRA}	> 0.9999
Bachelor π^+	p	> 2 GeV/c
	p_T	$> 0.4\,{\rm GeV}/c$
	χ^2_{IP}	> 36
	χ^2_{track}/nDoF	< 2
	isMuon	$= 0$
	DLL($\pi - K$)	< 0
D^-_s	$m(KK\pi)$	$\in [1933,2003]\,{\rm MeV}/c^2$
	χ^2_{IP}	> 4
π^-	χ^2_{IP}	> 9
	χ^2_{track}/nDoF	< 2.5
	DLL($\pi - K$)	< 8.0
$K^\pm$	χ^2_{IP}	> 9
	χ^2_{track}/nDoF	< 2.5
	DLL($K - \pi$)	$>$ -2.0

5.2.1 BDT-based track classification

To simplify the problem that the NN has to solve and to improve the performance of the flavor tagging algorithm, a Boosted Decision Tree (BDT) is utilized to assign a probability to each track of being same-side fragmentation (SSF), opposite-side decay (OSD), opposite side fragmentation (OSF), or background. For this task, the BDT implementation provided by XGBoost [90] is used.

Training the BDT requires simulation samples, as true information about the tracks is needed for performing the supervised training. To validate the training of the BDT, each of the simulated samples is split into the train (75% of total statistics) and test (25% of total statistics) samples. The input features used for the training are listed in Table 5.4. These features consist of both individual per-track information (listed in the first block of Table 5.4), and track features calculated concerning the signal B track (listed in the second block of Table 5.4).

TABLE 5.4: Input features used for the NN separated in pure track features (first block) and differences between track and signal B (second block).

Feature	Description
$\Delta\mathcal{L}_{e\pi}$, $\Delta\mathcal{L}_{K\pi}$, $\Delta\mathcal{L}_{\mu\pi}$, $\Delta\mathcal{L}_{p\pi}$	Particle identification of the track
ProbNNe, mu,k,p, pi, ghost	NN probability of the track being e,μ, p, π or a ghost
P, PT	Momentum and transverse momentum of the track
Charge, VeloCharge	Track charge and reconstructed charge in the VELO
BPVIP, BPVIPCHI2	Impact Parameter and χ^2 of the IP fit of a track with respect to the PV of the signal B
SumBDT_ult	BDT based isolation variable
IP_trMother	Impact Parameter of a track concerning its respective mother
$\chi^2_{track}/nDoF$	Normalized χ^2 from track fit
diff_z	Difference in z-coordinate between the track reconstructed PV and the signal PV
diff_eta	Difference of pseudorapidity between the signal B and the track
cos_diff_phi	Cosine of the difference of the azimuth angle between a track and the signal B
Pproj	Projection of the track's momentum on the momentum of the signal B

The strategy for the IFT training consists of two steps:

- Train a per-year BDT for assigning to each track a probability of being OSF, SSF, OSD, or background.

- Add the output of the BDT (four probabilities) to the input features used for the training of the DeepSet NN.

The number of tracks is highly dependent on the category to which the track belongs. Most tracks have nothing to do with the $b\bar{b}$ pair produced and are thus categorized as background tracks (approximately 80%). Around $\sim$ 8% are SSF tracks, $\sim$ 5% are OSD tracks and the remaining $\sim$ 7% are OSF tracks. To account for this imbalance during the training, a weight is applied for each category defined as follows:

$$w_{\text{cat}} = \frac{N_{\text{tot}}}{4N_{\text{cat}}} \tag{5.2}$$

where N_{tot} is the total number of tracks and N_{cat} is the number of tracks for each of the SSF, OSD, OSF, and background categories. This weight ensures that each of the track categories is trained with the same amount of effective statistics. The BDT output distributions obtained for 2018 $B^0 \to J/\psi K^{*0}$ and for 2018 $B_s^0 \to D_s^- \pi^+$ simulation samples are shown in Fig. 5.1 and Fig. 5.2, respectively. Only the 2018 results are shown as an example, as the distributions for the other years are similar.

As expected, the OSD tracks are easy to distinguish from the background and fragmentation tracks. This is mainly because the decay of a B meson has certain kinematic features that are easy to exploit in the LHCb detector (see Chapter 2 for details). Additionally, the SSF and OSF output distributions are, as expected, quite similar as they belong to the same physical process[1]. Finally, the background distributions have some small differences compared to the fragmentation tracks. The reason for this is that while these tracks do not come from a B decay, and therefore they are not as easy to distinguish as the OSD category, the SSF (OSF) tracks are kinematically correlated with the signal (opposite) B meson. By exploiting this correlation, the BDT can detect some differences between both distributions.

5.2.2 DeepSet training

The Inclusive Flavor Tagging approach described in this chapter uses a Neural Network called DeepSet [89]. The DeepSet classifier operates on a matrix (X) that comprises an arbitrary number of input vectors $\vec{x_i}$, transforming it into a single output vector $\phi(X)$. This constitutes the first component of the NN, denoted by $\phi-$network. Subsequently, the second component, denoted as $\rho-$network, evaluates ϕ to generate the NN response. An illustrative scheme of the process can be seen in Fig. 5.3.

[1]The differences could come from the trigger as the trigger strategy is Triggered on Signal (TOS)

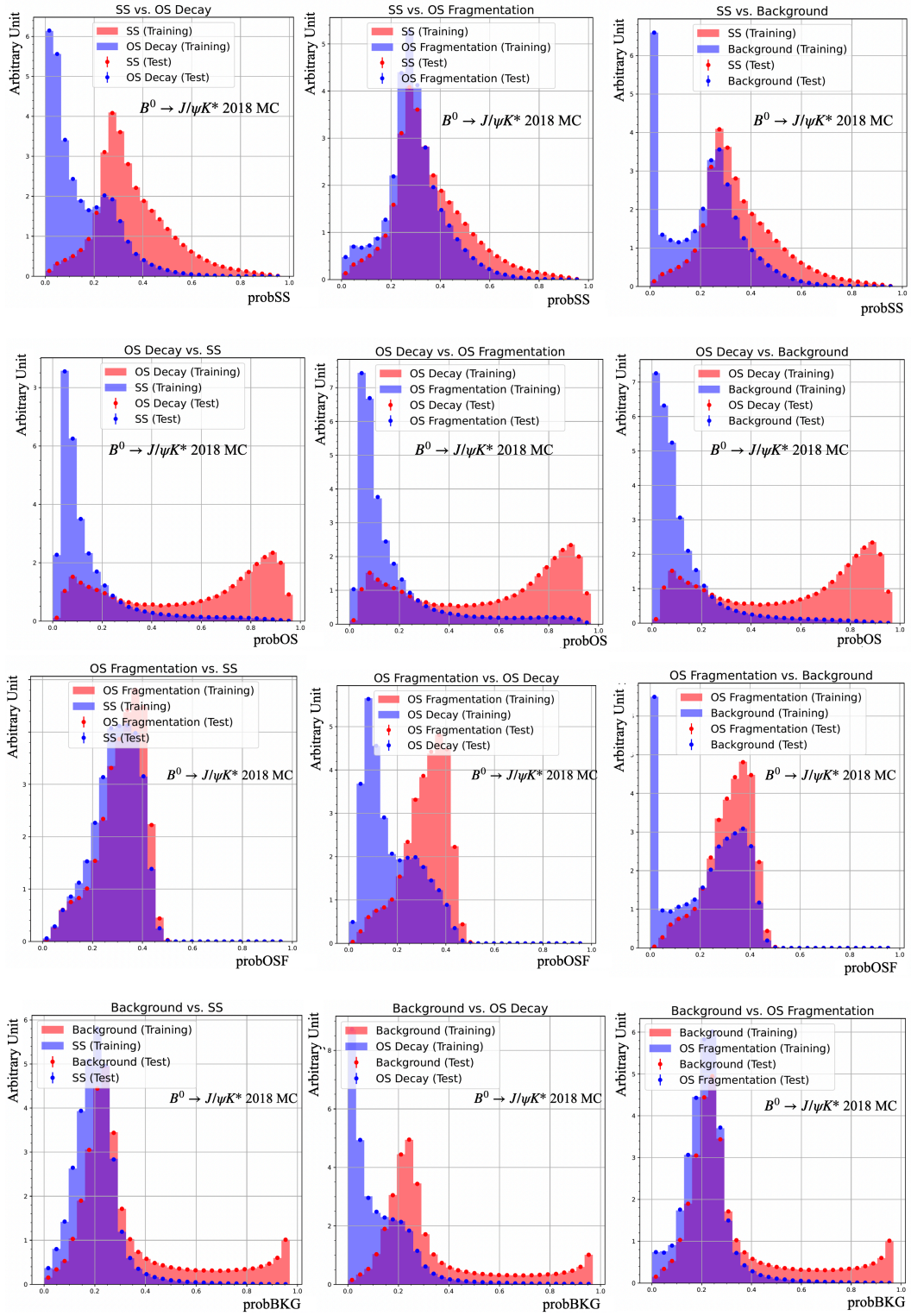

FIGURE 5.1: From top to bottom, the BDT track classification output for SSF, OSD, OSF, and background is shown in red, compared with the distributions of the rest of categories in blue for $B^0 \to J/\psi K^{*0}$. Filled histograms show the distributions for the training sample, while data points represent the corresponding output obtained in the validation sample.

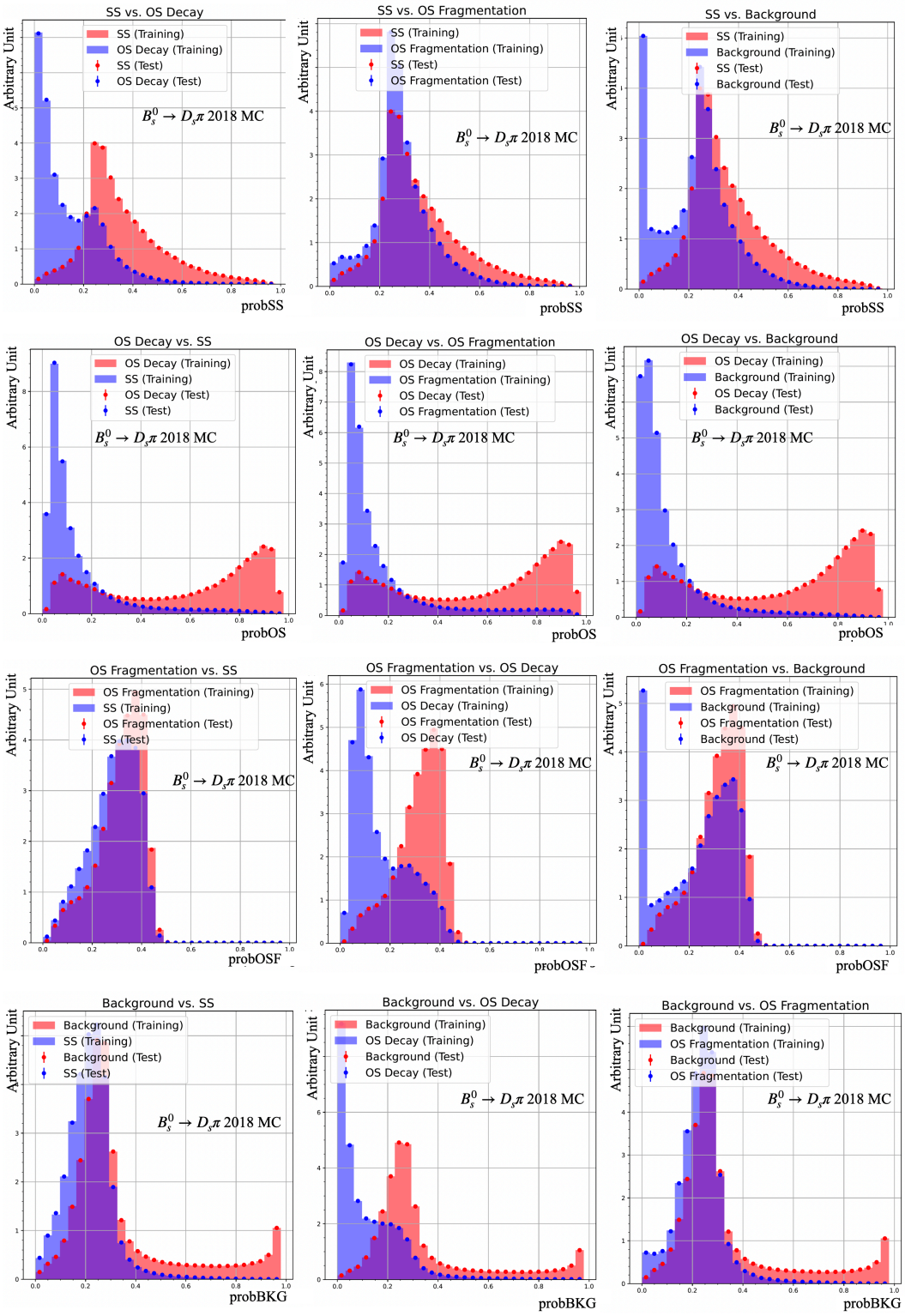

FIGURE 5.2: From top to bottom, the BDT track classification output for SSF, OSD, OSF, and background is shown in red, compared with the distributions of the rest of categories in blue for $B_s^0 \to D_s^- \pi^+$. Filled histograms show the distributions for the training sample, while data points represent the corresponding output obtained in the validation sample.

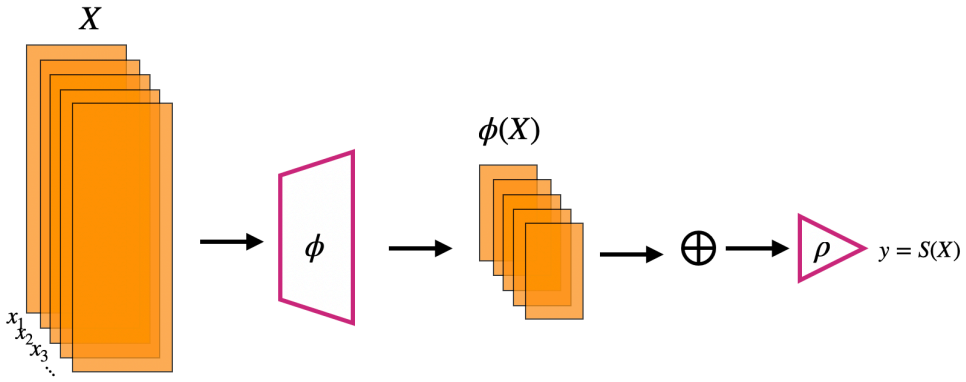

FIGURE 5.3: Schematic representation of the DeepSet classifier.

During the training procedure weights and biases for both $\phi-$ and $\rho-$ networks are determined. The output of the NN, denoted by $y \in [0,1]$, describes how likely the signal candidate is a $B^0_{(s)}$ meson (contains a $\bar{b}$ quark). According to the value of the y variable, the tagging decision (d) and the mistag prediction (η) are computed as follows:

$$
\begin{aligned}
d &= \begin{cases} 1 & \text{if} \quad y > 0.5 \\ -1 & \text{if} \quad y < 0.5 \end{cases} \\
\eta &= \begin{cases} 1-y & \text{if} \quad y > 0.5 \\ y & \text{if} \quad y < 0.5 \end{cases}
\end{aligned}
\tag{5.3}
$$

The list of input features used for the NN training is the same as those used for the BDT track classification (see Table 5.4), with the addition of the BDT outputs (four probabilities of belonging to each track category) and the output of the classical taggers (per-event information), which includes the decision and mistag probabilities of the classical algorithms. The additional input features are shown in Table 5.5.

TABLE 5.5: Additional input features to those described in Table 5.4 used for the DeepSet training.

Feature	Description
4 BDT outputs	probSSF, probOSD, probOSF and probBKG (see §5.2.1)
8 classical taggers	Dilution per decision calculated for each classical tagger according to $d(1-2\eta)$

To perform the NN training the samples are split into two categories, one used for training (75% of the combined simulation sample) and another used for validation (the remaining 25%). The biases and weights of the NN are obtained by minimizing the loss function via back-propagation. The binary cross entropy is chosen as the loss function, which is defined as follows:

$$\mathcal{L} = \frac{1}{N} \sum_{i=1}^{N=\text{batch size}} y_{i,true} \log(y_i) + (1 - y_{i,true}) \log(1 - y_i) \tag{5.4}$$

where y_i is the NN output, and $y_{i,true}$ is the correct label for each event. N is a hyper-parameter called batch size, which is set to 1000 during the training procedure. It represents the number of events used in a forward and backward pass through the network. Another very important hyper-parameter used in deep learning is the number of epochs (n_{epoch}), which corresponds to the number of complete iterations (full data set) used for the training of the NN. This hyper-parameter is set to 100, so during the training the full data set is used 100 times.

Fig. 5.4 and Fig. 5.5 show the evolution of the loss function during the training as well as the Receiving Operator Characteristic (ROC) curve for B_s^0 and B^0 NNs. The final training model is obtained by the one with a minimum loss function obtained during the training procedure. As seen in Fig. 5.4 and Fig. 5.5, the loss function for both training and validation samples, converge before the $n_{\text{epoch}} = 100$, achieving a similar value for both training and validation samples. These features imply that the training is fast (convergence in less than 100 epochs) and reliable (similar loss functions for training and validation samples). Overtraining is tested using the k-folding method, finding very minor differences between the optimal loss function obtained in each of the k-folds (up to 0.2% of relative difference) indicating that, any overtraining, if present, should have a very small impact. The output of the NN is shown for $B^0_{(s)}$ and $\bar{B}^0_{(s)}$ in Fig. 5.6.

5.3 Calibration

To test the performance of our implementation of the IFT, our results will be compared with the performance achieved by the combination of classical taggers, comprising the OS Combination and the SS taggers. The OS Combination is formed by combining all available OS taggers, including information from the OS Kaon, OS Muon, OS Electron, OS Vertex Charge, and OS Charm. The SS taggers include the SS Kaon for the case of the B_s^0 meson and the SS Combination, consisting of the SS pion and the SS proton tagger for the B^0 meson as detailed in §5.1.

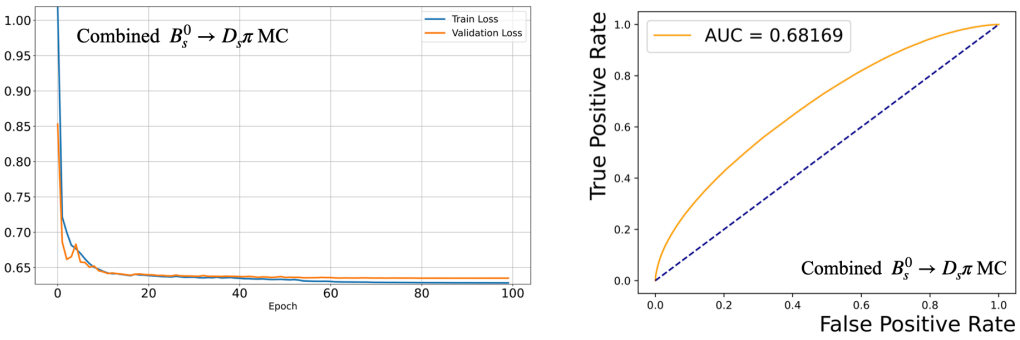

FIGURE 5.4: On the left, loss function of the training sample (blue) and validation sample (orange) as a function of the epoch for the training of $B_s^0 \to D_s^- \pi^+$ simulation candidates. On the right, ROC curve obtained by the training model (solid orange) versus random guessing.

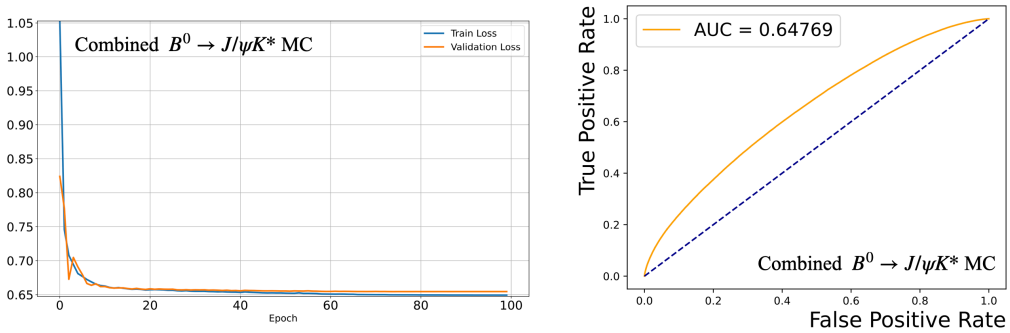

FIGURE 5.5: On the left, loss function of the training sample (blue) and validation sample (orange) as a function of the epoch of the training for $B^0 \to J/\psi K^{*0}$ simulation candidates. On the right, ROC curve obtained by the training model (solid orange) versus random guessing (dot blue).

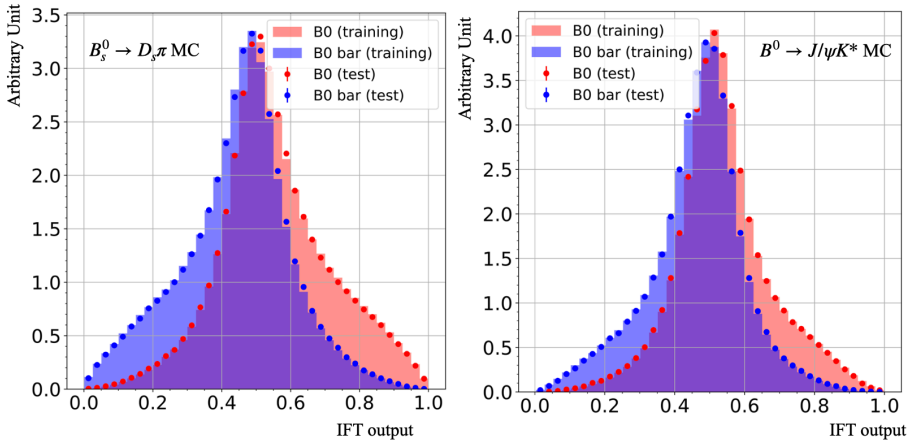

FIGURE 5.6: NN output per B-species for $B_s^0 \to D_s^- \pi^+$ (left) and $B^0 \to J/\psi K^{*0}$ for the training (histogram) and test (points).

The combination of multiple flavor tag decisions (q_i) and mistag estimations (η_i) of different flavor tagging algorithms is performed by calculating the probability of the signal candidate containing a b quark ($\bar{b}$ quark) denoted as $P(b)$ ($P(\bar{b})$):

$$P(b) = \frac{p(b)}{p(b) + p(\bar{b})}, \;\; P(\bar{b}) = 1 - P(b) \tag{5.5}$$

where the probabilities $p(b)$ and $p(\bar{b})$ are defined as:

$$\begin{aligned} p(b) &= \prod_i \left(\frac{1+q_i}{2} - q_i(1-\eta_i) \right), \\ p(\bar{b}) &= \prod_i \left(\frac{1-q_i}{2} + q_i(1-\eta_i) \right), \end{aligned} \tag{5.6}$$

The combined tagging decision and the combined mistag estimation are given by:

$$\begin{aligned} d_{comb} &= sign(P(\bar{b}) - P(b)), \\ \eta_{comb} &= 1 - max(P(b), P(\bar{b})). \end{aligned} \tag{5.7}$$

The following procedure is performed to combine the outputs of the OS and SS individual taggers:

- First, the combination of the individual OS taggers is performed into the OS combination decision and the OS combination mistag estimate. For B^0 this is done with the SS combination accordingly.
- Subsequently, the OS combination mistag estimate and the SS kaon (SS combination) mistag estimate are calibrated assuming a linear dependence between the estimated and the true mistag probabilities.
- Finally, the OS combination and the SS kaon (SS combination) are again combined into the combination decision and the combination mistag estimation, which is further calibrated, again assuming linear dependence between the estimated and the true mistag probabilities.

Note that for the IFT, no combination is needed as the output of the NN is already a unique tag decision and mistag estimation. This is an advantage of the IFT implementation, as it does not require additional steps beyond those strictly needed for the data analysis. Additionally, the correlation between features is naturally taken into account in the IFT, while some assumptions are needed to treat and combine the regular taggers. For example, it is assumed that all individual taggers are uncorrelated when combining them, which is generally a good approximation. For both

IFT and classical taggers, events with a mistag greater than 0.5 are treated as not tagged by convention.

5.3.1 $B_s^0 \to D_s^- \pi^+$ calibration

The mistag probability, estimated by the flavor tagging algorithms for the B_s^0 meson, is calibrated using the flavor-specific decay $B_s^0 \to D_s^- \pi^+$. The calibration of this channel requires an unbinned likelihood fit to the decay time to resolve the $B_s^0 - \bar{B}_s^0$ flavor oscillation as described in §4.4.6.4 (see Eq. 4.33).

The background subtraction for $B_s^0 \to D_s^- \pi^+$ candidates is described in §5.3.1.1. The decay time resolution G of Eq. 4.33 is modeled by a per-event single Gaussian function where the per-event decay time error, σ_t, is used as a conditional variable. The calibration of σ_t is determined by studying prompt D_s^- decays combined with a π^+ track coming from the same proton-proton collision point. The strategy used for the decay-time resolution calibration, detailed in §5.3.1.2, adopts the same analytical approach as in Ref. [91], differing slightly from the semi-numerical method described in §4.4.2.

5.3.1.1 Further selection and sPlot technique

In addition to the selection criteria of Table 5.3, the purity of the signal candidates is improved with tighter PID requirements. Additionally, some vetoes are applied to the misidentified backgrounds, which include a random D^0 combined with a pion, $D^+ \to K^+\pi^+\pi^-$ where the π^- is misidentified with a K^- and $\Lambda_c^+ \to pK^-\pi^+$ where the proton is misidentified with a K^+. The additional requirements are shown in Table 5.6.

TABLE 5.6: Selection criteria on top of Table 5.3 applied for selection of $B_s^0 \to D_s^- \pi^+$ candidates.

Particle	Description	Requirement
$K^\pm$ from D_s^-	DLL$(K-\pi)$	>5.0
D^0 veto	$m(K^+K^-)$	$<1840\,\mathrm{MeV}/c^2$
$D^\pm$ veto	DLL$(K-\pi)$	>10.0
	or $m(K\pi\pi)$	$\notin [1840,1900]\,\mathrm{MeV}/c^2$
Λ_c veto	DLL$(K-p)$	>5.0
	or $m(p\pi K)$	$\notin [2255,2315]\,\mathrm{MeV}/c^2$

The mass distribution of selected $B_s^0 \to D_s^- \pi^+$ ($m(D_s^-\pi^+)$) is fitted with a Hypatia function [92] for signal, an exponential for combinatorial background and the shapes of $B_s^0 \to D_s^- K^+$, $B^0 \to D^-\pi^+$, $B_s^0 \to D_s^{*-}\pi^+$, $B_s^0 \to D_s^-\rho^+$ and $\Lambda_b \to \Lambda_c^-\pi^+$

are extracted from simulations. The strategy for background subtraction consists of three steps:

- Fit to simulation for extracting the signal shape in the wide mass region [5100-5600] MeV/c^2.
- Fit in the wide region [5100-5600] MeV/c^2 to data. The signal shape parameters are fixed to the values from the previous step while the slope of the combinatorial background, as well as the fractions of each component, are left free.
- Fit in the narrow region [5300-5600] MeV/c^2 to data, with all parameters fixed except for the signal and total background fractions.

The total background in the narrow region is subtracted through the sWeights procedure. The total number of $B_s^0 \to D_s^- \pi^+$ candidates is 85942 ± 338, 89115 ± 340 and 103272 ± 368 for 2016, 2017 and 2018, correspondingly. The fit results to data are shown in Fig. 5.7.

5.3.1.2 Calibration of the decay time error

Samples of prompt D_s^-, where the D_s^- meson is reconstructed as $D_s^- \to \phi\pi^-$, combined with a π^+ track, are used to calibrate the decay time resolution for the years 2016, 2017 and 2018 of Run 2. The strategy as well as the selection of the prompt samples are the same as the one described in Ref. [91]. Samples of prompt D_s^- data are split into ten, approximately equipopulated, bins of the decay time error. In each of the ten bins, the background is statistically subtracted using the sPlot method after fitting the $m(K^-K^+\pi^+)$ distribution, where the signal is modeled by a Hypatia function and the combinatorial background with an exponential. The fit results for each of the years can be found in Fig. 5.8.

The decay time of the background-subtracted prompt D_s^- data sample is fitted in each of the ten σ_t bins though an unbinned likelihood fit to the following PDF:

$$P(t) = \mathcal{G}(t) \circledast (f_{prompt}\delta(t) + f_{ll}e^{-t/\tau_2}) + f_{wpv}e^{-|t|/\tau_1} \tag{5.8}$$

Where $\mathcal{G}(t)$ is composed of two Gaussian functions with a shared mean. Two background components are taken into account, prompt D_s^- candidates with a wrong PV associated, described by two symmetric tails $e^{-|t|/\tau_1}$ and a contribution from D_s^- originating from real decays and parametrized as e^{-t/τ_2}. The fits to the prompt D_s^- data are shown in Fig. 5.9.

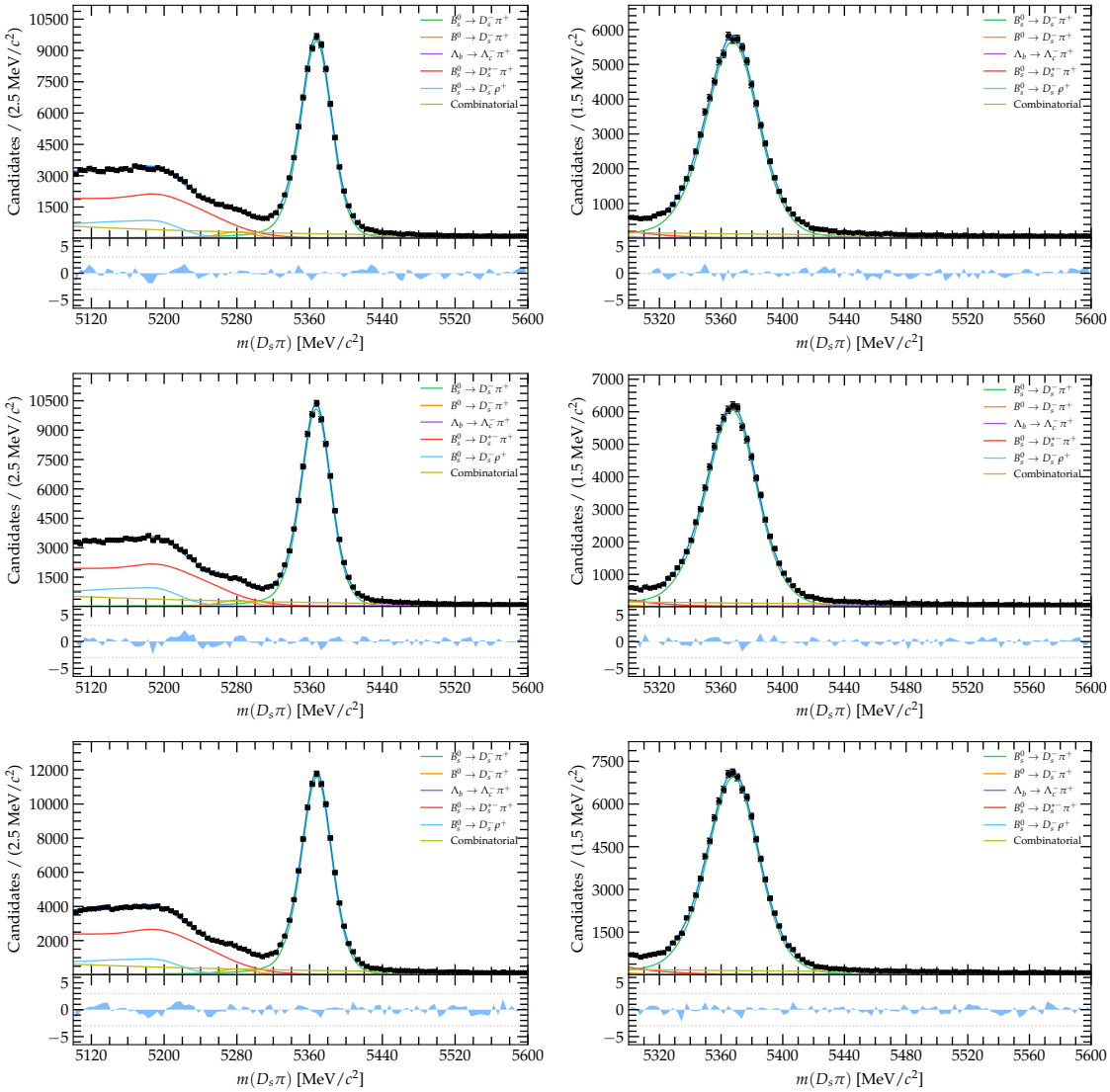

FIGURE 5.7: The mass fit results of selected $B_s^0 \to D_s^- \pi^+$ candidates in the wide region of [5100,5600] MeV/c^2 (left) and in the narrow region [5300-5600] Mev/c^2 (right). From top to bottom, the results for 2016, 2017, and 2018 are shown, respectively.

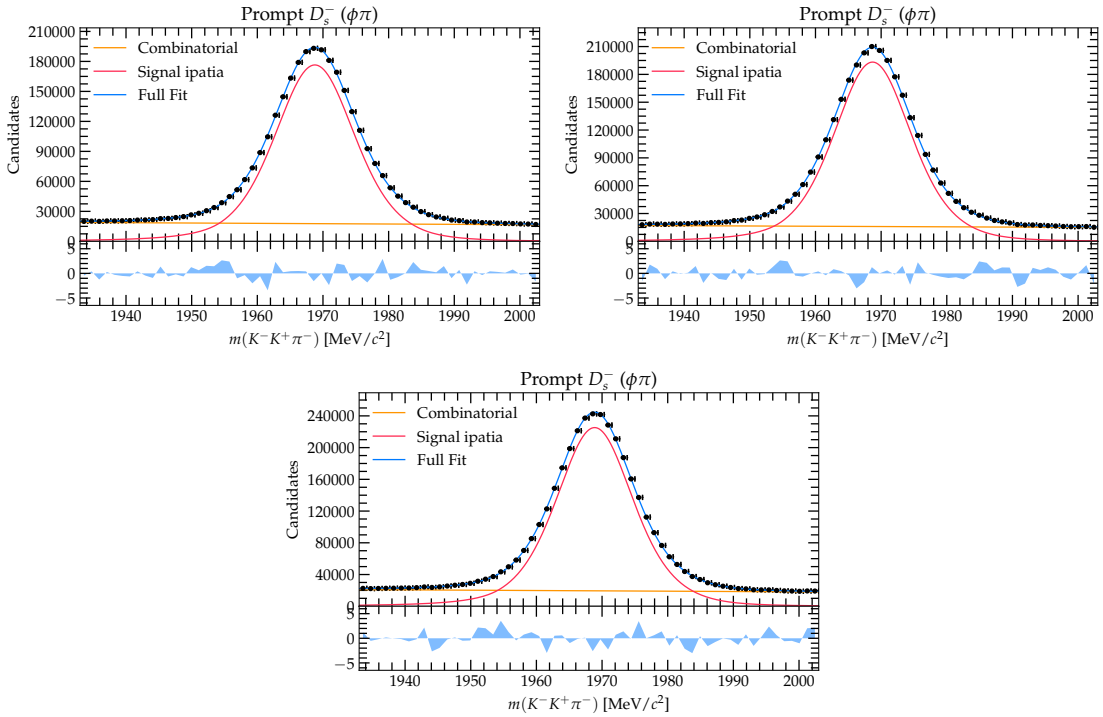

FIGURE 5.8: Fits to the D_s^- mass distribution for 2016, 2017 and 2018 prompt D_s^- data.

The resolutions of the two Gaussians obtained from the fit in Fig. 5.9 are combined into one effective resolution, as follows:

$$D = f_1 e^{-\sigma_1^2 \Delta m_s^2/2} + (1 - f_1) e^{-\sigma_2^2 \Delta m_s^2/2}, \qquad \sigma_{eff} = \sqrt{-2 \ln D}/\Delta m_s, \tag{5.9}$$

The values of σ_t in the prompt D_s^- sample are multiplied by the ratios of the resolutions between the $B_s^0 \to D_s^- \pi^+$ simulation and the prompt D_s^- simulation for every bin of the decay time error to account for differences in the selection between prompt D_s^- and real B_s^0 decays.

A binned linear χ^2 fit is performed to the obtained σ_{eff} distributions. The obtained calibration parameters for each of the years can be found in Table 5.7. The fit results are displayed in Fig. 5.10.

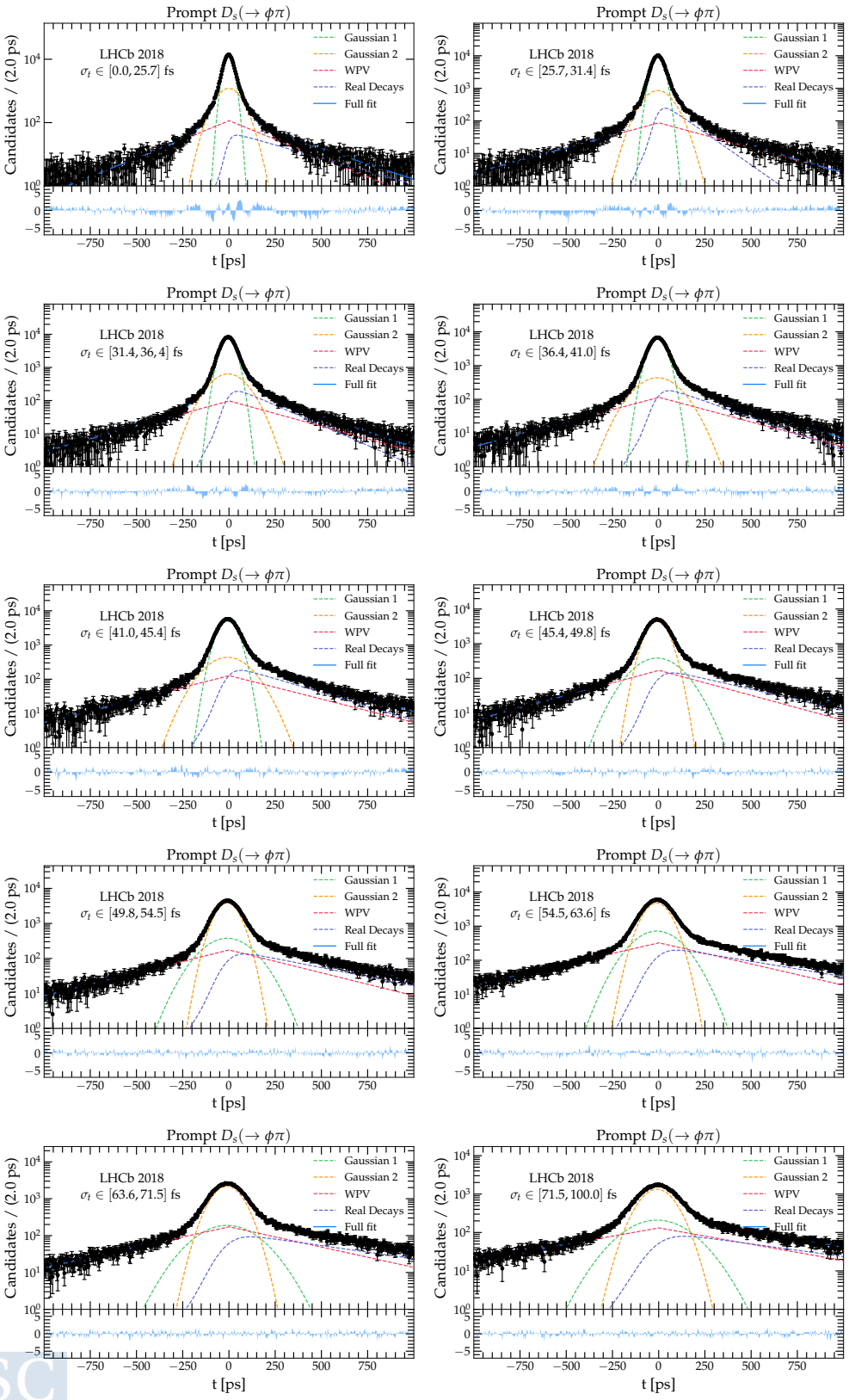

FIGURE 5.9: Fit to the decay time distributions of prompt D_s^- candidates collected in 2018 in each of the decay time error bins.

TABLE 5.7: Linear calibration parameters obtained for the calibration of the per-event decay time error in $B_s^0 \to D_s^- \pi^+$.

Category	2016	2017	2018
q_0 [fs]	14.5 ± 2.1	13.7 ± 1.7	11.9 ± 1.7
q_1	0.898 ± 0.052	0.856 ± 0.040	0.875 ± 0.041

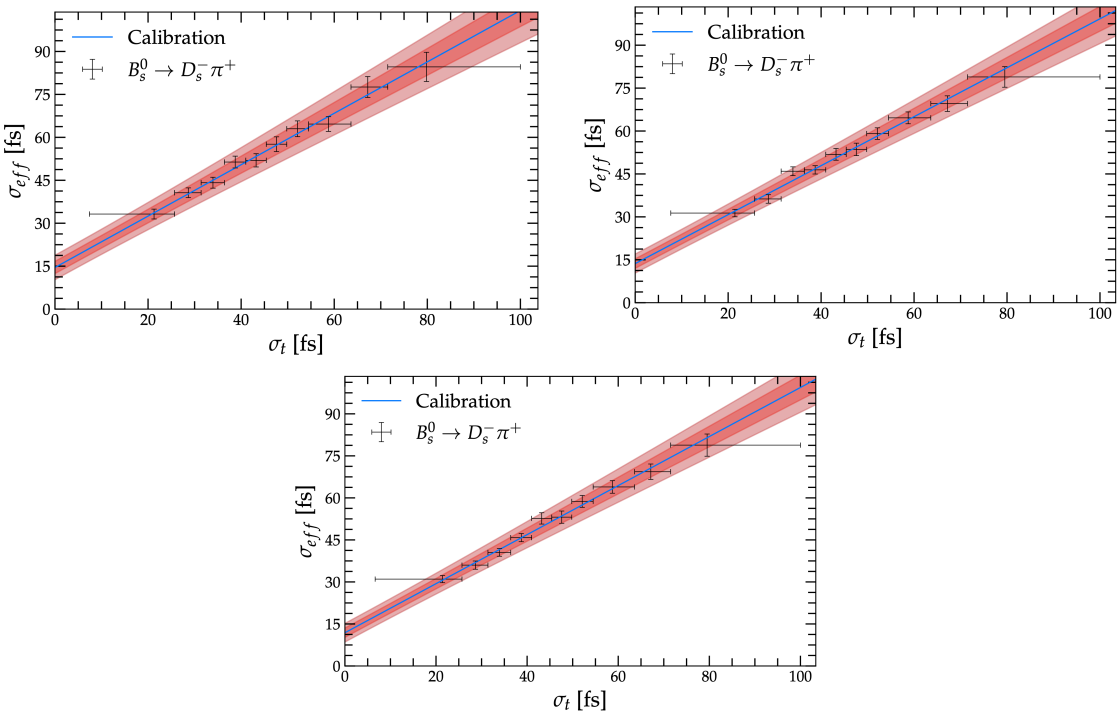

FIGURE 5.10: Calibration of the decay time error σ_t of $B_s^0 \to D_s^- \pi^+$ for the years 2016, 2017 and 2018. The confidence intervals corresponding to one and two standard deviations are indicated in dark and light red respectively.

5.3.1.3 Decay time bias effect

To ensure the accuracy of the tagging power estimation, the impact of the VELO misalignment is cross-checked (see §4.4.3 for details). For this, the tagging power is estimated considering no bias, and the reported biases in $B_s^0 \to D_s^- \pi^+$ [83] and $B_s^0 \to J/\psi\phi$ [82]. This was done by using the reported bias as the mean of the Gaussian that convolves the full pdf in Eq. 4.33. The results for $B_s^0 \to D_s^- \pi^+$ are shown in Table 5.8. The impact of the decay time bias produced by the known VELO misalignment in the tagging power estimation is found negligible, and from now on all the B_s^0 results will be given with the bias reported in $B_s^0 \to D_s^- \pi^+$ analysis.

TABLE 5.8: Results of the estimated tagging powers using different offset for $B_s^0 \to D_s^- \pi^+$.

Parameter	No bias	bias $B_s \to J/\psi\phi$	bias $B_s \to D_s\pi$	Error	Diff.
2016 $\epsilon D^2(\%)[IFT]$	7.87 ± 0.44	7.92 ± 0.44	7.90 ± 0.44	$+0.438$	$+0.043$
2017 $\epsilon D^2(\%)[IFT]$	7.36 ± 0.38	7.42 ± 0.38	7.41 ± 0.38	$+0.377$	$+0.054$
2018 $\epsilon D^2(\%)[IFT]$	7.34 ± 0.35	7.33 ± 0.35	7.35 ± 0.35	$+0.345$	$+0.013$

5.3.1.4 NN output calibration

To obtain the calibration curve of the output of the NN (η) compared to the true mistag (ω), an unbinned maximum likelihood fit to the $B_s^0 \to D_s^- \pi^+$ decay time distribution is performed. The decay time resolution calibration parameters shown in Table 5.7 with their correlation considering statistical uncertainty, are allowed to float in the fit with a Gaussian constraint to their uncertainties. The physics parameters $\Delta\Gamma_s$, Δm_s and $\tau_{B_s^0}$ are also Gaussian constrained to the values $\Delta m_s = 17.766 \pm 0.0057$ ps^{-1} [83], $\Delta\Gamma_s = 0.085 \pm 0.004$ ps^{-1}[93] and $\tau_{B_s^0} = 1.520 \pm 0.005$ ps [1]. The decay time acceptance coefficients are free in the fit.

The linear calibration plots for each of the flavor tagging algorithms are displayed in Fig. 5.11 for 2018 as an example. The unbinned approach, shown with a blue curve, is compared with the binned results, represented by black dots. The binned points are derived from likelihood decay time fits obtained to each of the eight η bins. A good agreement is observed between unbinned and binned approaches for all the flavor tagging algorithms. The obtained calibration parameters in each of the likelihood maximum fits are shown in Table 5.10.

The estimated tagging power for each of the years and each of the flavor tagging algorithms, using Eq. 4.34, is shown in Table 5.9. A consistent improvement is observed for all years of the data collection when using the IFT technique. Concretely, a relative improvement of 22%, 24%, and 21% for 2016, 2017, and 2018, respectively is observed.

TABLE 5.9: Tagging performances evaluated in $B_s^0 \to D_s^- \pi^+$ for the combination of OS&SS taggers versus the IFT.

	$\epsilon(\%)$	D^2	$\epsilon D^2(\%)$
2016 SS&OS	73.81 ± 0.16	0.0877 ± 0.0054	6.47 ± 0.40
2016 IFT	91.85 ± 0.10	0.0860 ± 0.0048	7.90 ± 0.44
2017 SS&OS	79.05 ± 0.15	0.0758 ± 0.0043	5.99 ± 0.34
2017 IFT	97.989 ± 0.051	0.0756 ± 0.0039	7.41 ± 0.38
2018 SS&OS	74.34 ± 0.15	0.0819 ± 0.0042	6.09 ± 0.31
2018 IFT	95.709 ± 0.068	0.0768 ± 0.0036	7.35 ± 0.35

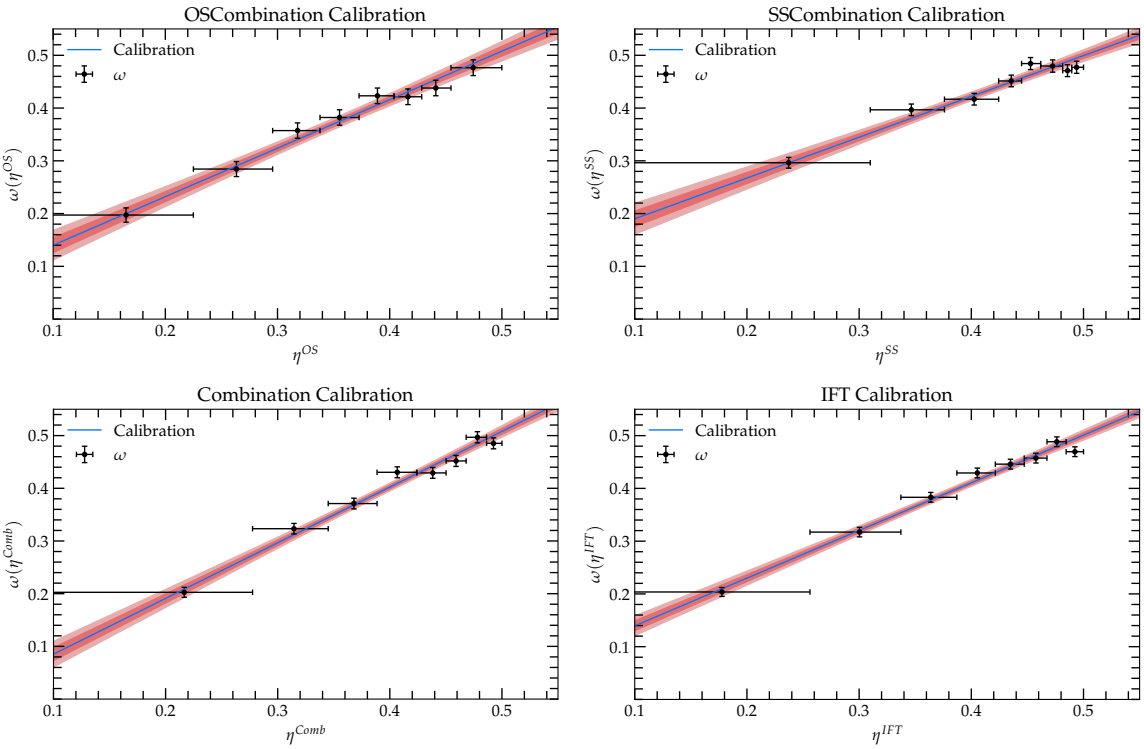

FIGURE 5.11: Unbinned calibration of each of the flavor tagging algorithms for 2018 $B_s^0 \to D_s^- \pi^+$ data.

TABLE 5.10: Result of the unbinned decay time fit for each of the flavor tagging algorithms by fitting the decay time distribution of background subtracted $B_s^0 \to D_s^- \pi^+$ candidates

Algorithm	p_0	p_1	Δp_0	Δp_1
2016 OSComb	0.3707 ± 0.0063	1.055 ± 0.062	0.0114 ± 0.0059	0.043 ± 0.060
2016 SSKaon	0.4353 ± 0.0048	0.788 ± 0.053	-0.0191 ± 0.0045	-0.023 ± 0.053
2016 Classical	0.3892 ± 0.0046	1.007 ± 0.046	-0.0077 ± 0.0043	-0.050 ± 0.044
2016 IFT	0.4015 ± 0.0040	0.985 ± 0.037	0.0099 ± 0.0037	0.076 ± 0.035
2017 OSComb	0.3718 ± 0.0057	0.933 ± 0.055	0.0086 ± 0.0058	0.064 ± 0.058
2017 SSKaon	0.4291 ± 0.0043	0.718 ± 0.049	-0.0196 ± 0.0044	0.039 ± 0.052
2017 Classical	0.3956 ± 0.0040	0.996 ± 0.043	-0.0115 ± 0.0040	-0.021 ± 0.044
2017 IFT	0.4008 ± 0.0036	0.916 ± 0.033	-0.0042 ± 0.0036	0.086 ± 0.035
2018 OSComb	0.3724 ± 0.0052	0.919 ± 0.051	0.0091 ± 0.0053	-0.009 ± 0.054
2018 SSKaon	0.4338 ± 0.0039	0.773 ± 0.045	-0.0110 ± 0.0041	0.040 ± 0.048
2018 Classical	0.3994 ± 0.0037	1.057 ± 0.039	-0.0072 ± 0.0038	-0.060 ± 0.041
2018 IFT	0.4007 ± 0.0033	0.904 ± 0.030	0.0065 ± 0.0033	0.107 ± 0.032

5.3.2 $B^0 \to J/\psi K^{*0}$ calibration

The mistag probability estimated by the IFT algorithm in the B^0 mode is calibrated using the flavor-specific decay $B^0 \to J/\psi K^{*0}$. The model used is the same as the one described in Eq. 4.33, where a decay time fit is needed to disentangle the B^0 mixing and determine the true mistag probability (ω).

5.3.2.1 Further selection and sPlot technique

The distribution of the $J/\psi K^+\pi^-$ invariant mass is already very clean after the selection used for training due to the low presence of backgrounds, and only loose rectangular PID requirements are applied in addition to the ones described in Table 5.2. The additional selection requirements are shown in Table 5.11.

TABLE 5.11: Selection criteria in addition to Table 5.2 applied in the selection of $B^0 \to J/\psi K^{*0}$ candidates.

	Variable	Cut
π^-	DLL($\pi - K$)	< 0
	ProbNNp	< 0.9
	ProbNNK	< 0.9

The mass distribution of selected $B^0 \to J/\psi K^{*0}$ candidates is fitted with a Hypatia function [92] as the signal model, where the parameter values of its tails are obtained from a fit to simulation. The parameters of the mean, μ, and deviation, σ, are fitted on the data. To model the contribution from $B_s^0 \to J/\psi K^{*0}$ decays, the same function as for the signal is used, though the mean is shifted by the known mass difference of $m(B_s^0) - m(B^0) = 87.19\,\text{MeV}/c^2$ [33]. The combinatorial background is

described with an exponential function. The total background in the narrow region is subtracted through the sWeights procedure. The total number of $B^0 \to J/\psi K^{*0}$ candidates is 398558 ± 515, 394435 ± 484 and 471160 ± 507 for 2016, 2017 and 2018, correspondingly. The fit results are shown in Fig. 5.12.

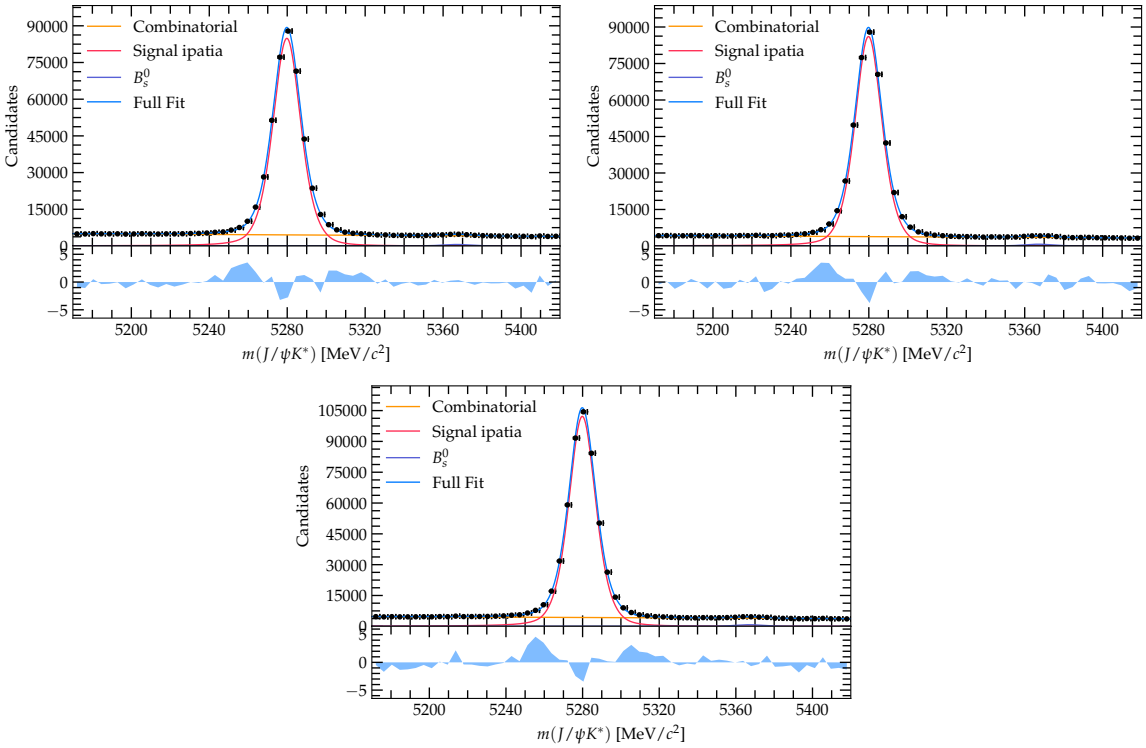

FIGURE 5.12: Fits to the $J/\psi K\pi$ invariant mass distributions for 2016, 2017, and 2018 respectively.

5.3.2.2 Calibration of the decay time error

The B^0 oscillation rate is slower than the B_s^0 oscillation rate ($\Delta m_s > \Delta m_d$), which implies that the decay time resolution impact on the tagging power estimation has a lower effect in the case of the B^0 meson ($D_{\text{timeres}} = \exp\left(-(\sigma_t \Delta m_d)^2/2\right) \sim 1$). For this reason, the calibration of the B^0 decay time error is purely based on simulated $B^0 \to J/\psi K^{*0}$ decays. The procedure is the same as the one explained in §5.3.1.2, with the exception that only resolution effects and wrong PV components need to be considered when fitting the difference between the reconstructed and true decay time distributions.

The fits to the difference between the reconstructed and true decay time of 2018 simulated $B^0 \to J/\psi K^{*0}$ decays are shown in Fig. 5.13 as an example. The distributions for the other years are similar. The two Gaussian resolutions are combined for each of the decay time error bins following Eq. 5.9. Then, as done for the case of the

$B_s^0 \to D_s^- \pi^+$ decay, a binned linear χ^2 fit is performed to obtain the calibration parameters of the per-event decay time error. The obtained calibration parameters are shown in Table 5.12, while the fit results are displayed for each of the years of the data taking in Fig. 5.14.

To cross-check the possible impact of relying on simulated samples for obtaining the per-event decay time error calibration, the obtained calibration parameters in Table 5.12 are varied by up to 5 statistical standard deviations. This check has a relative impact on the tagging power estimation of $< 0.01\,\%$, which is considered negligible.

TABLE 5.12: Linear calibration parameters for the per-event decay time error obtained from $B^0 \to J/\psi K^{*0}$ simulation samples.

Category	2016	2017	2018
q_0 [fs]	6.3 ± 0.90	7.9 ± 1.3	7.8 ± 1.2
q_1	1.003 ± 0.031	0.947 ± 0.047	0.964 ± 0.042

5.3.2.3 Decay time bias effect

As done previously with the $B_s^0 \to D_s^- \pi^+$ case, the effect of the VELO misalignment on the determination of the tagging power is estimated by comparing the tagging powers obtained with no bias ($\mu = 0$), and the biases reported in $B_s^0 \to D_s^- \pi^+$ [83] and $B_s^0 \to J/\psi\phi$ [82]. The results are shown in Table 5.13. As in the case of the $B_s^0 \to D_s^- \pi^+$ analysis, the effect in the determination of the tagging power is negligible. Therefore, all B^0 results will be presented with the bias reported in the $B_s^0 \to J/\psi\phi$ analysis [82], due to similar final state and selection compared to the calibration mode $B^0 \to J/\psi K^{*0}$.

TABLE 5.13: Results of the estimated tagging powers using different offsets in the decay time resolution model due to VELO misalignment for $B^0 \to J/\psi K^{*0}$.

Parameter	No bias	bias $B_s \to J/\psi\phi$	bias $B_s \to D_s\pi$	Error	Diff.
2016 $\epsilon D^2(\%)[IFT]$	5.56 ± 0.10	5.58 ± 0.10	5.57 ± 0.10	$+0.105$	$+0.013$
2017 $\epsilon D^2(\%)[IFT]$	5.85 ± 0.10	5.87 ± 0.10	5.86 ± 0.10	$+0.104$	$+0.016$
2018 $\epsilon D^2(\%)[IFT]$	5.840 ± 0.096	5.853 ± 0.097	5.846 ± 0.096	$+0.096$	$+0.013$

5.3.2.4 NN output calibration

For obtaining the calibration curve of the output of the NN (η) versus the true mistag observed in the decay time distribution (ω), an unbinned maximum likelihood fit

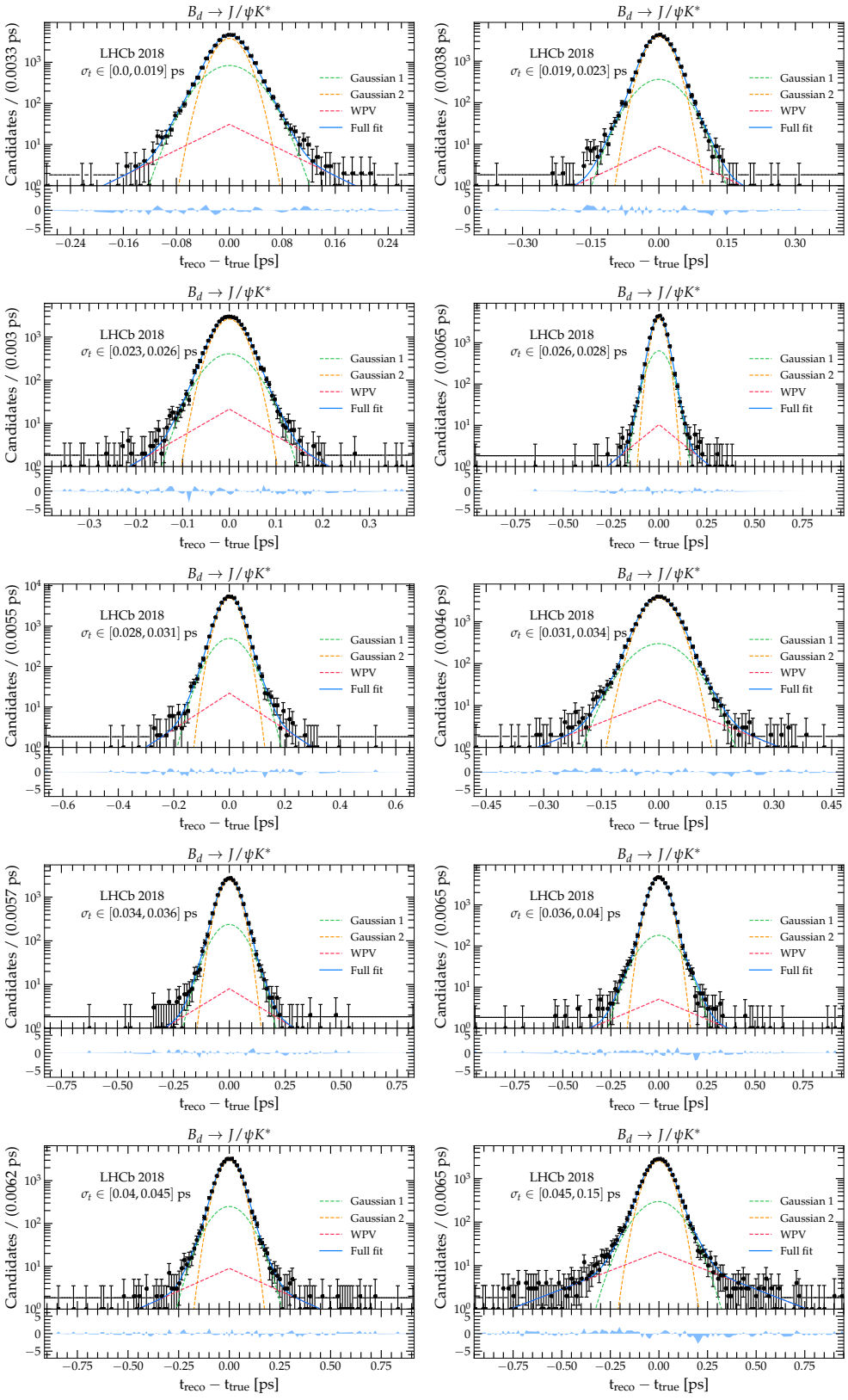

FIGURE 5.13: Fit to the difference between reconstructed and true decay time distributions for simulated $B^0 \to J/\psi K^{*0}$ decays in each of the decay time error bins. The results are shown in a logarithmic scale to distinguish better each contribution.

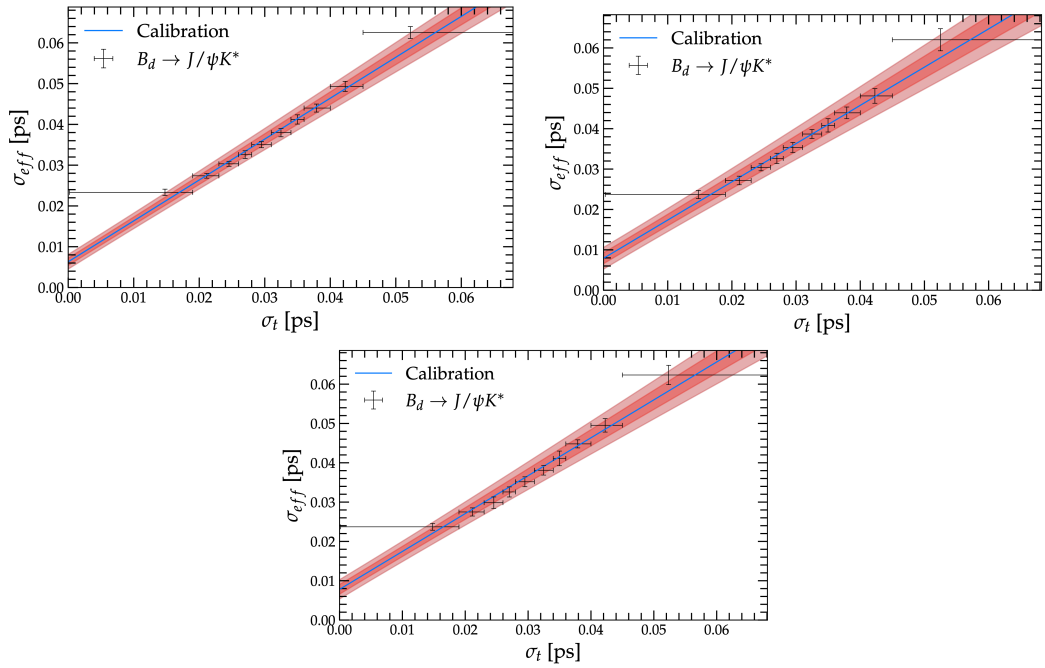

FIGURE 5.14: Calibration of the decay time error σ_t of $B^0 \to J/\psi K^{*0}$ decays for 2016, 2017 and 2018. The confidence intervals corresponding to one and two standard deviations are indicated in dark and light red respectively.

to the background subtracted $B^0 \to J/\psi K^{*0}$ candidates is performed. The decay time resolution calibration parameters are allowed to float in the fit with a Gaussian constraint to their statistical uncertainties. The physics parameters Δm_d and τ_{B^0} are also Gaussian constrained to the wolrd average values $\Delta m_d = 0.5065 \pm 0.0019$ ps^{-1} and $\tau_{B^0} = 1.519 \pm 0.004$ ps [1]. The parameter $\Delta\Gamma_d$ is assumed to be 0. The decay time acceptance coefficients are free in the fit.

The linear calibration plots for each of the flavor tagging algorithms are displayed in Fig. 5.15 for 2018 as an example; the distributions for the other years are similar. The obtained calibration parameters in each of the decay time fits are shown in Table 5.14.

Using Eq. 4.34 the tagging power is estimated for each of the years of the data taking. The results are summarized in Table 5.15. A consistent improvement for all the years is observed when using the IFT technique compared to the combination of classical taggers. Specifically, a relative improvement of 38%, 39%, and 35% for 2016, 2017, and 2018, respectively is reported. This indicates a significant advancement in the understanding of flavor tagging techniques.

Note that the tagging power obtained in the $B^0 \to J/\psi K^{*0}$ is significantly lower than in the case of $B_s^0 \to D_s^- \pi^+$. This difference is expected and is due to the trigger

requirements. The tagging power is calculated as an efficiency, where the denominator is the triggered and selected data. The trigger selection of the hadronic trigger is tighter than in the case of the muonic trigger [2]. This implies that comparisons between tagging powers in different analyses or analyses from different experiments should be done with caution, as higher tagging power does not necessarily imply more performant FT algorithms (could just imply tighter selections).

TABLE 5.14: Result of the unbinned decay time fit for each of the algorithms of flavor tagging in $B^0 \to J/\psi K^{*0}$ data

Algorithm	p_0	p_1	Δp_0	Δp_1
2016 OSComb	0.3918 ± 0.0020	0.881 ± 0.021	0.0106 ± 0.0030	0.012 ± 0.031
2016 SSComb	0.4458 ± 0.0013	0.921 ± 0.026	0.0051 ± 0.0019	-0.049 ± 0.038
2016 Classical	0.4192 ± 0.0013	0.985 ± 0.016	0.0043 ± 0.0019	-0.008 ± 0.024
2016 IFT	0.4146 ± 0.0012	0.896 ± 0.012	0.0006 ± 0.0017	-0.189 ± 0.018
2017 OSComb	0.3865 ± 0.0020	0.881 ± 0.020	0.0111 ± 0.0029	0.045 ± 0.031
2017 SSComb	0.4466 ± 0.0013	0.932 ± 0.025	0.0027 ± 0.0019	-0.030 ± 0.038
2017 Classical	0.4184 ± 0.0013	0.988 ± 0.016	0.0028 ± 0.0019	-0.008 ± 0.023
2017 IFT	0.4124 ± 0.0012	0.922 ± 0.012	-0.0016 ± 0.0017	-0.234 ± 0.018
2018 OSComb	0.3865 ± 0.0018	0.889 ± 0.019	0.0074 ± 0.0027	0.021 ± 0.028
2018 SSComb	0.4452 ± 0.0012	0.921 ± 0.023	-0.0001 ± 0.0018	-0.034 ± 0.034
2018 Classical	0.4163 ± 0.0012	0.973 ± 0.014	0.0002 ± 0.0017	-0.026 ± 0.021
2018 IFT	0.4128 ± 0.0011	0.926 ± 0.011	-0.0021 ± 0.0016	-0.182 ± 0.016

TABLE 5.15: Tagging performances evaluated in $B^0 \to J/\psi K^{*0}$ for the combination of classical taggers versus the Inclusive Flavour tagging (IFT).

	$\epsilon(\%)$	D^2	$\epsilon D^2(\%)$
2016 SS&OS	87.030 ± 0.058	0.0466 ± 0.0010	4.053 ± 0.091
2016 IFT	95.789 ± 0.035	0.0582 ± 0.0011	5.58 ± 0.10
2017 SS&OS	87.208 ± 0.058	0.0485 ± 0.0010	4.226 ± 0.092
2017 IFT	95.024 ± 0.038	0.0617 ± 0.0011	5.87 ± 0.10
2018 SS&OS	87.631 ± 0.052	0.04931 ± 0.00097	4.321 ± 0.085
2018 IFT	95.172 ± 0.034	0.0615 ± 0.0010	5.853 ± 0.097

5.4 Performance studies

In addition to the baseline results presented in §5.3 several performance studies were conducted. These include an alternative calibration model, assessing the impact of IFT results by removing tracks likely to be background, and, evaluating the tagging performance of the IFT in non-overlapping regions of the signal B meson's

[2] Additionally the efficiency in the low p_T region (low performance of FT algorithms) for the hadronic trigger is much smaller than in the muonic triggers.

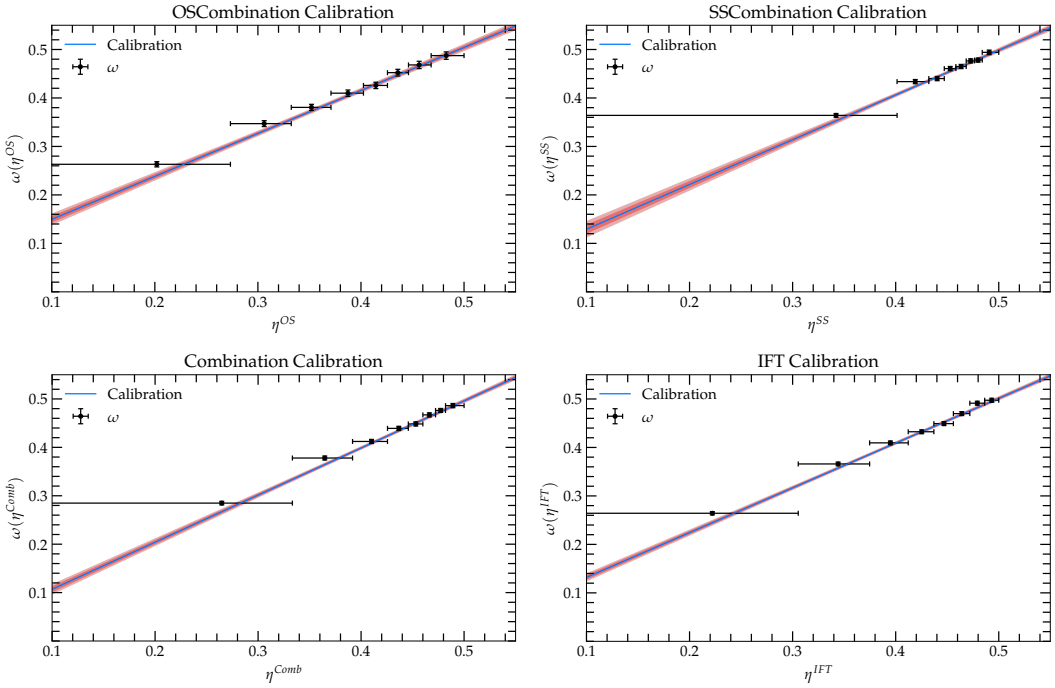

FIGURE 5.15: Unbinned calibration of each of the flavor tagging algorithms for 2018 $B^0 \to J/\psi K^{*0}$ data.

transverse momentum (p_T) and pseudorapidity. The studies also consider the number of tracks and primary vertices in the event.

5.4.1 Alternative calibration method

The model of the calibration followed assumes a linear dependency between the output of the NN (η) and the true mistag probability (ω):

$$\omega = p_0 + \frac{q}{2}\Delta p_0 + \left(p_1 + \frac{q}{2}\Delta p_1\right)(\eta - \bar{\eta}) \tag{5.10}$$

which allows the calibrated mistag ω to supersede 0.5, or in other words to assign a $D = (1 - 2\omega) \leq 0$. These events are called overflow events and are treated as not tagged by convention. An alternative model that controls this effect is calibrating the dilution instead of the mistag rate,

$$D' = fD \to \omega = f\eta + \frac{1}{2}(1 - f). \tag{5.11}$$

This can be easily generalized for the case of having asymmetries that are different from zero:

$$\omega_b = f_1\eta + \frac{1}{2}(1 - f_1), \quad \omega_{\bar{b}} = f_2\eta + \frac{1}{2}(1 - f_2) \tag{5.12}$$

A comparison between the estimated tagging power obtained for both models can be seen in Table 5.16. The difference is found to be negligible.

TABLE 5.16: Estimated tagging power in $B_s^0 \to D_s^- \pi^+$ using the traditional calibration model versus the estimated tagging power obtained when calibrating the dilution scale. The differences are found to be negligible.

	$\epsilon D^2(\%)$ [IFT, Old cal]	$\epsilon D^2(\%)$ [IFT, New cal.]	Error	Diff.
2016	7.90 ± 0.44	7.93 ± 0.44	0.44	0.03
2017	7.41 ± 0.38	7.45 ± 0.38	0.38	0.04
2018	7.35 ± 0.35	7.35 ± 0.35	0.44	0.00

5.4.2 Removing background tracks

The potential impact of removing background tracks for training the DeepSet NN is evaluated by applying different threshold cuts on the probability of each track being background after the track classification step. Subsequently, in each of the tuples obtained after the threshold cut, the training of the DeepSet NN and the calibration are performed. The results are shown in Fig. 5.16 for the 2016-2018 background subtracted $B^0 \to J/\psi K^{*0}$ candidates (left) and for the 2016-2018 background subtracted $B_s^0 \to D_s^- \pi^+$ candidates (right). The blue dots represent each of the obtained tagging powers in the combined data set by performing the threshold cut indicated on the x-axis (probBKG < threshold). Results without the track classification are shown in green, while those obtained with the classical combination are shown in red.

As observed, the track classification slightly improves the baseline result, by approximately one statistical uncertainty, while no significant gain is observed when removing background tracks. It is noteworthy that a drop occurs when applying a tight cut on the background probability of about 30% (probBKG < 0.3). This drop can be understood by observing Fig. 5.1 and Fig. 5.2, as at probBKG $\sim$ 0.3, significant information from the other track categories starts to be lost.

5.4.3 Dependence of the tagging power on kinematic and event properties

To cross-check that the Inclusive FT does not generate additional dependencies beyond those already seen in the combination of classical taggers, the estimated tagging power is calculated in bins of variables known to have some correlation with the performance of the flavor tagging algorithms: The transverse momentum (p_T) of

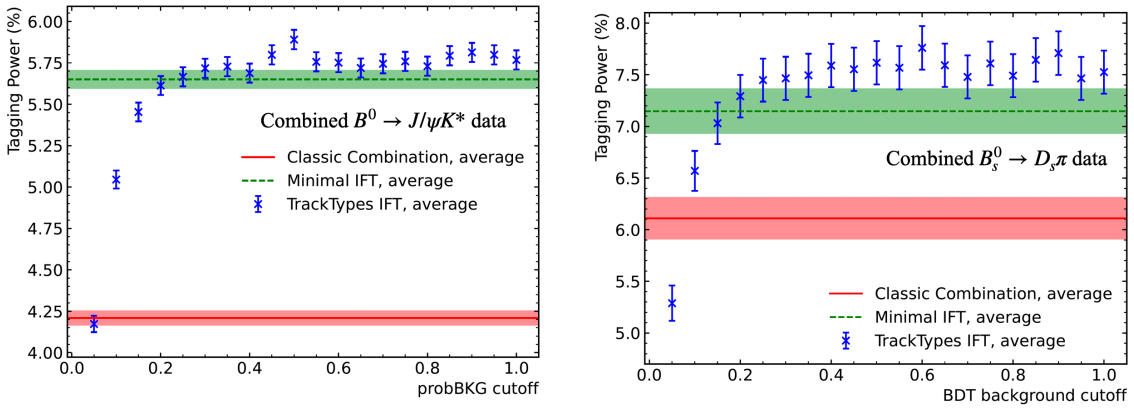

FIGURE 5.16: Combination of tagging powers obtained for 2016-2018 data for $B^0 \to J/\psi K^{*0}$ (left) and $B_s^0 \to D_s^- \pi^+$ (right) data. In blue results obtained for the baseline procedure (track classification + Deepset) for several cuts in the track probability of being background. The results when using only the DeepSet (without the track classification) are shown in green while the results for the classical combination are shown in red.

the signal B, the pseudorapidity of the signal B, the number of tracks (`nTracks`) and the number of PVs (`nPVs`) present in the event. Due to higher statistics in the data sample and a cleaner trigger selection, this study is done in the combined 2016-2018 $B^0 \to J/\psi K^{*0}$ data sample [3].

To achieve this, the full analysis is repeated in each of the bins of the variables. This includes the sWeight procedure to statistically subtract the background and the flavor tagging calibration through a decay time fit to the background subtracted $B^0 \to J/\psi K^{*0}$ candidates. As the time resolution has a very small impact on the estimation of the tagging power (for the B^0 case), the baseline calibration shown in Table 5.12 is used for all the bins. Table 5.17, Table 5.18, Table 5.19, and Table 5.20 show the tagging efficiency, the dilution, and the tagging power estimation for each of the bins of the transverse momentum of the signal B, pseudorapidity of the signal B, the number of tracks in the event and the number of primary vertex of the event, respectively.

The trends are consistent between the inclusive and classical techniques and are in accordance with expectations. Generally, one would expect the bigger performance of the SS algorithms with the p_T of the signal B, as the p_T of the fragmentation track is correlated with the p_T of the B meson. For the pseudorapidity variable, one expects lower performance for the SS taggers at high pseudorapidity, meaning closer to the beam. This is mostly because the misidentification of kaons, protons, and pions is higher for tracks with high momentum, and because of the correlation of the

[3] As explained the tagging power is an efficiency where the denominator is the number of triggered and selected events. Therefore, for example, for doing this study in $B_s^0 \to D_s^- \pi^+$ the non-uniform trigger efficiency concerning the p_T of the signal B should be taken into account.

pseudorapidity with the transverse momentum, as generally large pseudorapidity means small transverse momentum. Finally, for the multiplicity (number of tracks and number of PVs), one expects higher mistags when the multiplicity is high, as the number of tracks surrounding the B meson is larger, making it more difficult to find the correct tagging track. This is noteworthy because it suggests that, in general one would expect lower performance of the flavor tagging techniques under Run 3 conditions, as the number of PVs per event is expected to be higher.

TABLE 5.17: Tagging power estimations obtained in background subtracted $B^0 \to J/\psi K^{*0}$ in bins of the transverse momentum of the signal B.

	Parameter	$p_T^B < 4.9$ GeV	$4.9 < p_T^B \leqslant 7.3$ GeV	$7.3 < p_T^B \leqslant 11$ GeV	$p_T^B > 7.3$ GeV
SS&OS	$\epsilon(\%)$	76.974 ± 0.080	91.182 ± 0.054	91.933 ± 0.052	91.219 ± 0.054
	D^2	0.0385 ± 0.0011	0.0397 ± 0.0010	0.0504 ± 0.0012	0.0675 ± 0.0013
	$\epsilon D^2(\%)$	2.966 ± 0.086	3.624 ± 0.095	4.64 ± 0.11	6.16 ± 0.12
IFT	$\epsilon(\%)$	88.087 ± 0.062	94.100 ± 0.045	98.738 ± 0.021	97.492 ± 0.030
	D^2	0.0489 ± 0.0012	0.0547 ± 0.0012	0.0612 ± 0.0012	0.0850 ± 0.0014
	$\epsilon D^2(\%)$	4.31 ± 0.10	5.15 ± 0.11	6.04 ± 0.12	8.28 ± 0.13

TABLE 5.18: Tagging power estimations obtained in background subtracted $B^0 \to J/\psi K^{*0}$ in bins of the pseudorapidity (η) of the signal B.

	Parameter	$\eta \leqslant 3.1$	$3.1 < \eta <= 3.6$	$3.6 < \eta \leqslant 4.1$	$\eta > 4.1$
SS&OS	$\epsilon(\%)$	91.565 ± 0.046	91.462 ± 0.049	87.314 ± 0.065	68.16 ± 0.13
	D^2	0.0515 ± 0.0010	0.0463 ± 0.0010	0.0467 ± 0.0012	0.0510 ± 0.0015
	$\epsilon D^2(\%)$	4.716 ± 0.093	4.235 ± 0.094	4.08 ± 0.10	3.48 ± 0.11
IFT	$\epsilon(\%)$	97.134 ± 0.028	94.923 ± 0.039	96.488 ± 0.036	90.833 ± 0.078
	D^2	0.0648 ± 0.0011	0.0611 ± 0.0011	0.0586 ± 0.0012	0.0542 ± 0.0017
	$\epsilon D^2(\%)$	6.30 ± 0.10	5.80 ± 0.11	5.65 ± 0.12	4.92 ± 0.15

TABLE 5.19: Tagging power estimations obtained in background subtracted $B^0 \to J/\psi K^{*0}$ in bins of the number of tracks present on the event.

	Parameter	`nTracks` < 122	$122 <$ `nTracks` $\leqslant 184$	$122 <$ `nTracks` $\leqslant 184$	`nTracks` > 274
SS&OS	$\epsilon(\%)$	80.333 ± 0.067	86.214 ± 0.063	89.573 ± 0.061	91.072 ± 0.069
	D^2	0.0633 ± 0.0012	0.0509 ± 0.0011	0.0433 ± 0.0011	0.0354 ± 0.0013
	$\epsilon D^2(\%)]$	5.082 ± 0.097	4.388 ± 0.098	3.88 ± 0.10	3.23 ± 0.11
IFT	$\epsilon(\%)$	94.727 ± 0.038	95.824 ± 0.036	95.791 ± 0.040	95.254 ± 0.052
	D^2	0.0746 ± 0.0012	0.0611 ± 0.0012	0.0534 ± 0.0012	0.0459 ± 0.0014
	$\epsilon D^2(\%)$	7.06 ± 0.11	5.85 ± 0.11	5.11 ± 0.11	4.37 ± 0.13

5.5 $\phi_s^{c\bar{c}s}$ sensitivity study

The results showed are promising, as improving the performance of the flavor tagging technique in channels like $B_s^0 \to D_s^- \pi^+$ directly implies having a better sensitivity to a future measurement of the crucial quantity Δm_s. In this section, the goal is to go a step further and test the sensitivity to CPV observables, like $\phi_s^{c\bar{c}s}$. For this

TABLE 5.20: Tagging power estimations obtained in background subtracted $B^0 \to J/\psi K^{*0}$ in bins of the number of PVs present on the event.

	Parameter	nPVs = 1	nPVs = 2	nPVs >= 3
SS&OS	$\epsilon(\%)$	87.585 ± 0.048	86.674 ± 0.054	86.141 ± 0.077
	D^2	0.05091 ± 0.00090	0.04818 ± 0.00097	0.0436 ± 0.0013
	$\epsilon D^2(\%)$	4.459 ± 0.079	4.176 ± 0.084	3.76 ± 0.11
IFT	$\epsilon(\%)$	93.542 ± 0.036	96.176 ± 0.031	98.184 ± 0.030
	D^2	0.06555 ± 0.00097	0.05935 ± 0.00099	0.0520 ± 0.0013
	$\epsilon D^2(\%)$	6.132 ± 0.091	5.708 ± 0.095	5.10 ± 0.13

purpose, it is necessary to reprocess real data tuples of triggered and stripping selected $B_s^0 \to J/\psi\phi$ candidates to save all the underlying track information of each event. This is done only for the year 2018 as an example.

Subsequently, the NN trained on simulated $B_s^0 \to D_s^- \pi^+$ candidates (see §5.2) is applied to the $B_s^0 \to J/\psi\phi$ tuple to obtain the tag decision and the estimation of the mistag probability, as described in §5.2. Finally, it is necessary to select the signal candidates by suppressing the combinatorial background. This is done in two steps. First, the same BDT-based selection as described in §4.3.5 is applied. Secondly, the sPlot technique is used to statistically subtract the background by using the same strategy described in §4.3.7.

For calibrating the raw output of the NN, the strategy described in §4.4.6 is employed, using the flavor specific decay $B_s^0 \to D_s^- \pi^+$. To ensure the portability between the results of the $B_s^0 \to D_s^- \pi^+$ and the ones for $B_s^0 \to J/\psi\phi$, the GB-weighting procedure is applied in variables with a strong correlation with the tagging performance as the p_T of the B_s^0 candidate, the number of PVs, the pseudorapidity of the B_s^0 and the number of tracks of the event (see §5.4.3). The tagging power estimation obtained for the 2018 data using the baseline procedure is:

$$\epsilon_{eff}^{IFT} = 4.22 \pm 0.25\% \tag{5.13}$$

This is slightly lower than the tagging power estimation obtained with the combination of the classical taggers for 2018, which is $4.36 \pm 0.16\%$ (see Table 4.13). The result implies that the sensitivity to $\phi_s^{c\bar{c}s}$ would be worse than using classical taggers, which is somewhat disappointing. However, it is well known that the hadronic trigger of $B_s^0 \to D_s^- \pi^+$ is much tighter than the muonic trigger of the $B_s^0 \to J/\psi\phi$ decay. Note that using triggered and stripping selected simulated candidates to train the DeepSet NN, could result in the NN not being sensitive to some kinematic regions of the $B_s^0 \to J/\psi\phi$ phase space.

To cross-check this argument, another training based on simulated $B_s^0 \to J/\psi\phi$ samples is performed. For this, the step of the BDT track classification (see §5.2.1) is

repeated followed by the DeepSet training (see §5.2.2). The loss function as a function of the epoch, the ROC curve of the training model, and the raw output of the NN are displayed in Fig. 5.17.

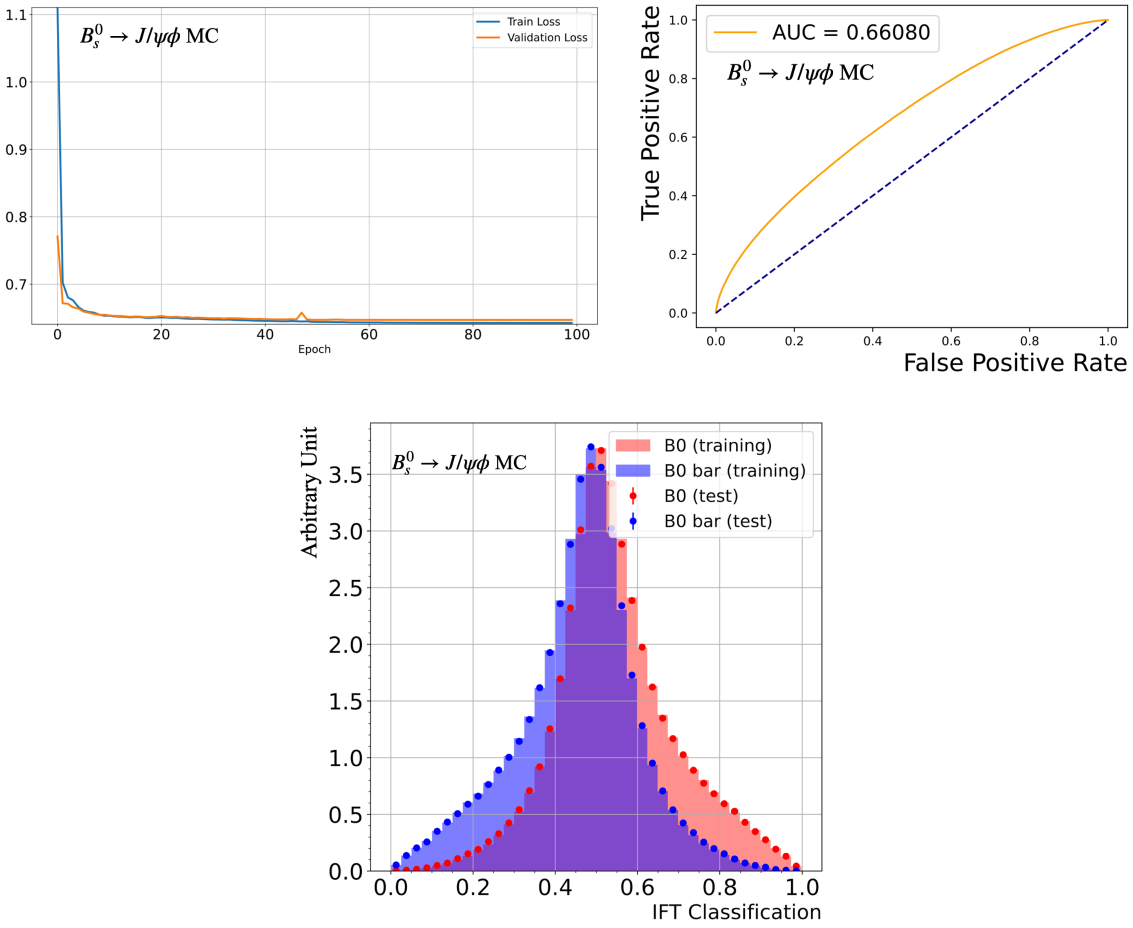

FIGURE 5.17: Top left, the evolution of the loss function for the training sample (blue) and validation sample (orange) as a function of the epoch during the training on $B_s^0 \to J/\psi\phi$. Top right, ROC curve (orange) of the training model compared with random guessing (blue). Bottom, NN output obtained in the training (histogram) and the validation sample (dots) for B_s^0 candidates (blue) and $\bar{B}_s^0$ candidates (red).

The model obtained during the training is applied to the $B_s^0 \to D_s^- \pi^+$ and $B_s^0 \to J/\psi\phi$ candidates. Subsequently, the calibration of the output of the NN is performed using the weighted and background subtracted flavor specific $B_s^0 \to D_s^- \pi^+$ data. After that, the tagging power is estimated in the sample of $B_s^0 \to J/\psi\phi$ candidates, yielding:

$$\epsilon_{eff}^{IFT} = 5.44 \pm 0.26\% \tag{5.14}$$

which implies a relative improvement of $\sim 25\%$ compared to the number quoted in Table 4.13. To ensure that this gain is real, the full decay time angular fit is repeated to the background subtracted $B_s^0 \to J/\psi KK$ candidates. For this, the angular and decay time efficiency obtained in Sections §4.4.4 and §4.4.5, respectively, are utilized to account for non-uniform efficiency in the decay time and helicity angles. Also, the S-wave and P-wave interference terms are modeled using the same CSPs factors of Section §4.4.1. Finally, the decay time resolution calibration obtained in Section §4.4.2 is used. Note that a significant improvement in the sensitivity to the $\phi_s^{c\bar{c}s}$ observable could lead to a potential reanalysis of $B_s^0 \to J/\psi KK$ decays. As this decision cannot depend on the measured value of $\phi_s^{c\bar{c}s}$, the result is blinded using the blinding string `IFTdeepset`. The obtained result from the flavor tagged angular and decay time fit to 2018 $B_s^0 \to J/\psi\phi$ background subtracted candidates is:

$$\phi_s^{*c\bar{c}s} = (-0.698 \pm 0.032) \text{ rad} \tag{5.15}$$

Where the symbol $*$ indicates that the observable is blinded, and therefore the nominal value is scaled randomly based on the blinding string `IFTdeepset`. Using only 2018 data, $\phi_s^{c\bar{c}s}$ is measured to be $\phi_s^{c\bar{c}s} = -0.051 \pm 0.035$ rad, as reported in [82], which implies a gain of 3 mrad in 2018 just by the improvement of the flavor tagging technique. This number is consistent with our previous estimation in Eq. 5.14 as $\epsilon_{\text{IFT}} \sim \epsilon_{\text{old}} * (\sigma_{\text{old}}/\sigma_{\text{IFT}})^2 = 5.2\%$.

Following our discussion, if the $B_s^0 \to J/\psi\phi$ trigger is more inclusive, the training results using $B_s^0 \to J/\psi\phi$ simulation should port to the $B_s^0 \to D_s^-\pi$ decay channel. To cross-check this, the tagging power is evaluated in background subtracted $B_s^0 \to D_s^-\pi^+$ candidates yielding $(7.22 \pm 0.35)\%$ which is compatible with the number displayed in Table 5.9. This check implies that the potential change in the training mode for the B_s^0 NN has no impact on the performance of a future measurement of Δm_s.

5.6 Summary of Results and Conclusions

In this chapter, a study of the DeepSet implementation of the inclusive FT technique to tag the flavor of the B mesons at the production stage is conducted. The current baseline procedure utilizes a BDT for track classification and a DeepSet NN to determine the tag decision and the mistag estimation. A relative improvement of 22 % and 37 % in the flavor-specific decays $B_s^0 \to D_s^-\pi^+$ and $B^0 \to J/\psi K^{*0}$, respectively is reported.

The potential impact of removing tracks that are likely to be background is investigated and no significant gain was found. The tagging power estimation across

bins of kinematic variables of the signal B meson (p_T^B and η) and event multiplicity (`nTracks` and `nPVs`) was also examined, where trends similar to those seen with classical taggers were observed.

The preliminary sensitivity study for $\phi_s^{c\bar{c}s}$ suggests that it may be necessary to adopt a more inclusive training mode than the $B_s^0 \to D_s^- \pi^+$, in terms of selection, to ensure portability of the training results across different modes. The possibility of training on $B_s^0 \to J/\psi\phi$ was examined, where a relative improvement of 19 % in the sensitivity to the $\phi_s^{c\bar{c}s}$ observable compared to the classical combination was reported, which is a promising result for future measurements of the $\phi_s^{c\bar{c}s}$ phase and other flavor-tagged analyses.

Chapter 6

Quark-flavor transitions in Supersymmetry

6.1 Introduction and Motivation

One of the most studied BSM theories is Supersymmetry (SUSY). SUSY requires the theory to be invariant under fermion-boson and boson-fermion transformations, which can be understood as a generalization of space-time symmetry in Quantum Field Theory. Nevertheless, SUSY has lost interest in recent years since no supersymmetric particles have been observed at particle colliders. One of the main reasons for expecting that SUSY particles should already have been discovered is because they were a natural candidate for solving the hierarchy problem introduced in Chapter 1. To assess this, SUSY particles should not lie beyond the TeV scale[1]. This distinguishes two types of supersymmetric models: low-scale SUSY and high-scale SUSY, the former being already quite constrained by direct searches performed at the LHC.

Nevertheless, high-scale SUSY still presents very attractive features [44]:

- Dark Matter. Under the R-Parity conservation assumption, the Lightest Supersymmetric Particle (LSP) is stable and can be neutral, making the LSP a natural candidate to explain the cold DM. Although no direct evidence for DM scattering with conventional matter or indirect DM annihilation has been found, which has placed strong constraints on SUSY TeV models, SUSY scenarios are still compatible with the measured cosmological DM density.
- CP-violation. In SUSY theories there are several new possible sources of CP-violation, which could potentially explain or alleviate[2] the matter-antimatter imbalance. As will be seen in the last section the most stringent constraints come from the Electric Dipole Moments (EDM), and observables sensitive to

[1] Although it depends on the particular definition of naturalness or acceptable fine-tuning

[2] Now that that neutrinos are known to have tiny but non-zero mass, CP violation in the lepton sector becomes unavoidable

the imaginary parts of the M_{12} box diagram: ϕ_s, ϕ_d and $|\epsilon_K|$ which have been measured with high precision.

- Unification of gauge interactions. As explained in Chapter 1, the coupling strengths tend to unify at $\sim 10^{16}$ GeV. However, exact unification cannot be obtained within the SM. Exact unification is possible in the MSSM since superpartners modify the SM Running Group (RG) flow. For this, the SUSY scale must be in the order of $M_{SUSY} < \mathcal{O}(100)$ TeV [94].
- Gravity. String theory needs to be supersymmetric to avoid the presence of tachyons, which are particles that travel faster than the speed of light. Furthermore, if SUSY is required to be a local symmetry, quantum gravity can be introduced naturally [44].
- Higgs mass. The Higgs boson mass in SUSY is naturally of the EW scale, consistent with the measured value at LHC [4, 5]. Additionally, the EWSB due to the negative Higgs mass term in the Lagrangian is dynamically explained in SUSY theories as an evolution from the GUT scale to the EW scale [44].
- $(g-2)_\mu$: The long-standing discrepancy of the anomalous magnetic moment of the muon (see Chapter 1) can be alleviated/explained by some regions of the SUSY parameter space, specifically in regions with sign$(\mu) > 0$, small $m_{\tilde{l}}$ ($\sim \mathcal{O}(10^2 - 10^3)$ GeV)[3], and high $\tan\beta$ [95].

6.1.1 Minimal Supersymmetric Standard Model

The Minimal Supersymmetric Standard Model (MSSM), is the minimal extension of the SM that includes supersymmetry, where each SM particle has a unique superpartner. There are two types of super-multiplets in renormalizable SUSY theories, chiral and vector superfields. SM Gauge fields lie in vector supermultiplets together with their spin-1/2 SUSY partners. The latter receives the SM field name plus the "-ino" suffix, e.g. the SUSY partner of the gluon is called gluino. The fermionic SM fields lie in the chiral supermultiplet along with his spin-0 superpartner. The prefix "s-" is added to the SM field name to designate the superpartner, such as in the case of the squark. Higgs fields, also live in the chiral supermultiplet, however, two Higgs doublets (instead of one as in the SM) are needed at least, to give mass to fermions[4]. A summary table of the particle content of the MSSM is summarized in Table 6.1.

Supersymmetric partners share with the SM fields, all the quantum numbers except for the spin. Utilizing the super-multiplets defined in Table 6.1, the Lagrangian is defined as the sum of three terms, $\mathcal{L}_{MSSM} = \mathcal{L}_{gauge} + \mathcal{L}_{kin} + \mathcal{L}_{int}$. Where $\mathcal{L}_{gauge}$

[3]Note that the excluding slepton mass from direct searches through $\tilde{l} \to l\chi_0^1$ is around 200-300 GeV so there is still available parameter space for explaining $(g-2)_\mu$ observable.

[4]In order not to violate supersymmetry.

TABLE 6.1: Particle content in the MSSM [3].

Supermult.	SM	spin	SUSY partner	spin	$SU(3) \times SU(2) \times U(1)$
Q	quarks $q = (u, d)_L$	$\frac{1}{2}$	squarks $\tilde{q} = (\tilde{u}, \tilde{d})_L$	0	$(3, 2, \frac{1}{6})$
$\bar{U}$	quarks $u_R^\dagger$	$\frac{1}{2}$	squarks $\tilde{u}_R^*$	0	$(\bar{3}, 1, -\frac{2}{3})$
$\bar{D}$	quarks $d_R^\dagger$	$\frac{1}{2}$	squarks $\tilde{d}_R^*$	0	$(\bar{3}, 1, \frac{1}{3})$
L	leptons (ν, e_L)	$\frac{1}{2}$	sleptons $(\tilde{\nu}, \tilde{e}_L)$	0	$(1, 2, -\frac{1}{2})$
$\bar{E}$	leptons $e_R^\dagger$	$\frac{1}{2}$	sleptons $\tilde{e}_R^*$	0	(1,1,1)
H_u	Higgs $H_u = (H_u^+, H_u^0)$	0	Higgsino $(\tilde{H}_u^+, \tilde{H}_u^0)$	$\frac{1}{2}$	$(1, 2, \frac{1}{2})$
H_d	Higgs $H_d = (H_d^0, H_d^-)$	0	Higgsino $(\tilde{H}_d^0, \tilde{H}_d^-)$	$\frac{1}{2}$	$(1, 2, -\frac{1}{2})$
W	$W^\pm, W^0$	1	Winos $\tilde{W}^\pm, \tilde{W}^0$	$\frac{1}{2}$	(1,3,0)
B	B^0	1	Bino $\tilde{B}$	$\frac{1}{2}$	(1,1,0)
G	g	1	gluino $\tilde{g}$	$\frac{1}{2}$	(8,1,0)

encapsulates all the gauge interactions while $\mathcal{L}_{kin}$ takes into account all the information about the kinematic parts of the chiral supermultiplets. These two contributions (following Chapter 1 notation) conform to the elegant part. The $\mathcal{L}_{int}$ contribution, is completely determined by a functional called superpotential, as follows [44]:

$$\begin{aligned} W_{MSSM} =& \bar{U} y_u Q H_u - \bar{D} y_d Q H_d - \bar{E} y_e L H_d + \mu H_u H_d \\ &+ \lambda ELL + \lambda' DLQ + \mu' L H_u + \lambda'' UDD. \end{aligned} \tag{6.1}$$

The chiral supermultiplets denoted by U, Q, H_u, D, H_d, E and L are listed in Table 6.1. The terms $y_{u,d,e}$ are the 3×3 Yukawa matrices, and μ is the Higgsino mass parameter. The first three terms of the second line of Eq. 6.1, violate the lepton number conservation while the last term violates the baryon number conservation. Although there is no theoretical reason to avoid these terms (they are gauge invariant and renormalizable), these processes have not been observed experimentally. To avoid this problem, it is usually common to define a discrete symmetry called R-parity as follows [44, 96]:

$$R = (-1)^{3(B-L)+2S}, \tag{6.2}$$

where B, L, and S are the baryonic number, lepton number, and spin respectively. By requiring the theory to be invariant under R-parity, only the first line of Eq. 6.1 is allowed [96].

Imposing this discrete symmetry has important phenomenological consequences. First, SUSY particles have $R = -1$, while SM particles have $R = 1$ [44]. This implies that the LSP is stable. Therefore, if it is also electrically neutral, it becomes an excellent DM candidate. Second, SUSY particles are produced in an even number at particle colliders, which affects the exclusion limits performed by direct searches at the LHC. Third, unstable massive SUSY particles should decay eventually to the

LSP. Fourth, A pair of SUSY particles may annihilate with each other or coannihilate with other SUSY particles to produce SM particles [97]. These last two consequences affect what is known as the neutralino freeze-out, which is one of the mechanisms used to explain within SUSY the current observed cold DM density.

6.1.2 SUSY Breaking

Until now, all terms were formulated respecting SUSY. However, this would imply that SUSY partners have the same mass as their corresponding SM fields. This contradicts the absence of experimental observation of SUSY particles. Hence, SUSY, if exists, must be broken. SUSY could be broken spontaneously, dynamically, or explicitly. Among those, only explicit breaking leads to a viable phenomenological model [44].

SUSY is explicitly broken by introducing terms into the Lagrangian that violate SUSY. Typically, this involves adding all possible terms containing positive mass terms to avoid quadratic divergences to the Higgs mass[5]. This procedure is known as soft explicitly breaking. The soft SUSY terms are given by [44]:

$$\begin{aligned}\mathcal{L}_{soft} = &-\frac{1}{2}\left(M_1\tilde{B}\tilde{B} + M_2\tilde{W}\tilde{W} + M_3\tilde{g}\tilde{g} + \text{c.c.}\right)\\ &-\left(\tilde{u}a_{\mathbf{u}}\tilde{q}H_u - \tilde{\tilde{d}}a_{\mathrm{d}}\tilde{q}H_d - \tilde{e}\mathbf{a}_{\mathrm{e}}\tilde{l} + \text{c.c.}\right)\\ &-\tilde{q}^{\dagger}\mathbf{m}^2_{\tilde{\mathrm{q}}}\tilde{q} - \tilde{l}^{\dagger}m^2_{\mathrm{L}}\tilde{l} - \tilde{u}^{\dagger}\mathbf{m}^2_{u}\tilde{u} - \tilde{d}^{\dagger}\mathbf{m}^2_{\tilde{d}}\tilde{d} - \tilde{e}^{\dagger}m^2_{\tilde{\mathbf{e}}}\tilde{e}\\ &-m^2_{H_u}H^*_uH_u - m^2_{H_d}H^*_dH_d - (bH_uH_d + \text{ c.c. }).\end{aligned} \tag{6.3}$$

The first line is formed by the gaugino mass terms, while the second line includes the trilinear couplings ($a_{u,d,e}$). The third line contains the mass terms $m^2_{\tilde{q},\tilde{l},\tilde{u},\tilde{d},\tilde{e}}$ which are 3×3 matrices in the family space. The last line shows the soft masses' contribution to the Higgs sector [44].

The inclusion of the soft-breaking part introduces a vast amount of free parameters in the model, spoiling the predictive power of the MSSM. Specifically, the number of free parameters added by the MSSM is 105, which includes 21 squark and slepton masses, 36 real mixing angles and 40 CP-violating phases in the slepton and squark sector, and 5 real and 3 CP-violating phases in the gaugino sector [98].

The traditional approach involves implementing further simplifications to reduce the number of free parameters to $\mathcal{O}(10)$ to phenomenologically study the input space of the MSSM. This is motivated by computational constraints as performing a scan with $\mathcal{O}(100)$ inputs is impossible. Moreover, many of these terms would

[5] This is because at the beginning SUSY was motivated to solve the hierarchy problem.

induce (in principle) FCNC and CP-violating effects incompatible with the experimental constraints. Unfortunately, this simplification results in a potential loss of valuable information. In §6.3, a novel scan approach based on GPUs is introduced, enabling us to increase the number of input parameters studied.

6.1.3 SUSY Dark Matter

One of the most interesting features of the MSSM with R-parity conservation is that it provides a viable DM candidate if the LSP is neutral. There are in principle three candidates, the sneutrino, the gravitino, and the neutralino. The sneutrino is ruled out by direct searches [97]. Gravitinos are a natural candidate in many gauge-mediated SUSY breaking scenarios, however, they interact too weakly to be detected [97]. Therefore, the most attractive candidate from a phenomenological point of view is the lightest neutralino. The lightest neutralino (χ_1^0) is supposed to account for the cold DM (CDM) relic density in all the models studied in this chapter.

After electroweak symmetry breaking (EWSB), the gauge eigenstates, Bino ($\tilde{B}$), Wino ($\tilde{W}$) and Higgsino ($\tilde{H}_d^0$, $\tilde{H}_u^0$), mix. The mass eigenstates (neutralinos) are obtained by diagonalizing the following mass term [44]:

$$\mathcal{L} = -\frac{1}{2}(\psi^0)^T \mathcal{M}_N \psi^0 + h.c., \tag{6.4}$$

where $\psi^0 = (\tilde{B}, \tilde{W}, \tilde{H}_d^0, \tilde{H}_u^0)$ are the gauge eigenstates and M_N is defined as [44]:

$$\mathcal{M}_N = \begin{pmatrix} M_1 & 0 & -M_Z c_\beta s_{\theta_W} & M_Z s_\beta s_{\theta_W} \\ 0 & M_2 & M_Z c_\beta c_{\theta_W} & -M_Z s_\beta c_{\theta_W} \\ -M_Z c_\beta s_{\theta_W} & M_Z c_\beta c_{\theta_W} & 0 & -\mu \\ M_Z s_\beta s_{\theta_W} & -M_Z s_\beta c_{\theta_W} m_{Z^0} & -\mu & 0 \end{pmatrix}. \tag{6.5}$$

The angle β is related to the ratio of vacuum expectation values of H_u^0 and H_d^0 ($\tan\beta = v_u/v_d$), and θ_W is the Weinberg angle. Note that the following notation is used: $c_\alpha = \cos\alpha$ and $s_\alpha = \sin\alpha$.

The lightest eigenvalue obtained in the diagonalization of M_N ($m_{\chi_1^0}$) is forced to be the LSP in this Chapter. In terms of the original gaugino fields, the LSP takes the following form:

$$\chi_1^0 = N_{11}\tilde{B} + N_{12}\tilde{W} + N_{13}\tilde{H}_d^0 + N_{14}\tilde{H}_u^0. \tag{6.6}$$

This allows us to classify the LSP by its composition. If the N_{11} term dominates then the LSP is primarily Bino, if N_{12} dominates then the LSP is mainly Wino. Finally if the term $\sqrt{N_{13}^2 + N_{14}^2}$ dominates the LSP is Higgsino-like [44]. This categorization and its relation to the mass of the LSP presents important phenomenological consequences in explaining the relic dark matter density.

6.1.3.1 Dark matter relic density

According to Planck data, the cold dark matter density was measured to be $\Omega h^2 = 0.1200 \pm 0.0012$ [99], with h being the Hubble constant.

A mechanism used to explain the observed dark matter within SUSY theories is known as freezing out of the neutralino [97]. In the early Universe ($T > m_\chi$), particles and sparticles were in thermal equilibrium, meaning that sparticles were rapidly converted to SM particles and vice versa. As the temperature decreased, heavier sparticles would have stopped being produced, eventually annihilating into SM particles or decaying into the LSP. Then, at $m_\chi > T$, the LSP density number decays exponentially ($n_\chi \propto e^{-m_\chi/T}$). Consequently, the annihilation process into SM particles, with rate $< \sigma v > n_\chi$, becomes less efficient than the cosmological expansion. This leaves a remnant of LSPs that explains the currently experimentally inferred dark matter density [97].

To achieve this, the total cross-section for the annihilation process of a pair of LSPs into SM particles must be $\sigma \sim 10^{-9}$ GeV^{-2} [44]. Neutralino annihilation processes include for example sfermion and chargino exchanges or annihilations via Higgs bosons (A^0, h^0, H^0) into SM particles [97]. The crucial point is that depending on the LSP mass and its relation to the rest of the SUSY spectrum, other processes could also be significant, adjusting the cross-section to match the observed DM relic density. For instance, if the LSP is nearly degenerate in mass with another sparticle, coannihilation processes become relevant, such as $\chi_1^\pm$, χ_2^0 or $\tilde{f}$ coannihilations [97].

If the LSP is mostly Higgsino or Wino, the annihilation processes are usually too efficient to fully explain CDM, unless the LSP is very heavy: 1 TeV or 3 TeV for Higgsino and Wino, respectively [100, 97]. Therefore, the remaining SUSY particles are even heavier, which means that these types of solutions are in general consistent with direct searches performed at the LHC. For the case of the Bino type LSP, typically, the annihilation cross-section is too low (LSP couplings are small and/or sparticles too heavy) [97]. However, depending on the mass spectrum of the remaining SUSY particles, coannihilation processes could bring the cold dark matter density to the correct value. Coannihilations with sfermions (charginos) become important when $m_{\tilde{f}} \sim m_{\chi_1^0}$ ($m_{\chi_1^0} \sim m_{\chi_1^\pm}$). Annihilation processes via Higgs bosons (A, H..) - known as A-H funnel regions - are relevant when $2m_{\chi_1^0} \sim m_H, m_A$ [97]. Depending on the composition of the LSP, its mass, and its relation to the rest of the SUSY spectrum,

different physical processes can make the neutralino fully explain the dark matter relic density.

6.2 Flavor Simplified models: cMSSM

As mentioned above, the lack of understanding of a particular SUSY breaking process reduces the MSSM power prediction. Due to the more than 100 free parameters of the MSSM, the MSSM is, phenomenologically speaking, hard to treat (if not impossible). This fact motivates making assumptions to reduce the number of degrees of freedom of the model. The Constrained MSSM (cMSSM) arises here as a benchmark model to try to study the MSSM, motivated by the idea that most of the free parameters of the soft Lagrangian will induce FCNC and CPV effects, extremely constrained by measured data. The cMSSM assumes that at a given input scale (in our case, the GUT scale) the soft SUSY breaking terms are flavor universal, namely [44]:

$$\begin{aligned} m_Q^2 = m_u^2 = m_d^2 = m_L^2 = m_e^2 = m_0^2 \mathbb{1}, \\ M_1 = M_2 = M_3 = m_{12}. \end{aligned} \tag{6.7}$$

Additionally, it assumes that the trilinear couplings are proportional to the Yukawa matrices and that this proportional factor is flavor universal. This ensures that only the third generation has large scalar couplings [44].

$$a_{u,d,e} = A_0 y_{u,d,e}. \tag{6.8}$$

Furthermore, it assumes that the soft Higgs sector parameters, $m_{H_u}^2$ and $m_{H_d}^2$, are also at the GUT scale, equal to the universal scalar mass (m_0^2)[6]. Finally, the last free parameters are the ratio between the vacuum expectation values of the Higgses, $\tan\beta = v_u/v_d$, and the sign of the electroweak Higgs mixing parameter, $\text{sign}(\mu)$. In conclusion, the degrees of freedom of this model are the following:

$$m_0 \quad m_{12} \quad A_0 \quad \tan\beta \quad \text{sign}(\mu). \tag{6.9}$$

In the context of the cMSSM, only the positive sign of μ is considered as it is the one favored for the observable $(g-2)_\mu$ [95]. Note that these assumptions imply the

[6] Relaxing this condition leads to the well-studied Non-Universal Higgs Masses models (NUHM).

following relation between gaugino masses at the TeV scale [44]:

$$M_3 = \frac{\alpha_s}{\alpha}\sin^2\theta_W M_2 = \frac{3}{5}\cos^2\theta_W M_1, \qquad M_3 : M_2 : M_1 \sim 6 : 2 : 1, \tag{6.10}$$

implying that the Wino-like LSP will be highly suppressed, as at the TeV range the Wino is heavier than the Bino ($M_2 > M_1$).

6.2.0.1 MasterCode framework

To study the simplest GUT-based MSSM model, the cMSSM, the MasterCode framework [101] is utilized. The MasterCode framework employs a frequentist approach for performing global fits. It consists of two main components: the core of the framework responsible for calculating the low energy SUSY observables, and the sampling algorithm, `Multinest` [102]. The `Multinest` algorithm based on the likelihood obtained for each point, iteratively adjusts the input space to find points with better likelihood. The process finishes when the required tolerance is achieved.

The core of the MasterCode framework is conformed by multiple programs. `SOFTSUSY` [103], is used to obtain the SUSY spectrum at the TeV scale by applying the Running Group Equations (RGE). Then, `FeynHiggs` [104] is used to improve to higher order the calculations of the Higgs sector. `SuFla` [105] and `SuperIso` [106] are used to obtain the flavour observables. Higgs observables constraints are calculated using `HiggsBounds` [107] and `HiggsSignals` [108]. The SUSY decay modes are obtained by `SDECAY` [109]. Finally, the Dark matter relic density is calculated using `Micromegas` [110].

The scan ranges of the input parameters sampled in this global analysis are shown in Table 6.2, which includes the segments used to define the 4th-dimensional boxes in `Multinest`. Throughout the scan, the sign(μ) is chosen to be positive. Each segment is scanned using soft priors, meaning that 80% of the distribution lies flat within the bounds of the segment, while 20% exceeds the bounds following a normal distribution. This configuration allows for overlapping between boxes to mitigate boundary effects.

TABLE 6.2: Input space sampled using MasterCode [101]. Only $\mu > 0$ is explored in this work.

Input Parameter	Range	Segments
m_0 [TeV]	(0, 10)	3
m_{12} [TeV]	(0, 10)	3
A_0 [TeV]	(-15, 15)	8
$\tan\beta$	(2, 70).	2

The observables, $m_t = 172.76 \pm 0.30$ GeV, $M_Z = 94.1876 \pm 0.0021$ GeV, $\Delta\alpha^{(5)}_{had} = 0.02766 \pm 0.00007$ and $\alpha_s(M_Z) = 0.1179 \pm 0.0010$, which are taken from Ref. [33], are treated as nuisance parameters. The total number of scanned points is approximately $\sim 7 \times 10^7$. The likelihood used by `Multinest` to explore the parameter space is defined as:

$$\chi^2(\theta) \equiv \sum_i \left(\frac{O_{i,\text{meas}} - O_{i,pred.}}{\sigma(O_i)} \right) + \sum_j \chi^2_{j,non-gaussian}, \tag{6.11}$$

where the first term includes all Gaussian contributions from observables and nuisance parameters, and the second term includes all non-Gaussian constraints where a more refined treatment is needed. The latter includes, the LHC Run2 constraints which are computed by extrapolating a χ^2 from the contour plots using the `FastLim` procedure [111]. $H/A \to \tau^+\tau^-$ included using `HiggsBounds` calculations [107]. $R_{\mu\mu} = BR^{SUSY}(B^0_s \to \mu\mu)/BR^{SM}(B^0_s \to \mu\mu) = BR^{SUSY}(B^0 \to \mu\mu)/BR^{SM}(B^0 \to \mu\mu)$ which is implemented by an asymmetric likelihood that takes into account correlation between both measurements [112]. Finally, spin-independent (SI) DM scattering constraints from `LUX` [113], `XENON-1T` [114], `PANDAX-II` [115], are considered by a two-dimensional log-likelihood in $(\sigma^{SI}, m_{\chi^0_1})$ plane. `PICO` constraint [116] on spin-dependent (SD) DM-proton scattering and `XENON-1T` constraint [117] on SD DM-neutron scattering are taken into account by extrapolating the two-dimensional log-likelihood in the planes $(\sigma^{SD}_p, m_{\chi^0_1})$ and $(\sigma^{SD}_n, m_{\chi^0_1})$, respectively.

A summary of the constraints included in this study are as follows:

- Higgs sector. The mass of the Higgs boson, $m_h = 125.09 \pm 0.17_{EXP} \pm 1.5_{MSSM}$ [33]. Higgs decay rates and masses measured by LHC and Tevatron are evaluated using `HiggsSignals` [108]. Constraints from the searches of $H/A \to \tau\tau$ are evaluated using `HiggsBounds` [107].
- Dark matter constraints. The overall density of CDM, $\Omega h^2 = 0.1200 \pm 0.0012_{EXP} \pm 0.012_{TEO}$ [99], where a conservative 10% of theoretical uncertainty is assumed. The CDM is assumed to be completely explained by the χ^0_1, meaning that the LSP is forced to be neutral. A two-dimensional likelihood function in the plane $(m_{\chi^0_1}, \sigma^{SI}_p)$ combining `LUX` [113], `XENON-1T` [114], `PANDAX-II` [115] experiments is used. The spin-dependent direct searches performed by `PICO` on DM-proton scattering [116] and XENON1T on DM-neutron scattering cross-section [117] are also considered by extrapolating likelihoods in $(\sigma^{SD}_p, m_{\chi^0_1})$ and $(\sigma^{SD}_n, m_{\chi^0_1})$, respectively.
- Electroweak Precision Observables, M_W and $Z-$pole observables are evaluated using the `FeynWZ` code [104] (see Ref. [3] for a complete list of observables).

- LHC 13 TeV constraints. Likelihood penalties are incorporated from direct SUSY searches using the `Fastlim` procedure, which is based on cross-section upper limits provided by ATLAS and CMS collaborations [111]. In the case of neutralinos and charginos, `EWKFast` [118] is used to compute the cross-section. A complete list of the topologies included can be seen in Table 6.3.
- Anomalous magnetic moment of the muon, $a_\mu = (g-2)_\mu/2$. In general, cMSSM contributions to this observable are expected to be small. In the baseline, the constraint is considered to be $\Delta a_\mu = (251 \pm 48) \times 10^{-11}$ [34, 36].
- Flavor constraints. The flavor observables considered in this study are listed in Table 6.4. The CKM matrix derived in Eq. 1.7 is utilized, avoiding potential observables sensitive to heavy NP. The most significant constraint for this study is $\mathcal{B}(B_s^0 \to \mu\mu)$. Under the assumption of Minimal Flavor Violation (expected in cMSSM), this constraint is combined with $\mathcal{B}(B^0 \to \mu\mu)$ into the single quantity $R_{\mu\mu}$, as described in Ref. [112].

6.2.0.2 Results

Two-dimensional projections for the regions of the input parameter spaces are shown in Fig. 6.1. The red and blue lines show 68% (one standard deviation) and 95% (two standard deviations) confidence levels (CL) respectively. The best-fit point is highlighted with a green star. The color scheme shows the dominant mechanism controlling SUSY DM relic density, as shown in the legend (see §6.1.3.1 for details). The points colored with cyan, show the focus-point Higgsino coannihilation regions. Well-tempered chargino coannihilations [146] are shown in yellow where the LSP is mostly Bino and the chargino is almost degenerate in mass with the lightest neutralino. A/H funnel regions, where the neutralino mass is approximately $M_{A,H}/2$, are shown in blue. The points where the stau coannihilation dominates, are colored in red and have the $\tilde{\tau}_1$ almost degenerate in mass with the LSP. A similar situation for stop coannihilation points colored in gray, where in this case the $\tilde{t}_1$ is almost degenerate in mass with the lightest neutralino.

In the (m_0,m_{12}) plane shown in Fig. 6.1, a small region at $m_0, m_{12} \sim 2.5$ TeV can be seen, where stau coannihilation dominates (with A/H funnel). Stop coannihilation islands can be seen in the region of low $m_{12} \sim 2$ TeV, small $\tan\beta \sim (10-20)$, and negative A_0. The dominant DM mechanism in most of the planes shown in Fig. 6.1, particularly dominating in (m_0, m_{12}), (m_0, A_0) and (m_{12}, A_0) planes, is the annihilation via A/H poles.

There are also large focus-point Higgsino coannihilation regions observed for very high $m_0 \sim 10$ TeV and $m_{12} \sim 4$ TeV in Fig. 6.1. In these regions of the parameter space, the LSP has an important Higgsino component. The most effective approach to further constrain these regions is through direct searches of DM scattering

TABLE 6.3: List of LHC Run-2 constraints taken into account in this study.

Observable	Constraint (Reference)
$\tilde{g} \to q\bar{q}\chi_1^0, b\bar{b}\chi_1^0$	LL in $(m_{\tilde{g}}, m_{\chi_1^0})$ plane ([119, 120])
$\tilde{g} \to q\bar{q}Z\chi_1^0, q\bar{q}W^{\pm}\chi_1^0$	LL in $(m_{\tilde{g}}, m_{\chi_1^0})$ plane ([119, 121])
$\tilde{g} \to t\bar{t}\chi_1^0$	LL in $(m_{\tilde{g}}, m_{\chi_1^0})$ plane ([119, 120, 121])
$\tilde{q} \to q\chi_1^0$	LL in $(m_{\tilde{q}}, m_{\chi_1^0})$ plane ([119, 120])
$\tilde{b} \to b\chi_1^0$	LL in $(m_{\tilde{b}}, m_{\chi_1^0})$ plane ([119, 120])
$\tilde{b}_1 \to tW^-\chi_1^0$	LL in $(m_{\tilde{b}_1}, m_{\chi_1^{\pm}})$ plane ([121])
$\tilde{t}_1 \to t\chi_1^0, c\chi_1^0, b\chi_1^{\pm}$	LL in $(m_{\tilde{t}_1}, m_{\chi_1^0})$ plane ([122])
$\tilde{t}_1 \to t\chi_1^0$	LL in $(m_{\tilde{t}_1}, m_{\chi_1^0})$ plane ([119, 120, 123])
$\tilde{t}_1 \to b\nu\tau^+\chi_1^0$	LL in $(m_{\tilde{t}_1}, m_{\chi_1^0})$ plane ([124])
$\tilde{t}_1 \to bW^{\pm}\chi_1^0$	LL in $(m_{\tilde{t}_1}, m_{\chi_1^0})$ plane ([123])
$\tilde{t}_2 \to Zt\chi_1^0, Ht\chi_1^0$	LL in $m_{\tilde{t}_2}, m_{\chi_1^0}$ plane ([125])
$\tilde{l} \to l\chi_1^0$	LL in $(m_l, m_{\chi_1^0})$ plane ([126])
$\tilde{\tau}^{\pm} \to \tau^{\pm}\chi_1^0$	LL in $(m_{\tilde{\tau}}, m_{\chi_1^0})$ plane ([127])
$\chi_1^{\pm} \to W^{\pm}\chi_1^0$	LL in $(m_{\chi_1^{\pm}}, m_{\chi_1^0})$ plane ([128])
$\chi_1^{\pm} \to \nu l^{\pm}\chi_1^0$	LL in $(m_{\chi_1^{\pm}}, m_{\chi_1^0})$ plane ([128, 129, 130])
$\chi_1^{\pm} \to \nu\tau^{\pm}\chi_1^0$	LL in $(m_{\chi_1^{\pm}}, m_{\chi_1^0})$ plane ([131])
$\chi_1^{\pm} \to qq\chi_1^0$	LL in $(m_{\chi_1^{\pm}}, m_{\chi_1^0})$ plane ([130])
$\chi_2^0 \to l^+l^-\chi_1^0$	LL in $(m_{\chi_2^0}, m_{\chi_1^0})$ plane ([128, 130])
$\chi_2^0 \to Z\chi_1^0$	LL in $(m_{\chi_2^0}, m_{\chi_1^0})$ plane ([128])
$\chi_2^0 \to \tau^+\tau^-\chi_1^0$	LL in $(m_{\chi_2^0}, m_{\chi_1^0})$ plane ([131])
$\chi_2^0 \to \gamma\gamma\chi_1^0, bb\chi_1^0$	LL in $(m_{\chi_2^0}, m_{\chi_1^0})$ plane ([130])
$H/A \to \tau^+\tau^-$	$(M_A, \tan\beta)$ plane ([132, 133, 134])

TABLE 6.4: Flavor observables included in this study.

Observable	Reference	Constraint
$R_{\mu\mu}$	[30, 31, 32, 135]	$0.965^{+0.10}_{-0.090}$
$BR^{EXP/SM}_{b\to s\gamma}$	[136, 1, 137]	$1.023 \pm 0.076_{EXP} \pm 0.050_{SUSY}$
$BR^{EXP/SM}_{b\to \tau\nu}$	[1, 137]	$0.98 \pm 0.23_{EXP+SM}$
$BR^{EXP/SM}_{b\to X_s ll}$	[138, 139, 140]	$0.96 \pm 0.28_{EXP+SM}$
$\Delta M^{EXP/SM}_{B_s}$	[17, 1]	$0.980 \pm 0.038_{EXP+SM}$
$\frac{\Delta M^{EXP/SM}_{B_s}}{\Delta M^{EXP/SM}_{B_d}}$	[17, 1]	$1.014 \pm 0.077_{EXP+SM}$
$BR^{EXP/SM}_{K\to\pi\bar{\nu}\nu}$	[141, 142, 143]	$1.32 \pm 0.44_{EXP+SM}$
$\lvert\epsilon_K^{EXP/SM}\rvert$	[144, 33]	$0.922 \pm 0.081_{EXP+SM}$
$BR^{EXP/SM}_{K\to\mu\nu}$	[145, 33]	$1.0142 \pm 0.0077_{EXP+SM}$

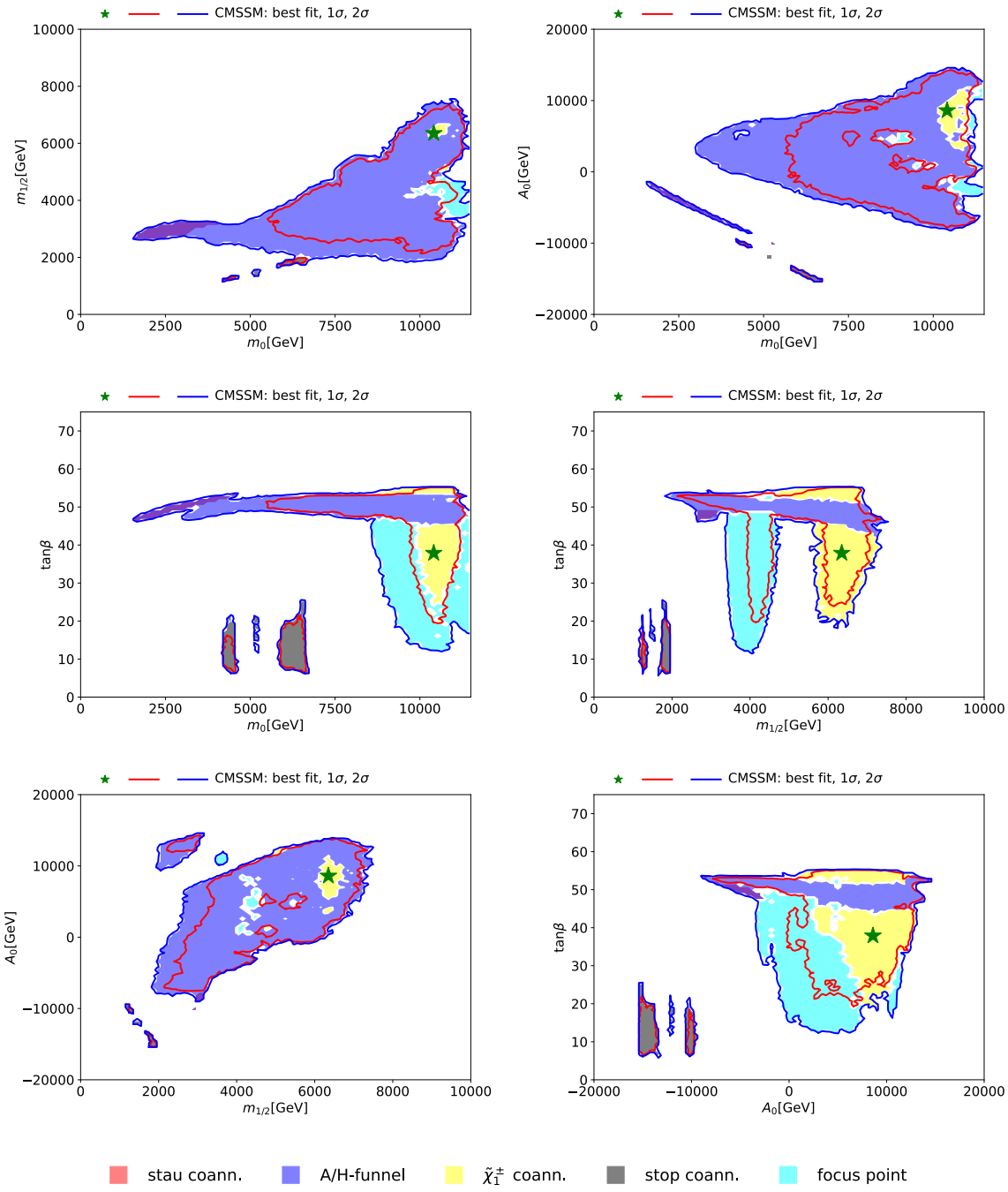

FIGURE 6.1: Input space projections for $\mu > 0$. Only points allowed at two standard deviations are shown (95% CL). The best-fit point is highlighted by a green star. The dominance of DM (co-)annihilation mechanisms is represented using a color scheme as indicated in the legend.

processes, given the typically significant predicted DM scattering cross-section (see §6.1.3.1 for details). Conversely, in stau and stop coannihilation regions, where the LSP is predominantly Bino and closely matched in mass with the lightest sfermions, the LHC can play a crucial role in tightening the input parameter space. In these scenarios, the expected DM scattering cross-section is predicted to be small, and direct searches at the LHC provide one of the best ways of constraining them. The best-fit point lies in an island dominated by well-tempered chargino coannihilation, in the region of very large A_0, m_0, and m_{12}. In these regions of the parameter space, the LSP has an important Bino component

The upper left panel of Fig. 6.2 illustrates the (M_A, $\tan\beta$) plane. In contrast with the rest of the planes shown, the A/H funnel mechanism only dominates in a small region corresponding to large $\tan\beta$ and relatively small M_A. The focus-point island appears at $m_{\chi_1^0} \sim 1$ TeV where $m_{\chi_1^0} \sim \mu$ and the LSP has an important Higgsino component. The lower left panel of Fig. 6.2 shows the mass of the LSP versus $m_{\tilde{\tau}_1}$. In the small strip where $m_{\tilde{\tau}_1} \sim m_{\chi_1^0}$ both annihilations via A/H funnel and stau coannihilation dominate. In the region of low χ_1^0 mass ($m_{\chi_1^0} \sim 1$ TeV), the stop coannihilation islands can be seen. This is also seen in the bottom right panel of Fig. 6.2. These features indicate that stau and stop coannihilation strips are particularly constrained by direct searches performed at the LHC (see Table 6.3) compared to the rest of DM mechanisms.

One dimensional profile likelihood of the anomalous magnetic moment of the muon is shown in Fig. 6.3. As expected cMSSM contributions to this observable are small (in general heavy sleptons) and cannot alleviate the tension between the SM value [36] and the world average [34], shown in the plot with a red band. In green it is shown the band corresponding to the constraint when considering lattice estimation of hadronic contributions to a_μ^{SM} [38]. As can be seen in Fig. 6.3, the need for NP highly depends on the theoretical prediction used.

In this type of flavor-simplified model, the importance of the flavor constraints is generally small. This is due to two reasons. First, the model construction is chosen such that it has no major contributions to FCNCs and CPV observables; this is why all the inputs are flavor universal at a given scale. Second, in principle, RGE induces non-minimal flavor violation effects that are assumed to be negligible in this study. Therefore, the most relevant flavor constraint in this study is $R_{\mu\mu}$. The one-dimensional profile likelihood for this observable and the plane ($R_{\mu\mu}$,$\tan\beta$) are shown in Fig. 6.4. Since $\mu > 0$ in this scan, the region of $R_{\mu\mu} > 1$ is preferred. One would expect large contributions to this observable for low M_A and high $\tan\beta$; however, due to the rest of the constraints, only the region of $\tan\beta \sim 50$ survives and presents significant contributions to $R_{\mu\mu}$.

In conclusion, in cMSSM, the LSP can still explain the CDM density observed in our Universe. However, because of the limited freedom in input parameters as long as

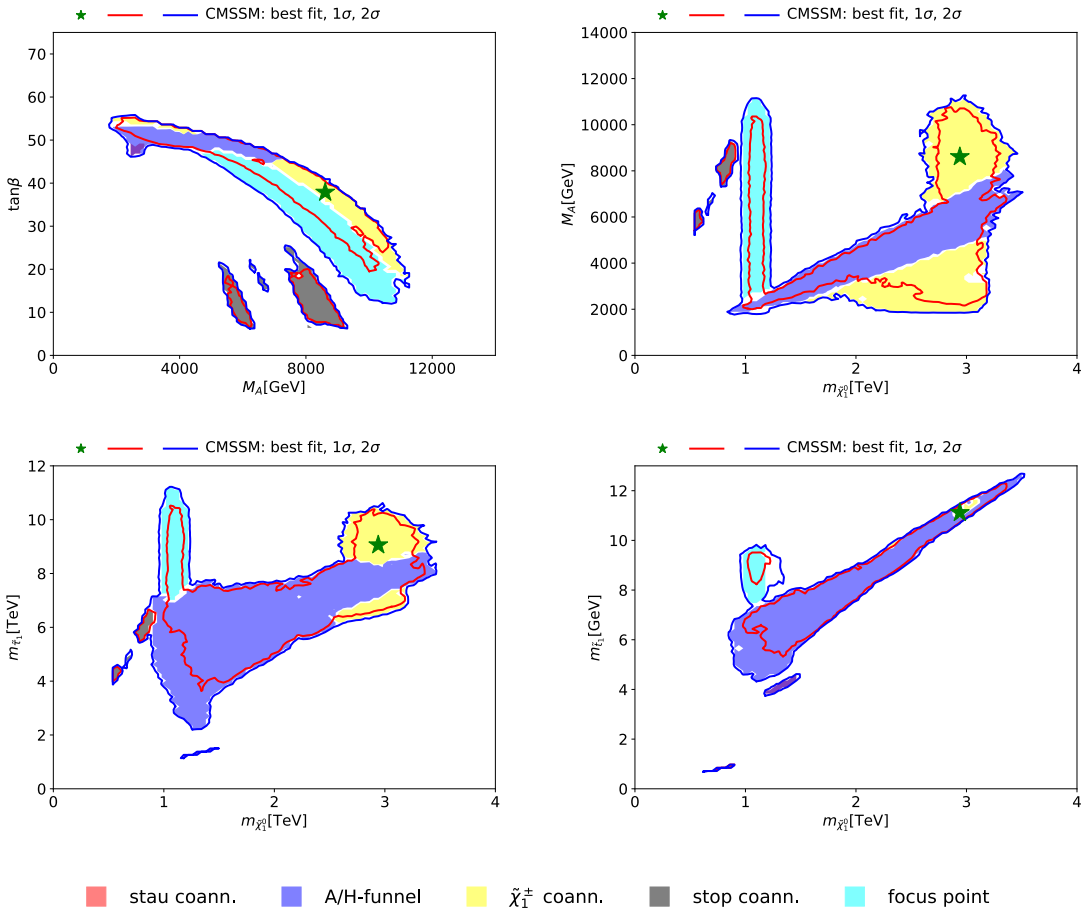

FIGURE 6.2: Upper left, $(M_A, \tan\beta)$, upper right $(m_{\chi_1^0}, M_A)$, bottom left, $(m_{\chi_1^0}, m_{\tilde{\tau}_1})$, and bottom right $(m_{\chi_1^0}, m_{\tilde{t}_1})$, plane projections for $\mu > 0$. Only points allowed at two standard deviations are shown (95% CL). The best-fit point is highlighted by a green star. The dominance of DM (co-)annihilation mechanisms is represented using a color scheme as indicated in the legend.

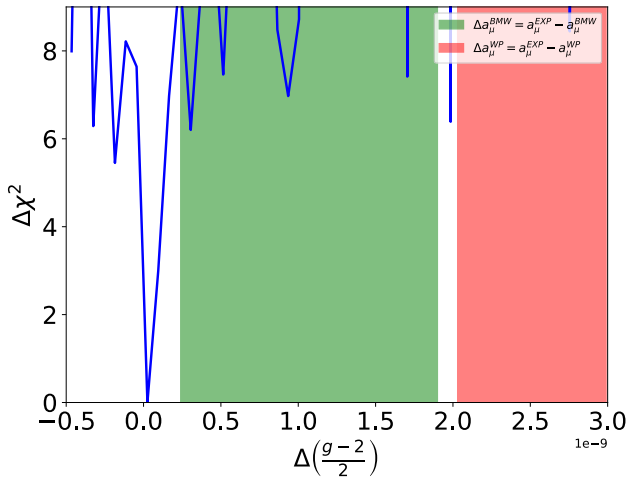

FIGURE 6.3: Profile likelihood obtained for $a_\mu = (g-2)_\mu/2$ observable. The red band shows the constraint when considering the SM prediction of [36] and the green band the one using lattice calculation to estimate the hadronic contribution based on Ref. [37]. The cMSSM contribution is found to be negligible.

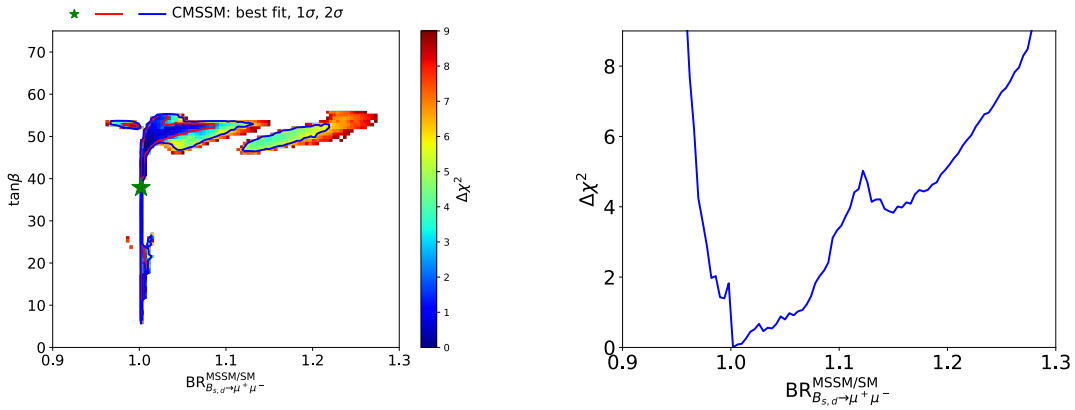

FIGURE 6.4: On the left two dimensional projection in the $(R_{\mu\mu}, \tan\beta)$ plane as a function of the $\Delta\chi^2$ highlighted with a color scheme. On the right one-dimensional likelihood profile of the $R_{\mu\mu}$ observable. The region of $R_{\mu\mu} > 1$ is preferred due to $\mu > 0$.

the LHC constraints, the contributions to the anomalous magnetic moment of the muon are found to be negligible. As explained, in these types of flavor-simplified models, the flavor phenomenology is very restricted by construction. This is motivated by the fact that performing scans with a large number of input parameters is difficult. In the next section, this point will be emphasized, and an attempt will be made to merge DM and flavor phenomenology in the same study.

6.3 Full model in Mass Insertion approximation

As mentioned, primarily due to computational constraints, further simplifications in the input space of the general MSSM are needed to phenomenologically study the model. One of the simplest cases, the cMSSM, was examined in §6.2. Other models, such as the phenomenological MSSM (pMSSM), which considers CP-conserving and Minimal Flavor Violation (MFV), have also been studied in the bibliography, for example in Ref. [147]. However, these models fail to provide a full study of the flavor phenomenology available in the MSSM.

In the work presented in this section, one step further is taken by including non-Minimal Flavor Violation contributions (NMFV) in the quark sector, particularly in $3 \to 2$ and $3 \to 1$ transitions. As explained in Chapter 1, indirect searches through B meson decays are excellent probes for NP, especially where BSM (SUSY in this case) is far beyond the reach of direct detection at the LHC. As mentioned in Chapter 1, there are some anomalies to follow up, but for the moment, no clear hint of NP has been found in the LHC. Therefore, by stressing this point, an attempt is made to understand how the lack of NP observations constrains the NMFV MSSM, as indirect searches could be already providing some insights into the scale of NP.

In this study, the MSSM contributions to $\Delta F = 2$, $\Delta F = 0$, and $\Delta F = 1$ transitions are considered. Details on the formalism will be given in §6.3.1. To handle the high dimensionality problem, the parameter space of the MSSM will be studied by using Graphics Processing Units (GPU), as detailed in §6.3.2. The observables considered are given in §6.3.3. Finally, the results obtained are discussed in §6.3.4.

6.3.1 Formalism

The soft SUSY breaking scalar mass terms of Eq. 6.3 ($m^2_{\tilde{q},\tilde{u},\tilde{d}}$) induce FV contributions to the effective low energy Lagrangian. Note that this is true even in the case of universal GUT scenarios (like the cMSSM) as RGE induces non-universal effects. Another FV effect comes from the soft SUSY trilinear terms ($a_{\tilde{u},\tilde{d}}$), which after EWSB, mixes left-handed with right-handed scalars [44]. Additionally, there is a contribution that comes from the SUSY-conserving term and is proportional to the mass

squared of the SM partners (non-negligible for the 3rd generation of squarks). The last contribution to the squark mass matrix arises from the scalar potential after the EWSB ($H_{u,d}$ acquire VEVs) [44]. The squark mass-matrices are 6×6 hermitian matrices that can be decomposed as [44]:

$$M^2_{U,D} = \begin{pmatrix} (M^2_{U,D})_{LL} & (M^2_{U,D})_{LR} \\ (M^2_{U,D})_{LR} & (M^2_{U,D})_{RR} \end{pmatrix}. \tag{6.12}$$

The approach followed for studying Non-Minimal Flavor Violation (NMFV) effects is the Mass Insertion Approximation (MIA) [148]. In this model, a basis is chosen where the quark-squark-neutral gaugino couplings are flavor diagonal, and all the flavor violation effects are encoded by the off-diagonal terms of the sfermion mass matrix [44]. For this study, the notations of Ref. [95, 149] are followed. The two-left handed squarks have the same mass due to $SU(2)_L$ symmetry, the mass matrix is given by m^2_Q and the average Q mass is denoted by $\tilde{m}^2_Q$. The mass matrices for the right-handed down and up squarks are denoted by m^2_D and m^2_U, while the average masses are given by $\tilde{m}^2_D$ and $\tilde{m}^2_U$, respectively. The mass insertions (MI) are defined as:

$$\begin{aligned}
\left(\delta_d^{LL}\right)_{ij} &= \frac{\left[\left(\mathcal{M}^2_D\right)_{LL}\right]_{ij}}{\tilde{m}^2_Q} = \frac{(m^2_Q)_{ji}}{\tilde{m}^2_Q}, \\
\left(\delta_u^{LL}\right)_{ij} &= \frac{\left[\left(\mathcal{M}^2_U\right)_{LL}\right]_{ij}}{\tilde{m}^2_Q} = \frac{(V m^2_Q V^\dagger)_{ji}}{\tilde{m}^2_Q}, \\
\left(\delta_d^{RR}\right)_{ij} &= \frac{\left[\left(\mathcal{M}^2_D\right)_{RR}\right]_{ij}}{\tilde{m}^2_d} = \frac{(m^2_D)_{ij}}{\tilde{m}^2_d}, \\
\left(\delta_u^{RR}\right)_{ij} &= \frac{\left[\left(\mathcal{M}^2_U\right)_{RR}\right]_{ij}}{\tilde{m}^2_u} = \frac{(m^2_U)_{ij}}{\tilde{m}^2_u},
\end{aligned} \tag{6.13}$$

where V is the CKM matrix defined in Eq. 1.7. The running coupling constants are defined as [150]:

$$\begin{aligned}
\alpha_1 &= \frac{g_1^2}{4\pi} = \frac{5}{3}\frac{g'^2}{4\pi}, \\
\alpha_2 &= \frac{g_2^2}{4\pi} = \frac{g^2}{4\pi}, \\
\alpha_3 &= \frac{g_3^2}{4\pi} = \frac{g_s^2}{4\pi},
\end{aligned} \tag{6.14}$$

where g', g and g_s are the $U(1)$, $SU(2)_L$ and $SU(3)$ group coupling constants, respectively. These couplings are evaluated at $\mu_{SUSY} = \sqrt{m_{\tilde{g}} m_Q}$. Following the same strategy as described in Ref. [150].

6.3.2 Parameter scan

The parameter scan is performed using the `Ipanema-`β framework [151] utilizing different GPU-GeForce GTX 3090. Different scenarios mostly based on the nature of the DM candidate are explored by following a similar strategy as Ref. [150]. Five different scenarios are studied:

- Scenario A. A generic scenario with universal gaugino masses where the LSP is mostly Bino, except for some regions of the parameter space where it is Higgsino-like. Apart from the LSP being the neutralino, no further constraints are applied to the DM relic density.
- Scenario B. Motivated by a Higgsino-like LSP. The DM relic density in this type of scenario is almost uniquely a function of the LSP mass. The measured density is fulfilled at $m_{\chi_1^0} \sim 1$ TeV [100]. Therefore μ is fixed to 1 TeV and the Bino is forced to be heavier ($M_1 > \mu$), to ensure that the LSP is dominated by the Higgsino component.
- Scenario C. Motivated by a Wino-like LSP, possible in the minimal Anomaly-Mediated Supersymmetry Breaking (mAMSB) [152] and in the pMSSM [147]. The DM relic density is also mostly a function of the χ_1^0 mass, and the experimental value is fulfilled at $m_{\chi_1^0} \sim 3$ TeV [152]. Therefore, a scan with the mass of the Wino set to 3 TeV and heavier μ, M_1 and M_3 is made. The Bino mass is set to 5 TeV for simplicity, however it can be changed without modifying the results.
- Scenario D. Exploring the non-universal squark approach in the up sector, $m_{\tilde{u}_R} \neq m_{\tilde{Q}_L}$. This model is motivated by scenarios with conservative predictions for EDMs and a heavy right-handed stop.
- Scenario E. Scenario for exploring the effect of $A_t \neq 0$, motivated by aggressive EDM predictions. As $A_t \neq 0$, also the MI $(\delta^u_{RR})_{31}$ is floated to investigate cancellations in the calculations of the EDMs observables.

Table 6.5 shows a summary of the scan ranges used in this study. For each scenario, a combination of samples, based on genetic algorithms and flat scan samples, are performed.

TABLE 6.5: Scan ranges for each scenario. All masses are in TeV and $\alpha_{1,2,3}$ are defined at μ^{SUSY}.

Parameter	Scenario A	Scenario B	Scenario C	Scenario D	Scenario E
$\tilde{m}_Q$	[2, 10]	[2, 10]	[4, 10]	[2, 5]	[2,10]
$\tilde{m}_Q^2/\tilde{m}_d^2$	[0.25, 4]	[0.25, 4]	[0.25, 4]	[0.25, 4]	[0.25, 4]
$\tilde{m}_u$	$\tilde{m}_Q$	$\tilde{m}_Q$	$\tilde{m}_Q$	10	$\tilde{m}_Q$
M_3	[2, 10]	[4.5, 15]	[4, 15]	[2, 10]	[2, 10]
$\tan\beta$	[2, 50]	[10, 50]	[10, 50]	[2, 50]	[2, 50]
A_t	0	0	0	0	$[-3, 3]$
M_A	[2, 10]	[2, 10]	[5, 20]	[2, 10]	[2, 10]
$\lvert\mu\rvert$	[1,10]	1	[5, 20]	[2, 10]	[2, 10]
M_1	$(\alpha_1/\alpha_3)M_3$	$(\alpha_1/\alpha_3)M_3$	5	$(\alpha_1/\alpha_3)M_3$	$(\alpha_1/\alpha_3)M_3$
M_2	$(\alpha_2/\alpha_3)M_3$	$(\alpha_2/\alpha_3)M_3$	3	$(\alpha_2/\alpha_3)M_3$	$(\alpha_2/\alpha_3)M_3$
$\lvert\mathrm{Re}\left[(\delta_d^{LL})_{23}\right]\rvert$	[0, 0.4]	[0, 0.4]	[0, 0.4]	[0, 0.4]	[0, 0.4]
$\lvert\mathrm{Im}\left[(\delta_d^{LL})_{23}\right]\rvert$	[0, 0.4]	[0, 0.4]	[0, 0.4]	[0, 0.4]	[0, 0.4]
$\lvert\mathrm{Re}\left[(\delta_d^{RR})_{23}\right]\rvert$	[0, 0.4]	[0, 0.4]	[0, 0.4]	[0, 0.4]	[0, 0.4]
$\lvert\mathrm{Im}\left[(\delta_d^{RR})_{23}\right]\rvert$	[0, 0.4]	[0, 0.4]	[0, 0.4]	[0, 0.4]	[0, 0.4]
$\lvert\mathrm{Re}\left[(\delta_d^{LL})_{13}\right]\rvert$	[0, 0.4]	[0, 0.4]	[0, 0.4]	[0, 0.4]	[0, 0.4]
$\lvert\mathrm{Im}\left[(\delta_d^{LL})_{13}\right]\rvert$	[0, 0.4]	[0, 0.4]	[0, 0.4]	[0, 0.4]	[0, 0.4]
$\lvert\mathrm{Re}\left[(\delta_d^{RR})_{13}\right]\rvert$	[0, 0.4]	[0, 0.4]	[0, 0.4]	[0, 0.4]	[0, 0.4]
$\lvert\mathrm{Im}\left[(\delta_d^{RR})_{13}\right]\rvert$	[0, 0.4]	[0, 0.4]	[0, 0.4]	[0, 0.4]	[0, 0.4]
$\lvert\mathrm{Re}\left[(\delta_u^{RR})_{31}\right]\rvert$	0	0	0	0	[0, 0.4]
$\lvert\mathrm{Im}\left[(\delta_u^{RR})_{31}\right]\rvert$	0	0	0	0	[0, 0.4]

6.3.3 Observables

To constrain the available input space of the models analyzed in this study, different flavor observables related to $\Delta F = 2$, $\Delta F = 1$, and $\Delta F = 0$ transitions are calculated. Additionally, the points are required to have a valid SUSY spectrum and Higgs boson mass according to the SOFTSUSY package [103]. A summary of the constraints included in this study can be found in Table 6.6. The specific observables considered in this analysis are described in detail below.

6.3.3.1 $\Delta F = 0$ transitions

The Electric Dipole Moments (EDMS) are predicted within the SM, to be very small; therefore, they are excellent probes of NP. In this study, the SM predictions for the EDMs are assumed to be zero. The proton, neutron, and mercury EDMs are computed following Ref. [153] and Ref. [154]:

$$\begin{aligned} d_n &= 0.73\, d_d - 0.18\, d_u + e\,(0.20\, d_d^c + 0.10\, d_u^c)\ , \\ d_p &= 0.73\, d_u - 0.18\, d_d - e\,(0.40\, d_u^c + 0.049\, d_d^c)\ , \\ d_{Hg} &\simeq -2.1 \times 10^{-4}\left(1.9\, d_n + 0.2\, d_p\right)\ , \end{aligned} \tag{6.15}$$

where $d_{d,u}$ and $d^c_{d,u}$ are the flavored and chromo EDMs for the d and u quark respectively. The effective Hamiltonian is given by:

$$\mathcal{H}_{\text{eff}} = \frac{i}{2}\sum_q \left(d_q \bar{q}\sigma_{\mu\nu}\gamma_5 q F^{\mu\nu} + d_q^c g_s \bar{q}\sigma_{\mu\nu} T^a \gamma_5 q G^a_{\mu\nu}\right)\ . \tag{6.16}$$

The coefficients d_q and d_q^c are matched at $\mu = \mu_{SUSY}$ and properly evolved to $\mu = 2$ GeV using the LO QCD RGE taken from Ref. [155]. The leading MSSM contributions are given in App. C.2.

6.3.3.2 $\Delta F = 1$ Observables

In this study the following $\Delta F = 1$ observables are considered: $\mathcal{B}(B_{(s)} \to \mu^+\mu^-)$, $\mathcal{B}(B^+ \to \tau\nu)$ and $b \to s\gamma$ transitions. For $B^0_{(s)} \to \mu\mu$, assuming alignment and degenerate approximation (see Eq. C.9), the leading MSSM contributions are coming from the scalar and pseudo-scalar operators. The computed contributions are given in App. C.3.1. Note that at leading order these Wilson coefficients do not receive QCD RG contributions. The branching ratios are calculated as [24]:

$$\begin{aligned}\mathcal{B}(B^0_{s,d} \to \mu^+\mu^-) &= \frac{\tau_{B_{s,d}}}{1-y_{s,d}}\Gamma(B^0_{s,d} \to \mu^+\mu^-) \\ &= \frac{1}{32\pi\Gamma^{(s,d)}_H} f^2_{B_{s,d}} M^3_{B_{s,d}} \beta_{B_{s,d}\mu} \left(\left| A_{B_{s,d}} \right|^2 + \beta^2_{B_{s,d}\mu} \left| B_{B_{s,d}} \right|^2 \right) ,\end{aligned} \tag{6.17}$$

with

$$\begin{aligned}\beta_{B_{s,d}\mu} &= \sqrt{1 - \frac{4m^2_\mu}{M^2_{B_{s,d}}}} , \\ A_{B_{s,d}} &= \frac{2m_\mu}{M_{B_{s,d}}} \left(C_A - \tilde{C}_A\right) + \frac{m_b M_{B_{s,d}}}{m_b + m_{s,d}} \left(C_P - \tilde{C}_P\right) , \\ B_{B_{s,d}} &= \frac{m_b M_{B_{s,d}}}{m_b + m_{s,d}} \left(C_S - \tilde{C}_S\right) .\end{aligned} \tag{6.18}$$

Note that in the SM only C_A emerges while the rest are almost negligible [24, 25]. The $\mathcal{B}(B^+ \to \tau\nu)$ is also computed at the leading one-loop correction level. The expression is given in App. C.3.2. Additionally, the observable $\mathcal{B}(K^+ \to \mu\nu)$ which is also sensitive to $\tan\beta$ and heavy Higgs mass contributions is calculated following Ref. [150] and Ref. [95].

The last $\Delta F = 1$ observables considered in this study are $b \to s\gamma$ transitions. The effective Hamiltonian is given by [95]:

$$\mathcal{H}_{\text{eff}} = -\frac{4G_F}{\sqrt{2}} V_{tb}V^*_{ts} \left(C_7\mathcal{O}_7 + C_8\mathcal{O}_8 + \tilde{C}_7\tilde{\mathcal{O}}_7 + \tilde{C}_8\tilde{\mathcal{O}}_8\right) + \text{h.c} , \tag{6.19}$$

with [95]

$$\begin{aligned}\mathcal{O}_7 &= \frac{e}{16\pi^2} m_b \bar{s}\sigma^{\mu\nu} P_L b F_{\mu\nu} , \\ \mathcal{O}_8 &= \frac{g_s}{16\pi^2} m_b \bar{s}\sigma^{\mu\nu} T_A P_L b G^A_{\mu\nu} ,\end{aligned} \tag{6.20}$$

The $\tilde{\mathcal{O}}_{7,8}$ operators are obtained by replacing left projectors with right projectors. The Wilson coefficients C_7 and C_8 are matched at $\mu = \mu_{SUSY}$ and evolved to $\mu = m_b$ considering LO QCD RG contributions [156]. The computed expressions can be found in App. C.3.3. The computed C_7 and C_8 are used to calculate the difference of CP asymmetries in $B^\pm \to X^\pm_s\gamma$ and $B^0 \to X_s\gamma$. This observable is sensitive to imaginary parts of $C_{7,8}$ [157]:

$$\begin{aligned}\Delta A_{CP}(b\to s\gamma) &= A_{\rm CP}(B^-\to X_s^-\gamma) - A_{\rm CP}(\bar{B}^0\to X_s^0\gamma)\\ &= 4\pi^2\alpha_s(\mu_{\rm 2GeV})\frac{\tilde{\Lambda}_{78}}{m_b}{\rm Im}\left[\frac{C_7^* C_8 + \tilde{C}_7^*\tilde{C}_8}{|C_7|^2+|\tilde{C}_7|^2}\right],\end{aligned}$$

Note that in the SM this observable is predicted to be negligible $\Delta A_{CP}^{SM}\sim 0$. The hadronic parameter Λ_{78} is obtained from Ref. [157]. Possible flavor universal contributions to C_9 and C_{10} are also explored in this study. Global fits indicate that large lepton-universal contributions to C_9 can explain $b\to sll$ data [19]. For testing these observables, the equations presented in Ref. [158] were introduced in this framework.

6.3.3.3 $\Delta F = 2$ Processes

The meson-antimeson oscillation is described by the following mixing amplitude [150]:

$$\mathcal{M}_{12}^{(M)} \equiv \left\langle M\left|\mathcal{H}_{\rm eff}^{\Delta F=2}\right|\overline{M}\right\rangle \qquad \text{for } M = K^0, B_{d,s}^0\,, \tag{6.21}$$

where $\mathcal{H}_{\rm eff}^{\Delta F=2}$ is the effective Hamiltonian. Within the MSSM, the effective Hamiltonian takes the following form:

$$\mathcal{H}_{\rm eff}^{\Delta F=2} = \sum_{i=1}^{5} C_i\mathcal{O}_i + \sum_{i=1}^{3}\tilde{C}_i\tilde{\mathcal{O}}_i + \text{h.c.}\,, \tag{6.22}$$

with the operators $\mathcal{O}_i$ defined, in the case of B_s^0 mixing, as follows:

$$\begin{aligned}\mathcal{O}_1 &= (\bar{s}^\alpha\gamma_\mu P_L b^\alpha)(\bar{s}^\beta\gamma^\mu P_L b^\beta)\,,\\ \mathcal{O}_2 &= (\bar{s}^\alpha P_L b^\alpha)(\bar{s}^\beta P_L b^\beta)\,,\\ \mathcal{O}_3 &= (\bar{s}^\alpha P_L b^\beta)(\bar{s}^\beta P_L b^\alpha)\,,\\ \mathcal{O}_4 &= (\bar{s}^\alpha P_L b^\alpha)(\bar{s}^\beta P_R b^\beta)\,,\\ \mathcal{O}_5 &= (\bar{s}^\alpha P_L b^\beta)(\bar{s}^\beta P_R b^\alpha)\,,\end{aligned} \tag{6.23}$$

where α,β are color indices and $P_{L,R} = \frac{1}{2}(1\mp\gamma_5)$. The operators $\mathcal{O}_{1,2,3}$ are obtained from $\mathcal{O}_{1,2,3}$ by the replacement $L\to R$. B^0 operators are obtained from those in Eq. 6.23 by the replacement $s\to d$. K^0 mixing operators are obtained by replacing $b\to s$ and $s\to d$ in Eq. 6.23. Note that only $\mathcal{O}_1$ arises in SM. For the case of the $B_{(s)}^0$ systems, the following observables are calculated:

$$\begin{aligned}
\Delta\phi_{s,d}^{NP} &= \arg\left(\frac{M_{12}^{(s,d)}}{M_{SM,12}^{s,d}}\right), \\
\Delta M_{s,d}^{NP} &= \frac{|M_{12}^{(s,d)}|}{|M_{SM,12}^{s,d}|}, \\
\Delta^{NP}\left(\frac{\Delta M_s a_{fs}^s}{\Delta\Gamma_s}\right) &= \tan\left(\phi_{s,12}^{SM} + \Delta\phi_s\right) - \tan\left(\phi_{s,12}^{SM}\right).
\end{aligned} \tag{6.24}$$

The computed MSSM contributions are given in App. C.1. The computed Wilson coefficients are matched at $\mu = \mu^{SUSY}$, and then evolved to $\mu = m_b$ using the running group equations from Ref. [159].

The constraints on the phases are calculated using the CKM parameters obtained in Eq. 1.7, resulting in:

$$\begin{aligned}
\phi_s^{SM} &= -2\beta_s = -0.0415 \pm 0.0021 \text{ rad}, \\
\phi_d^{SM} &= 2\beta = 0.895 \pm 0.040 \text{ rad}.
\end{aligned} \tag{6.25}$$

For the experimental values, the latest HFLAV combinations are utilized for the B_s^0 and B^0 sectors. These includes measurements of ϕ_s from $B_s^0 \to J/\psi\phi$ decays[7], and ϕ_d measurements from $B^0 \to J/\psi K^0$ decays [1]:

$$\begin{aligned}
\phi_s^{EXP,J/\psi\phi} &= -0.061 \pm 0.014 \text{ rad}, \\
\phi_d^{EXP,J/\psi K^0} &= 0.787 \pm 0.017 \text{ rad}.
\end{aligned} \tag{6.26}$$

Two possible approaches are followed for evaluating the constraint. The first approach is the classical one where penguins' contributions are assumed to be negligible and their measurement is considered merely a cross-check. Under this approach (aggressive) the following constraints are obtained:

$$\begin{aligned}
(\phi_s - \phi_s^{\text{SM}})_{\text{no peng.}} &= (-19 \pm 14) \text{ mrad}, \\
(\phi_d - \phi_d^{\text{SM}})_{\text{no peng.}} &= (-108 \pm 44) \text{ mrad}.
\end{aligned} \tag{6.27}$$

[7] A naive average with the latest CMS result [88] is used for $\phi_s^{EXP,J/\psi\phi}$.

For the second approach, the estimation of the penguin shifts based on SU(3) symmetry is taken from Ref. [61], utilizing the largest asymmetric error. This approach yields the following constraints:

$$\begin{aligned} \Delta\phi_s^{NP} &= (-22 \pm 18) \quad \text{mrad}, \\ \Delta\phi_d^{NP} &= (-95 \pm 46) \quad \text{mrad}. \end{aligned} \tag{6.28}$$

Note that the results of Ref. [61] assume exactly $SU(3)$ symmetry and do not take into account exchange and penguin annihilation topologies which justifies our choice of taking the biggest asymmetric error as baseline. It is well known (see for example Ref. [59]) that the measurement of $\phi_s^{c\bar{c}s}$ phase is sensitive to:

$$\phi_s^{c\bar{c}s} = -2\beta_s^{SM} + \Delta\phi_s^{NP} + \Delta\phi_s^{\text{peng,SM}} + \Delta\phi_s^{\text{peng,BSM}}, \tag{6.29}$$

where $\Delta\phi_s^{NP}$ is the NP phase induced in the mixing (M_{12} diagram). So the possible NP contributions through higher-order topologies to the decay $B_s^0 \to J/\psi\phi$ are neglected. This is justified for two reasons. First, the conclusions of Chapter 4, where no polarization dependence was observed, implying that penguin contributions (SM and BSM) if present, should be small. Second, because the main SUSY contribution to these decays comes from one-loop correction to $b \to d, s$ gluino exchanges, where the MIs involved are $(\delta^d_{LR,RL})_{23,13}$, which are set to zero in the scans explored [160]. Note that the pollution from higher-order decay topologies is not present in the $a_{fs}^{(s)}$ observable, motivating a more precise measurement of this quantity in the future. Currently, the experimental precision of this observable is low [1], resulting in a negligible expected impact on our results.

The contributions of App. C.1 for the K^0 system are negligible as the MI $(\delta^{LL,RR}_{d,u})_{12}$ are zero in the scan. However, $(3 \to 2)$ and $(3 \to 1)$ transitions generate effective higher order $(2 \to 1)$ transitions. Although these contributions are fourth-order MI suppressed, they are important for this analysis. These contributions are taken from Ref. [95]. The following observables are calculated for the K^0 system [150]:

$$\begin{aligned} \Delta M_K &= 2\text{Re}[M_{12}^K], \\ \epsilon_K &= \frac{\kappa_\epsilon e^{i\phi_\epsilon} \text{Im}[M_{12}^k]}{\sqrt{2}\Delta M_K^{EXP}}, \end{aligned} \tag{6.30}$$

where $\kappa_\epsilon = 0.94 \pm 0.02$ [161]. The full list, containing all the observables and constraints imposed in this study, is given in Table 6.6.

TABLE 6.6: Physics observables constraints considered in this study.

Observable	Constraint	Reference
$\Delta m_s / \Delta m_s^{\rm SM}$	0.980 ± 0.038	[17, 1]
$\Delta m_s^{EXP/SM} / \Delta m_d^{EXP/SM}$	1.014 ± 0.077	[17, 1]
$(\phi_s - \phi_s^{\rm SM})_{\text{no peng.}}$	(-19 ± 14) mrad	[1]
$(\phi_d - \phi_d^{\rm SM})_{\text{no peng.}}$	(-108 ± 44) mrad	[1]
$\Delta\phi_s^{NP}$	(-22 ± 18) mrad	[1, 61]
$\Delta\phi_d^{NP}$	(-95 ± 46) mrad	[1, 61]
$\mathcal{B}(B_s^0 \to \mu^+\mu^-)^{\rm EXP/SM}$	0.954 ± 0.094	[30, 31, 32, 135]
$\mathcal{B}(B_d^0 \to \mu^+\mu^-)^{\rm EXP/SM}$	4.0 ± 4.5	[30, 31, 32, 135]
$\Delta m_s A_{SL} / \Delta\Gamma_s - (\Delta m_s A_{SL} / \Delta\Gamma_s)^{\rm SM}$	-0.13 ± 0.60	[17, 1]
$\mathcal{B}(B^+ \to \tau^+\nu_\tau)^{\rm EXP/SM}$	0.98 ± 0.23	[1, 137]
ΔC_7	0.0 ± 0.02	[19]
$\Delta A_{CP}(b \to s\gamma)$	$(5.0 \pm 3.9_{\rm stat} \pm 1.5_{\rm syst})\%$	[162]
$\Delta m_K / \Delta m_K^{\rm SM}$	1 ± 1	[150]
$\lvert\epsilon_K^{EXP/SM}\rvert$	0.922 ± 0.081	[144, 33]
$\lvert d_n \rvert$	$(0.0 \pm 1.1) \times 10^{-26}$ e cm	[163]
$\lvert d_{Hg} \rvert$	$(2.20 \pm 3.12) \times 10^{-30}$ e cm	[164]
$BR_{K\to\mu\nu}^{EXP/SM}$	1.0142 ± 0.0077	[145, 33]
m_H	125.25 ± 2.0 GeV	[33]
$\tan\beta$:M_A plane	ATLAS limits hMSSM	[133]
LSP	Lightest neutralino	

6.3.4 Results

The total χ^2 for each point is calculated by summing the contributions from each of the observables listed in Table 6.6. The samples consist of combined scans performed using flat priors and genetic algorithms [150]. The statistical analysis considers a total of 15 degrees of freedom, corresponding to all the constraints listed in Table 6.6, except for the constraint in the $(\tan\beta, m_A)$ plane, the Δm_K observable (due to poor theoretical knowledge of this observable) and the constraint forcing the LSP to be the lightest neutralino.

The mass of the Higgs boson is calculated using the mass spectrum generator SOFTSUSY [103], where a conservative theoretical uncertainty of 2 GeV is considered for evaluating the constraint. Additionally, the output of SOFTSUSY [103] is used to validate the physical validity of each point. The lightest mass eigenstates of the squark mass matrices are required to be heavier than 1 TeV to avoid issues with direct searches placed by the LHC[8].

The plots are shown as scatter plots in various two-dimensional projections. Different thresholds, according to the number of degrees of freedom, are obtained to assess the effect of particular constraints. The baseline procedure shows the constraints $\Delta\phi_{s,d}$ when considering the penguin pollution estimated in Ref. [61] (second approach). The effect of the different approaches (neglecting or considering the penguin pollution) is illustrated in Fig. D.1, Fig. D.3, and Fig. D.2. As expected, including the estimation of the penguin pollution relaxes the tightness of the constraint, highlighting the importance of controlling these subleading SM contributions in the future.

Fig. 6.5 shows the scatter plot for the $(\Delta\phi_s^{NP}, \arg\left((\delta^d_{LL})_{23}(\delta^d_{RR})_{23}\right))$ plane. A very clear correlation is observed: a negative argument of the product of MIs implies a negative value of $\Delta\phi_s$. This correlation arises because this product of mass insertions appears in the C_4 and C_5 Wilson coefficients, which have an enhanced loop function compared to the rest of the Wilson coefficients. The black points indicate the 95% CL interval for all the sampled points when the $\Delta\phi_s$ constraint is not considered. The red points indicate the points that satisfy the constraints listed in Table 6.6, except for m_h. The green points indicate the red points that have a valid mass spectrum and also fulfill the m_h constraint according to SOFTSUSY [103]. In general, the effect of SOFSUSY is more pronounced in scenario C and scenario D, where the masses are heavier, and thus, the RG-induced effects are more significant.

The same information but for the B^0 system is displayed in Fig. 6.6. The region of the negative product of MIs is preferred due to the experimental constraint. It is noteworthy that even at large values of the argument of the product of mass insertions, one can still fulfill the experimental restrictions. Due to the low precision

[8]Note that this approach is conservative, as most of the direct searches constraints apply to simplified models rather than models with flavor violation.

of the experimental measurement of a^s_{fs}, this constraint has a small impact on this study. It would be interesting to see how this evolves in the future, considering that this observable is theoretically cleaner than $\phi_s^{c\bar{c}s}$, as can be measured independently of penguin pollutions.

Fig. 6.7 shows the scatter plot for the two-dimensional ($\Delta\phi_s^{NP}$, $\Delta m_s/\Delta m_s^{SM}$) plane. The black points represent the 95% CL regions for the studied plane when no constraints on Δm_s and $\Delta\phi_s$ are applied. Blue (Orange) points satisfy all the constraints except for Δm_s ($\Delta\phi_s$). The red and green points show the same information as previously indicated in Fig. 6.5. As seen in Fig. 6.7, significant contributions that are in tension with the experimental paradigm, can be observed for $\Delta\phi_s$ and Δm_s. The same information for the B^0 system is displayed in Fig. D.4. A similar legend, replacing the Δm_s with the $\mathcal{B}(B_s \to \mu\mu)$ constraint, is displayed in Fig. 6.8. Regarding the $\mathcal{B}(B^0 \to \mu\mu)$ observable, the constraint has a large uncertainty due to the lack of observation of this decay in experiments, resulting in a negligible impact on the scan.

Fig. 6.9 illustrates the importance of $|\epsilon_K|$ constraint in this study. As can be seen, very delicate cancellations are needed to satisfy the experimental constraint. This is particularly intriguing since we are neglecting the main contributions to this observable ($(\delta^d_{LL,RR})_{12}$ are set to zero). These results indicate that, as anticipated, the Kaon sector is highly sensitive to high-scale NP and can provide significant insights in the future when constructing NP models.

The ($\log d_n$, $\log d_{Hg}$) plane is shown in Fig. 6.11. The phenomenology for the EDM observables is, as expected, much richer in scenario E. In this scenario, due to non-zero A_t and $(\delta^{RR}_u)_{31}$, contributions from gluino-squark exchanges in the up-sector are activated (see Eq. C.11).

The EDM observables are sensitive to the imaginary part of products of mass insertions in $3 \to 1$ transitions, thus they are correlated with $\Delta\phi_d^{NP}$ observable. This correlation is depicted in Fig. 6.10. Large contributions to $\Delta\phi_d^{NP}$ imply potential large contributions to EDMs. The constraint $\Delta\phi_d^{NP}$ is in tension with the SM prediction ($\sim 2\sigma$), mainly due to the use of V_{cb} from the inclusive determination. If this tension persists, this correlation could have important implications in the future. To conclude the discussion on EDMs, Fig. D.5 shows the plane ($\log d_n$, $\log d_p$). This plot illustrates the potential impact of a proton EDM measurement, which could further constrain this plane and reduce possible NP contributions in $3 \to 1$ transitions.

The plane (A_{CP}, $\Delta\phi_d$) is shown in Fig. D.6. Generally, contributions to A_{CP} observable, which is sensitive to the imaginary parts of C_7 and C_8, are small in the studied scenarios. This observable is included for completeness, as the SM prediction is nearly zero and could potentially be in tension with future measurements. However, due to its large experimental and theoretical uncertainty, it is currently not relevant for this study.

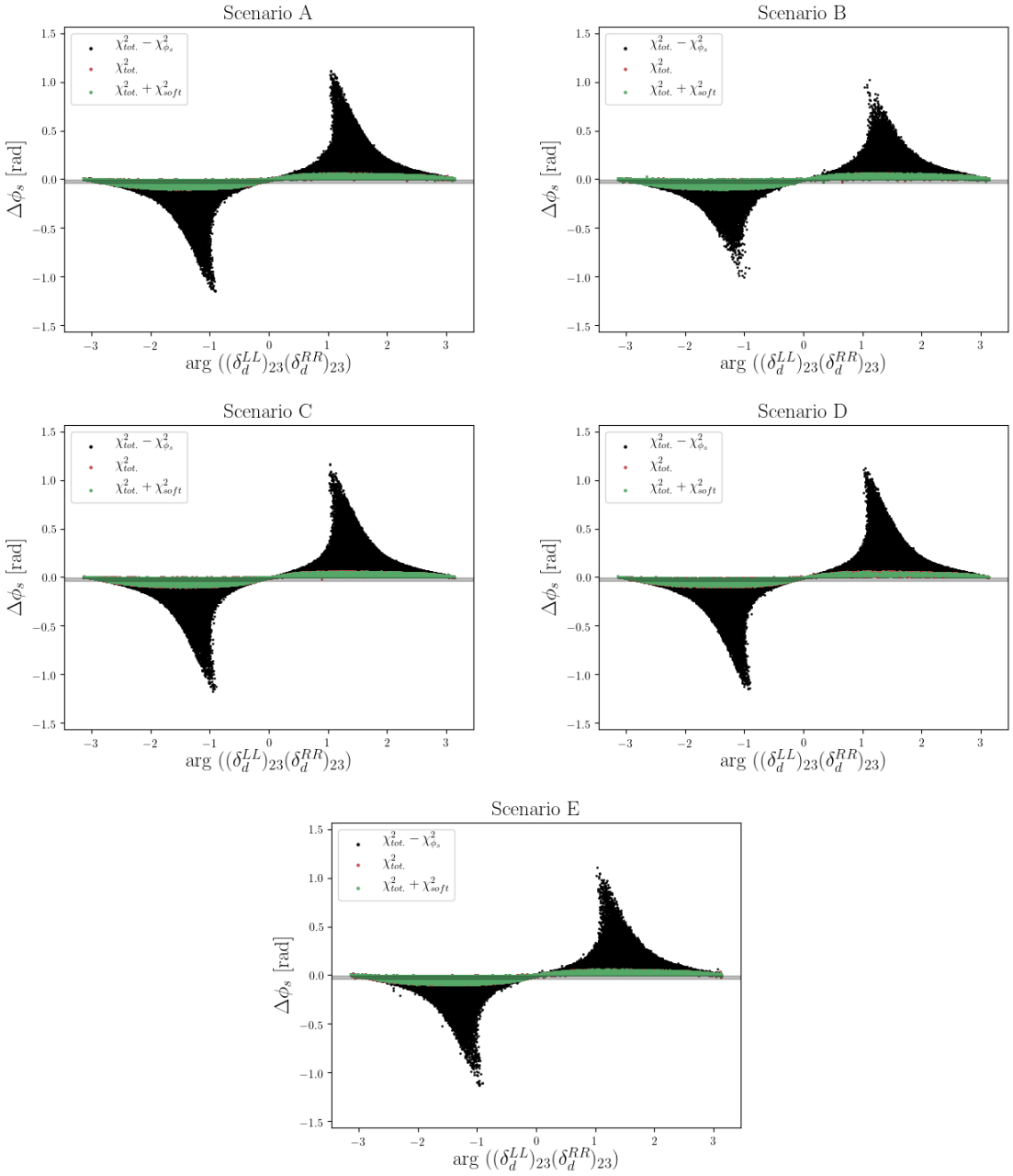

FIGURE 6.5: $\Delta\phi_s^{NP}$ vs arg $\left((\delta^d_{LL})_{23}(\delta^d_{RR})_{23}\right)$ for scenarios A (upper left), B (upper right), C (middle left), D (middle right) and E (bottom). Black points show the 95% CL when all the constraints except for $\Delta\phi_s$ are included. Red points indicate the points that fulfill all the constraints at 95% of CL. Green points indicate the red points that give a correct mass spectrum according to the SOFTSUSY software [103]. The constraints on $\Delta\phi^{NP}_{s,d}$ incorporate penguin pollution estimation based on SU(3) symmetry [61].

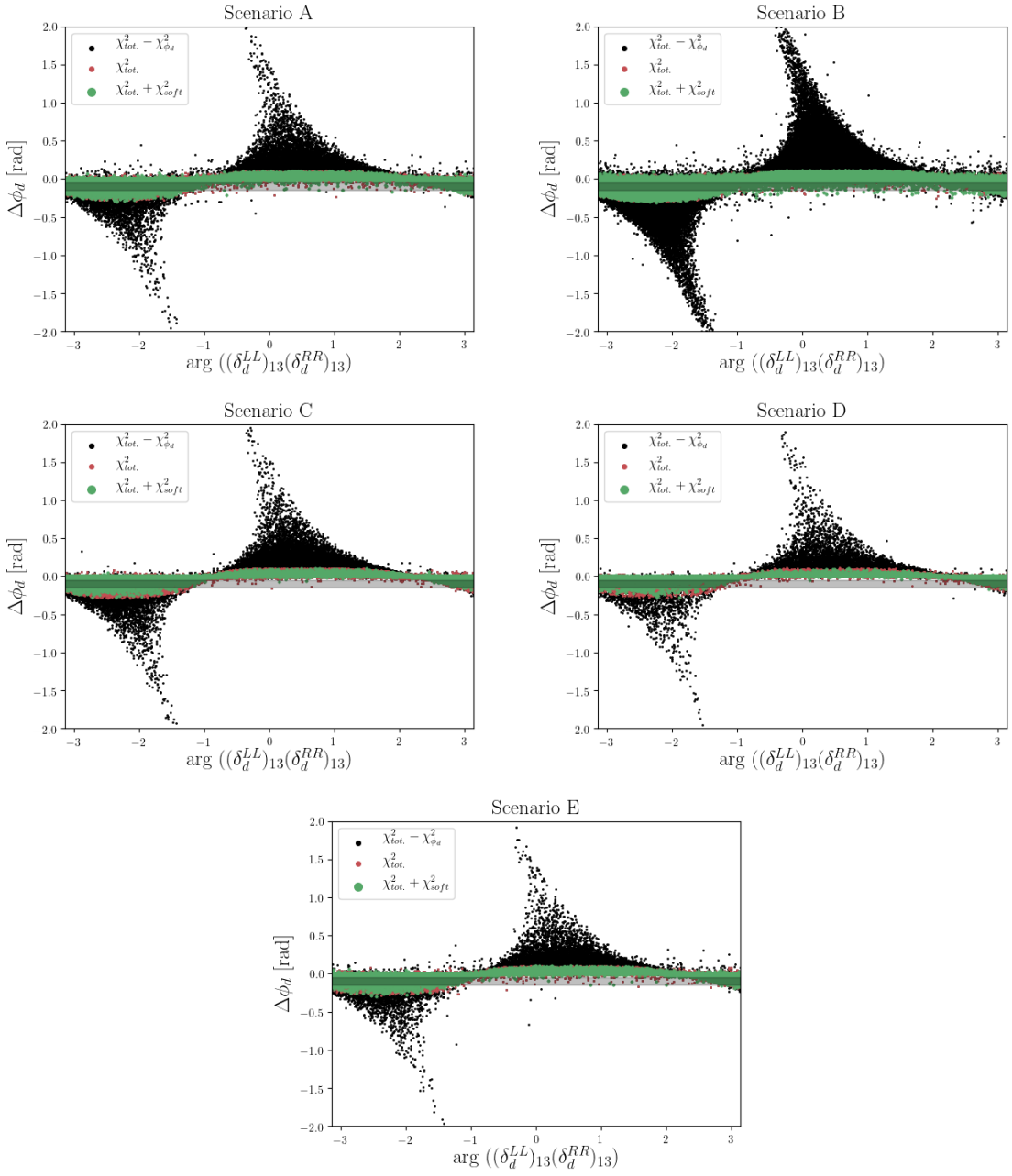

FIGURE 6.6: $\Delta\phi_d^{NP}$ vs arg $\left((\delta^d_{LL})_{13}(\delta^d_{RR})_{13}\right)$ for scenarios A (upper left), B (upper right), C (middle left), D (middle right) and E (bottom). Black points show the 95% CL when all the constraints except for $\Delta\phi_d$ are included. Red points indicate the points that fulfill all the constraints at 95% of CL. Green points indicate the red points that give a correct mass spectrum according to the SOFTSUSY software [103]. The constraints on $\Delta\phi_{s,d}^{NP}$ incorporate penguin pollution estimation based on SU(3) symmetry [61].

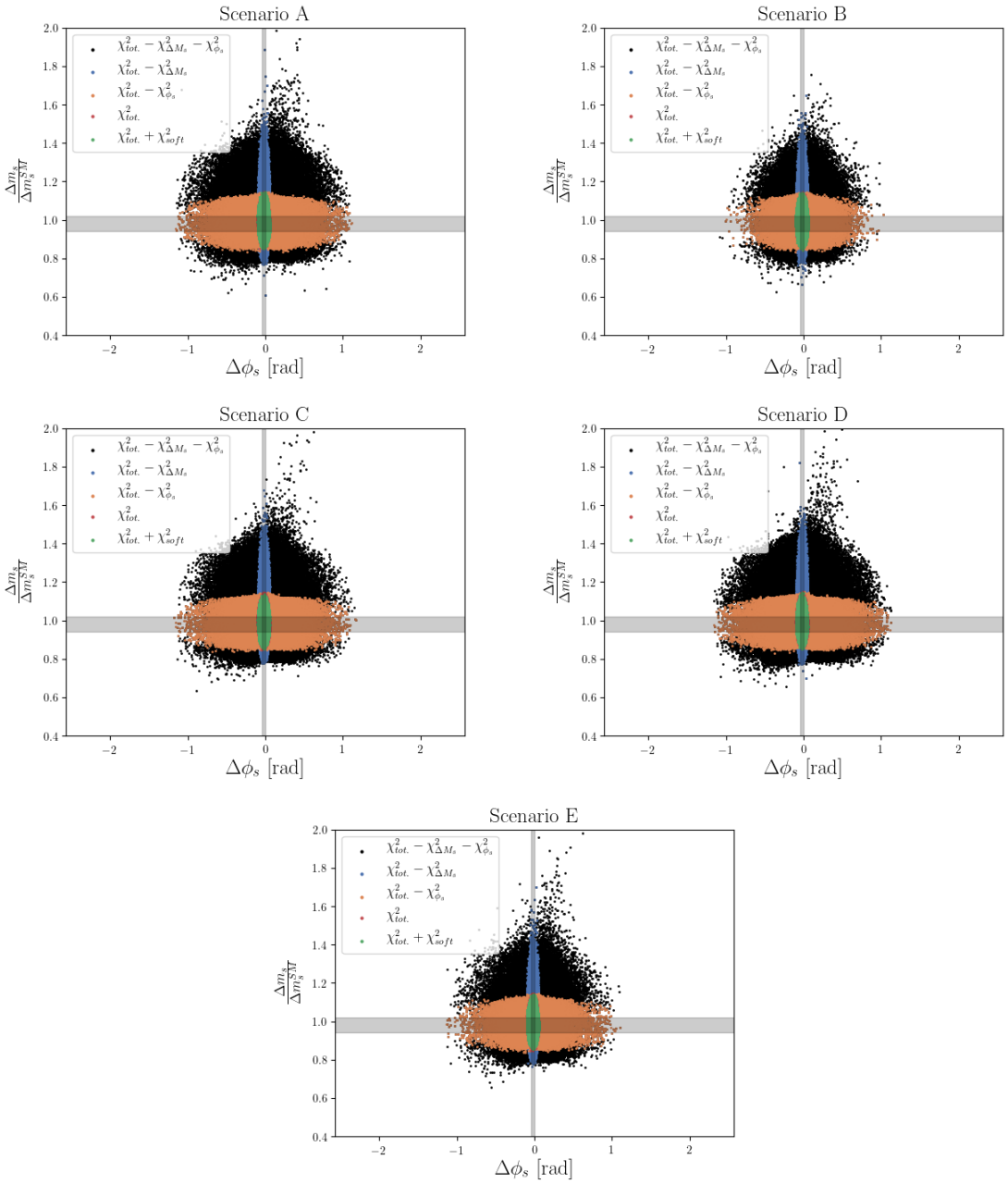

FIGURE 6.7: $\Delta\phi_s^{NP}$ vs $\Delta m_s^{EXP/SM}$ for scenarios A (upper left), B (upper right), C (middle left), D (middle right) and E (bottom). Black points show the 95% CL when all the constraints except for $\Delta\phi_s$ and Δm_s are included. Blue (orange) points show the 95% CL interval when all the constraints excluding Δm_s ($\Delta\phi_s$) are included. Red points indicate the points that fulfill all the constraints at 95% of CL. Green points indicate the red points that give a correct mass spectrum according to the SOFTSUSY software [103]. The constraints on $\Delta\phi_{s,d}^{NP}$ incorporate penguin pollution estimation based on SU(3) symmetry [61].

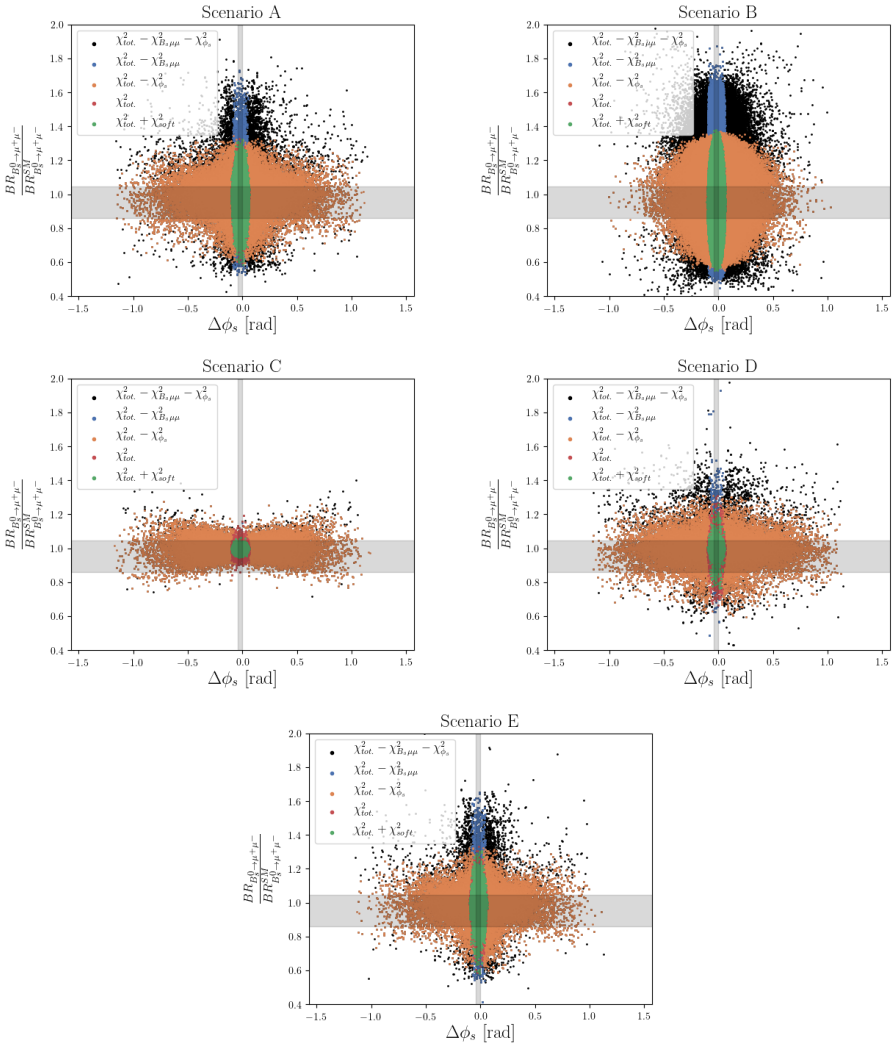

FIGURE 6.8: $\Delta\phi_s^{NP}$ vs $\mathcal{B}(B_s^0 \to \mu\mu)^{EXP/SM}$ for scenarios A (upper left), B (upper right), C (middle left), D (middle right) and E (bottom). Black points show the 95% CL when all the constraints except for $\Delta\phi_s^{NP}$ and $\mathcal{B}(B_s^0 \to \mu\mu)^{EXP/SM}$ are included. Blue (orange) points show the 95% CL interval when all the constraints excluding $\mathcal{B}(B_s^0 \to \mu\mu)^{EXP/SM}$ ($\Delta\phi_s^{NP}$) are included. Red points indicate the points that fulfill all the constraints at 95% of CL. Green points indicate the red points that give a correct mass spectrum according to the SOFTSUSY software [103]. The constraints on $\Delta\phi_{s,d}^{NP}$ incorporate penguin pollution estimation based on SU(3) symmetry [61].

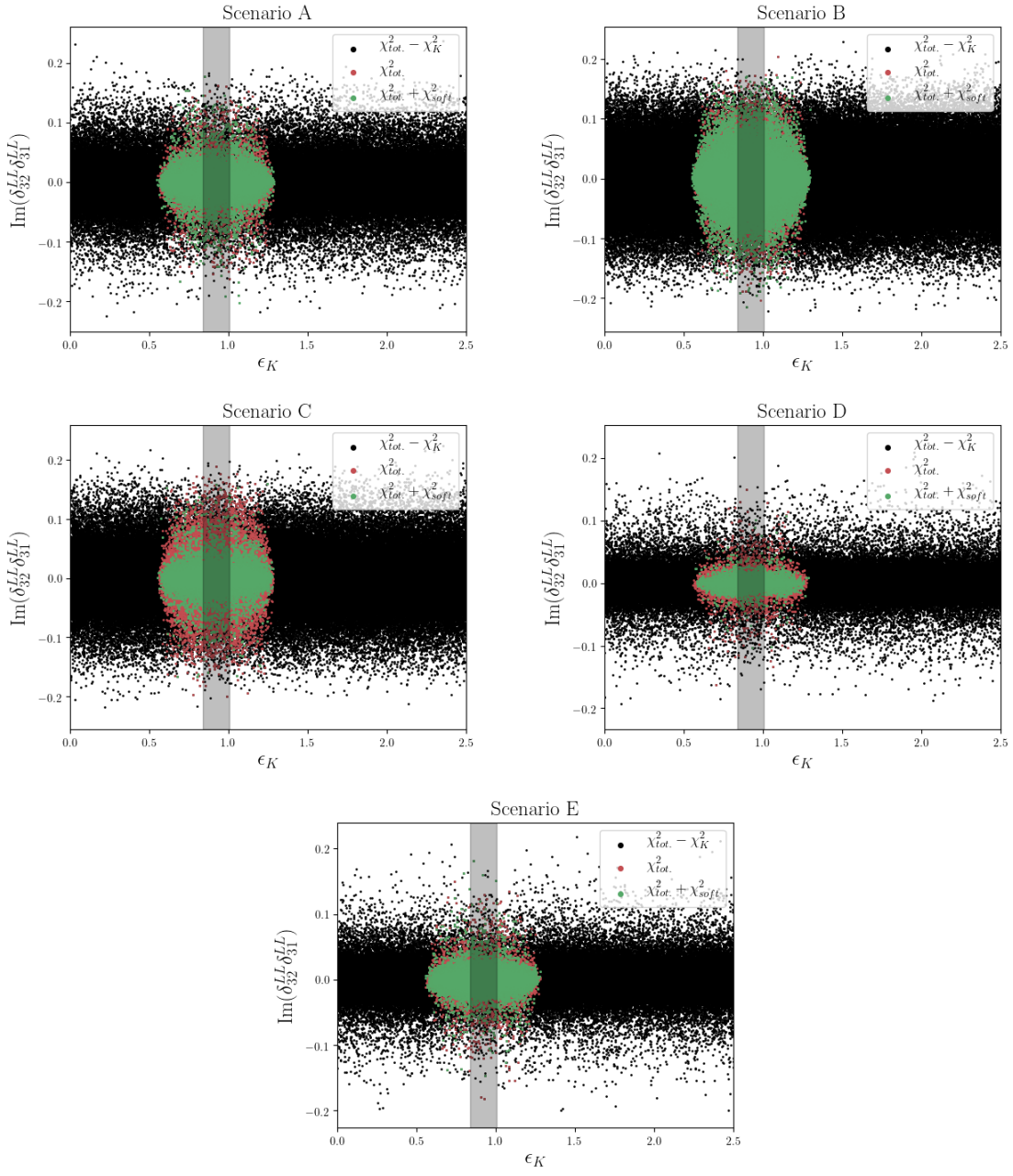

FIGURE 6.9: $|\epsilon_K|^{EXP/SM}$ vs Im $\left[(\delta^d_{LL})_{13}(\delta^d_{LL})_{23}\right]$ for scenarios A (upper left), B (upper right), C (middle left), D (middle right) and E (bottom). Black points show the 95% CL when all the constraints except for $|\epsilon_K|$ are included. Red points indicate the points that fulfill all the constraints at 95% of CL. Green points indicate the red points that give a correct mass spectrum according to the SOFTSUSY software [103]. The constraints on $\Delta\phi^{NP}_{s,d}$ incorporate penguin pollution estimation based on SU(3) symmetry [61].

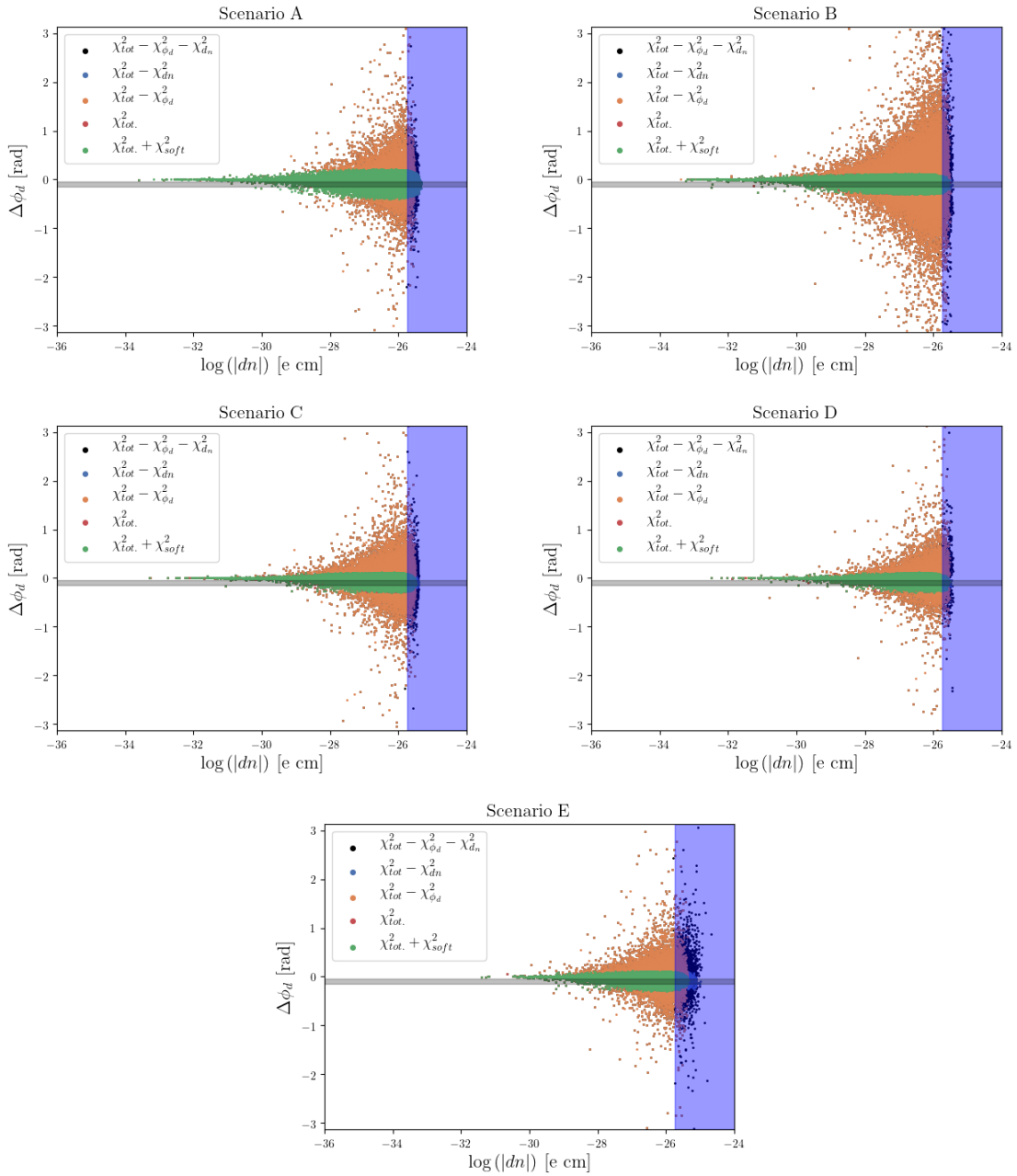

FIGURE 6.10: $\log d_n$ vs $\Delta\phi_d^{NP}$ for scenarios A (upper left), B (upper right), C (middle left), D (middle right), and E (bottom). Black points show the 95% CL when all the constraints except for d_n^{EXP} and $\Delta\phi_d$ are included. Blue (orange) points show the 95 % of CL when all the constraints excluding d_n ($\Delta\phi_d$) are included. Red points indicate the points that fulfill all the constraints at 95% of CL. Green points indicate the red points that give a correct mass spectrum according to the SOFTSUSY software [103]. The constraints on $\Delta\phi_{s,d}^{NP}$ incorporate penguin pollution estimation based on SU(3) symmetry [61].

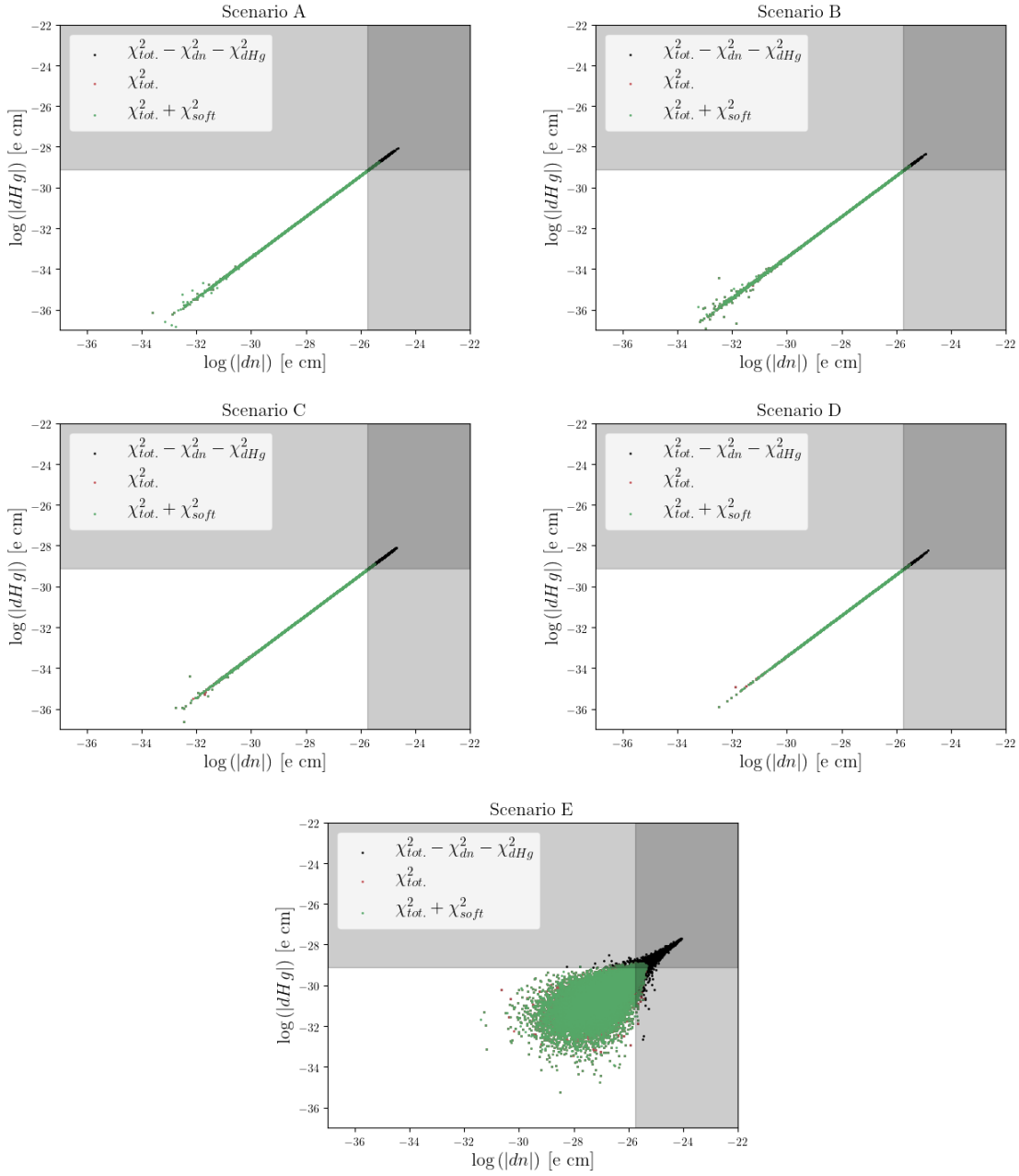

FIGURE 6.11: $\log d_n$ vs $\log d_{Hg}$ for scenarios A (upper left), B (upper right), C (middle left), D (middle right), and E (bottom). Black points show the 95% CL when all the constraints except for d_n^{EXP} and $d_{H_g}^{EXP}$ are included. Red points indicate the points that fulfill all the constraints at 95% of CL. Green points indicate the red points that give a correct mass spectrum according to the SOFTSUSY software [103]. The constraints on $\Delta\phi_{s,d}^{NP}$ incorporate penguin pollution estimation based on SU(3) symmetry [61].

Finally, Fig. 6.12 displays the points in the (C_7,C_9) plane that satisfy the experimental constraints. As observed, due to the high SUSY scale, and setting the MIs ^{LR} to zero, the contributions to these observables are found to be small. Therefore, in the scenarios studied in this work, the lepton flavor universal contributions to C_9 are insufficient to explain $b \to sll$ data [19].

6.4 Conclusions

In §6.2, the status of a benchmark GUT SUSY model, the cMSSM was studied. In these types of models, the importance of flavor is generally small for two reasons: First, the model is flavor universal at the GUT scale, precisely to avoid problems with CPV and FCNC observables. Second, the RG contributions to the off-diagonal mass terms are supposed to be negligible. Both effects make $\mathcal{B}(B_s^0 \to \mu\mu)$ the most important observable in the flavor sector. An important point is that even with just five degrees of freedom, the cMSSM can still explain the measured Dark Matter relic density though the freeze-out of the neutralino[9]. Additionally, potential contributions within the cMSSM to the anomalous magnetic moment of the muon are investigated and found to be negligible. Within the cMSSM, the tension between the experimental value of Ref. [34] and the traditional SM prediction of Ref [36] cannot be explained. However, as explained in this thesis, the situation might change due to tension between the SM prediction of Ref. [36] and lattice estimations of Ref. [35].

The flavor implications of non-zero mass insertions in $3 \to 1$ ($\delta_{31} \neq 0$) and $3 \to 2$ transitions ($\delta_{32} \neq 0$) were investigated in §6.3. Specifically, potential SUSY contributions to $\Delta F = 2$, $\Delta F = 1$, and $\Delta F = 0$ processes were explored. The conclusions drawn from this study are highly relevant for several reasons. Firstly, it was observed that points satisfying experimental constraints can generally be found across the entire range studied in all scenarios. This suggests that the traditional approach of neglecting flavor violation contributions to avoid experimental restrictions may not always be justified. Additionally, a noteworthy finding of this study is the critical importance of the constraints placed on the Kaon system, even in the designed scenarios of Table 6.5 where the primary contributions (direct $2 \to 1$ transitions) are neglected. This finding motivates future experiments dedicated to the study of strangeness. Finally, it was found that the lepton flavor universal contributions to C_9 present in the models studied in Table 6.5 are not enough to explain $b \to sll$ data, according to Ref. [19]. This study introduces a tool extending beyond the application of SUSY models, providing a method for conducting GPU scans applicable to other NP models with a large number of degrees of freedom.

[9] An update of this result is needed with the latest direct dark matter searches: `PandaX-4T` [165], `LZ` [166], `XENONnT` [167], which were not available at the time of completing this project.

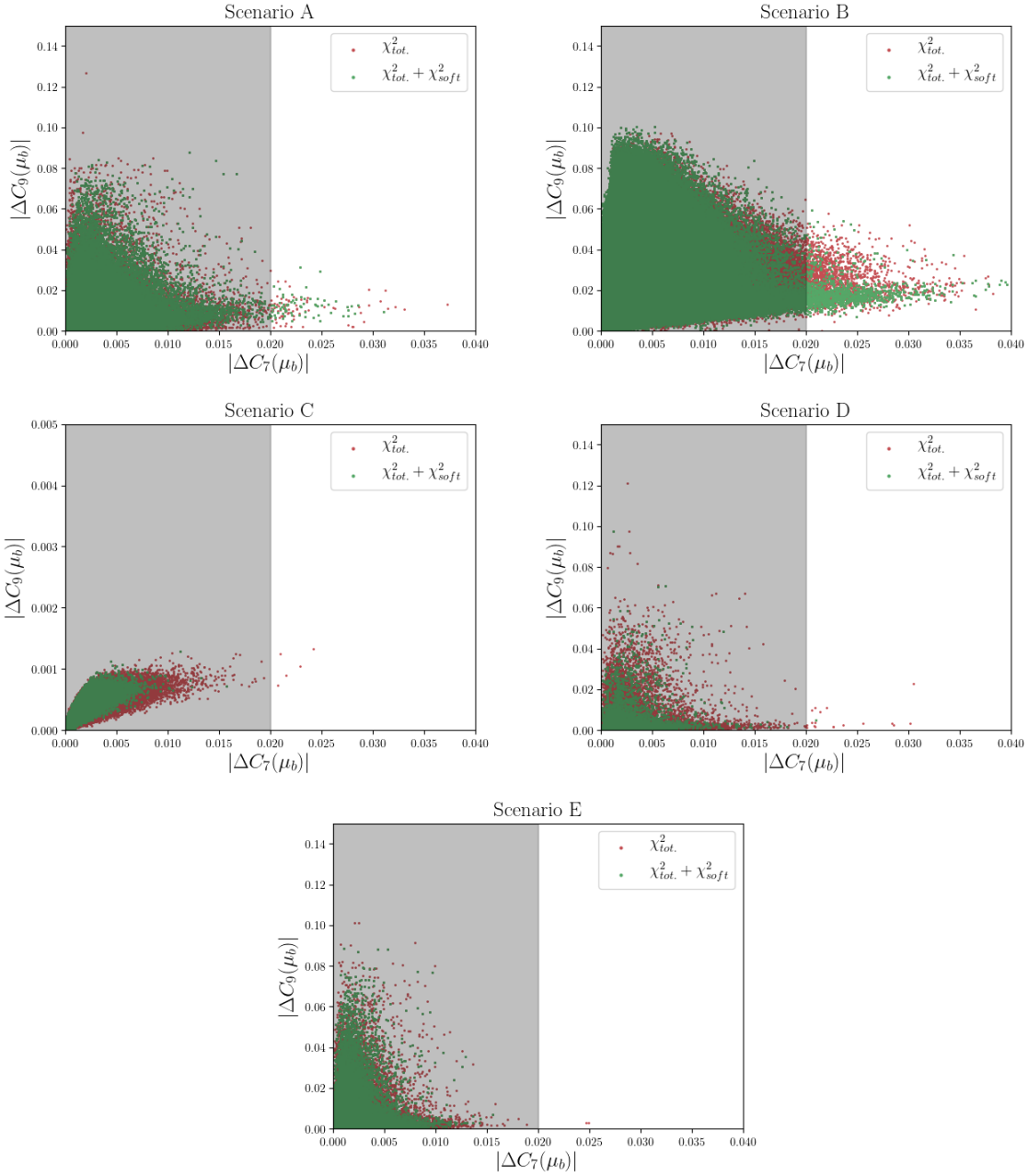

FIGURE 6.12: C_7 vs C_9 for scenarios A (upper left), B (upper right), C (middle left), D (middle right), and E (bottom). Red points indicate the points that fulfill all the constraints at 95% of CL. Green points indicate the red points that give a correct mass spectrum according to the SOFTSUSY software [103]. The constraints on $\Delta\phi^{NP}_{s,d}$ incorporate penguin pollution estimation based on SU(3) symmetry [61].

Chapter 7

Results and conclusions

The world's best measurement of $\phi_s^{c\bar{c}s}$ was presented in Chapter 4 through a flavor-tagged decay-time and angular analysis of background subtracted $B_s^0 \to J/\psi KK$ decays using the Run 2 data collected by the LHCb experiment during the period 2015-2018. Also, the CPV parameter $|\lambda|$ and the decay width differences of the B_s^0 system were measured with the world's best accuracy. The results are found to be:

$$\begin{aligned} \phi_s^{c\bar{c}s} &= -39 \pm 22 \pm 6 \text{ mrad}, \\ \Delta\Gamma_s &= 0.0845 \pm 0.0044 \pm 0.0024 \text{ ps}^{-1}, \\ \Delta\Gamma_d^s &= -0.0056^{+0.0013}_{-0.0015} 0.0014 \text{ ps}^{-1}, \\ |\lambda| &= 1.001 \pm 0.0011 \pm 0.0005, \end{aligned} \tag{7.1}$$

which show no evidence of CP violation (CPV), neither direct CPV nor CPV in the interference between decay and mixing. No dependence on the polarization state was observed for the CP violation parameters. The results are consistent with SM predictions and with previous LHCb measurements. This corresponds to an important step further in the constraining of NP contributions in the B_s^0 system.

In Chapter 5, advancements in the experimental technique for inferring the B mesons flavor at the production stage were reported, concretely in the implementation of the inclusive approach using a DeepSet architecture. Relative improvements of 22% and 37% were observed for the calibration channels $B_s^0 \to D_s^- \pi^+$ and $B^0 \to J/\psi K^{*0}$, respectively. The preliminary sensitivity study for the CPV parameter $\phi_s^{c\bar{c}s}$ suggests a possible change in the training mode for obtaining more inclusive results. Specifically, the potential training mode of $B_s^0 \to J/\psi\phi$ was studied, yielding a relative improvement of 19% in the sensitivity to the $\phi_s^{c\bar{c}s}$ observable compared to the classical combination reported in Chapter 4. This result enlightens the FT possibilities for future measurements of CPV observables in the LHCb.

Finally, in Chapter 6 the phenomenological consequences of this type of precision measurement were studied in SUSY theories. The first part of Chapter 6 was dedicated to the study of a simplified GUT benchmark model, the cMSSM, where flavor phenomenology is restricted by construction. The results yield, that cMSSM can explain DM through the freeze out of the neutralino, however, it cannot explain the longstanding anomaly in $(g-2)_\mu$ observable, as the contributions from SUSY particles in this model are found to be negligible. The last part of Chapter 6 was dedicated to the proof of concept of studying all the flavor phenomenology present within the full MSSM by using GPUs. Specifically, the case of FV in B decays was examined in detail, evaluating the implications of the latest flavor precision measurements in $\Delta F = 0, 1, 2$ transitions. It was shown, that points respecting the experimental constraints can be found in the overall range of the input space studied. Additionally, kaon constraints play an important role in constraining NP even if the model is chosen to have a major impact on the B system. In the models studied lepton flavor universal contributions to C_9 are not enough to explain $b \to sll$ data. Last but not least, it is noteworthy to understand that the development of this GPU framework goes beyond the applications to SUSY models and could have a beneficial impact on other NP models with a large number of degrees of freedom.

Chapter 8

Resumo

8.1 Introducción

O SM considérase polo momento a mellor descrición a escalas enerxéticas grandes (ou o que é o mesmo a máis pequenas escalas de lonxitude) das partículas fundamentais e de tres das catro interaccións consideradas fundamentais, a interacción forte, a electromagnética e a feble (o SM non ofrece unha descrición cuántica da gravidade). O SM é unha teoría cuántica de campos no que se distinguen dous tipos de partículas elementais en función do seu spin, por un lado están os fermións con spin semienteiro que conforma os bloques fundamentais da materia e por outro lado os bosón, que son os mediadores das interaccións e están caracterizados por ter un spin enteiro. Do mesmo xeito, os fermións clasifícanse en quarks e leptons, os primeiros sofren a interacción forte o que os mantén confinados en mesóns e barións e os segundos non, e polo tanto, poden existir libremente na natureza. Finalmente, ambos leptóns e quarks agrúpanse en tres xeracións, onde a primeira é a que conforma toda a materia que observamos na natureza. A xeración dúas e tres parece consistir simplemente en copias máis masivas (e por tanto inestables) da primeira xeración, e polo tanto a única diferencia entre xeracións consiste na interacción destas co campo de Higgs. Isto é o que se coñece como problema do sabor, xa que considérase que o SM dá unha descrición insatisfactoria da presenza destas distintas xeracións.

Unha curiosidade da interacción feble, é que os estados propios de sabor dos quarks (interacción coa forza feble) non son os mesmos que os estados propios de masa (cos que o quark se propaga no espazo tempo). Este fenómeno da lugar a matriz CKM que relaciona ambos estados propios. Esta matriz pódese parametrizar con tres números reais e unha fase complexa, sendo esta última o único parámetro observado que viola a simetría CP no SM. Este feito é fundamental posto que a violación CP é unha das condicións necesarias para entender o universo que observamos actualmente, no que a materia domina sobre a antimateria. A matriz CKM é case a matriz identidade, onde as transicións máis probables son aquelas entre a mesma xeración, mostrando unha estrutura xerárquica para o resto. Dun axuste global aos

datos, excluíndo observables con potenciais contribucións de nova física (NP) pesada, obtense:

$$V_{CKM} = \begin{pmatrix} 0.97461 & 0.22386 & 0.00167-0.00384i \\ -0.22373-0.00017i & 0.97374 & 0.042160 \\ 0.00780-0.00374i & -0.04147-0.00086i & 0.99910 \end{pmatrix}.$$

A pesar do seu éxito experimental o SM non explica fenómenos observados na natureza como poden ser a materia escura e a asimetría observada entre materia é antimateria. Este último fenómeno e debido a que a violación CP presente na matriz CKM que comentabamos antes non é suficiente para explicar esta asimetría. Polo tanto, estamos convencidos que o SM debe ser unha teoría efectiva as escalas enerxéticas que observamos no experimento pero non pode ser o modelo definitivo. Unha das maneiras de buscar esta nova física, é a través das procuras indirectas, que consiste en facer medidas de precisión de observables e comparalos coas predicións teóricas do SM. As potencias novas partículas poden entrar en correccións cuánticas a estes observables modificando así o seu valor observado no experimento. Durante esta tese, centrarémonos neste modo de buscar nova física, posto que ten a vantaxe de non ser necesario producir directamente a partícula de NP, e polo tanto non está restrinxida a potencial enerxía á cal se traballa no acelerador.

8.2 Experimento LHCb

O LHC é o acelerador de partículas máis grande do mundo, está localizado no CERN e consiste nun anel circular de 27 km de lonxitude. Os feixes de partículas fanse colidir en catro puntos correspondentes aos catro detectores máis grandes ATLAS, CMS, ALICE e o LHCb. Este último é do que se extraerán os datos analizados nesta tese.

O LHCb é un detector dun só brazo situado na rexión cara adiante con respecto ao punto de colisión. A súa particular forma é debido a que os mesóns B, as partículas que se estudan principalmente neste detector, prodúcense preto do feixe. O detector LHCb cobre a zona de aceptancia angular entre 15 e 300 (250) mrad no plano perpendicular (paralelo) ao campo magnético. O LHCb conta cos seguintes detectores:

- Imán: Curva as partículas cargadas, permitindo así a posterior medida do seu momento.
- Sistema de trazado: Mide as traxectorias das partículas cargadas. Está formado polo VELO, que distingue o punto onde se produciu o mesón B (vértice primario) e onde decaeu (vértice secundario). O TT, situado antes do imán e, finalmente, tres detectores de trazas (T1,T2,T3) situadas despois do imán.

- Sistema de identificación de partículas: Detectores que identifican as partículas que produciu a traxectoria medida polo sistema de trazado. Está formado por dous RICH, que distinguen partículas en función do efecto Cherenkov producido, o ECAL, utilizado principalmente para detectar electróns e fotóns, o HCAL, empregado para detectar hadróns e, finalmente, as cámaras de muóns situadas ao final do detector e utilizadas para detectar muóns.

A cantidade de datos producida no detector non se pode gardar debido aos límites de computación e de almacenamento. O sistema do trigger, formado polo L0 e o HLT, selecciona eventos con sinaturas particulares de desintegracións de mesóns B, limitando a cantidade de ruído ao tempo que maximiza a cantidade de sinal presente nos datos.

8.3 A mellor medida do mundo da fase feble $\phi_s^{c\bar{c}s}$

Nesta sección resumimos a medida do fase cuántica $\phi_s^{c\bar{c}s}$, utilizando os datos recollidos polo detector LHCb durante os anos 2015-2018 de decaementos do tipo $B_s^0 \to J/\psi KK$. Esta fase cuántica, está directamente relacionada coa fase presente na matriz CKM e polo tanto, a súa medida de precisión conforma un importante test da viabilidade do SM, que como xa dixemos non é capaz de explicar a asimetría observada no universo entre materia e antimateria. Esta fase xurde da interferencia entre o decaemento e o decaemento a través da mestura $B_s^0 - \bar{B}_s^0$. Ademais, da medida de $\phi_s^{c\bar{c}s}$, a análise desta canle de desintegración permite a medición coa mellor precisión do mundo doutros parámetros físicos do mesón B_s^0, como a diferenza de anchura de desintegración entre os estados propios de masa do mesón B_s^0, $\Delta\Gamma_s$, a anchura de desintegración Γ_s e o parámetro $|\lambda|$, relacionado coa violación CP no decaemento (violación CP directa).

A fase feble $\phi_s^{c\bar{c}s}$, é unha cantidade que se pode extraer por axustes globais aos datos, ignorando contribucións de ordes maiores no SM: $\phi_s^{c\bar{c}s} \approx -2\beta_s = 36.8^{+0.9}_{-0.6}$ mrad. Polo tanto, este observable é moi pequeno e ademais coñecese con moita precisión resultando nun test perfecto para a viabilidade do SM.

Esta fase é medida utilizando decaementos do tipo $B_s^0 \to J/\psi KK$. Para levala a cabo, é necesario unha análise do tempo de decaemento (para distinguir a oscilación de sabor do mesón B_s^0) e angular (co obxectivo de poder diferenciar a mestura de estados propios CP do estado final). A análise realizase en 6 rexións do espectro de masas KK, para ter en conta distinta contribucións da onda S presentes en cada rexión.

Unha vez recollidos os datos, cómpre seleccionalos, isto é debido a que nos datos recollidos hai moito ruído, é dicir datos recollidos que non son en realidade decaementos do tipo $B_s^0 \to J/\psi KK$. En primeiro lugar, os datos fanse pasar a través dunha

BDT, que ten como obxectivo suprimir o máximo posíbel o ruído combinatorio. Posteriormente fanse uns VETOs, isto é un conxunto de cortes en distintas hipóteses de masa e na probabilidade da hipótese de masa, co obxectivo de vetar ruídos producidos por canles similares á estudada onde un dos estados finais foi confundido con outra partícula (por exemplo confundir un pión cun kaón). Posteriormente úsase o técnica sPlot, que a través dun axuste a masa invariante reconstruída do mesón B_s^0 permite subtraer estatisticamente o ruído. Cabe resaltar que en todos estes pasos, é moi importante a información extraída das simulacións, polo tanto realízanse distintas correccións a estas últimas co obxectivo de mellorar a eficiencia do proceso de selección.

Antes de realizar a medida final, temos que corrixir certos efectos experimentais, producidos polo propio detector e polo proceso de selección. Para iso empregamos datos reais e simulacións. A resolución temporal, consiste nun error na estimación do tempo de desintegración por evento, esta calibrase en mesóns J/ψ que proveñen do vértice primario. A eficiencia temporal, consiste nunha eficiencia non uniforme co tempo de desintegración do mesón B_s^0. Este fenómeno é producido polo trigger e por cortes de selección, e corríxese usando datos reais do decaemento $B^0 \to J/\psi K^*$. A eficiencia angular é similar a temporal, pero nos ángulos de helicidade, onde a corrección obtense utilizando datos simulados. A distinta contribución de onda S presente no espectro de masas do dikaon é tida en conta polo uso dos factores C_{SP}, que consisten en correccións a interferencia de ondas P é S en cada un dos rexións do espectro KK nas que se realiza a análise. Finalmente, a identificación do mesón B_s^0 que se produciu na colisión de protóns utiliza as técnicas de marcado de sabor. Estas técnicas consisten en redes neuronais que asignan unha decisión así como unha probabilidade de que esta decisión séa errada a cada evento. O produto de estas redes neuronais é calibrado utilizando decaementos de sabor específico como $B^+ \to J/\psi K^+$ e $B_s^0 \to D_s^- \pi^+$.

Unha vez obtemos todas as correccións experimentais, as medidas dos parámetros físicos obtense por un axuste de máxima verosimilitude aos datos co ruído estatisticamente subtraído. Diversas comprobacións destes resultados realízanse en subconxuntos dos datos, observando unha concordancia óptima. Ademais estúdanse diversas fontes de incerteza sistemática. O resultado final é:

$$\begin{aligned}
\phi_s^{c\bar{c}s} &= -39 \pm 22 \pm 6 \text{ mrad}, \\
\Delta\Gamma_s &= 0.0845 \pm 0.0044 \pm 0.0024 \text{ ps}^{-1}, \\
\Delta\Gamma_d^s &= -0.0056^{+0.0013}_{-0.0015} 0.0014 \text{ , ps}^{-1} \\
|\lambda| &= 1.001 \pm 0.0011 \pm 0.0005,
\end{aligned}$$

sendo a primeira incerteza estatística e a segunda sistemática. Os resultados son consistentes con previas medidas deste observable. Non se encontra evidencia de

violación CP, nin de violación CP directa ($|\lambda|$ compatible con 1) nin na interferencia ($\phi_s^{c\bar{c}s}$ compatible con 0). Os resultados son consistentes con axustes globais asumindo a estrutura do SM. Nestes resultados asúmese que os parámetros de violación CP, son independentes da polarización dos estados finais. Relaxando esta condición, non se observa ningunha dependencia entre o estado de polarización final e os parámetros físicos de violación CP.

8.4 Melloras nas técnicas de etiquetado de sabor

As medidas da oscilación de sabor dos mesóns B e o estudo de asimetrías CP dependentes do tempo require coñecer o sabor do mesón B que se produciu despois da colisión de protóns. Este paso conséguese a través de distintas redes neuronais, que utilizan a información de diversas trazas de partículas producidas ao redor dos mesóns B. Este paso é moi importante posto que a estatística efectiva para medir estes observables dependen criticamente do correcto funcionamento destes algoritmos. Concretamente, a cantidade do poder de etiquetado (ϵ_{eff}) sintetiza a información da porcentaxe de estatística que é realmente efectiva, e no LHCb, é xeralmente menor do 7%, utilizando as técnicas convencionais.

Nesta tese estudamos o chamado enfoque inclusivo, que consiste en unicamente ter unha rede neuronal que use toda a información do evento, para identificar o sabor do mesón que se produciu. Os mesóns B, xeralmente prodúcense en pares, un deles correspondese co mesón de sinal e o outro o denominamos como mesón B do outro lado (OS B).

Para simplificar o problema que a rede neuronal ten que resolver, utilizamos unha BDT previa que asigna unha probabilidade a cada traza do evento de ser SS (producida co mesón sinal), OSD (producido no decaemento do OS B), OSF (producido na produción do OS B) ou ruído. Para a aprendizaxe da rede neuronal úsanse simulacións e explótase distinta tipo de información entre a que destaca, a probabilidade de identificación de ser unha partícula ou outra, variables cinemáticas, a carga da traza ou variables relacionadas co "illamento" da traza.

Posteriormente, é necesario calibrar a saída destes algoritmos para estar seguro que correspondese cunha probabilidade estatística. Para levalo a cabo, é necesario un axuste de máxima verosimilitude ao tempo de desintegración de decaementos reais $B_s^0 \to D_s^- \pi^+$ e $B^0 \to J/\psi K^*$. Para iso é necesario a corrección de efectos experimentais que inclúen a resolución temporal e a eficiencia temporal así como a subtracción estatística do ruído na mostra de sinal. Posteriormente estímase o poder de etiquetado nas mostras de datos reais observando unha mellora relativa do 22% e 37% en $B_s^0 \to D_s^- \pi^+$ e $B^0 \to J/\psi K^*$, respectivamente.

Realízanse diversos estudos dos resultados obtidos. Un destes estudos analiza o impacto de eliminar da rede neuronal principal trazas que moi probablemente son

ruído, onde aparentemente non se acada ningunha mellora. Ademais estúdase a dependencia do poder de etiquetado con variables cinemáticas e propiedades do evento, onde obsérvanse tendencias similares as obtidas cos algoritmos clásicos.

Finalmente realizase un estudo de sensibilidade do observable $\phi_s^{c\bar{c}s}$ usando esta nova técnica. O estudo utiliza primeiramente a rede neuronal que usou para a súa aprendizaxe $B_s^0 \to D_s^- \pi^+$, con todo observase que os resultados son similares aos obtidos usando técnicas clásicas. O estudo suxire de que $B_s^0 \to D_s^- \pi^+$, pode non ser unha canle suficientemente inclusiva (debido a un trigger restritivo) para aplicarse a outros modos de desintegración. Para comprobar esta hipótese, realízase unha nova rede neuronal que realiza a aprendizaxe en decaementos $B_s^0 \to J/\psi\phi$ simulados. Os resultados obtidos usando este cambio amosan un 19% de mellora relativa con respecto as tácticas clásicas, mantendo a mellora relativa na canle $B_s^0 \to D_s^- \pi^+$. Esta comprobación é moi sólida posto que implica cos resultados da rede neuronal usando $B_s^0 \to J/\psi\phi$ si que son suficientemente inclusivos para observar a mesma mellora en decaementos do tipo $B_s^0 \to D_s^- \pi^+$ validando a nosa hipótese.

8.5 Estudo fenomenolóxica de modelos super simétricos

Unha das teorías de nova física mais estudada debido a cantidade de problemas do SM que resolve son os modelos súper simétricos (SUSY), entre estes encóntranse un candidato para explicar a materia escura (DM), e numerosas fontes de violación CP que poden aliviar ou incluso explicar a asimetría observada entre materia e antimateria. Estas teorías pódense entender como xeneralizacións das simetrías do espazotempo, mantendo invariante as transformacións bosón-fermión e viceversa. Estas teorías predín moitas partículas novas a lo menos unha compañeira súper simétrica por cada partícula do SM.

Sen embargo, a súper simetría tamén predí que as masas das partículas súper simétricas teñen que ser iguas cas da súas respectivas compañeiras presentes no SM. Isto é imposíbel tendo en conta a evidencia experimental, por tanto SUSY de existir ten que estar rota. Posto que non se coñece o mecanismo particular de ruptura desta simetría, o enfoque tradicional usa todos os termos posibles que violan SUSY pero que non producen termos cuadráticos na masa do bosón de Higgs, isto coñécese como ruptura suave. O problema é que este enfoque provoca que o modelo teña 105 parámetros libres, o cal reduce o poder de predición do modelo, ademais de provocar que sexa unha teoría difícil (senón imposible) de estudar.

O candidato a materia escura estudado durante esta tese e o neutralino, que é un estado de masa resultado da mestura dos gauginos (compañeiros SUSY dos bosóns gauge no SM). O mecanismo que explica a densidade de materia escura observada na actualizade coñecese como "conxelación" do neutralino, e normalmente require a

presenza dunha nova simetría denominada paridade R (para que a partícula súper simétrica mais lixeira (LSP) sexa estable).

O primeiro modelo estuda e o denominado como MSSM restrinxido (cMSSM), e conta con unicamente 5 parámetros libres (en lugar de 105). Isto é o que denominamos enfoque clásico, como debido aos límites de computación é moi difícil estudar unha teoría con 105 parámetros libres, fanse simplificacións e suposicións para intentar reducir o número de entradas requiridas, aquí é onde aparece o cMSSM, que un dos modelos SUSY máis estudados (senón o que máis). Para estudalo, usase a ferramenta de MasterCode. Esta ferramenta permite facer análises frecuentistas para realizar axustes globais. Consiste nun algoritmo de exploración, Multinest [102] e nun conxunto de programas que calculan os observables de baixa enerxía. No axuste, inclúense medidas experimentais de moi diversa índole, observables relacionadas co bosón de Higgs, restricións de medidas relacionadas coa materia escura, restricións de buscas directas (realizadas principalmente en ATLAS e CMS), observables de precisión da interacción feble e restricións de medidas de precisión no sector do sabor. Estas últimas non son moi importantes debido a que estas teorías son universais dende o punto de vista do sabor, para reducir o número de parámetros libres da teoría, e ser dende un punto de vista fenomenolóxico máis doadas de estudar.

Os resultados do estudo do modelo cMSSM, amosan que esta teoría pode explicar a densidade de materia escura con soamente 5 parámetros libres. Outro punto interesante desta teoría e que contribúe ao observábel do momento anómalo magnético do muón. Este observable, e considerada unha anomalía posto que o valor medido experimentalmente non coincide co predito polo SM. Sen embargo as contribucións no contexto do cMSSM a este observable son insignificantes e non poden explicar a tensión entre o experimento e a predición teórica.

Posteriormente un modelo con toda a fenomenoloxía de sabor é estudado no contexto da aproximación das insercións de masa (MIA). Esta aproximación é en xeral valida cando as contribucións de violación de sabor son pequenas con respecto as universais. Concretamente estudamos un modelo, activando as transicións de xeración $3 \rightarrow 1$ e $3 \rightarrow 2$. Para levar a cabo este proxecto, créase un marco de traballo baseado en exploracións que usan tarxetas gráficas (GPU). Esta tecnoloxía permítenos incrementar o número de parámetros libres estudados da teoría, polo seu alto poder de paralización, resultando en exploracións de moitas dimensión nun tempo de computación razoable. Como restricións experimentais, calcúlanse as contribucións do MSSM a observables de precisión (como $\phi_s^{c\bar{c}s}$) relacionadas con transicións de sabor.

Os resultados obtidos no estudo de contribucións de violación de sabor as transicións $3 \rightarrow 1$ e $3 \rightarrow 2$ no contexto do MSSM son moi relevantes. En primeiro lugar, comprobouse que, en xeral, se pode atopar puntos que satisfagan as restricións experimentais para o rango global estudado en todos os escenarios. Isto implica,

que o enfoque clásico de supoñer que certos termos deber ser insignificantes para satisfacer o observado experimentalmente pode non ser apropiado, posto que cancelacións no cálculo final dos observables poden producirse. En segundo lugar, é interesante que as restricións impostas no sector dos kaóns son moi relevantes para este estudo, posto que os escenarios designados tiñan como obxectivo precisamente que as contribucións principais a este sector foran nulas (transicións $2 \to 1$ non permitidas). Este resultado mostra a importancia dos observables no sector dos kaóns para as restricións en construcións de teorías de NP. Finalmente, comprobouse que as contribucións de sabor universais do sabor leptónico presentes nestes modelos non son suficientes para explicar os datos observados experimentalmente nos datos de transicións $b \to sll$.

8.6 Conclusions

Nesta tese presentase a mellor medida do mundo da fase feble relacionada coa violación CP, $\phi_s^{c\bar{c}s}$. Os resultados non amosan observación de violación CP e son consistentes coas predicións de axustes globais asumindo SM. Esta medida corresponde a unha importante mellora na restrición de nova física no mesón B_s^0. Seguidamente, preséntanse tamén futuras melloras nos algoritmos de etiquetado de sabor a través do estudo do denominado enfoque inclusivo. Os resultados amosan melloras relativas do 22% e 37% nos canais en $B_s^0 \to D_s^- \pi^+$ e $B^0 \to J/\psi K^*$, respectivamente. Estes resultados amosan unha importante potencial mellora en futuras medidas de observables de violación CP no LHCb. Finalmente, estudamos as consecuencias fenomenolóxicas para modelos súper simétricos deste tipo de medidas de precisión no sector do sabor utilizando dous enfoques. Por un lado o clásico estudando o cMSSM coa ferramenta MasterCode. Este modelo é capaz de explicar a materia escura, sen embargo as contribucións ao momento anómalo magnético do muón non son suficientes para aliviar a tensión entre experimento e predición teórica. Por outro lado, na última parte da tese a posibilidade estudar teorías con máis grados de liberdade facendo uso de GPUs foi amosada para o caso particular de violación de sabor en transicións $3 \to 1$ e $3 \to 2$. Estes resultados van mais alá do modelo en si posto que pode ser unha ferramenta moi interesante para estudar outros modelos de nova física que presentan un elevado número de parámetros libres.

Appendix A

Inputs used for SM predictions

TABLE A.1: Inputs used for obtaining SM predictions.

Parameter	Value	Reference
V_{ud}	0.97373 ± 0.00031	[33]
V_{us}	0.2231 ± 0.0006 ($\mathcal{K}l3$)	[33]
V_{cb}	$(42.16 \pm 0.51) \times 10^{-3}$	[168]
V_{ub}	$(4.19 \pm 0.17) \times 10^{-3}$	[1]
γ	1.159 ± 0.063 rad (without $-2\beta_s$)	[1]
f_{B_s}	0.2303 ± 0.0013 GeV	[169]
f_{B_s}/f_{B^0}	1.207 ± 0.0035	[169]
f_{B^+}	0.1894 ± 0.0014 GeV	[169]
$\hat{\eta}_B$	0.8393 ± 0.0034	[170]
$B_1^s(\mu_b)$	0.849 ± 0.023	[159]
$B_1^s(\mu_b)$	0.835 ± 0.028	[159]
r_{fk}	1.1932 ± 0.0021	[169]
r_{Kl2}	0.9930 ± 0.0035	[171]
G_F	$1.1663786(6) \times 10^{-12}\text{GeV}^{-2}$	[33]
$\alpha_s(M_Z)$	0.1179 ± 0.0016	[33]
m_{B_s}	5.36688 ± 0.00014 GeV	[33]
m_{B_d}	5.27965 ± 0.00012 GeV	[33]
m_τ	1.77686 ± 0.00012 GeV	[33]
m_{Bu}	5.27934 ± 0.00012 GeV	[33]
τ_H^s	$(1.624 \pm 0.009) \times 10^{-12}$ s	[1]
τ^d	$(1.519 \pm 0.004) \times 10^{-12}$ s	[1]
τ^u	$(1.638 \pm 0.004) \times 10^{-12}$ s	[1]
$m(K^\pm)$	493.677 ± 0.016 MeV	[33]
τ_K	$(12380 \pm 20) \times 10^{-12}$ s	[33]
$m(\pi)$	139.57039 ± 0.00018 MeV	[33]
τ_π	$(26033 \pm 5) \times 10^{-12}$ s	[33]
$\mathcal{B}(\pi \to \mu\nu)$	0.9998770 ± 0.0000004	[33]
m_W	(80.377 ± 0.012) GeV	[33]
$m_t(m_t)$	(162.9 ± 0.33) GeV	[33]
$m_c(m_c)$	(1.275 ± 0.005) GeV	[169]
η_{tt}	0.5765 ± 0.0065	[172]
η_{ct}	0.496 ± 0.047	[173]
η_{cc}	1.72 ± 0.27	[174]

Appendix B

Simulation samples used in $\phi_S^{c\bar{c}s}$ measurement

During the analysis of $B_s^0 \to J/\psi K^+K^-$ decays, several simulation samples are used for different analysis parts. For the decay time acceptance correction, simulation samples of $B^0 \to J/\psi K^*$ decays (control sample) and a special MC of $B_s^0 \to J/\psi\phi$ simulated with the physics parameter $\Delta\Gamma$ set to 0 (decay time and angular distribution factorize) are used. For the angular efficiency estimation, both $B_s^0 \to J/\psi\phi$ simulation samples are used, one with $\Delta\Gamma \neq 0$ and the one used for the decay time acceptance correction with $\Delta\Gamma = 0$. To get the C_{SP} factors a simulation sample that includes S-wave contribution (f_0) is used. Additionally, prompt $J/\psi \to \mu^+\mu^-$ simulation sample is used for studying the decay time resolution and $B^+ \to J/\psi K^+$ and $B_s^0 \to D_s^-\pi^+$ simulation candidates are used for studying the flavor tagging. Finally, a simulation sample of $\Lambda_b^0 \to J/\psi pK$ is used for analyzing the peaking background and the potential pollution in the mass window of the analysis and a simulation of $B_c^+ \to B_s^0(\to J/\psi\phi)\pi^+$ is used for assessing the bias introduced in the lifetime parameters by potential B_c^+ decays polluting the data sample. The physics parameters used in the signal and control simulation samples are summarized in Table B.1 and Table B.2, respectively.

TABLE B.1: Decay model parameters used for generating $B_s^0 \to J/\psi KK$ simulation samples.

Parameter	$B_s^0 \to J/\psi\phi$	$B_s^0 \to J/\psi\phi$ ($\Delta\Gamma = 0$)	$B_s^0 \to J/\psi KK$ (S-wave + P-wave)
Δm_s [ps^{-1}]	17.8	17.8	17.8
$\Delta\Gamma_s$ [ps^{-1}]	0.08543	0	0.08543
Γ_s [ps^{-1}]	0.6614	0.6614	0.6614
$\phi_s^{c\bar{c}s}$ [rad]	-0.03	-0.03	-0.03
$\lvert A_0(0)\rvert^2$	0.5242	0.5242	0.5242
$\lvert A_\parallel(0)\rvert^2$	0.2256	0.2256	0.2256
$\lvert A_\perp(0)\rvert^2$	0.2500	0.2500	0.2500
$\lvert A_S(0)\rvert^2$	-	-	0.07
$\delta_\parallel - \delta_0$ [rad]	3.26	3.26	3.26
$\delta_S - \delta_0$[rad]	-	-	3.315
$\delta_\perp - \delta_0$ [rad]	3.08	3.08	3.08
$\delta_S - \delta_0$ [rad]	-	-	3.315

TABLE B.2: Decay model parameters for $B^0 \to J/\psi K^*$ simulation samples.

Parameter	$B^0 \to J/\psi K^*$
$\lvert A_0(0)\rvert^2$	0.6001
$\lvert A_\parallel(0)\rvert^2$	0.2398
$\lvert A_\perp(0)\rvert^2$	0.1601
$\lvert A_S(0)\rvert^2$	-
$\delta_\parallel - \delta_0$ [rad]	2.501
$\delta_\perp - \delta_0$ [rad]	-0.170
Γ_d [ps^{-1}]	0.65833

Appendix C

MSSM contributions

C.1 $B^0_{(s)}$ mixing

The most important contributions are given by gluino-box contributions. These are calculated to be [175]:

$$
\begin{aligned}
C_1^{\tilde{g}} &= -\frac{(\alpha_s)^2}{\tilde{m}_Q^2}\left[(\delta_d^{LL})_{32}\right]^2 g_1^{(1)}\left(x_Q^3\right), \\
C_4^{\tilde{g}} &= -\frac{(\alpha_s)^2}{M_3^2}\left[(\delta_d^{LL})_{32}(\delta_d^{RR})_{32}\right] g_4^{(1)}\left(x_Q^3, x_d^3\right), \\
C_5^{\tilde{g}} &= -\frac{(\alpha_s)^2}{M_3^2}\left[(\delta_d^{LL})_{32}(\delta_d^{RR})_{32}\right] g_5^{(1)}\left(x_Q^3, x_d^3\right), \\
\tilde{C}_1^{\tilde{g}} &= -\frac{(\alpha_s)^2}{\tilde{m}_d^2}\left[(\delta_d^{RR})_{32}\right]^2 g_1^{(1)}\left(x_d^3\right),
\end{aligned}
\tag{C.1}
$$

where we use the notation $x_B^A = \frac{m_A^2}{m_B^2}$. The loop functions $g_1^{(1)}(x)$, $g_4^{(1)}(x,y)$ and $g_5^{(1)}(x,y)$ are defined as [175]:

$$
\begin{aligned}
g_1^{(1)}(x) =& -\frac{11+144x+27x^2-2x^3}{108(1-x)^4} - \frac{x(13+17x)}{18(1-x)^5}\ln x, \\
g_4^{(1)}(x,y) =& -\frac{x^2 y \ln x}{3(x-y)^3(1-x)^3}\left\{x^2(5+7x)+y\left[2+7(x-3)x\right]\right\} \\
&-\frac{y^2 x \ln y}{3(y-x)^3(1-y)^3}\left\{y^2(5+7y)+x\left[2+7(y-3)y\right]\right\} \\
&+\frac{xy}{3(1-x)^2(1-y)^2(x-y)^2}\left(x+y-13x^2-13y^2+8xy+15x^2y+15xy^2-14x^2y^2\right),
\end{aligned}
\tag{C.2}
$$

$$
\begin{aligned}
g_5^{(1)}(x,y) = &-\frac{x^2 y \ln x}{9(x-y)^3(1-x)^3}\left[x^2(11+x)+(x-5)(x+2)y\right] \\
&-\frac{y^2 x \ln y}{9(y-x)^3(1-y)^3}\left[y^2(11+y)+(y-5)(y+2)x\right] \\
&-\frac{xy}{9(1-x)^2(1-y)^2(x-y)^2}\left(5x+5y+7x^2+7y^2-32xy+3x^2y+3xy^2+2x^2y^2\right) .
\end{aligned}
\tag{C.3}
$$

Chargino-box and leading neutralino contributions are given by:

$$
\begin{aligned}
C_1^{\tilde{\chi}} = &-\frac{\alpha_2\alpha_s}{6\tilde{m}_Q^2}\left[(\delta_d^{LL})_{32}\right]^2 g_{\tilde{g}\tilde{w}}^{(1)}\left(x_Q^3, x_Q^2\right) - \frac{(\alpha_2)^2}{8\tilde{m}_Q^2}\left[(\delta_d^{LL})_{32}\right]^2 g_{\tilde{w}}^{(1)}\left(x_Q^2\right) \\
&-\frac{(\alpha_2)^2}{8\tilde{m}_u^2}\frac{m_t^4}{M_W^4}\left(V_{tb}V_{ts}^*\right)^2 f_1\left(x_u^\mu\right) , \\
\tilde{C}_3^{\tilde{\chi}} = &-\frac{(\alpha_2)^2}{8}\frac{m_b^2\mu^2 A_t^2}{\tilde{m}_Q^4\tilde{m}_u^4}\frac{m_t^4}{M_W^4}\frac{\tan^2\beta}{[1+(\epsilon_g+\epsilon_Y)\tan\beta]^2}\left(V_{tb}V_{ts}^*\right)^2 f_3\left(x_Q^\mu, x_u^\mu\right) ,
\end{aligned}
\tag{C.4}
$$

where ϵ_g and ϵ_Y, which are one-loop suppressed, are given by [175]

$$
\begin{aligned}
\epsilon_g &= \frac{2\alpha_s}{3\pi}\frac{\mu M_3}{\tilde{m}_Q^2}F\left(x_Q^3, x_Q^d\right) , \\
\epsilon_Y &= -\frac{\alpha_2}{8\pi}\frac{\mu A_t}{\tilde{m}_Q^2}\frac{m_t^2}{M_W^2}F\left(x_Q^\mu, x_Q^u\right) .
\end{aligned}
\tag{C.5}
$$

The loop functions $g_{\tilde{g}\tilde{w}}^{(1)}(x,y)$, $g_{\tilde{w}}^{(1)}(x)$, $f_1(x)$ and $f_3(x,y)$ are given by [175]:

$$
\begin{aligned}
g_{\tilde{g}\tilde{w}}^{(1)}(x,y) = &-\sqrt{xy}\left[\frac{x\ln x}{(x-y)(1-x)^4}+\frac{y\ln y}{(y-x)(1-y)^4}\right. \\
&\left.+\frac{11-7(x+y)+2(x^2+y^2)-10xy+5xy(x+y)-x^2y^2}{6(1-x)^3(1-y)^3}\right] \\
&-\frac{x^2\ln x}{2(x-y)(1-x)^4}-\frac{y^2\ln y}{2(y-x)(1-y)^4} \\
&-\frac{2+5(x+y)-(x^2+y^2)-22xy+5xy(x+y)+2x^2y^2}{12(1-x)^3(1-y)^3} ,
\end{aligned}
\tag{C.6}
$$

$$
\begin{aligned}
g^{(1)}_{\tilde{w}}(x) &= \frac{-5-67x-13x^2+x^3}{12(1-x)^4} - \frac{x(3+4x)}{(1-x)^5}\ln x\,,\\
f_1(x) &= -\frac{x+1}{4(1-x)^2} - \frac{x}{2(1-x)^3}\ln x\,,\\
f_3(x,y) &= -\frac{x^2[x(1+x+y)-3y]}{(x-y)^3(1-x)^3}\ln x - \frac{y^2[y(1+x+y)-3x]}{(y-x)^3(1-y)^3}\ln y\\
&\quad - 2\frac{x^2+y^2-xy-x^2y-xy^2+x^2y^2}{(1-x)^2(1-y)^2(x-y)^2}\,,
\end{aligned}
\tag{C.7}
$$

The loop functions $F(x,y)$ and $G(x,y)$ are given by [175]:

$$
\begin{aligned}
F(x,y) &= \frac{x\ln x}{(x-1)(x-y)} + \frac{y\ln y}{(y-1)(y-x)}\,,\\
G(x,y) &= \frac{x\ln x}{(x-1)^2(x-y)} + \frac{y\ln y}{(y-1)^2(y-x)} + \frac{1}{(x-1)(y-1)}\,,
\end{aligned}
\tag{C.8}
$$

Double Higgs penguin contributions are also taken into account in an alignment and degenerate approximation:

$$
\alpha \approx \beta - \frac{\pi}{2} \qquad M_H \approx M_A \tag{C.9}
$$

The only non negligible contributions are found to Wilson Coefficient, C_4 [175]:

$$
\begin{aligned}
C_4^H \simeq &-\frac{8(\alpha_s)^2\alpha_2}{9\pi}\frac{m_b^2}{M_W^2}\frac{\tan^4\beta}{(1+\epsilon_g\tan\beta)^2[1+(\epsilon_g+\epsilon_Y)\tan\beta]^2}\frac{\mu^2M_3^2}{M_A^2\tilde{m}_d^2\tilde{m}_Q^2}\\
&\times\left[(\delta_d^{LL})_{32}(\delta_d^{RR})_{32}\right]G\left(x_d^3,x_d^Q\right)G\left(x_Q^3,x_Q^d\right)\\
&+\frac{(\alpha_2)^2\alpha_s}{6\pi}\frac{m_b^2}{M_W^2}\frac{\tan^4\beta}{(1+\epsilon_g\tan\beta)^2[1+(\epsilon_g+\epsilon_Y)\tan\beta]^2}\frac{\mu^2M_3}{M_A^2\tilde{m}_d^2}(\delta_d^{RR})_{32}G\left(x_d^3,x_d^Q\right)\\
&\times\left[\frac{m_t^2}{M_W^2}\frac{A_t}{\tilde{m}_Q^2}V_{tb}V_{ts}^*F\left(x_Q^\mu,x_Q^u\right)+\frac{2M_2}{\tilde{m}_Q^2}(\delta_u^{LL})_{32}G\left(x_Q^2,x_Q^\mu\right)\right]
\end{aligned}
\tag{C.10}
$$

The loop functions $F(x,y)$ and $G(x,y)$ are defined in C.8. The $B0$ formulas are obtained by replacing V_{ts}, $(\delta^{LL}_{d,u})_{32}$ and $(\delta^{RR}_d)_{32}$ by V_{td}, $(\delta^{LL}_{d,u})_{31}$ and $(\delta^{RR}_d)_{31}$.

C.2 Electric Dipole Moments (EDMs)

The leading MSSM contributions come from one-loop gluino-squarks diagrams:

$$\begin{aligned}\left\{\frac{d_{d_i}}{e}, d^c_{d_i}\right\}^{\tilde{g}} &= -\frac{\alpha_s}{4\pi}\frac{m_b\mu}{M_3^3}\frac{\tan\beta}{1+(\epsilon_g+\epsilon_Y)\tan\beta}\,\mathrm{Im}\Big\{[(\delta_d^{LL})_{i3}(\delta_d^{RR})_{3i}]\Big\}f_{\tilde{g}}^{d}\left(x_3^Q, x_3^d\right),\\ \left\{\frac{d_u}{e}, d^c_u\right\}^{\tilde{g}} &= -\frac{\alpha_s}{4\pi}\frac{m_t A_t}{M_3^3}\,\mathrm{Im}\Big\{[(\delta_u^{LL})_{13}(\delta_u^{RR})_{31}]\Big\}f_{\tilde{g}}^{u}\left(x_3^Q, x_3^u\right).\end{aligned} \tag{C.11}$$

The loop functions $f_{\tilde{g}}^{d,u}(x,y)$ are given by:

$$\begin{aligned}f_{\tilde{g}}^{d}(x,y) &= \left\{-\frac{4}{9}E_0^{\tilde{g}(2)}(x,y), -\frac{1}{6}E_0^{\tilde{g}(2)}(x,y)+\frac{3}{2}E_1^{\tilde{g}(2)}(x,y)\right\},\\ f_{\tilde{g}}^{u}(x,y) &= \left\{\frac{8}{9}E_0^{\tilde{g}(2)}(x,y), -\frac{1}{6}E_0^{\tilde{g}(2)}(x,y)+\frac{3}{2}E_1^{\tilde{g}(2)}(x,y)\right\},\end{aligned} \tag{C.12}$$

The loop functions $E_{0,1}^{\tilde{g}(2)}(x,y)$ are given by

$$\begin{aligned}E_0^{\tilde{g}(2)}(x,y) &= xy\left[-\frac{2\left(x+y+2xy-4x^2\right)\ln x}{(x-y)^3(1-x)^4}+\frac{2\left(x+y+2xy-4y^2\right)\ln y}{(x-y)^3(1-y)^4}\right.\\ &\left.+\frac{4-6x+13x^2-5x^3-6y-14xy+3x^2y-x^3y+13y^2+3xy^2+2x^2y^2-5y^3-xy^3}{(x-y)^2(1-x)^3(1-y)^3}\right],\\ E_1^{\tilde{g}(2)}(x,y) &= xy\left[\frac{2x\left(3x^2-2y-xy\right)\ln x}{(x-y)^3(1-x)^4}-\frac{2y\left(3y^2-2x-xy\right)\ln y}{(x-y)^3(1-y)^4}\right.\\ &\left.+\frac{2x+5x^2-x^3+2y-22xy+7x^2y-5x^3y+5y^2+7xy^2+6x^2y^2-y^3-5xy^3}{(x-y)^2(1-x)^3(1-y)^3}\right],\end{aligned} \tag{C.13}$$

The one-loop charged-Higgsino-squark contributions are also computed based on [176]:

$$\left\{\frac{d_{d_i}}{e}, d^c_{d_i}\right\}^{\tilde{\chi}^\pm} = \frac{\alpha_2}{8\pi}\frac{m_b}{\tilde{m}^2_Q}\frac{\mu M_2}{\tilde{m}^2_Q}\frac{\epsilon_R \tan^2\beta}{3[1+(\epsilon_g+\epsilon_Y)\tan\beta]^2}\,\mathrm{Im}\Big\{[(\delta^{LL}_u)_{i3}(\delta^{RR}_d)_{3i}]\Big\} f_{\tilde{H}^\pm\tilde{W}^\pm}\left(x^2_Q, x^\mu_Q\right)$$
$$+\frac{\alpha_2}{16\pi}\frac{m_b A_t}{\mu^3}\frac{m^2_t}{M^2_W}\frac{\epsilon_R \tan^2\beta}{3[1+(\epsilon_g+\epsilon_Y)\tan\beta]^2}\,\mathrm{Im}\Big\{[V^*_{3i}(\delta^{RR}_d)_{3i}]\Big\} f_{\tilde{H}^\pm}\left(x^Q_\mu, x^u_\mu\right), \tag{C.14}$$

with [175]:

$$\epsilon_R = -\frac{2\alpha_s}{\pi}\frac{\mu M_3}{\tilde{m}^2_d} G\left(x^3_d, x^Q_d\right).$$

The loop function $f_{\tilde{H}^\pm\tilde{W}^\pm}(x,y)$ and $f_{\tilde{H}^\pm}(x,y)$ are given by [175]:

$$\begin{aligned} f_{\tilde{H}^\pm}(x,y) &= \left\{\frac{2}{3}E_{f\phi\phi\phi\mathrm{box}}(x,y) - E_{ff\phi\phi\mathrm{box}}(x,y), E_{f\phi\phi\phi\mathrm{box}}(x,y)\right\}, \\ f_{\tilde{H}^\pm\tilde{W}^\pm}(x,y) &= \left\{\frac{2}{3}g^{(1)}_0(x,y) - g^{(1)}_1(x,y), g^{(1)}_0(x,y)\right\}, \end{aligned} \tag{C.15}$$

Finally, we compute charged Higgs contributions to the down-type quarks [176, 177]:

$$\left\{\frac{d_{d_i}}{e}, d^c_{d_i}\right\}^{H^\pm} = -\frac{\alpha_2}{16\pi}\frac{m_b}{M^2_{H^\pm}}\frac{m^2_t}{M^2_W}\frac{(1-\epsilon'_g\tan\beta)\epsilon_R\tan\beta}{3[1+(\epsilon_g+\epsilon_Y)\tan\beta]^2}\,\mathrm{Im}\Big\{[V^*_{3i}(\delta^{RR}_d)_{3i}]\Big\} f_{H^\pm}\left(x^t_{H^\pm}\right)$$
$$-\frac{\alpha_2}{16\pi}\frac{m_b}{M^2_{H^\pm}}\frac{m^2_t}{M^2_W}\frac{\epsilon'_L\epsilon_R\tan^2\beta}{9[1+(\epsilon_g+\epsilon_Y)\tan\beta]^2}\,\mathrm{Im}\Big\{[(\delta^{LL}_d)_{i3}(\delta^{RR}_d)_{3i}]\Big\} f_{H^\pm}\left(x^t_{H^\pm}\right), \tag{C.16}$$

with [175]:

$$\begin{aligned} \epsilon'_g &= \frac{2\alpha_s}{3\pi}\frac{\mu M_3}{\tilde{m}^2_Q} F\left(x^3_Q, x^u_Q\right), \\ \epsilon'_L &= -\frac{2\alpha_s}{\pi}\frac{\mu M_3}{\tilde{m}^2_Q} G\left(x^3_Q, x^u_Q\right), \end{aligned} \tag{C.17}$$

where the loop function $f^\pm_H(x)$ is given by [175]:

$$f_{H^\pm}(x) = \left\{ \frac{2}{3} f_1^{(0)}(x) - f_0^{(0)}(x) \, , f_1^{(0)}(x) \right\} , \tag{C.18}$$

with:

$$\begin{aligned} f_0^{(0)}(x) &= \frac{1 - x^2 + 2x \ln x}{(1-x)^3} , \\ f_1^{(0)}(x) &= \frac{3 - 4x + x^2 + 2 \ln x}{(1-x)^3} , \end{aligned} \tag{C.19}$$

C.3 $\Delta F = 1$ processes

C.3.1 $B^0_{s,d} \to \mu\mu$

In the approximation C.9, the main MSSM contributions to the scalar and pseudoscalar operator are given by[1] [175]:

$$\begin{aligned} C_S^H = &- \frac{2}{3} \frac{\alpha_s \alpha_2 m_\mu}{M_W^2} \frac{\mu M_3}{M_A^2 \tilde{m}_Q^2} \left(\delta_d^{LL}\right)_{32} \frac{\tan^3\beta}{\epsilon_{corr}} G\left(x_Q^3, x_Q^d\right) \\ &+ \frac{(\alpha_2)^2 m_\mu m_t^2}{8 M_W^4} \frac{\mu A_t}{M_A^2 \tilde{m}_Q^2} V_{tb} V_{ts}^* \frac{\tan^3\beta}{\epsilon_{corr}} F\left(x_Q^\mu, x_Q^u\right) \\ &+ \frac{(\alpha_2)^2 m_\mu}{4 M_W^2} \frac{\mu M_2}{M_A^2 \tilde{m}_Q^2} \left(\delta_u^{LL}\right)_{32} \frac{\tan^3\beta}{\epsilon_{corr}} G\left(x_Q^2, x_Q^\mu\right) , \\ \tilde{C}_S^H = &- \frac{2}{3} \frac{\alpha_s \alpha_2 m_\mu}{M_W^2} \frac{\mu M_3}{M_A^2 \tilde{m}_d^2} (\delta_d^{RR})_{32} \frac{\tan^3\beta}{\epsilon_{corr}} G\left(x_d^3, x_d^Q\right) , \\ \epsilon_{corr} = &[1 + \epsilon_g \tan\beta][1 + (\epsilon_g + \epsilon_Y)\tan\beta](1 + \epsilon_\ell \tan\beta) \end{aligned} \tag{C.20}$$

The pseudoscalars Wilson coefficients are simply obtained from the scalar ones by:

$$C_P^H = -C_S^H , \quad \tilde{C}_P^H = \tilde{C}_S^H , \tag{C.21}$$

where [175]:

$$\epsilon_\ell \simeq -\frac{3\alpha_2}{16\pi} . \tag{C.22}$$

For $B_d^0 \to \mu^+\mu^-$ branching ratio, the Wilson coefficients are obtained just by replacing V_{ts}^*, $(\delta_{d,u}^{LL})_{32}$, $(\delta_d^{RR})_{32}$ with V_{td}^*, $(\delta_{d,u}^{LL})_{31}$, $(\delta_d^{RR})_{31}$, respectively.

[1] Note that $\tilde{C}_A$ are induced by $(\delta_{LR})_{i3}$ with $i \neq 3$ terms, so they are negligible for our study

C.3.2 $B^+ \to \tau\nu$

The MSSM tree-level contribution arises from charged-Higgs exchange [95]. We found at the leading one-loop level, the following expression for $\mathcal{B}(B^+ \to \tau\nu)$

$$\begin{aligned}\mathcal{B}\left(B^+ \to \tau^+\nu\right) = \mathcal{B}\left(B^+ \to \tau^+\nu\right)_{\rm SM} \\ \times \left|1 - \frac{m^2_{B^\pm}}{M^2_{H^\pm}} \frac{\tan^2\beta}{(1+\epsilon_g \tan\beta)\left[1+(\epsilon_g+\epsilon_Y)\tan\beta\right](1+\epsilon_\ell\tan\beta)}\right. \\ \left. \times \left[1 + (\epsilon_g+\epsilon_Y)\tan\beta + \frac{\epsilon_L \tan\beta}{3}\frac{(\delta_u^{LL})_{31}}{V_{ub}}\right]\right|^2 ,\end{aligned}$$

C.3.3 $b \to s\gamma$ transitions

We compute gluino contributions at $\mu = \mu^{SUSY}$:

$$\begin{aligned}\{C_7, C_8\}^{\tilde g} &= \frac{\pi\alpha_s}{\sqrt{2}G_F}\frac{\mu}{M_3^3}\frac{\tan\beta}{1+(\epsilon_g+\epsilon_Y)\tan\beta}\frac{(\delta_d^{LL})_{32}}{V_{tb}V_{ts}^*} f_{\tilde g}\left(x_3^Q, x_3^d\right) , \\ \{\tilde C_7, \tilde C_8\}^{\tilde g} &= \frac{\pi\alpha_s}{\sqrt{2}G_F}\frac{\mu}{M_3^3}\frac{\tan\beta}{1+(\epsilon_g+\epsilon_Y)\tan\beta}\frac{(\delta_d^{RR})_{32}}{V_{tb}V_{ts}^*} f_{\tilde g}\left(x_3^d, x_3^Q\right) ,\end{aligned} \tag{C.23}$$

Where the loop functions $f_{\tilde g}(x,y)$

$$f_{\tilde g}(x,y) = \left\{-\frac{4}{9}E_0^{\tilde g(1)}(x,y), -\frac{1}{6}E_0^{\tilde g(1)}(x,y) + \frac{3}{2}E_1^{\tilde g(1)}(x,y)\right\} , \tag{C.24}$$

with:

$$\begin{aligned}E_0^{\tilde g(1)}(x,y) =& x\left[\frac{2\left(3x^2-y-2xy\right)\ln x}{(x-y)^2(1-x)^4} + \frac{2y\ln y}{(x-y)^2(1-y)^3}\right. \\ &\left. + \frac{2-9y+5y^2-x^2(1+y)+x(5-2y+y^2)}{(x-y)(1-x)^3(1-y)^2}\right] , \\ E_1^{\tilde g(1)}(x,y) =& x\left[\frac{2x\left(x+2x^2-2y-xy\right)\ln x}{(x-y)^2(1-x)^4} + \frac{2y^2\ln y}{(x-y)^2(1-y)^3}\right. \\ &\left. + \frac{(-3+y)y-x^2(-1+3y)-x(-5+6y-5y^2)}{(x-y)(1-x)^3(1-y)^2}\right] ,\end{aligned} \tag{C.25}$$

Chargino's contributions are found to be:

$$\{C_7, C_8\}^{\tilde{\chi}^\pm} = -\frac{\tan\beta}{2\left[1+(\epsilon_g+\epsilon_Y)\tan\beta\right]}\times \left[\frac{M_W^2}{\tilde{m}_Q^2}\frac{\mu M_2}{\tilde{m}_Q^2}\frac{(\delta_u^{LL})_{32}}{V_{ts}^*} f_{\tilde{H}^\pm\tilde{W}^\pm}\left(x_Q^2, x_Q^\mu\right) + \frac{m_t^2 A_t}{2\mu^3} f_{\tilde{H}^\pm}\left(x_\mu^Q, x_\mu^u\right)\right], \tag{C.26}$$

where the loop functions are given in Eq. C.15. Finally charged-Higgs contributions are computed to be:

$$\{C_7, C_8\}^{H^\pm} = \left\{\frac{1-\epsilon_g'\tan\beta}{1+(\epsilon_g+\epsilon_Y)\tan\beta} + \frac{\epsilon_L'\tan\beta}{3[1+(\epsilon_g+\epsilon_Y)\tan\beta]}\frac{(\delta_d^{LL})_{32}}{V_{ts}^*}\right\}\frac{m_t^2}{8M_{H^\pm}^2} f_{H^\pm}\left(x_{H^\pm}^t\right), \tag{C.27}$$

The loop functions are given in Eq. C.18.

Appendix D

Plot projections NMFV

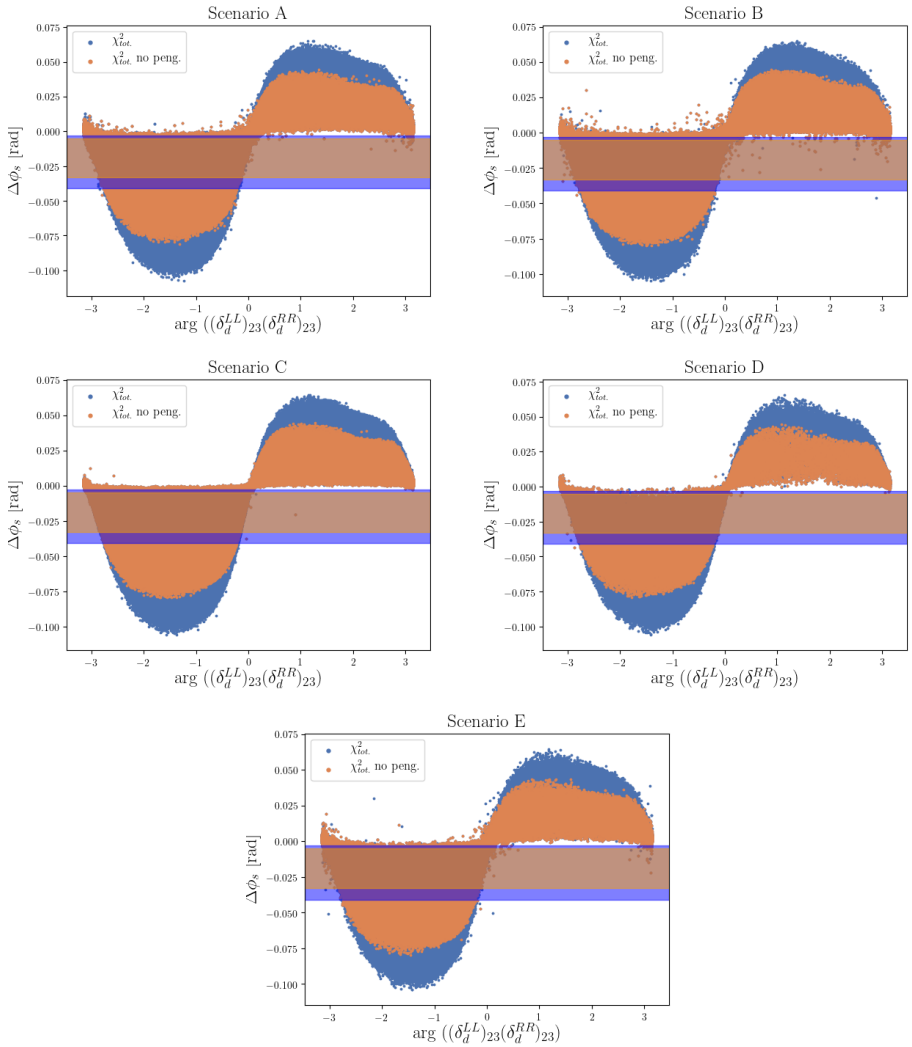

FIGURE D.1: $\Delta\phi_s^{NP}$ vs arg $(\delta^d_{LL})_{23}(\delta^d_{RR})_{23}$ for scenarios A (upper left), B (upper right), C (middle left), D (middle right) and E (bottom). Blue (orange) points indicate the points that fulfill all the constraints at 95% by (not) considering the penguin pollution estimated using SU(3) symmetry.

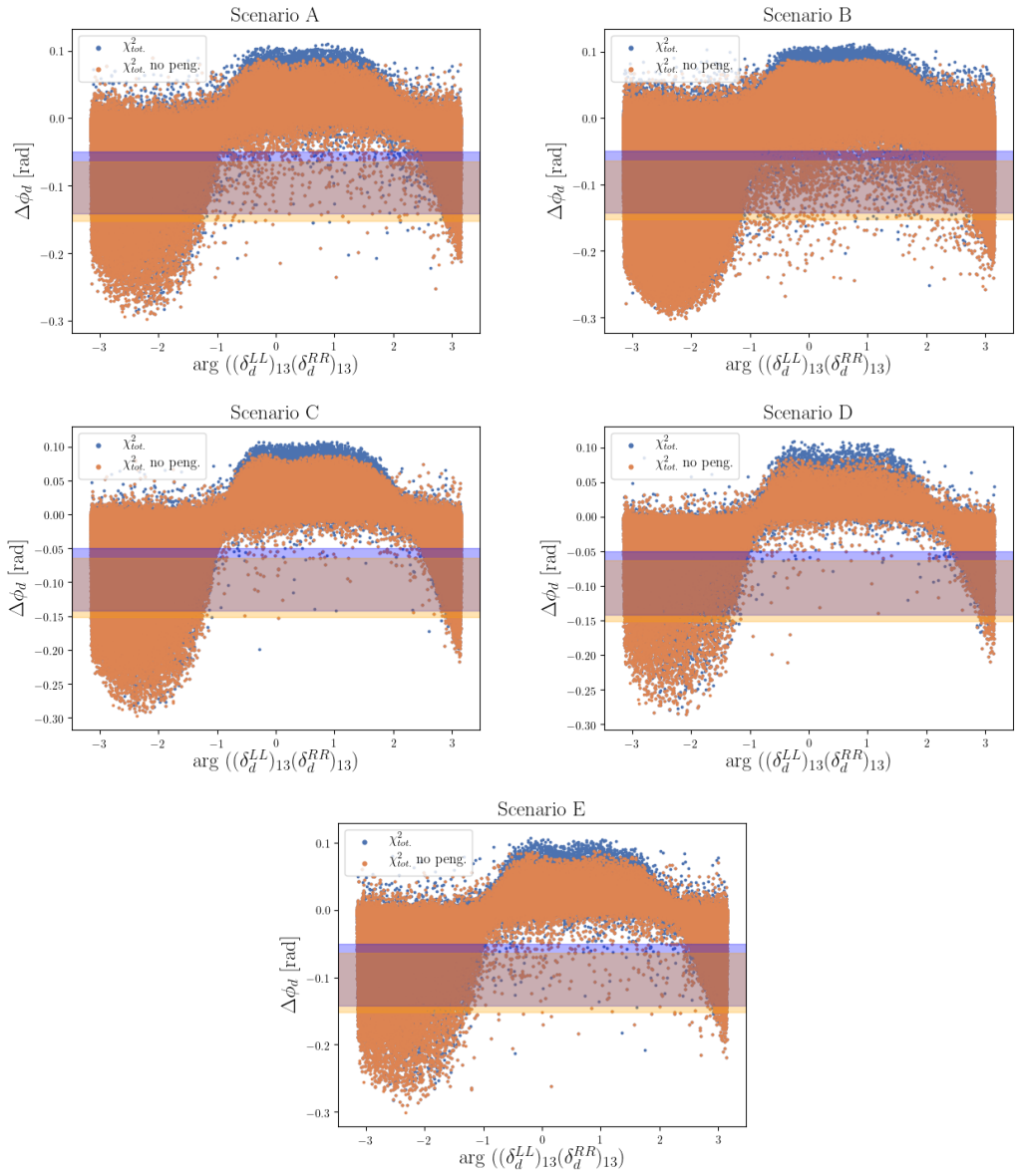

FIGURE D.2: $\Delta\phi_d^{NP}$ vs arg $(\delta^d_{LL})_{13}(\delta^d_{RR})_{13}$ for scenarios A (upper left), B (upper right), C (middle left), D (middle right) and E (bottom). Blue (orange) points indicate the points that fulfill all the constraints at 95% by (not) considering the penguin pollution estimated using SU(3) symmetry.

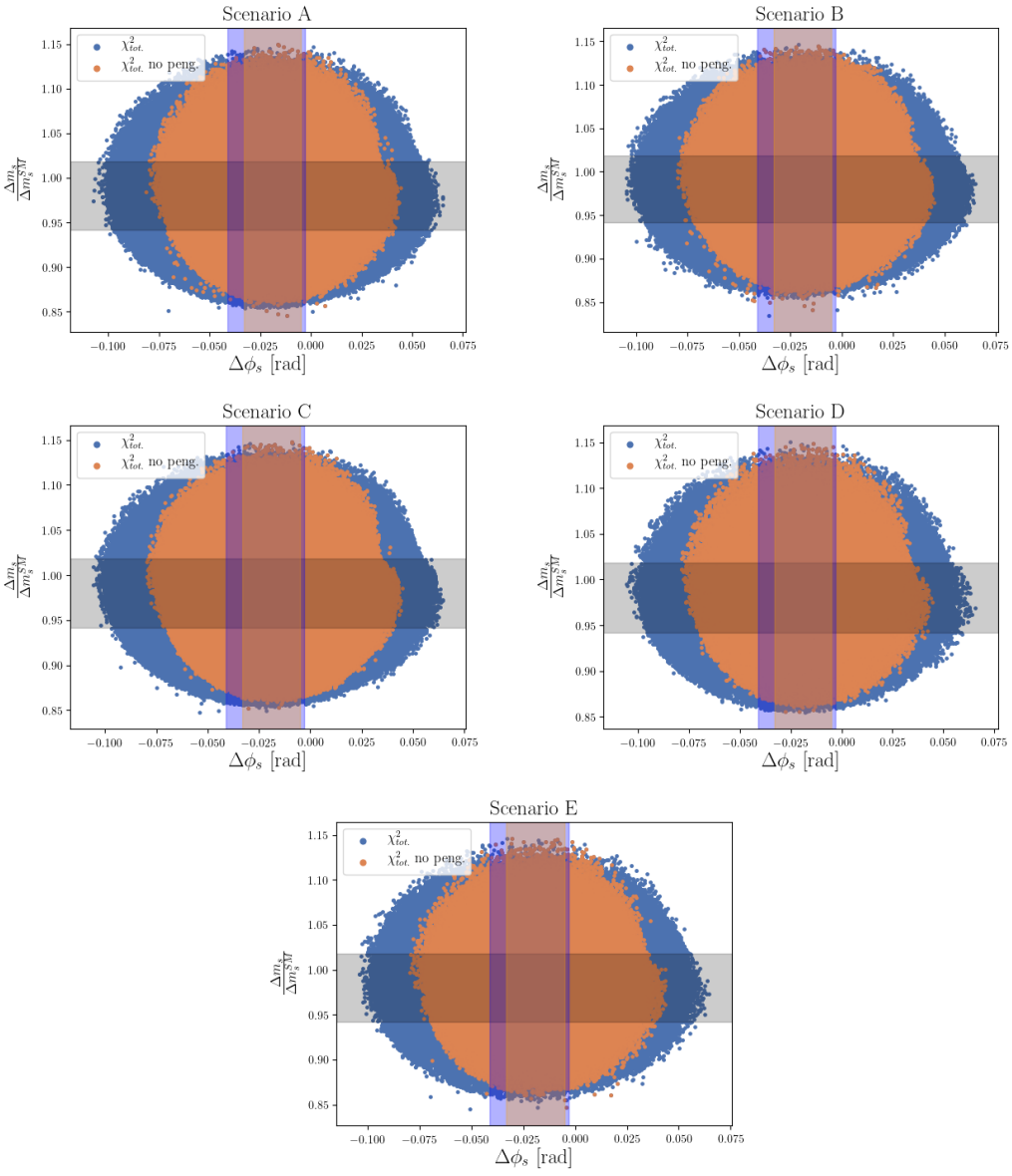

FIGURE D.3: $\Delta\phi_s^{NP}$ vs $\Delta m_s^{EXP/SM}$ for scenarios A (upper left), B (upper right), C (middle left), D (middle right) and E (bottom). Blue (orange) points indicate the points that fulfill all the constraints at 95% by (not) considering the penguin pollution estimated using SU(3) symmetry.

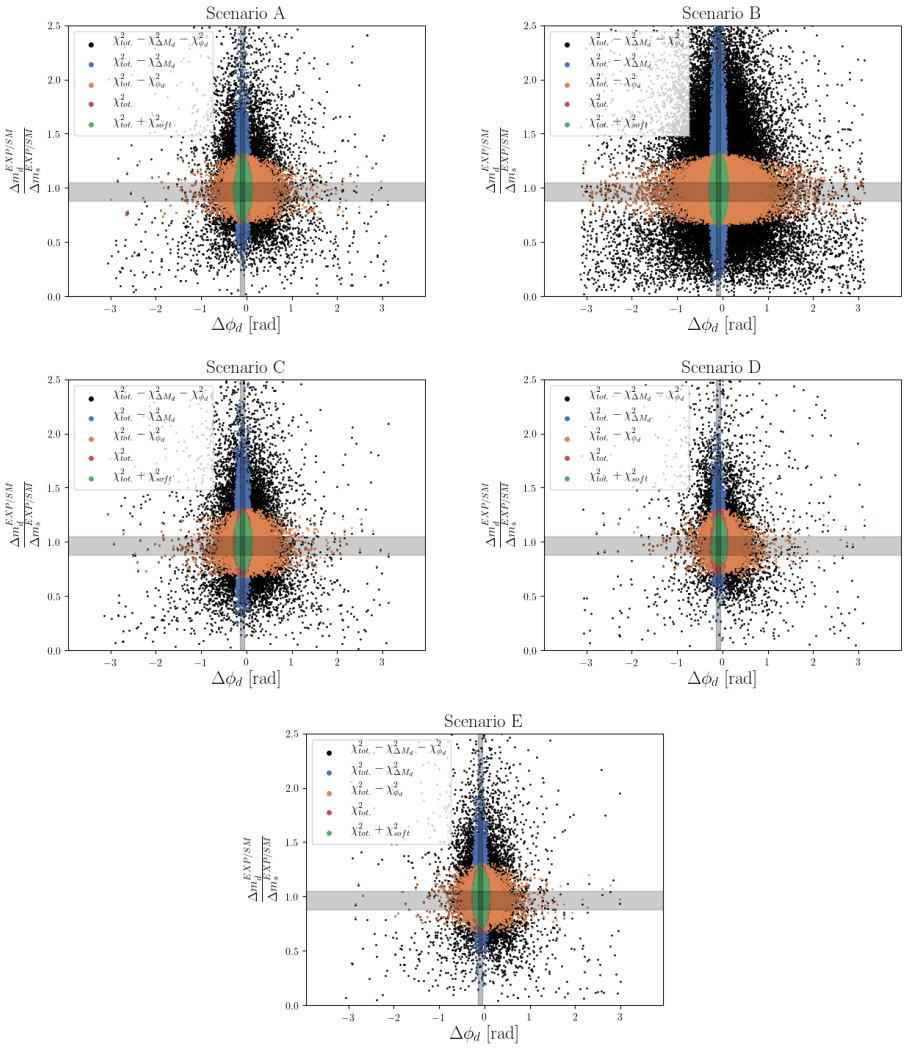

FIGURE D.4: $\Delta\phi_d^{NP}$ vs $\Delta m_{d/s}^{EXP/SM}$ for scenarios A (upper left), B (upper right), C (middle left), D (middle right) and E (bottom). Black points show the 95% CL when all the constraints except for $\Delta\phi_d$ and $\Delta m_{d/s}$ are included. Blue (orange) points show the 95 % of CL when all the constraints excluding $\Delta m_{d/s}$ ($\Delta\phi_d$) are included. Red points indicate the points that fulfill all the constraints at 95% of CL. Green points indicate the red points that give a correct mass spectrum according to the SOFTSUSY software [103]. The constraint of $\Delta\phi_{s,d}$ is calculated considering the penguin pollution estimation based on SU(3) symmetry [61].

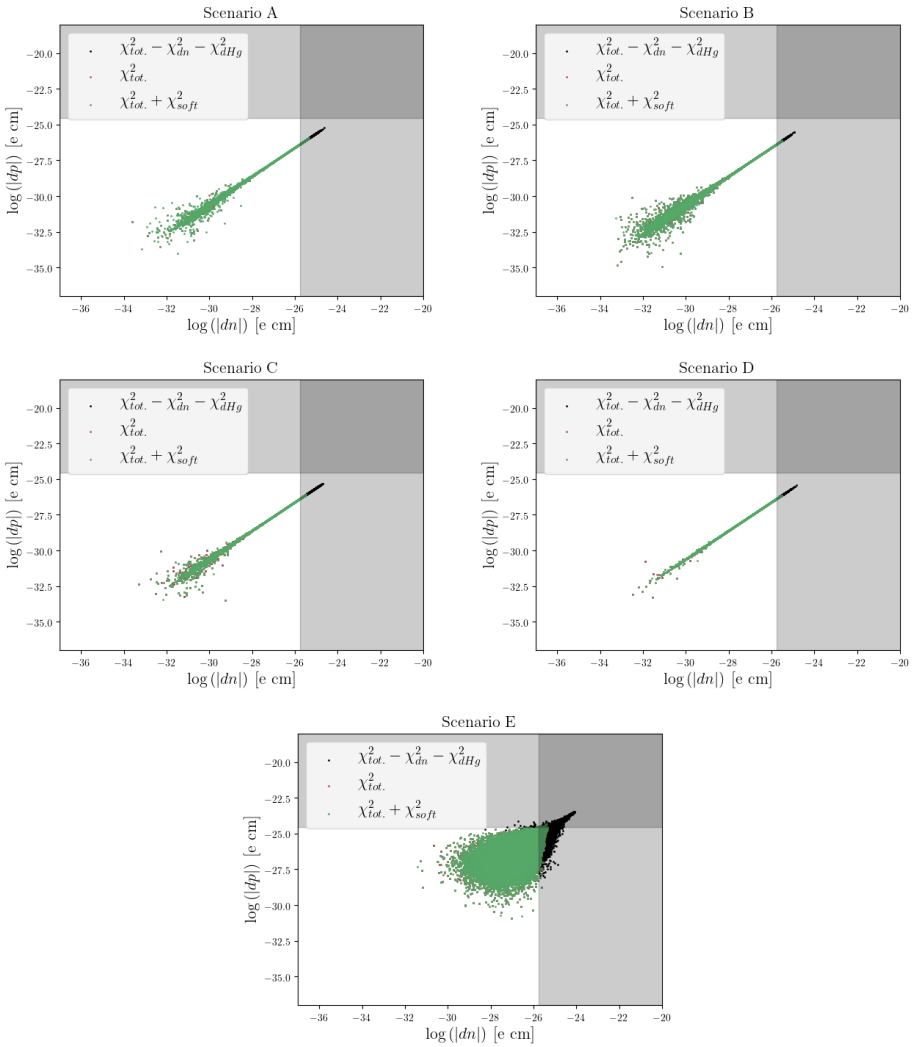

FIGURE D.5: $\log d_n$ vs $\log d_p$ for scenarios A (upper left), B (upper right), C (middle left), D (middle right), and E (bottom). Black points show the 95% CL when all the constraints except for d_n^{EXP} and d_p^{EXP} are included. Red points indicate the points that fulfill all the constraints at 95% of CL. Green points indicate the red points that give a correct mass spectrum according to the SOFTSUSY software [103]. The constraint of $\Delta\phi_{s,d}$ is calculated considering the penguin pollution estimation based on SU(3) symmetry [61].

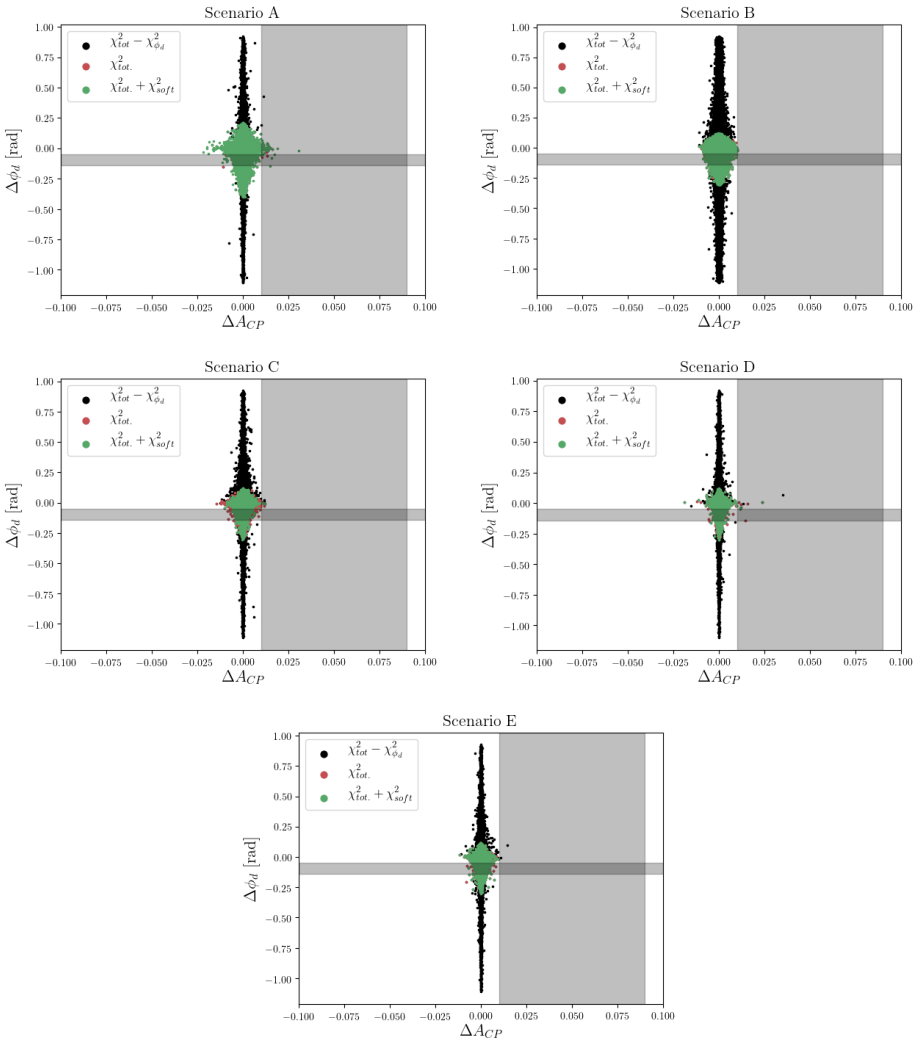

FIGURE D.6: A_{CP} vs $\Delta^{NP}\phi_d$ for scenarios A (upper left), B (upper right), C (middle left), D (middle right), and E (bottom). Black points show the 95% CL when all the constraints except for $\Delta\phi_d$. Red points indicate the points that fulfill all the constraints at 95% of CL. Green points indicate the red points that give a correct mass spectrum according to the SOFTSUSY software [103]. The constraint of $\Delta\phi_{s,d}$ is calculated considering the penguin pollution estimation based on SU(3) symmetry [61].

Appendix E

Figure authorisation

Fig. 4.2, Fig. 4.20 and Fig. 4.21 were provided by the HFLAV collaboration [1]. These figures are licensed under CC BY 4.0, granting me the necessary permissions to include them in my thesis.

Bibliography

[1] Y. Amhis et al. "Averages of b-hadron, c-hadron, and τ-lepton properties as of 2021". In: *Phys. Rev. D* 107 (2023), p. 052008. DOI: 10.1103/PhysRevD.107.052008. arXiv: 2206.07501 [hep-ex].

[2] Andrzej Buras. *Gauge Theory of Weak Decays*. Cambridge University Press, June 2020. ISBN: 978-1-139-52410-0, 978-1-107-03403-7. DOI: 10.1017/9781139524100.

[3] Ramón Ángel Ruiz Fernández. "Testing New Physics with MasterCode". MA thesis. Universidad de Santiago de Compostela, 2020.

[4] Georges Aad et al. "Observation of a new particle in the search for the Standard Model Higgs boson with the ATLAS detector at the LHC". In: *Phys. Lett. B* 716 (2012), pp. 1–29. DOI: 10.1016/j.physletb.2012.08.020. arXiv: 1207.7214 [hep-ex].

[5] Serguei Chatrchyan et al. "Observation of a New Boson at a Mass of 125 GeV with the CMS Experiment at the LHC". In: *Phys. Lett. B* 716 (2012), pp. 30–61. DOI: 10.1016/j.physletb.2012.08.021. arXiv: 1207.7235 [hep-ex].

[6] Y. Fukuda et al. "Evidence for oscillation of atmospheric neutrinos". In: *Phys. Rev. Lett.* 81 (1998), pp. 1562–1567. DOI: 10.1103/PhysRevLett.81.1562. arXiv: hep-ex/9807003.

[7] Frans R. Klinkhamer and N. S. Manton. "A Saddle Point Solution in the Weinberg-Salam Theory". In: *Phys. Rev. D* 30 (1984), p. 2212. DOI: 10.1103/PhysRevD.30.2212.

[8] Nicola Cabibbo. "Unitary Symmetry and Leptonic Decays". In: *Phys. Rev. Lett.* 10 (1963), pp. 531–533. DOI: 10.1103/PhysRevLett.10.531.

[9] Makoto Kobayashi and Toshihide Maskawa. "CP Violation in the Renormalizable Theory of Weak Interaction". In: *Prog. Theor. Phys.* 49 (1973), pp. 652–657. DOI: 10.1143/PTP.49.652.

[10] B. Pontecorvo. "Mesonium and anti-mesonium". In: *Sov. Phys. JETP* 6 (1957), p. 429.

[11] Ziro Maki, Masami Nakagawa, and Shoichi Sakata. "Remarks on the unified model of elementary particles". In: *Prog. Theor. Phys.* 28 (1962), pp. 870–880. DOI: 10.1143/PTP.28.870.

[12] A. D. Sakharov. "Violation of CP Invariance, C asymmetry, and baryon asymmetry of the universe". In: *Pisma Zh. Eksp. Teor. Fiz.* 5 (1967), pp. 32–35. DOI: 10.1070/PU1991v034n05ABEH002497.

[13] Maxim Pospelov and Adam Ritz. "Theta induced electric dipole moment of the neutron via QCD sum rules". In: *Phys. Rev. Lett.* 83 (1999), pp. 2526–2529. DOI: 10.1103/PhysRevLett.83.2526. arXiv: hep-ph/9904483.

[14] Lus Lavoura, Joao Paulo Silva, and Gustavo Castelo Branco. *CP Violation*. Oxford University Press. 1999.

[15] Marina Artuso, Gino Isidori, and Sheldon Stone. *New Physics in b Decays*. World Scientific, May 2022. ISBN: 978-981-12-5129-0, 978-981-12-5131-3. DOI: 10.1142/12696.

[16] Andrzej J. Buras. "Weak Hamiltonian, CP violation and rare decays". In: *Les Houches Summer School in Theoretical Physics, Session 68: Probing the Standard Model of Particle Interactions*. June 1998, pp. 281–539. arXiv: hep-ph/9806471.

[17] Marina Artuso, Guennadi Borissov, and Alexander Lenz. "CP violation in the B_s^0 system". In: *Rev. Mod. Phys.* 88.4 (2016). [Addendum: Rev.Mod.Phys. 91, 049901 (2019)], p. 045002. DOI: 10.1103/RevModPhys.88.045002. arXiv: 1511.09466 [hep-ph].

[18] Alexander Lenz and Gilberto Tetlalmatzi-Xolocotzi. "Model-independent bounds on new physics effects in non-leptonic tree-level decays of B-mesons". In: *JHEP* 07 (2020), p. 177. DOI: 10.1007/JHEP07(2020)177. arXiv: 1912.07621 [hep-ph].

[19] Marcel Alguero et al. "To (b)e or not to (b)e: no electrons at LHCb". In: *Eur. Phys. J. C* 83.7 (2023), p. 648. DOI: 10.1140/epjc/s10052-023-11824-0. arXiv: 2304.07330 [hep-ph].

[20] J. P. Lees et al. "Measurements of direct CP asymmetries in $B \to X_s\gamma$ decays using sum of exclusive decays". In: *Phys. Rev. D* 90.9 (2014), p. 092001. DOI: 10.1103/PhysRevD.90.092001. arXiv: 1406.0534 [hep-ex].

[21] R. Aaij et al. "Test of lepton universality in $b \to s\ell^+\ell^-$ decays". In: *Phys. Rev. Lett.* 131.5 (), p. 051803. DOI: 10.1103/PhysRevLett.131.051803. arXiv: 2212.09152 [hep-ex].

[22] Marco Ciuchini et al. "Constraints on lepton universality violation from rare B decays". In: *Phys. Rev. D* 107.5 (2023), p. 055036. DOI: 10.1103/PhysRevD.107.055036. arXiv: 2212.10516 [hep-ph].

[23] Roel Aaij et al. "Search for the decays $B_s^0 \to \tau^+\tau^-$ and $B^0 \to \tau^+\tau^-$". In: *Phys. Rev. Lett.* 118.25 (2017), p. 251802. DOI: 10.1103/PhysRevLett.118.251802. arXiv: 1703.02508 [hep-ex].

[24] Christoph Bobeth et al. "$B_{s,d} \to l^+l^-$ in the Standard Model with Reduced Theoretical Uncertainty". In: *Phys. Rev. Lett.* 112 (2014), p. 101801. DOI: 10.1103/PhysRevLett.112.101801. arXiv: 1311.0903 [hep-ph].

[25] Martin Beneke, Christoph Bobeth, and Robert Szafron. "Power-enhanced leading-logarithmic QED corrections to $B_q \to \mu^+\mu^-$". In: *JHEP* 10 (2019), p. 232. DOI: 10.1007/JHEP10(2019)232. arXiv: 1908.07011 [hep-ph].

[26] N. K. Nisar et al. "Search for the rare decay $D^0 \to \gamma\gamma$ at Belle". In: *Phys. Rev. D* 93.5 (2016), p. 051102. DOI: 10.1103/PhysRevD.93.051102. arXiv: 1512.02992 [hep-ex].

[27] R. Aaij et al. "Search for Rare Decays of D0 Mesons into Two Muons". In: *Phys. Rev. Lett.* 131.4 (2023), p. 041804. DOI: 10.1103/PhysRevLett.131.041804. arXiv: 2212.11203 [hep-ex].

[28] Giancarlo D'Ambrosio and Teppei Kitahara. "Direct CP Violation in $K \to \mu^+\mu^-$". In: *Phys. Rev. Lett.* 119.20 (2017), p. 201802. DOI: 10.1103/PhysRevLett.119.201802. arXiv: 1707.06999 [hep-ph].

[29] Roel Aaij et al. "Constraints on the $K_S^0 \to \mu^+\mu^-$ Branching Fraction". In: *Phys. Rev. Lett.* 125.23 (2020), p. 231801. DOI: 10.1103/PhysRevLett.125.231801. arXiv: 2001.10354 [hep-ex].

[30] Morad Aaboud et al. "Study of the rare decays of B_s^0 and B^0 mesons into muon pairs using data collected during 2015 and 2016 with the ATLAS detector". In: *JHEP* 04 (2019), p. 098. DOI: 10.1007/JHEP04(2019)098. arXiv: 1812.03017 [hep-ex].

[31] Armen Tumasyan et al. "Measurement of the $B_S^0 \to \mu^+\mu^-$ decay properties and search for the $B^0 \to \mu^+\mu^-$ decay in proton-proton collisions at $\sqrt{s} = 13$ TeV". In: *Phys. Lett. B* 842 (2023), p. 137955. DOI: 10.1016/j.physletb.2023.137955. arXiv: 2212.10311 [hep-ex].

[32] R. Aaij et al. "Analysis of Neutral B-Meson Decays into Two Muons". In: *Phys. Rev. Lett.* 128.4 (2022), p. 041801. DOI: 10.1103/PhysRevLett.128.041801. arXiv: 2108.09284 [hep-ex].

[33] R. L. Workman and Others. "Review of Particle Physics". In: *PTEP* 2022 (2022), p. 083C01. DOI: 10.1093/ptep/ptac097.

[34] D. P. Aguillard et al. "Measurement of the Positive Muon Anomalous Magnetic Moment to 0.20 ppm". In: *Phys. Rev. Lett.* 131.16 (2023), p. 161802. DOI: 10.1103/PhysRevLett.131.161802. arXiv: 2308.06230 [hep-ex].

[35] G. W. Bennett et al. "Final Report of the Muon E821 Anomalous Magnetic Moment Measurement at BNL". In: *Phys. Rev. D* 73 (2006), p. 072003. DOI: 10.1103/PhysRevD.73.072003. arXiv: hep-ex/0602035.

[36] T. Aoyama et al. "The anomalous magnetic moment of the muon in the Standard Model". In: *Phys. Rept.* 887 (2020), pp. 1–166. DOI: 10.1016/j.physrep.2020.07.006. arXiv: 2006.04822 [hep-ph].

[37] Sz. Borsanyi et al. "Leading hadronic contribution to the muon magnetic moment from lattice QCD". In: *Nature* 593.7857 (2021), pp. 51–55. DOI: 10.1038/s41586-021-03418-1. arXiv: 2002.12347 [hep-lat].

[38] F. V. Ignatov et al. "Measurement of the $e^+e^- \to \pi^+\pi^-$ cross section from threshold to 1.2 GeV with the CMD-3 detector". In: (Feb. 2023). arXiv: 2302.08834 [hep-ex].

[39] Andreas Crivellin and Bruce Mellado. "Anomalies in Particle Physics". In: (Sept. 2023). arXiv: 2309.03870 [hep-ph].

[40] Marcel Alguero et al. "A new B-flavour anomaly in $B_{d,s} \to K^{*0}\bar{K}^{*0}$: anatomy and interpretation". In: *JHEP* 04 (2021), p. 066. DOI: 10.1007/JHEP04(2021)066. arXiv: 2011.07867 [hep-ph].

[41] Marzia Bordone et al. "A puzzle in $\bar{B}^0_{(s)} \to D^{(*)+}_{(s)}\{\pi^-, K^-$ decays and extraction of the $\frac{f_s}{f_d}$ fragmentation fraction". In: *The European Physical Journal C* 80.10 (Oct. 2020). ISSN: 1434-6052. DOI: 10.1140/epjc/s10052-020-08512-8. URL: http://dx.doi.org/10.1140/epjc/s10052-020-08512-8.

[42] Raphaël Berthiaume et al. "Anomalies in Hadronic B Decays". In: (Nov. 2023). arXiv: 2311.18011 [hep-ph].

[43] S. Schael et al. "Precision electroweak measurements on the Z resonance". In: *Phys. Rept.* 427 (2006), pp. 257–454. DOI: 10.1016/j.physrep.2005.12.006. arXiv: hep-ex/0509008.

[44] Stefano Moretti and Shaaban Khalil. *Supersymmetry Beyond Minimality: From Theory to Experiment*. CRC Press, 2019. ISBN: 978-0-367-87662-3.

[45] Roel Aaij et al. "LHCb Detector Performance". In: *Int. J. Mod. Phys. A* 30.07 (2015), p. 1530022. DOI: 10.1142/S0217751X15300227. arXiv: 1412.6352 [hep-ex].

[46] *Proceedings of the Workshop on Standard Model Physics (and more) at the LHC: CERN, Geneva, Switzerland 25 - 26 May 1999. CERN Workshop on Standard Model Physics (and more) at the LHC*. CERN. Geneva: CERN, 2000. DOI: 10.5170/CERN-2000-004. URL: https://cds.cern.ch/record/425440.

[47] LHCb collaboration. "LHCb magnet: Technical design report". In: (2000).

[48] LHCb collaboration. "LHCb VELO TDR: Vertex locator. Technical design report". In: (May 2001).

[49] A. Augusto Alves Jr. et al. "The LHCb Detector at the LHC". In: *JINST* 3 (2008), S08005. DOI: 10.1088/1748-0221/3/08/S08005.

[50] LHCb collaboration. "Inner tracker technical design report". In: *CERN-LHCC-2002-029* (Nov. 2002).

[51] LHCb collaboration. "Outer tracker technical design report". In: *CERN-LHCC-2001-024* (Sept. 2001).

[52] W.D. Hulsbergen. "The global covariance matrix of tracks fitted with a Kalman filter and an application in detector alignment". In: *Nuclear Instruments and Methods in Physics Research Section A: Accelerators, Spectrometers, Detectors and Associated Equipment* 600.2 (). ISSN: 0168-9002. DOI: 10.1016/j.nima.2008.11.094. URL: http://dx.doi.org/10.1016/j.nima.2008.11.094.

[53] LHCb collaboration. "LHCb calorimeters: Technical design report". In: (Sept. 2000).

[54] T Head. "The LHCb trigger system". In: *JINST* 9 (2014), p. C09015. DOI: 10.1088/1748-0221/9/09/C09015. URL: https://cds.cern.ch/record/2200130.

[55] G. Barrand et al. "GAUDI - A software architecture and framework for building HEP data processing applications". In: *Comput. Phys. Commun.* 140 (2001), pp. 45–55. DOI: 10.1016/S0010-4655(01)00254-5.

[56] M. Clemencic et al. "The LHCb simulation application, Gauss: Design, evolution and experience". In: *J. Phys. Conf. Ser.* 331 (2011). Ed. by Simon C. Lin, p. 032023. DOI: 10.1088/1742-6596/331/3/032023.

[57] Christian Bierlich et al. "A comprehensive guide to the physics and usage of PYTHIA 8.3". In: *SciPost Phys. Codeb.* 2022 (2022), p. 8. DOI: 10.21468/SciPostPhysCodeb.8. arXiv: 2203.11601 [hep-ph].

[58] S. Agostinelli et al. "GEANT4–a simulation toolkit". In: *Nucl. Instrum. Meth. A* 506 (2003), pp. 250–303. DOI: 10.1016/S0168-9002(03)01368-8.

[59] Alexander J. Lenz. "A simple relation for B_s mixing". In: *Phys. Rev. D* 84 (2011), p. 031501. DOI: 10.1103/PhysRevD.84.031501. arXiv: 1106.3200 [hep-ph].

[60] J. Charles et al. "Predictions of selected flavour observables within the Standard Model". In: *Phys. Rev.* D84 (2011). with updated results and plots available at http://ckmfitter.in2p3.fr, p. 033005. DOI: 10.1103/PhysRevD.84.033005. arXiv: 1106.4041 [hep-ph].

[61] Marten Z. Barel et al. "In pursuit of new physics with $B_d^0 \to J/\psi K^0$ and $B_s^0 \to J/\psi\phi$ decays at the high-precision Frontier". In: *J. Phys. G* 48.6 (2021), p. 065002. DOI: 10.1088/1361-6471/abf2a2. arXiv: 2010.14423 [hep-ph].

[62] Ulrich Nierste. "Penguin pollution in β and β_s". In: *PoS* CKM2016 (2017), p. 081. DOI: 10.22323/1.291.0081. arXiv: 1704.04529 [hep-ph].

[63] Georges Aad et al. "Flavor tagged time-dependent angular analysis of the $B_s \to J/\psi\phi$ decay and extraction of $\Delta\Gamma$s and the weak phase ϕ_s in ATLAS". In: *Phys. Rev. D* 90.5 (2014), p. 052007. DOI: 10.1103/PhysRevD.90.052007. arXiv: 1407.1796 [hep-ex].

[64] Georges Aad et al. "Measurement of the CP-violating phase ϕ_s in $B_s^0 \to J/\psi\phi$ decays in ATLAS at 13 TeV". In: *Eur. Phys. J. C* 81.4 (2021), p. 342. DOI: 10.1140/epjc/s10052-021-09011-0. arXiv: 2001.07115 [hep-ex].

[65] Vardan Khachatryan et al. "Measurement of the CP-violating weak phase ϕ_s and the decay width difference $\Delta\Gamma_s$ using the $B_s^0 \to J/\psi\phi(1020)$ decay channel in pp collisions at $\sqrt{s} = 8$ TeV". In: *Phys. Lett. B* 757 (2016), pp. 97–120. DOI: 10.1016/j.physletb.2016.03.046. arXiv: 1507.07527 [hep-ex].

[66] Albert M Sirunyan et al. "Measurement of the CP-violating phase ϕ_s in the $B_s^0 \to J/\psi\,\phi(1020) \to \mu^+\mu^-K^+K^-$ channel in proton-proton collisions at $\sqrt{s} = 13$ TeV". In: *Phys. Lett. B* 816 (2021), p. 136188. DOI: 10.1016/j.physletb.2021.136188. arXiv: 2007.02434 [hep-ex].

[67] R Aaij et al. "Measurement of CP violation and the B_s^0 meson decay width difference with $B_s^0 \to J/^+K^-$ and $B_s^0 \to J/\psi\pi^+\pi^-$ decays". In: *Phys. Rev. D* 87.11 (2013), p. 112010. DOI: 10.1103/PhysRevD.87.112010. arXiv: 1304.2600 [hep-ex].

[68] Roel Aaij et al. "Updated measurement of time-dependent CP-violating observables in $B_s^0 \to J/\psi K^+K^-$ decays". In: *Eur. Phys. J. C* 79.8 (2019). [Erratum: Eur.Phys.J.C 80, 601 (2020)], p. 706. DOI: 10.1140/epjc/s10052-019-7159-8. arXiv: 1906.08356 [hep-ex].

[69] Roel Aaij et al. "First study of the CP -violating phase and decay-width difference in $B_s^0 \to \psi(2S)\phi$ decays". In: *Phys. Lett. B* 762 (2016), pp. 253–262. DOI: 10.1016/j.physletb.2016.09.028. arXiv: 1608.04855 [hep-ex].

[70] Roel Aaij et al. "Measurement of the CP-violating phase ϕ_s in $\bar{B}_s^0 \to D_s^+D_s^-$ decays". In: *Phys. Rev. Lett.* 113.21 (2014), p. 211801. DOI: 10.1103/PhysRevLett.113.211801. arXiv: 1409.4619 [hep-ex].

[71] Roel Aaij et al. "Measurement of the CP-violating phase ϕ_s in $\overline{B}_s^0 \to J/\psi\pi^+\pi^-$ decays". In: *Phys. Lett. B* 736 (2014), pp. 186–195. DOI: 10.1016/j.physletb.2014.06.079. arXiv: 1405.4140 [hep-ex].

[72] Roel Aaij et al. "Measurement of the CP-violating phase ϕ_s from $B_s^0 \to J/\psi\pi^+\pi^-$ decays in 13 TeV pp collisions". In: *Phys. Lett. B* 797 (2019), p. 134789. DOI: 10.1016/j.physletb.2019.07.036. arXiv: 1903.05530 [hep-ex].

[73] Roel Aaij et al. "Resonances and CP violation in B_s^0 and $\overline{B}_s^0 \to J/\psi K^+K^-$ decays in the mass region above the $\phi(1020)$". In: *JHEP* 08 (2017), p. 037. DOI: 10.1007/JHEP08(2017)037. arXiv: 1704.08217 [hep-ex].

[74] R. Aaij et al. "First measurement of the CP-violating phase in $B_s^0 \to J/\psi(\to e^+e^-)\phi$ decays". In: *Eur. Phys. J. C* 81.11 (2021), p. 1026. DOI: 10.1140/epjc/s10052-021-09711-7. arXiv: 2105.14738 [hep-ex].

[75] T. Aaltonen et al. "Measurement of the Bottom-Strange Meson Mixing Phase in the Full CDF Data Set". In: *Phys. Rev. Lett.* 109 (2012), p. 171802. DOI: 10.1103/PhysRevLett.109.171802. arXiv: 1208.2967 [hep-ex].

[76] Victor Mukhamedovich Abazov et al. "Measurement of the CP-violating phase $\phi_s^{J/\psi\phi}$ using the flavor-tagged decay $B_s^0 \to J/\psi\phi$ in 8 fb^{-1} of $p\bar{p}$ collisions". In: *Phys. Rev. D* 85 (2012), p. 032006. DOI: 10.1103/PhysRevD.85.032006. arXiv: 1109.3166 [hep-ex].

[77] M. Kirk, A. Lenz, and T. Rauh. "Dimension-six matrix elements for meson mixing and lifetimes from sum rules". In: *JHEP* 12 (2017). [Erratum: JHEP 06, 162 (2020)], p. 068. DOI: 10.1007/JHEP12(2017)068. arXiv: 1711.02100 [hep-ph].

[78] Anton Poluektov. *Correction of simulated particle identification response in LHCb using kernel density estimation*. Tech. rep. Geneva: CERN, 2017. URL: https://cds.cern.ch/record/2260281.

[79] A. Rogozhnikov. "Reweighting with Boosted Decision Trees". In: *J. Phys. Conf. Ser.* 762.1 (2016). Ed. by Luis Salinas and Claudio Torres, p. 012036. DOI: 10.1088/1742-6596/762/1/012036. arXiv: 1608.05806 [physics.data-an].

[80] Muriel Pivk and Francois R. Le Diberder. "SPlot: A Statistical tool to unfold data distributions". In: *Nucl. Instrum. Meth. A* 555 (2005), pp. 356–369. DOI: 10.1016/j.nima.2005.08.106. arXiv: physics/0402083.

[81] Tomasz Skwarnicki. "A study of the radiative CASCADE transitions between the Upsilon-Prime and Upsilon resonances". PhD thesis. Cracow, INP, 1986.

[82] Ia. Bezshyiko et al. "Improved Measurement of CP Violation Parameters in Bs0J/ψK+K- Decays in the Vicinity of the ϕ(1020) Resonance". In: *Phys. Rev. Lett.* 132.5 (2024), p. 051802. DOI: 10.1103/PhysRevLett.132.051802. arXiv: 2308.01468 [hep-ex].

[83] R. Aaij et al. "Precise determination of the B_s^0–$\overline{B}_s^0$ oscillation frequency". In: *Nature Phys.* 18.1 (2022), pp. 1–5. DOI: 10.1038/s41567-021-01394-x. arXiv: 2104.04421 [hep-ex].

[84] Yuehong Xie. *Iterative method to improve simulation-based detector efficiency description in angular analysis*. Tech. rep. Geneva: CERN, 2013. URL: https://cds.cern.ch/record/1519055.

[85] T Du Pree and G Raven. *Methods for Angular Analyses of $B \to J/\psi X$*. Tech. rep. Geneva: CERN, 2009. URL: https://cds.cern.ch/record/1162609.

[86] Roel et al. Aaij. Tech. rep.

[87] R Aaij et al. "Measurement of the polarization amplitudes in $B^0 \to J/\psi K^*(892)^0$ decays". In: *Phys. Rev. D* 88 (2013), p. 052002. DOI: 10.1103/PhysRevD.88.052002. arXiv: 1307.2782 [hep-ex].

[88] Alberto Bragagnolo et al. *Probing fundamental properties of nature with Heavy Quark Physics at CMS*. Presented in 58th Rencontres de Moriond. March 2024. URL: https://indico.in2p3.fr/event/32664/contributions/137033/attachments/83651/124590/3_ABragagnolo-v2.pdf.

[89] Manzil Zaheer et al. "Deep Sets". In: *CoRR* abs/1703.06114 (2017). arXiv: 1703.06114. URL: http://arxiv.org/abs/1703.06114.

[90] Tianqi Chen and Carlos Guestrin. "XGBoost: A Scalable Tree Boosting System". In: *Proceedings of the 22nd ACM SIGKDD International Conference on Knowledge Discovery and Data Mining*. ACM, Aug. 2016. DOI: 10.1145/2939672.2939785. URL: http://dx.doi.org/10.1145/2939672.2939785.

[91] *Measurement of CP asymmetry in $B_s^0 \to D_s^{\mp}K^{\pm}$ decays*. Tech. rep. Geneva: CERN, 2023. URL: https://cds.cern.ch/record/2873713.

[92] Diego Martinez Santos and Frederic Dupertuis. "Mass distributions marginalized over per-event errors". In: *Nucl. Instrum. Meth. A* 764 (2014), pp. 150–155. DOI: 10.1016/j.nima.2014.06.081. arXiv: 1312.5000 [hep-ex].

[93] P. A. Zyla et al. "Review of Particle Physics". In: *PTEP* 2020.8 (2020), p. 083C01. DOI: 10.1093/ptep/ptaa104.

[94] D. I. Kazakov. "Supersymmetry in particle physics: the renormalization group viewpoint". In: *Phys. Rept.* 344 (2001), pp. 309–353. DOI: 10.1016/S0370-1573(00)00129-0. arXiv: hep-ph/0001257.

[95] Wolfgang Altmannshofer et al. "Anatomy and Phenomenology of FCNC and CPV Effects in SUSY Theories". In: *Nucl. Phys. B* 830 (2010), pp. 17–94. DOI: 10.1016/j.nuclphysb.2009.12.019. arXiv: 0909.1333 [hep-ph].

[96] Adrian Signer. "ABC of SUSY". In: *J. Phys. G* 36 (2009), p. 073002. DOI: 10.1088/0954-3899/36/7/073002. arXiv: 0905.4630 [hep-ph].

[97] Stephen P. Martin. "A Supersymmetry primer". In: *Adv. Ser. Direct. High Energy Phys.* 18 (1998). Ed. by Gordon L. Kane, pp. 1–98. DOI: 10.1142/9789812839657_0001. arXiv: hep-ph/9709356.

[98] Howard E. Haber. "The Status of the minimal supersymmetric standard model and beyond". In: *Nucl. Phys. B Proc. Suppl.* 62 (1998). Ed. by M. Cvetic and P. Langacker, pp. 469–484. DOI: 10.1016/S0920-5632(97)00688-9. arXiv: hep-ph/9709450.

[99] N. Aghanim et al. "Planck 2018 results. VI. Cosmological parameters". In: *Astron. Astrophys.* 641 (2020). [Erratum: Astron.Astrophys. 652, C4 (2021)], A6. DOI: 10.1051/0004-6361/201833910. arXiv: 1807.06209 [astro-ph.CO].

[100] E. Bagnaschi et al. "Likelihood Analysis of the pMSSM11 in Light of LHC 13-TeV Data". In: *Eur. Phys. J. C* 78.3 (2018), p. 256. DOI: 10.1140/epjc/s10052-018-5697-0. arXiv: 1710.11091 [hep-ph].

[101] MasterCode collaboration. *The MasterCode Project*. For information and latest updates visit: http://cern.ch/mastercode/.

[102] F. Feroz and M.P. Hobson. "Title of the Article". In: *Mon. Not. Roy. Astron. Soc.* 384 (2008). [arXiv:0704.3704 [astro-ph]] F. Feroz, M.P. Hobson and M. Bridges, Mon. Not. Roy. Astron. Soc. 398 (2009) 1601-1614 [arXiv:0809.3437 [astro-ph]] F. Feroz, M.P. Hobson, E. Cameron and A.N. Pettitt, [arXiv:1306.2144 [astro-ph]], p. 449.

[103] B. C. Allanach. "SOFTSUSY: a program for calculating supersymmetric spectra". In: *Comput. Phys. Commun.* 143 (2002), pp. 305–331. DOI: 10.1016/S0010-4655(01)00460-X. arXiv: hep-ph/0104145.

[104] S. Heinemeyer, W. Hollik, and G. Weiglein. In: *Comput. Phys. Commun.* 124 (2000). [arXiv:hep-ph/9812320] S. Heinemeyer, W. Hollik and G. Weiglein, Eur. Phys. J. C 9 (1999) 343 [arXiv:hep-ph/9812472] G. Degrassi, S. Heinemeyer, W. Hollik, P. Slavich and G. Weiglein, Eur. Phys. J. C 28 (2003) 133 [arXiv:hep-ph/0212020] M. Frank et al., JHEP 0702 (2007) 047 [arXiv:hep-ph/0611326] T. Hahn, S. Heinemeyer, W. Hollik, H. Rzehak and G. Weiglein, Comput. Phys. Commun. 180 (2009) 1426 T. Hahn, S. Heinemeyer, W. Hollik, H. Rzehak and G. Weiglein, Phys. Rev. Lett. 112 (2014) 14, 141801 [arXiv:1312.4937 [hep-ph]] H. Bahl and W. Hollik, Eur. Phys. J. C 76 (2016) no.9, 499 [arXiv:1608.01880 [hep-ph]] H. Bahl, S. Heinemeyer, W. Hollik and G. Weiglein, Eur.

Phys. J. C 78 (2018) no.1, 57 [arXiv:1706.00346 [hep-ph]] H. Bahl, T. Hahn, S. Heinemeyer, W. Hollik, S. Paeßer, H. Rzehak and G. Weiglein, Comput. Phys. Commun. 249 (2020) 107099 [arXiv:1811.09073 [hep-ph]], p. 76. URL: http://www.feynhiggs.de.

[105] Gino Isidori and Paride Paradisi. "Hints of large tan(beta) in flavour physics". In: *Phys. Lett. B* 639 (2006), pp. 499–507. DOI: 10.1016/j.physletb.2006.06.071. arXiv: hep-ph/0605012.

[106] F. Mahmoudi. "SuperIso: A Program for calculating the isospin asymmetry of $B \to K^*$ gamma in the MSSM". In: *Comput. Phys. Commun.* 178 (2008), pp. 745–754. DOI: 10.1016/j.cpc.2007.12.006. arXiv: 0710.2067 [hep-ph].

[107] Philip Bechtle et al. "Applying Exclusion Likelihoods from LHC Searches to Extended Higgs Sectors". In: *Eur. Phys. J. C* 75.9 (2015), p. 421. DOI: 10.1140/epjc/s10052-015-3650-z. arXiv: 1507.06706 [hep-ph].

[108] Philip Bechtle et al. "*HiggsSignals*: Confronting arbitrary Higgs sectors with measurements at the Tevatron and the LHC". In: *Eur. Phys. J. C* 74.2 (2014), p. 2711. DOI: 10.1140/epjc/s10052-013-2711-4. arXiv: 1305.1933 [hep-ph].

[109] A. Djouadi, M. M. Muhlleitner, and M. Spira. "Decays of supersymmetric particles: The Program SUSY-HIT (SUspect-SdecaY-Hdecay-InTerface)". In: *Acta Phys. Polon. B* 38 (2007). Ed. by K. Fialkowski and B. Muryn, pp. 635–644. arXiv: hep-ph/0609292.

[110] G. Belanger et al. "micrOMEGAs: Version 1.3". In: *Comput. Phys. Commun.* 174 (2006), pp. 577–604. DOI: 10.1016/j.cpc.2005.12.005. arXiv: hep-ph/0405253.

[111] Michele Papucci et al. "Fastlim: a fast LHC limit calculator". In: *Eur. Phys. J. C* 74.11 (2014), p. 3163. DOI: 10.1140/epjc/s10052-014-3163-1. arXiv: 1402.0492 [hep-ph].

[112] O. Buchmueller et al. "The CMSSM and NUHM1 after LHC Run 1". In: *Eur. Phys. J. C* 74.6 (2014), p. 2922. DOI: 10.1140/epjc/s10052-014-2922-3. arXiv: 1312.5250 [hep-ph].

[113] D. S. Akerib et al. "Results from a search for dark matter in the complete LUX exposure". In: *Phys. Rev. Lett.* 118.2 (2017), p. 021303. DOI: 10.1103/PhysRevLett.118.021303. arXiv: 1608.07648 [astro-ph.CO].

[114] Xiangyi Cui et al. "Dark Matter Results From 54-Ton-Day Exposure of PandaX-II Experiment". In: *Phys. Rev. Lett.* 119.18 (2017), p. 181302. DOI: 10.1103/PhysRevLett.119.181302. arXiv: 1708.06917 [astro-ph.CO].

[115] E. Aprile et al. "Dark Matter Search Results from a One Ton-Year Exposure of XENON1T". In: *Phys. Rev. Lett.* 121.11 (2018), p. 111302. DOI: 10.1103/PhysRevLett.121.111302. arXiv: 1805.12562 [astro-ph.CO].

[116] C. Amole et al. "Dark Matter Search Results from the Complete Exposure of the PICO-60 C_3F_8 Bubble Chamber". In: *Phys. Rev. D* 100.2 (2019), p. 022001. DOI: 10.1103/PhysRevD.100.022001. arXiv: 1902.04031 [astro-ph.CO].

[117] E. Aprile et al. "Constraining the spin-dependent WIMP-nucleon cross sections with XENON1T". In: *Phys. Rev. Lett.* 122.14 (2019), p. 141301. DOI: 10.1103/PhysRevLett.122.141301. arXiv: 1902.03234 [astro-ph.CO].

[118] E. Bagnaschi et al. in preparation.

[119] The CMS Collaboration et al. "Search for supersymmetry in proton-proton collisions at 13 TeV in final states with jets and missing transverse momentum". In: *JHEP* 10 (2019), p. 244. DOI: 10.1007/JHEP10(2019)244. arXiv: 1908.04722 [hep-ex].

[120] The CMS Collaboration. "Searches for new phenomena in events with jets and high values of the M_{T2} variable, including signatures with disappearing tracks, in proton-proton collisions at $\sqrt{s} = 13$ TeV". In: (2019).

[121] The CMS Collaboration. "Search for direct τ slepton pair production in proton-proton collisions at $\sqrt{s} = 13$ TeV". In: (2019).

[122] Albert M Sirunyan et al. "Search for new phenomena with the M_{T2} variable in the all-hadronic final state produced in proton–proton collisions at $\sqrt{s} = 13$ TeV". In: *Eur. Phys. J. C* 77.10 (2017), p. 710. DOI: 10.1140/epjc/s10052-017-5267-x. arXiv: 1705.04650 [hep-ex].

[123] M. Aaboud et al. "Search for direct top squark pair production in final states with two leptons in $\sqrt{s} = 13$ TeV pp collisions with the ATLAS detector". In: *Eur. Phys. J. C* 77.12 (2017), p. 898. DOI: 10.1140/epjc/s10052-017-5445-x. arXiv: 1708.03247 [hep-ex].

[124] The CMS collaboration. "Search for top squark pair production in a di-tau final state in proton-proton collisions at $\sqrt{s} = 13$ TeV". In: (2019).

[125] "Search for physics beyond the standard model in events with two same-sign leptons or at least three leptons and jets in proton-proton collisions at $\sqrt{s} = 13$ TeV." In: (2019).

[126] Albert M. Sirunyan et al. "Search for supersymmetric partners of electrons and muons in proton-proton collisions at $\sqrt{s} = 13$ TeV". In: *Phys. Lett. B* 790 (2019), pp. 140–166. DOI: 10.1016/j.physletb.2019.01.005. arXiv: 1806.05264 [hep-ex].

[127] The CMS Collaboration. "Search for direct τ slepton pair production in proton-proton collisions at $\sqrt{s} = 13$ TeV". In: (2019).

[128] A. M. Sirunyan et al. "Search for electroweak production of charginos and neutralinos in multilepton final states in proton-proton collisions at $\sqrt{s} = 13$ TeV". In: *JHEP* 03 (2018), p. 166. DOI: 10.1007/JHEP03(2018)166. arXiv: 1709.05406 [hep-ex].

[129] Albert M Sirunyan et al. "Search for supersymmetry with a compressed mass spectrum in the vector boson fusion topology with 1-lepton and 0-lepton final states in proton-proton collisions at $\sqrt{s} = 13$ TeV". In: *JHEP* 08 (2019), p. 150. DOI: 10.1007/JHEP08(2019)150. arXiv: 1905.13059 [hep-ex].

[130] Morad Aaboud et al. "Search for chargino and neutralino production in final states with a Higgs boson and missing transverse momentum at $\sqrt{s} = 13$ TeV with the ATLAS detector". In: *Phys. Rev. D* 100.1 (2019), p. 012006. DOI: 10.1103/PhysRevD.100.012006. arXiv: 1812.09432 [hep-ex].

[131] CMS collaboration. "Search for supersymmetry in events with tau leptons and missing transverse momentum in proton-proton collisions at sqrt(s)=13 TeV". In: (2017).

[132] Philip Bechtle et al. "Applying Exclusion Likelihoods from LHC Searches to Extended Higgs Sectors". In: *Eur. Phys. J. C* 75.9 (2015), p. 421. DOI: 10.1140/epjc/s10052-015-3650-z. arXiv: 1507.06706 [hep-ph].

[133] Morad Aaboud et al. "Search for additional heavy neutral Higgs and gauge bosons in the ditau final state produced in 36 fb^1 of pp collisions at $\sqrt{s} = 13$ TeV with the

ATLAS detector". In: *JHEP* 01 (2018), p. 055. DOI: 10.1007/JHEP01(2018)055. arXiv: 1709.07242 [hep-ex].

[134] Albert M Sirunyan et al. "Search for additional neutral MSSM Higgs bosons in the $\tau\tau$ final state in proton-proton collisions at $\sqrt{s} = 13$ TeV". In: *JHEP* 09 (2018), p. 007. DOI: 10.1007/JHEP09(2018)007. arXiv: 1803.06553 [hep-ex].

[135] Martin Beneke, Christoph Bobeth, and Robert Szafron. "Power-enhanced leading-logarithmic QED corrections to $B_q \to \mu^+\mu^-$". In: *JHEP* 10 (2019). [Erratum: JHEP 11, 099 (2022)], p. 232. DOI: 10.1007/JHEP10(2019)232. arXiv: 1908.07011 [hep-ph].

[136] M. Misiak et al. "Updated NNLO QCD predictions for the weak radiative B-meson decays". In: *Phys. Rev. Lett.* 114.22 (2015), p. 221801. DOI: 10.1103/PhysRevLett.114.221801. arXiv: 1503.01789 [hep-ph].

[137] M. Bona et al. "New UTfit Analysis of the Unitary Triangle in the Cabibbo-Kobayashi-Maskawa scheme". In: *Rend. Lincei Sci. Fis. Nat.* 34 (2023), pp. 37–57. DOI: 10.1007/s12210-023-01137-5.

[138] Tobias Huber, Tobias Hurth, and Enrico Lunghi. "Inclusive $\overline{B} \to X_s\ell^+\ell^-$: complete angular analysis and a thorough study of collinear photons". In: *JHEP* 06 (2015), p. 176. DOI: 10.1007/JHEP06(2015)176. arXiv: 1503.04849 [hep-ph].

[139] J. P. Lees et al. "Measurement of the $B \to X_s l^+ l^-$ branching fraction and search for direct CP violation from a sum of exclusive final states". In: *Phys. Rev. Lett.* 112 (2014), p. 211802. DOI: 10.1103/PhysRevLett.112.211802. arXiv: 1312.5364 [hep-ex].

[140] M. Iwasaki et al. "Improved measurement of the electroweak penguin process $B \to X_s l^+ l^-$". In: *Phys. Rev. D* 72 (2005), p. 092005. DOI: 10.1103/PhysRevD.72.092005. arXiv: hep-ex/0503044.

[141] Andrzej J. Buras et al. "$K^+ \to \pi^+\nu\overline{\nu}$ and $K_L \to \pi^0\nu\overline{\nu}$ in the Standard Model: status and perspectives". In: *JHEP* 11 (2015), p. 033. DOI: 10.1007/JHEP11(2015)033. arXiv: 1503.02693 [hep-ph].

[142] A. V. Artamonov et al. "Study of the decay $K^+ \to \pi^+\nu\bar{\nu}$ in the momentum region $140 < P_\pi < 199$ MeV/c". In: *Phys. Rev. D* 79 (2009), p. 092004. DOI: 10.1103/PhysRevD.79.092004. arXiv: 0903.0030 [hep-ex].

[143] Eduardo Cortina Gil et al. "Measurement of the very rare $K^+ \to \pi^+\nu\overline{\nu}$ decay". In: *JHEP* 06 (2021), p. 093. DOI: 10.1007/JHEP06(2021)093. arXiv: 2103.15389 [hep-ex].

[144] Weonjong Lee et al. "2022 update on ε_K with lattice QCD inputs". In: *PoS* LATTICE2022 (2023), p. 297. DOI: 10.22323/1.430.0297. arXiv: 2301.12375 [hep-lat].

[145] William J. Marciano. "Precise determination of |V(us)| from lattice calculations of pseudoscalar decay constants". In: *Phys. Rev. Lett.* 93 (2004), p. 231803. DOI: 10.1103/PhysRevLett.93.231803. arXiv: hep-ph/0402299.

[146] N. Arkani-Hamed, A. Delgado, and G. F. Giudice. "The Well-tempered neutralino". In: *Nucl. Phys. B* 741 (2006), pp. 108–130. DOI: 10.1016/j.nuclphysb.2006.02.010. arXiv: hep-ph/0601041.

[147] E. Bagnaschi et al. "Likelihood Analysis of the pMSSM11 in Light of LHC 13-TeV Data". In: *Eur. Phys. J. C* 78.3 (2018), p. 256. DOI: 10.1140/epjc/s10052-018-5697-0. arXiv: 1710.11091 [hep-ph].

[148] F. Gabbiani and A. Masiero. "FCNC in Generalized Supersymmetric Theories". In: *Nucl. Phys. B* 322 (1989), pp. 235–254. DOI: 10.1016/0550-3213(89)90492-6.

[149] Janusz Rosiek. "Complete set of Feynman rules for the MSSM: Erratum". In: (Nov. 1995). arXiv: hep-ph/9511250.

[150] Veronika Chobanova et al. "Probing SUSY effects in $K_S^0 \to \mu^+\mu^-$". In: *JHEP* 05 (2018), p. 024. DOI: 10.1007/JHEP05(2018)024. arXiv: 1711.11030 [hep-ph].

[151] D. Martínez Santos et al. "Ipanema-\beta : tools and examples for HEP analysis on GPU". In: (June 2017). arXiv: 1706.01420 [hep-ex].

[152] E. Bagnaschi et al. "Likelihood Analysis of the Minimal AMSB Model". In: *Eur. Phys. J. C* 77.4 (2017), p. 268. DOI: 10.1140/epjc/s10052-017-4810-0. arXiv: 1612.05210 [hep-ph].

[153] Kunio Kaneta et al. "Quantifying limits on CP violating phases from EDMs in supersymmetry". In: *JHEP* 03 (2023), p. 250. DOI: 10.1007/JHEP03(2023)250. arXiv: 2303.02822 [hep-ph].

[154] W. Dekens et al. "The phenomenology of electric dipole moments in models of scalar leptoquarks". In: *JHEP* 01 (2019), p. 069. DOI: 10.1007/JHEP01(2019)069. arXiv: 1809.09114 [hep-ph].

[155] Andreas Crivellin and Francesco Saturnino. "Correlating tauonic B decays with the neutron electric dipole moment via a scalar leptoquark". In: *Phys. Rev. D* 100.11 (2019), p. 115014. DOI: 10.1103/PhysRevD.100.115014. arXiv: 1905.08257 [hep-ph].

[156] Francesca Borzumati and Christoph Greub. "2HDMs predictions for anti-B —> X(s) gamma in NLO QCD". In: *Phys. Rev. D* 58 (1998), p. 074004. DOI: 10.1103/PhysRevD.58.074004. arXiv: hep-ph/9802391.

[157] Motoi Endo et al. "Gluino-mediated electroweak penguin with flavor-violating trilinear couplings". In: *JHEP* 04 (2018), p. 019. DOI: 10.1007/JHEP04(2018)019. arXiv: 1712.04959 [hep-ph].

[158] M. A. Boussejra, F. Mahmoudi, and G. Uhlrich. "Flavor anomalies in supersymmetric scenarios with nonminimal flavor violation". In: *Phys. Rev. D* 106.1 (2022), p. 015018. DOI: 10.1103/PhysRevD.106.015018. arXiv: 2201.04659 [hep-ph].

[159] Luca Di Luzio et al. "ΔM_s theory precision confronts flavour anomalies". In: *JHEP* 12 (2019), p. 009. DOI: 10.1007/JHEP12(2019)009. arXiv: 1909.11087 [hep-ph].

[160] Cheng-Wei Chiang et al. "New Physics in $B0(s) \to J/psiphi$: A General Analysis". In: *JHEP* 04 (2010), p. 031. DOI: 10.1007/JHEP04(2010)031. arXiv: 0910.2929 [hep-ph].

[161] Andrzej J. Buras, Diego Guadagnoli, and Gino Isidori. "On ϵ_K Beyond Lowest Order in the Operator Product Expansion". In: *Phys. Lett. B* 688 (2010), pp. 309–313. DOI: 10.1016/j.physletb.2010.04.017. arXiv: 1002.3612 [hep-ph].

[162] J. P. Lees et al. "Measurements of direct CP asymmetries in BX_s decays using sum of exclusive decays". In: *Phys. Rev. D* 90.9 (2014), p. 092001. DOI: 10.1103/PhysRevD.90.092001. arXiv: 1406.0534 [hep-ex].

[163] C. Abel et al. "Measurement of the Permanent Electric Dipole Moment of the Neutron". In: *Phys. Rev. Lett.* 124.8 (2020), p. 081803. DOI: 10.1103/PhysRevLett.124.081803. arXiv: 2001.11966 [hep-ex].

[164] B. Graner et al. "Reduced Limit on the Permanent Electric Dipole Moment of Hg199". In: *Phys. Rev. Lett.* 116.16 (2016). [Erratum: Phys.Rev.Lett. 119, 119901 (2017)], p. 161601. DOI: 10.1103/PhysRevLett.116.161601. arXiv: 1601.04339 [physics.atom-ph].

[165] Yue Meng et al. "Dark Matter Search Results from the PandaX-4T Commissioning Run". In: *Phys. Rev. Lett.* 127.26 (2021), p. 261802. DOI: 10.1103/PhysRevLett.127.261802. arXiv: 2107.13438 [hep-ex].

[166] J. Aalbers et al. "First Dark Matter Search Results from the LUX-ZEPLIN (LZ) Experiment". In: *Phys. Rev. Lett.* 131.4 (2023), p. 041002. DOI: 10.1103/PhysRevLett.131.041002. arXiv: 2207.03764 [hep-ex].

[167] E. Aprile et al. "First Dark Matter Search with Nuclear Recoils from the XENONnT Experiment". In: *Phys. Rev. Lett.* 131.4 (2023), p. 041003. DOI: 10.1103/PhysRevLett.131.041003. arXiv: 2303.14729 [hep-ex].

[168] Marzia Bordone, Bernat Capdevila, and Paolo Gambino. "Three loop calculations and inclusive Vcb". In: *Phys. Lett. B* 822 (2021), p. 136679. DOI: 10.1016/j.physletb.2021.136679. arXiv: 2107.00604 [hep-ph].

[169] Y. Aoki et al. "FLAG Review 2021". In: *Eur. Phys. J. C* 82.10 (2022), p. 869. DOI: 10.1140/epjc/s10052-022-10536-1. arXiv: 2111.09849 [hep-lat].

[170] A. Lenz et al. "Anatomy of New Physics in $B - \bar{B}$ mixing". In: *Phys. Rev. D* 83 (2011), p. 036004. DOI: 10.1103/PhysRevD.83.036004. arXiv: 1008.1593 [hep-ph].

[171] William J. Marciano. "Precise determination of |V(us)| from lattice calculations of pseudoscalar decay constants". In: *Phys. Rev. Lett.* 93 (2004), p. 231803. DOI: 10.1103/PhysRevLett.93.231803. arXiv: hep-ph/0402299.

[172] Andrzej J. Buras and Diego Guadagnoli. "Correlations among new CP violating effects in Δ F = 2 observables". In: *Phys. Rev. D* 78 (2008), p. 033005. DOI: 10.1103/PhysRevD.78.033005. arXiv: 0805.3887 [hep-ph].

[173] Joachim Brod and Martin Gorbahn. "$_K$ at Next-to-Next-to-Leading Order: The Charm-Top-Quark Contribution". In: *Phys. Rev. D* 82 (2010), p. 094026. DOI: 10.1103/PhysRevD.82.094026. arXiv: 1007.0684 [hep-ph].

[174] Jon A. Bailey et al. "Standard Model evaluation of ε_K using lattice QCD inputs for $\hat{B}_K$ and V_{cb}". In: *Phys. Rev. D* 92.3 (2015), p. 034510. DOI: 10.1103/PhysRevD.92.034510. arXiv: 1503.05388 [hep-lat].

[175] Miriam Lucio Martinez. "New Physics implications and searches at LHCb". PhD thesis. Universidad de Santiago de Compostela, 2019.

[176] Junji Hisano, Minoru Nagai, and Paride Paradisi. "Flavor effects on the electric dipole moments in supersymmetric theories: A beyond leading order analysis". In: *Phys. Rev. D* 80 (2009), p. 095014. DOI: 10.1103/PhysRevD.80.095014. arXiv: 0812.4283 [hep-ph].

[177] Junji Hisano, Minoru Nagai, and Paride Paradisi. "New Two-loop Contributions to Hadronic EDMs in the MSSM". In: *Phys. Lett. B* 642 (2006), pp. 510–517. DOI: 10.1016/j.physletb.2006.07.073. arXiv: hep-ph/0606322.

Agradecimientos

Antes de terminar, me gustaría agradecer a todo el mundo que me he encontrado en este camino y que de una manera o otra me ha ayudado a escribir esta tesis doctoral. Me temo, por desgracia, que las pocas palabras que escriba aquí no serán suficientes para mostrar el enorme agradecimiento que siento por muchas de las personas aquí mencionadas. La experiencia del doctorado ha sido una época increíble, llena de altibajos, pero sin duda considero que ha merecido la pena y en gran parte es gracias a vosotros.

Me gustaría empezar por agradecer a mis maestros en el día a día, Veronika y Diego. Desde el punto de vista académico siempre digo que si he aprovechado este tiempo para adquirir un 10% de la intuición de Diego y un 10% de la capacidad de liderazgo de Veronika, me voy siendo un muy buen científico. Sin embargo, mi agradecimiento va más allá del mundo académico, y os quería dar las gracias de verdad por haberme ayudado tanto y por haber confiado siempre en mi.

Las siguientes personas que quiero agradecer personalmente son a Marcos y a Miriam, que vienen siendo mis hermanos mayores académicos. Me gustaría agradeceros por todas las horas que hemos estado discutiendo, tanto de física como de la vida, por todos los problemas que hemos resuelto juntos y por todo lo que me habéis ayudado, siempre que lo he pedido, sin esperar nada a cambio. De verdad, todo lo que escriba no os hace justicia, no sabéis lo importantes que habéis sido para mí a lo largo de este proceso.

Los siguientes son mis amigos del despacho 26, con los que he compartido esta vivencia tan única, y desesperante a veces, de ser estudiante de doctorado en la Universidad de Santiago. Desde la vieja guardia, Miguelito, Alex, Adrián, Gonzalo y Gabi, hasta la nueva con John, Dullas, Saúl, Pablo y Asier. Con estos tres últimos he vivido quizá más momentos si cabe, por haberme acompañado en todo el proceso y por habernos pasado horas y horas quejándonos de todo, os doy las gracias. Que difícil habría sido este camino sin vosotros. Quiero también agradecer a otros compañeros del IGFAE, como Ale, Vero, Oscar, Juanito, Jorge Castelo, Alicia y Carlos con los que también tuve el privilegio de compartir grandes momentos.

Agradecer a Máximo, por introducirme en la Física de Partículas y por amablemente aceptar a leer y mejorar esta tesis doctoral.

Agradecido también a Carlos, Eloi y Erl, que han hecho de mi estancia en el soporífero St Gennis una experiencia inolvidable.

To all the awesome scientists with whom I have the privilege to work, and that have shown me the real meaning of science. I will try not to forget anyone, but unfortunately, memory is not my greatest quality. To the phis analysis crew, especially to Kechen, Sevda, Lera, and Peilian for all the hours we dedicated to such a stupid angle. To the MasterCode collaboration, especially to John, Ian, and Emanuele. To Quentin, my FT friend. To Teppei Kitahara, for everything you have taught me about physics and for always being available to discuss with me. To Nazila and Amine, for the warm welcome to your wonderful Lyon group. To Johannes for allowing me to give my first seminar, and for teaching me so much in such a short time.

A mis amigos de la carrera de Física, el legendario grupo del Squad Tordoya.

Quiero agradecer también a mis amigos de Ourense, mi querida ciudad, que de una manera u otra me han formado como persona.

A Uxía, por ser la primera sonrisa con la que compartir la celebración, y mi último y más importante apoyo cuando sentía que me iba a caer.

Finalmente, agradecer a mi querida familia, mis abuelos, mi tía, mis hermanas y mis padres. Por enseñarme los valores que ahora rigen mi vida y por mostrarme el significado del amor incondicional.

The Standard Model (SM) is a quantum field theory that describes elementary particles and their interactions. While its predictions have been repeatedly confirmed by experiments, it cannot explain several phenomena such as dark matter and the matter-antimatter asymmetry. Therefore, new physics (NP) models are needed. This thesis explores these issues in three ways. First, the most accurate measurement of the CP-violation parameter φs, is achieved to test the SM. Second, advancements in the flavor tagging algorithm using the inclusive approach are analyzed to enhance future measurements. Finally, the implications of the latest flavor precision measurements in the context of supersymmetric models, which address some of the limitations of the SM, are reported in this thesis.